MODELING AND TECHNOLOGY DEVELOPMENT FOR SENSITIVE NEAR-SOLAR PARTICLE MEASUREMENTS

by

Pran R. Mukherjee

A dissertation submitted in partial fulfillment
of the requirements for the degree of
Doctor of Philosophy
(Atmospheric and Space Sciences)
in The University of Michigan
2008

Doctoral Committee:

Professor Thomas H. Zurbuchen, Co-chair
Associate Professor Lingjie Jay Guo, Co-chair
Professor Brian E. Gilchrist
Fred A. Herrero, NASA Goddard Space Flight Center

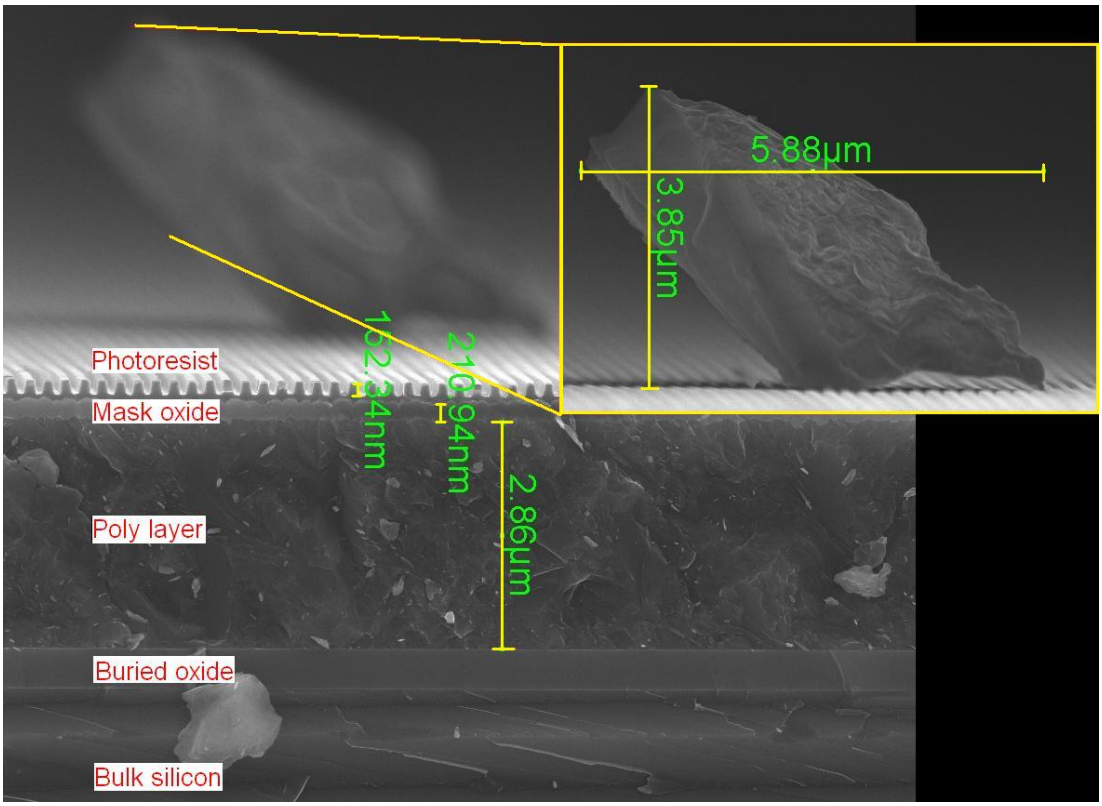

Foreign Body

To Jennifer, the love of my life.

ACKNOWLEDGEMENTS

This is the part where I get to thank all the people who helped me get through this. And there were a lot of them. Chief among them are my parents, Prasun and Chumkie, who were always there to cheer me on through successes, encourage me after failures, and generally just listen to me ramble on about things that they likely neither understood nor cared about. My fiancée, Jennifer Wass, did all those things as well, and I also need to thank her for letting me stay up until stupid o'clock working on this document for night after night after night.

My committee, of course, have been very important to this entire process. Thomas Zurbuchen, my advisor, has always believed that I was on to something even during the bad parts of this research when all the stacked failures had me wondering what it was all for. Jay Guo, my co-advisor, helped immensely with the fabrication portion of the research, and without him and his group I would never have gotten traction in the lab. Fred Herrero from Goddard Space Flight Center not only helped with some of the technical aspects of the work, but he also was instrumental in funding it in the first place. And Brian Gilchrist was always there to listen when I needed an outside ear to bounce ideas off of.

I would also like to thank the staff and users of the University of Michigan's Lurie Nanofabrication Facility for their assistance with tools and process parameters. Rob Hower taught me most of what I know about lab operations. Brian Vanderelzen helped me build and endlessly tweak my etch recipes. Matt Oonk and Cedric Whitney trained me on most of the thin film tools. Phil Collica always hooked me up with

the good stuff at the lab store. Ning Gulari, Katharine Beach, and Ed Tang helped with all those niggling process details that are so essential at the sharp end of the spear. And an endless list of students and outside users have helped with one thing or another; if we hadn't helped one another out so many things would remain undone.

My two groups of collegiate colleagues in particular have been of great help. Myung-Gyu Kang, Larry Cheng, Phil Choi, Tao Ling, Se-Hyun Ahn, and Brandon Lucas helped with everything from nanoimprinting to taking optical transmission spectra. Sue Lepri, Pat Koehn, Angie Richard, and Jason Gilbert all went through the same rigamarole as I did, and helped with the day-to-day things. Thanks, guys!

My tidally shifting group of friends kept me sane through all of this. They mostly skipped my blog posts about lab work, but that's OK. From my Ann Arbor group are: Earl Brown, Joel Dillon and Holly Richardson, Sarah Rigg and Jeff Kaatz, Janann Dawkins, Rob Frazine, Mark Renouf, Joe and Kim Mancuso, Dave Morris, Markus Nee, Norm and Lena Adams, Judy Yu and Bret Squire. From the Boston Crew, a.k.a. Ann Arbor East: Mark Stock and Eleanor Howe, Chris and Jen Dwan, Len Smith and Claudia Bowman. Thanks for being my friends, guys; that's what it's all about.

Thanks also go to Mark Stock, Patrick Koehn, Benjamin Lynch, and Jared Bell for the LaTeX templates they provided, and to Jason Gilbert for working with me to sort through the varied versions and find/build the best one.

And last, and for once actually least, I must thank my fuzzy beasties for helping keep my mood positive. So to the ever-squishable R.T. Moose (Artemis), who once lived as a Latvian paratrooper, and the dainty Thena, thanks for being such good pillows and bookends.

If I forgot anyone, it's because my brain has turned to pudding in the past weeks, not because I don't appreciate you. So, to all those others in my life, thanks for being here and sorry about the omission.

TABLE OF CONTENTS

LIST OF FIGURES

Figure

LIST OF TABLES

Table

LIST OF APPENDICES

Appendix

LIST OF ABBREVIATIONS

ACE Advanced Composition Explorer, a NASA mission

ALD atomic layer deposition

AU astronomical unit

BATSRUS Block Adaptive-Tree Solar Wind Roe-Type Upwind Scheme, a global MHD model

BHF buffered hydrofluoric acid

BOX buried oxide

CMOS complementary metal oxide semiconductor

CVD chemical vapor deposition

DRIE deep-reactive ion etch

ECR electron-cyclotron resonance

EDM electro-discharge machining

EDP ethelene-diamine pyrocatechol

EIT Extreme Ultraviolet Imaging Telescope, on SOHO

ENA energetic neutral atoms

ESA electrostatic analyzer

EUV extreme ultraviolet

FIB focused ion beam

FIPS Fast Imaging Plasma Spectrometer, on the NASA MESSENGER mission

HF hydrofluoric acid

HMDS hexamethyldisilazane (from Transene Corp.)

GSFC Goddard Space Flight Center

HNA a mixture of hydrofluoric acid, nitric acid, and acetic acid

IC integrated circuit

ICP inductively coupled plasma

IMAGE Imaging from the Magnetopause to the Aurora for Global Exploration, a NASA mission

KOH potassium hydroxide

LENA Low Energy Neutral Atom, on IMAGE

LIL laser interference lithography

LPCVD low pressure chemical vapor deposition

Ly-α Lyman-alpha

MCP microchannel plate

MEMS microelectromechanical systems

MENA Medium Energy Neutral Atom, on IMAGE

MESSENGER MErcury Surface, Space ENvironment, GEochemistry, and Ranging, a NASA mission

MHD magneto-hydrodynamic

MIT Massachusetts Institute of Technology

MPI multiphoton ionization

NASA the National Aeronautics and Space Administration

NEMS nanoelectromechanical systems

NIL nanoimprint lithography

OBT optical breakdown threshold

PECVD plasma enhanced chemical vapor deposition

PFPE perfluoropolyether

PMMA polymethyl methacrylate

PUI pickup ions

PVD physical vapor deposition

RF radio frequency

RIE reactive ion etching

SCS single crystal silicon

SEM scanning electron microscope

SFIL step-and-flash imprint lithography

SI the International System of Units

SOI silicon-on-insulator

SOHO Solar and Heliospheric Observatory, a joint mission between NASA and the European Space Agency

SRIM Stopping Range of Ions in Matter

SSD solid-state detector

SPP surface plasmon polaritons

SWICS Solar Wind Ion Composition Spectrometer, on ACE

TE transverse electric

TEM transverse electromagnetic

TM transverse magnetic

TMAH tetramethylammonium hydroxide

TOF time-of-flight

UV ultraviolet

ABSTRACT

MODELING AND TECHNOLOGY DEVELOPMENT FOR SENSITIVE NEAR-SOLAR PARTICLE MEASUREMENTS

by

Pran R. Mukherjee

Co-Chairs: Thomas H. Zurbuchen and Lingjie Jay Guo

The focus of this dissertation is the advancement of near-solar in-situ particle measurement techniques. Populations of dust, neutral atoms, and pickup H^+ ions from 1.4 to 305 solar radii ($R_\odot$) are numerically modeled and scaled to measured data at 1.35 AU, and a measurement-enabling ultraviolet (UV) suppression grating for near-solar sensors is designed, fabricated, and tested.

Dust grains within heliocentric distances of 50 $R_\odot$ absorb solar wind ions and re-emit them as neutral atoms that are quickly ionized and picked up by the solar wind. A parameterized model demonstrates the importance of the grains' azimuthal velocity and the high speed of near-solar Alfvén waves on the dynamic evolution of these ions. Pickup ion density is calculated using the continuity equation and adiabatic cooling models. This analysis shows very clearly that these additional velocity components cause density peaks much sharper and closer to the Sun than previously assumed, definitely inside of 15 $R_\odot$ and quite possibly within five $R_\odot$.

An instrument for the Solar Probe Plus mission is designed and fluxes of neutral hydrogen and solar Lyman-alpha are calculated. This instrument design is used to

develop constraints for a UV blocking filter which enables the needed measurements. The micromachining technologies used in CMOS and MEMS are applied to the fabrication of freestanding, self-supported silicon nanogratings to block solar UV while allowing particles through for subsequent measurement. Nanoimprint lithography patterns 120 nm half-pitch gratings which are then etched to aspect ratios of >20 by breakthrough deep-reactive ion etch techniques. A custom carrier allows double-sided etching to free the grating without damage while leaving a built-in support grid.

The efficacy of a grating in blocking UV light depends upon the grating geometry, the material or materials it is built with, and the polarization of the light. Silicon is far stronger than the gold previously used for this purpose, and when complemented by conformal thin film coatings should be capable of meeting the design specification. The slit widths of the fabricated gratings are currently too wide for the target application, but the measured transmission of the grating between 190-250 nm is shown to be 10^{-4}.

CHAPTER I

Introduction and Background

The study of solar and heliospheric phenomena has advanced by leaps and bounds since man first looked at the stars in awe. The beginning of the space age, marked by the launches of Sputnik in 1957 and Explorer 1 in 1958, was a milestone in our understanding of the physical phenomena outside the Earth's atmosphere. Since then, both ground-based and space-based instruments have steadily increased in capability, and the data they have collected has been used to enhance our knowledge of the space environment. Spacecraft have orbited Earth, flown to the Moon, visited inner and outer planets, and even soared to the boundary of our heliosphere, using a wide variety of instruments to sample their environment both in-situ and remotely. But there are still many unanswered questions. Among them are the physical mechanisms controlling the heating of the Sun's upper atmosphere; the acceleration of the solar wind; and the source, ionization, and acceleration of neutral particles near the Sun.

Measurements of near-solar phenomena have, by necessity, all been remote. For example, the Zeeman Effect has been used to optically measure the magnetic field on the Sun (*Landi Degl'Innocenti*, 2003). Also, ultraviolet (UV) and white-light measurements have been used to model the velocity distributions of protons, electrons, and minor ions near the Sun, outflow velocities of protons, and densities of electrons (*Romoli et al.*, 1998; *Cranmer et al.*, 1999; *Strachan et al.*, 2002; *Kohl et al.*,

2006). These measurements, often line-integrated or time-averaged, lead to models with built-in assumptions of local conditions. In-situ data would be invaluable in validating and enhancing the accuracy of the models (*McComas et al.*, 2007). In order for satellites to take such measurements close to the Sun, significant engineering breakthroughs are required. In particular, there need to be advances in the areas of detector technology, power management, and especially the filtration of background ultraviolet light. Miniaturization of components can significantly assist many of these goals since smaller parts have less mass, absorb less heat, and generally require less power (*JPL*, 1993; *Muller*, 1995; *Muller et al.*, 1996). This dissertation addresses one key problem of heliospheric physics: the detection of neutral ions near the Sun. First a model of the near-solar distributions of dust particles, neutral atoms, and pickup ions is derived. Then a freestanding nano-grating used to filter background ultraviolet light, a critica component for particle sensors near the Sun, is designed and manufactured.

The rest of this chapter will be organized as follows. Some basic facts about the Sun and solar wind will be introduced in § 1.1, and the state of current models will be discussed. Section 1.2 will cover neutral atoms, ionization mechanisms, and pickup ions. Current instrumentation and measurement techniques will be broadly summarized in § 1.3, and the need for miniaturization will be discussed in § 1.4. Finally, § 1.5 will provide an overview for the rest of the dissertation.

1.1 The Sun and the Solar Wind

The Sun is a normal main-sequence star with spectral class G2V, a yellow dwarf variable star, and magnitude 4.8, one of more than 100 billion stars in our galaxy. Its main interest to humans is that it floats at the heart of our home star system and provides the energy that drives life on Earth. By far the largest object in the Solar System, the Sun contains more than 99.8% of the system's total mass. Most

stars in our galaxy are probably under half the mass of the Sun. At present, the Sun is approximately 74.91% hydrogen and 23.77% helium, with everything else, the so-called "heavy elements" (C, N, O, Ne, Mg, Si, S, Fe, and so on), amounting to 1.33% (*Lodders*, 2003; *Asplund et al.*, 2006). The so-called "Standard Model" of the Sun is under constant modification based on new measurements from neutrino detectors and heliosiesmological sensors (*Guenther et al.*, 1992; *Turck-Chièze and Lopes*, 1993; *Couvidat et al.*, 2003; *Turck-Chièze et al.*, 2004; *Basu and Antia*, 2008).

At 4.57 billion years old, the Sun is almost halfway through its main sequence, meaning that it has used up nearly half of the hydrogen at its core. Table 1.1 summarizes some fundamental properties of the Sun from the National Aeronautics and Space Administration (NASA)'s Sun Fact Sheet[a].

Table 1.1: Fundamental Properties of the Sun

Property (units)	**Value**	**Sun/Earth Ratio**
Mass (kg)	1.9891×10^{30}	332,830
Equatorial Radius (m)	6.96×10^{8}	109.2
Mean density (kg/m^3)	1408	0.255
Luminosity (J/s)	3.846×10^{26}	
Mass conversion rate (kg/s)	4.3×10^{9}	
Mean energy production (J/kg)	1.937×10^{-4}	
Surface Gravity (m/s^2)	274.0	28
Surface escape velocity (km/s)	617.6	55.2
Rotation period, equatorial (in Earth days)	25.4	
Rotation period, polar (in Earth days)	up to 36	
Obliquity (tilt of axis degrees)	7.25	
Mean photospheric temperature (K)	5778	
Mean core temperature (K)	1.5710×10^{7}	

Much of the Sun, and in fact over 99% of the universe, is filled with plasma, the so-called fourth state of matter. A plasma is defined by *Chen* (1984) as "a quasi-neutral gas of charged and neutral particles which exhibits collective behavior". The term quasi-neutral is critical. It means that the number of positively-charged ions

[a]http://nssdc.gsfc.nasa.gov/planetary/factsheet/sunfact.html

and negatively-charged electrons in the plasma are in charge balance over a relatively small distance called the Debye Length. Plasmas can be very concentrated, such as those found inside the STS plasma etch tool used in the fabrication portion of this dissertation (ion density over 10^{12} cm^{-3} according to *Bhardwaj and Ashraf* (1995)), or very diffuse such as the plasmas found in space ($\sim$ 5 cm^{-3} at 1 astronomical unit (AU)[b]).

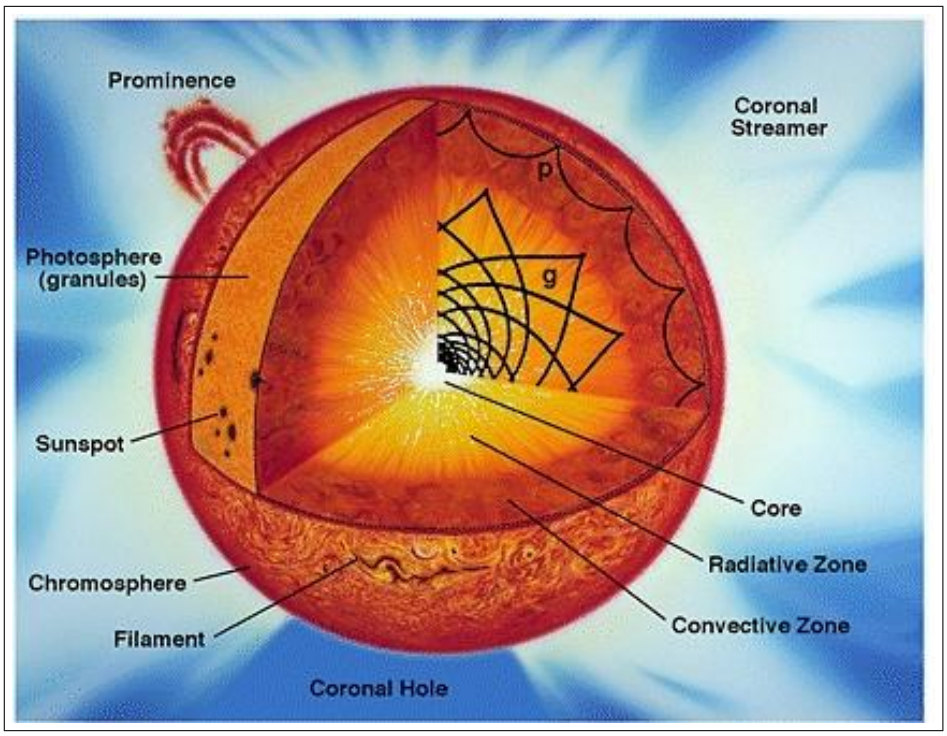

Figure 1.1: Schematic of the Sun and solar atmosphere. In addition to the solar structure, the illustration includes pressure (p-mode) and gravity (g-mode) waves in the interior of the Sun.

1.1.1 Solar Structure and Atmosphere

According to *Gombosi* (1998), the Sun is composed of four main regions: the core, the radiative zone, the convective zone, and the atmosphere, as seen in Figure 1.1. The

[b]One astronomical unit is defined as the distance from the center of the Sun at which a particle of negligible mass, in an unperturbed circular orbit, would have an orbital period of 365.2568983 days (one Gaussian year), or 149,597,870,691 $\pm$ 30 meters (nearly 150 million kilometers or 93 million miles). This definition gives a value that is slightly less than the mean Earth-Sun distance.

core is approximately 1/4 the radius of the Sun (1/64-th its volume), but contains about half its mass. The high temperature (1.5×10^7 K) and density (1.5×10^5 kg m^{-3}) at the Sun's core causes the continuous nuclear fusion of hydrogen into helium, called the proton-proton (or p-p) chain. The p-p chain is a four-step series of thermonuclear reactions that converts four protons to one helium nucleus, neutrinos, and energy equal to the net difference in mass. This reaction is the source of the majority of the Sun's energy—though there are many other fusion reactions taking place (*Adelberger et al.*, 1998)—and also the main reason that the Sun slowly loses mass over time. The core is hot enough that the plasma consists of electrons and bare atomic nuclei. To 0^{th} order, a hydrostatic equilibrium can be used to approximate the radial momentum balance inside the Sun, indicating that a combination of plasma pressure and radiative pressure balances the inward pull of gravity (*Gombosi*, 1998).

The energy produced in the core is transported through the radiative zone by radiation repeatedly absorbed and re-emitted for up to a million years before reaching plasma cool enough for atomic nuclei to retain electrons. This is the base of the convection zone, on the order of 10^6 Kelvin. The convection zone is the outermost 30% of the solar interior, a region of large radial temperature gradients composed of continuously "boiling" blobs of plasma that carry heat and magnetic flux outward, expanding and cooling as they rise. Once cooled, they then subduct back below the surface. This gives the surface of the Sun the appearance of boiling granules. As a non-solid body, the differentiation between the Sun and the solar atmosphere is a rather arbitrary one. From *Gombosi* (1998), "the solar surface is defined as the location where the optical depth of a $\lambda = 5000$ Å photon is 1, meaning the probability of a photon escaping this surface is 1/e".

Study of the interior of the Sun is primarily accomplished via detection and analysis of solar oscillations and electron neutrinos. The field of helioseismology uses the so-called 5-minute pressure (p-mode) waves to determine the speed of sound in,

and thus the density of, the convective zone (*Christensen-Dalsgaard*, 2003). Gravity (g-mode) waves are as-yet theoretical since they are evanescent outside the radiative zone, but *Turck-Chièze et al.* (2004) have claimed 90% likelihood of detection for groups of g-mode waves, as opposed to individual waves. Electron neutrinos are a by-product of the p-p fusion cycle in the core, and for years measurements of electron neutrinos did not match theoretical predictions from helioseismology, the so-called "solar neutrino problem". The problem was conditionally solved between 1998 and 2002 when it became clear that the bulk of the solar electron neutrino population was changing form to become tau neutrinos or muon neutrinos, a consequence of their newly-discovered non-zero mass. Experiments to prove this and bring the neutrino measurements and helioseismology together into a coherent model are still ongoing, though the majority of the problem has been solved (*Bandyopadhyay et al.*, 2003; *Fogli et al.*, 2003; *McDonald et al.*, 2003).

The Sun's atmosphere is divided into three layers: the photosphere, the chromosphere, and the corona. The photosphere is a nearly neutral gas layer under 1000 kilometers thick, but it emits over 99% of the energy generated in the solar core. It extends from the solar surface, where the temperature is 6500 K, to the point at which the temperature reaches a minimum of approximately 4300 K. The chromosphere is a layer of nearly transparent glowing gas a few thousand kilometers thick, in which the temperature rises to 20000 K. This temperature increase over such a short distance indicates a significant energy input, possibly absorption of acoustic waves from the convection zone.

Above the chromosphere is the corona, a tenuous, magnetically active region with temperatures well over 10^6 K. The source of energy that heats the corona to two orders of magnitude above the underlying chromosphere is unknown. Competing theories include Alfvén wave heating (*Priest et al.*, 2000), turbulence, magnetic reconnection, and dissipation of electric currents.

Older models include an atmospheric transition region between the chromosphere and the corona where the temperature rises from 10^4 to 10^6, but this does not adequately reflect the complexity of the region. The major energy source for the corona is known to be the intense and dynamic magnetic field of the Sun, which continuously evolves due to the Sun's internal and surface physical processes (*Curdt et al.*, 2005). The magnetic field is visible to UV and X-ray cameras as loops and streams of hot, glowing plasma, and the taller the loop the hotter the plasma riding the loop. Thus, the so-called "transition layer" is a region through which loops of varying height, and thus varying temperature, pass, with the higher, hotter loops only reaching the upper limits. Stratifying this dynamic system as a linear rise of mean temperature is no longer supported given the more recent observations.

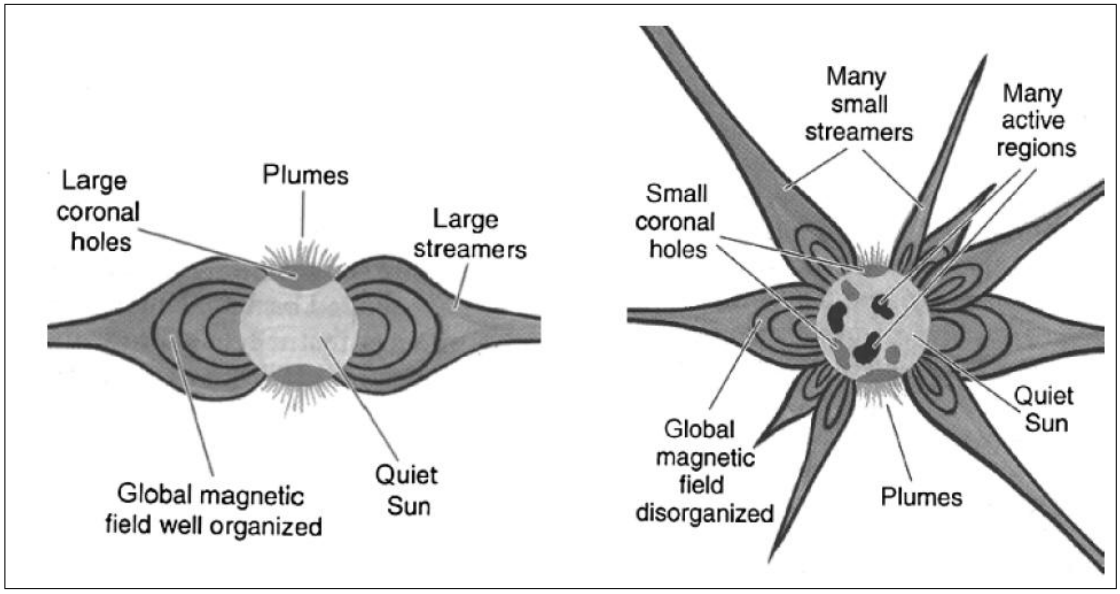

Figure 1.2: A schematic view of the solar corona during solar minimum (left) and maximum (right). From *Issautier* (2006).

The large-scale solar magnetic polarity reverses itself approximately every 11.6 years, a process known as the solar cycle. At solar minimum the coronal magnetic field is very organized, nearly a dipole, but during the maximum of solar activity a significant amount of disorder enters the system as seen in Figure 1.2. In particular,

during solar maximum one can find coronal holes—regions of cooler plasma and open magnetic field lines—at areas other than the poles (*Miralles et al.*, 2006).

Figure 1.3 shows images from various layers of the chromosphere and corona taken by the Extreme Ultraviolet Imaging Telescope (EIT) (*Delaboudinière et al.*, 1995) aboard the Solar and Heliospheric Observatory (SOHO)[c] (*Domingo et al.*, 1995), and demonstrates the sharp rise in temperature with altitude in the corona.

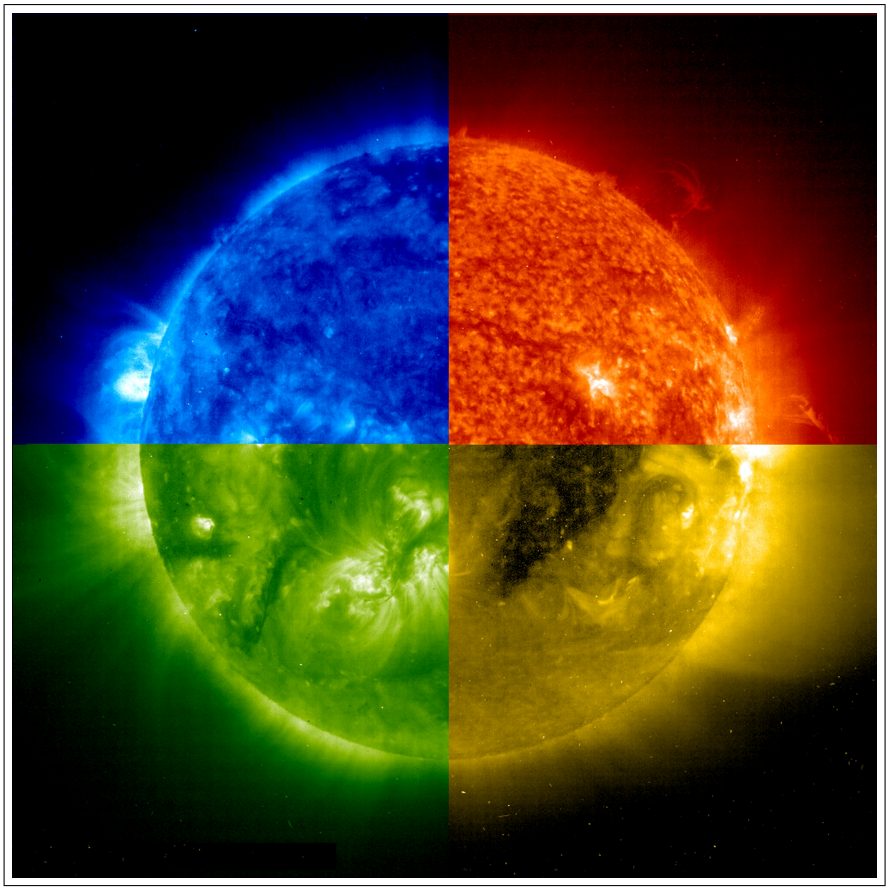

Figure 1.3: Four EUV images of the Sun taken on September 2, 2003 within 15 minutes of each other. Counter-clockwise from the top-right these move upward through the atmosphere. The wavelengths are: 304 Å, 171 Å, 195 Å, and 284 Å; from He II, Fe IX, Fe XII, and Fe XV ions. The first, in red-orange, is in the chromosphere at 60,000-80,000 Kelvin while the latter three are 1 million, 1.5 million, and 2 million Kelvin. Images taken by EIT on SOHO.

[c] http://sohowww.nascom.nasa.gov/

1.1.2 Solar Wind

Aside from its radiation losses, the other cause of mass loss in the Sun is the solar wind. This is defined by *Baumjohann and Treumann* (1996) as "the high-speed particle stream continuously blowing out from the solar corona into interplanetary space, extending far beyond the orbit of the Earth and terminating somewhere in interstellar space after having hit the weakly ionized interstellar gaseous medium around 160 AU." The hot corona expands radially into interplanetary space due to the pressure gradient between the solar surface and the vacuum of space.

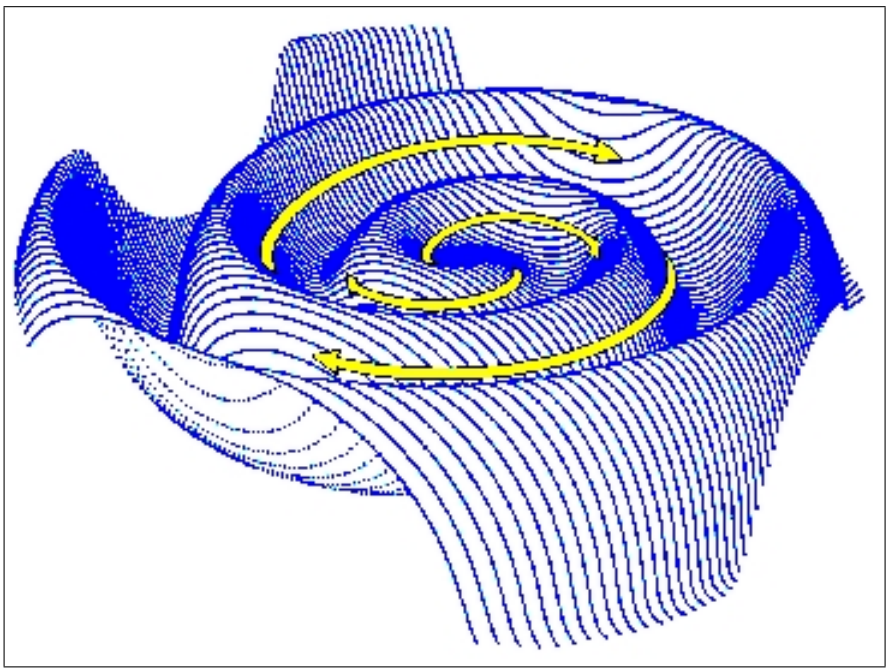

Figure 1.4: The "ballerina skirt" shape formed by the neutral current sheet. The Parker spiral is indicated by the arrows. Image is courtesy of J. Jokipii, University of Arizona via http://helios.gsfc.nasa.gov/solarmag.html; also *Jokipii and Thomas* (1981).

The solar wind is a plasma composed of mostly protons and electrons with a small addition of heavier elements and neutral particles. The heavier elements in the solar wind are usually highly-charged. For example, average iron charge states in the solar wind are typically around 9^+ to 11^+ (*Lepri et al.*, 2001).

The magnetic field of the Sun is "frozen" in the plasma since the plasma pressure is much larger than the magnetic pressure. The field lines are anchored in the photosphere and form an Archimedian spiral due to solar rotation (*Parker*, 1958, 1960), the so-called "Parker spiral". The magnetic field is primarily directed outward from the Sun in one hemisphere, and inward in the other. The thin layer between the different field directions is known as the "heliospheric[d] neutral current sheet". Since this dividing line between the outward and inward field directions is not exactly on the solar equator, the rotation of the Sun causes the current sheet to warp into a wavy spiral shape that has been compared to a ballerina's skirt, as in Figure 1.4. The current sheet is about 10,000 km thick and carries an electrical current density of 10^{-10} A m^{-2} (*Jokipii and Thomas*, 1981; *Winterhalter et al.*, 1994).

The solar wind is loosely divided into two categories, fast and slow (*Geiss et al.*, 1995b; *Cranmer*, 2005). Fast solar wind, moving at over 750 km/s, originates from coronal holes. The slow solar wind, clocking in at 300-500 km/s, appears to be associated with active magnetically closed field regions or the boundary regions of coronal holes (*Woo and Habbal*, 2005). Thus, due to the changing magnetic configuration of the Sun, the solar wind also shows a highly structured dependence on the magnetic solar cycle. Solar wind models must differentiate between fast and slow wind, and thus are generally easier to construct for solar minimum cases where the two come from different regions on the Sun. In addition to the difference in speed, the fast and slow wind vary in temperature and composition (*Fisk et al.*, 1998).

The solar wind is rapidly accelerated along open magnetic field lines streaming away from the Sun, becoming supersonic between 2 and 20 solar radii ($R_\odot$). The heating of the solar corona and the acceleration of the solar wind are closely tied together, but the exact method or methods of the relation are unclear. *Holzer* (2005) discusses these linked topics in some detail and *Quémerais et al.* (2007) add recent

[d]The heliosphere is the region of influence of the Sun, a bubble in space blown into the interstellar medium by the solar wind.

sensor data for consideration.

Cranmer (2008) identifies two types of models: reconnection/loop-opening and wave/turbulence driven. The first type is shown by *Fisk* (2003), who proposes that acceleration of the solar wind is a process linked with the diffusive transport of open flux tube footpoints. The second type is exemplified by Cranmer's own recent paper, which provides a series of linked models for coronal heating and solar wind acceleration based on magneto-hydrodynamic (MHD) turbulence (*Cranmer et al.*, 2007). The core of both models is the coronal magnetic field as measured by Ulysses. *Fisk* (2003) begins with the reconnection of open and closed magnetic field lines, and from this derives field line displacement, formation of coronal holes, energy deposition into the upper corona to form and accelerate the solar wind. *Cranmer et al.* (2007) use a 2D magnetic field model of coronal holes and streamers at solar minimum to derive emergent behavior such as the latitudinal bifurcation of fast and slow wind and the location of energy deposition (i.e. heating). Both types of model have shown remarkable predictive ability, and it may be that a combination of the two can best simulate reality.

1.2 Heliospheric Neutral Atoms, Pickup Ions, and Dust

1.2.1 Heliospheric Neutral Atoms

Interplanetary space has, in addition to the charged solar wind plasma, a variety of neutral atom components. For example, the motion of the heliosphere relative to the galaxy causes an interstellar wind that includes a neutral population. *Fahr* (1968) estimated an interstellar neutral particle flux at 1 AU, focused by solar gravitation, of $\sim 10^7$ cm^2 sec^{-1}. *Gloeckler et al.* (2001) calls this interstellar wind a "dominant source of neutral matter" in the heliosphere, but it is not the only source. Comets evaporate neutral gas from their surfaces that, according to *Gloeckler et al.* (2004a),

"moves out in roughly all directions at typical speeds of $\sim$ 1 km s^{-1}." Planetary exospheres expel neutral atoms that have escaped the pull of gravity. Asteroids and heliospheric dust particles have neutral particles sputtered or sublimated from their surfaces. And the solar wind has its own neutral component.

Gruntman (1994a) says that "Two different processes contributing to the production of a neutral component in the solar wind are [radiative] recombination in the expanding plasma, and charge exchange of the solar wind ions on neutral particles in interplanetary space." *Holzer* (1977) determined that charge exchange between the solar wind and neutral hydrogen would produce a neutral solar wind to total solar wind flux ratio of $\sim 3 \times 10^{-5}$ at 1 AU. The neutral solar wind is measured by the Low Energy Neutral Atom (LENA) instrument, which finds a neutral solar wind to total solar wind flux ratio of $\sim 10^{-4}$ within large error bars (*Collier et al.*, 2001). This matches Holzer's prediction.

These neutral atoms are completely unaffected by electric and magnetic fields. This makes them immune to the complex interactions ions undergo with planetary magnetospheres and their associated current sheets, the solar wind, and the heliospheric current sheet. Neutral atoms are, however, affected by gravity just like any other object with mass. The interstellar wind population is thus gravitionally focused downwind of the Sun. As *Ruciński and Bzowski* (1996) state, "Approaching the Sun, the atoms are subjected to the solar gravitation, solar radiation pressure, and various ionization processes, among which the charge-exchange with the solar wind protons plays the dominant role."

Studies of the gravitational "focusing cone" of both interstellar hydrogen and helium have been performed using optical measurements (*Michels et al.*, 2002), neutral gas instruments, and ion instruments (*Chalov and Fahr*, 2006). Those measurements and more have been used to model local interstellar populations (*Rucinski and Bzowski*, 1995; *Bzowski et al.*, 1997; *Ruciński et al.*, 2003), with final multi-sensor

synthesis in 2004 (*Lallement et al.*, 2004; *Lallement et al.*, 2004a,b; *Gloeckler et al.*, 2004b; *Gloeckler and Geiss*, 2004; *McMullin et al.*, 2004; *Möbius et al.*, 2004).

In the vicinity of planets, solar wind ions can charge exchange with the planetary exosphere (*Collier et al.*, 2001), creating a generally suprathermal population of energetic neutral atoms (ENA). *Gruntman* (1997a) thoroughly reviews ENA fluxes and properties, including measurement techniques and instruments. He says, "By recording ENA fluxes as a function of observational direction, one can reconstruct a global image of a planetary magnetosphere or the heliosphere. Plasma ion energy distribution and ion composition can be remotely measured by measuring ENA energies and masses."

1.2.2 Pickup Ions

An important point was brought up in the above quote by Ruciński: neutral atoms do not always remain neutral. Just as plasma ions can become neutral through charge exchange, the reverse process can happen, resulting in what are called pickup ions (PUI). Pickup ions are a powerful tool in modeling the same sorts of things as ENAs, and also injection and acceleration processes of the solar wind (*Gloeckler et al.*, 2001). *Kallenbach et al.* (2000) provides a review of pickup ion measurements in the heliosphere, and Figure 1.5 shows a schematic of their sources and sinks. *Gruntman and Izmodenov* (2004) model heliospheric PUI mass transport.

An interesting difference in composition has been noted between pickup ion populations from interstellar space and those created in the inner heliosphere (*Gloeckler and Geiss*, 1998; *Gloeckler et al.*, 1998, 2000a). In particular, the presence of C^+, N^+, O^+, and Ne^+ indicates a solar wind source, called the "inner source" (*Gloeckler et al.*, 2000a; *Schwadron et al.*, 2000) first discovered by *Geiss et al.* (1995a). These heavy elements are not present in significant amounts in interstellar pickup ion populations, and in the solar wind they are heavily charged.

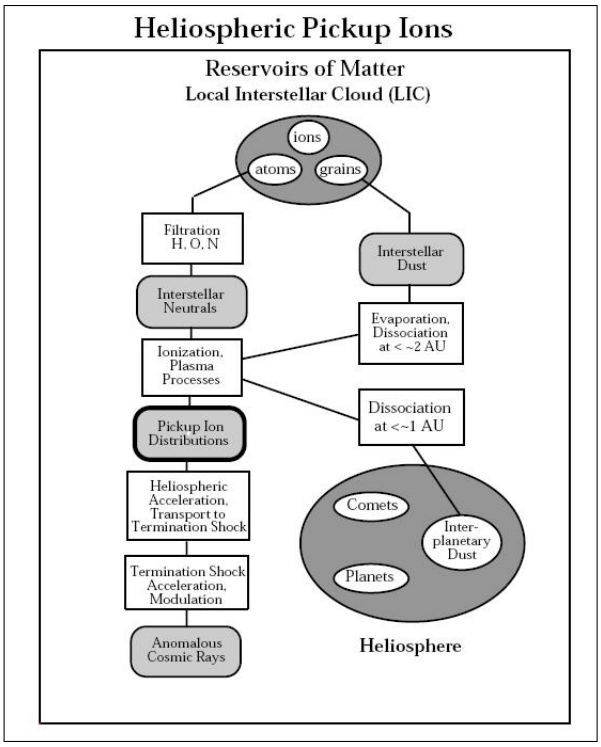

Figure 1.5: Schematic representation of sources and processes leading to the creation of pickup ions in the heliosphere. The large shaded ovals represent source regions of matter shown in small ovals. Physical processes are shown in clear boxes. These processes produce the particle populations shown in the lightly shaded boxes. Image credit to *Gloeckler and Geiss* (1998).

Gloeckler et al. (2000a) provide a table of elemental abundance ratios relative to neon of the inner source pickup ions and averaged (fast and slow) low solar wind (i.e. $<60°$). In this table, the PUI hydrogen to neon ratio is 7710 ± 1560, with the large error due to statistical uncertainty. This is significantly underabundant compared to the solar wind. The inner source C/Ne ratio is depleted by a factor of ~ 2 relative to the solar wind, and O/Ne by a factor of almost 4. This is potentially explained by the formation of molecules which can not be detected by plasma instruments. In addition, *Schwadron and Geiss* (2000) compares PUI protons ratio with oxygen to that of the solar wind, and find that the abundance of inner source protons is only $\sim 20\%$ that of the solar wind at high heliographic latitudes. They explain this by a combination of the aforementioned molecular losses and radiation pressure.

One proposed explanation for the presence of singly-charged heavy ion populations is that they embed in the ubiquitous heliospheric dust population, charge exchange with the ~ 1 μm diameter dust grains, and then are sputtered free as neutrals that get ionized by the solar wind. Ne^+ is of particular importance, because small heliospheric dust grains are not thought to contain neon, thus further emphasizing the likelihood of recycled solar wind ions.

Wimmer-Schweingruber and Bochsler (2003) dispute part of that explanation. They claim that the modeled charge-exchange cross sections of *Schwadron et al.* (2000) (see also *Schwadron* (1998)) are far too small, and that the ratio of sputtered dust material vs. recycled solar wind particles is $\sim 10^3$. Their conclusion is that the solar wind ions are slowed and neutralized by going *t*hrough a far more numerous population of ~ 250 Å diameter dust grains. They model distribution functions with both hypotheses, and cite the work of *Allegrini et al.* (2005) on elemental abundances(*Bochsler et al.*, 2006). However, since solar elemental abundances (*Grevesse et al.*, 2007), solar wind elemental (*Reisenfeld et al.*, 2007) and isotopic abundances (*Kallenbach et al.*, 2007), and even cometary elemental abundances (*Delanoye and de Keyser*, 2007) are all still being revised, in some cases significantly, it is difficult to be certain of that as a criterion for model accuracy.

Bzowski and Królikowska (2005) agree that "the source must be located very close to the Sun (<0.1 AU)." However, they cite a pair of pickup ion measurements from comet tails (*Gloeckler et al.*, 2000b, 2004a) to propose that a component, perhaps a large component, of the inner source is dissociated dust expelled from comets (which contains most of the inner source heavy elements) that charge exchanges with the solar wind. *Allegrini et al.* (2005) dispute this, claiming that the solar-wind-like abundances seen in the inner-source rules out the comet source entirely.

Fahr (2007) questions the existing models of the evolution of pickup ion distributions. He asks if adiabatic cooling is the process taking place, or if it is "pure magnetic

cooling of pickup ions simply resulting from their being convected in an interplanetary magnetic field which decreases in magnitude with increase of solar distance."

1.2.3 The Near-solar Dust Population

Though there may be other explanations for the inner source pickup ion population, the most prevalent ones all depend on charge exchange with dust from comets, planets, and/or asteroids. Unfortunately, the shape, density, and composition of the near-solar dust population is still uncertain. It is known that the interplanetary medium is a dusty plasma (*Hollenstein*, 2000; *Szegö et al.*, 2000; *Shukla*, 2001; *Ishihara*, 2007), also called a complex plasma, with dust mass per volume equivalent to that of the solar wind (*Mann*, 2008). *Leinert and Grün* (1990) assert that the dust cloud around the Sun follows roughly elliptical density contours with axial ratio 1:7, and that the dust is the cause of F-lines of the solar corona. Reflections from the dust can be seen after sunset as zodiacal light (*Leinert et al.*, 1998; *Mann*, 1998).

There is also an interstellar dust stream (*Czechowski and Mann*, 2003; *Krüger et al.*, 2007) that is useful for determining dust properties of the local interstellar medium (*Mann and Kimura*, 2000), but for purposes of this dissertation the population of concern is that arising within the heliosphere, in particular close to the Sun (*Krivov et al.*, 1998; *Mann et al.*, 2000, 2004).

Dust in the inner heliosphere, whether it arises from comets, planets, or asteroids, is subject to a variety of forces including solar gravity, solar radiation pressure, and electromagnetic interaction of charged dust grains with the interplanetary magnetic field. The most obvious of these forces is gravity, which dominates the particles' orbits around the Sun. Over time those orbits are modified by other forces. Photonic pressure offsets gravity to some extent by transfering momentum to the dust grains, especially close to the Sun. The ratio of radiation pressure to gravity on a particle is represented by the so-called β-value, and depends greatly upon the pho-

ton absorption cross section of a given particle (*Burns et al.*, 1979). *Draine and Lee* (1984) constructed dielectric functions for astronomical graphite (absorbing) and silicate (dielectric) material, the two most common constituents of interplanetary dust, and *Draine* (1985) followed that up with tabulated data. A subset of dust, very small particles generated close to the Sun, have β-values well over 1.0. These particles, called β-meteoroids, are accelerated by radiative pressure rapidly out of the solar system on hyperbolic orbits(*Grün and Landgraf*, 2001).

A nonradial component of radiation pressure on a particle, called the Poynting-Robertson effect (*Wyatt and Whipple*, 1950; *Burns et al.*, 1979; *Weidenschilling and Jackson*, 1993; *Wilck and Mann*, 1996), is when the particle's orbit "runs into" a photon and the momentum transfer is against the particle's direction of motion. In addition to photons, a particle can run into solar wind ions, resulting in a pseudo-Poynting-Robertson effect (*Mukai and Yamamoto*, 1982; *Minato et al.*, 2004) that also produces drag on the particle's orbit. Just as the β-value depends on the particle's absorption cross section, the combined Poynting-Robertson drag force depends greatly upon the particle's shape. *Mann et al.* (1994) modeled near-solar dust as fractal aggregates of smaller particles, and *Kimura et al.* (1997) examines the circumsolar dust cloud using this model. A detailed look at the effect of Poynting-Robertson drag and radiation pressure on those fluffy dust aggregates reveals that "the dynamical lifetimes of fluffy particles are determined by the material composition of the grains rather than by their morphological structures and sizes" (*Kimura et al.*, 2002). The overall effect of Poynting-Robertson drag is to circularize dust orbits and slow down the grains, resulting in circular Keplerian orbits that over periods of 10^6 to 10^7 years decay into the Sun.

The final force affecting dust grains is the Lorentz force, $v \times B$ (*Consolmagno*, 1979). Dust grains can be charged by a combination of photoionization from solar radiation and charge-exchange from solar wind ions and electrons. Once charged,

they are affected by the interplanetary magnetic field, which can scatter them into non-ecliptic orbits, or even retrograde orbits (*Krivov et al.*, 1998). In general, though, the Lorentz effect is much less than the Poynting-Robertson effect. The most notable exception is for small particles at large heliocentric distances, such as the interstellar stream. In this case, since the solar magnetic field strength falls off as r^{-1} (where r is the heliocentric distance) while the particle and photon flux falls off as r^{-2}, the Lorentz force dominates and creates a significant population of out-of-ecliptic grains (*Kimura and Mann*, 1998; *Krivov et al.*, 1998).

Losses of interplanetary dust include the aforementioned β-meteoroids, evaporation/sublimation, and sputtering. A critical question for purposes of this dissertation is how close the dust cloud approaches the Sun, and what its composition and morphology will be at the closest point. *Krivov et al.* (1998) model this in great detail.

Mann and Murad (2005) claim that "it is not reasonable to suggest the presence of Si nanoparticles in the vicinity of the Sun," because silicon sublimates at relatively low temperatures, which seems to counter the *Bochsler et al.* (2006) model for solar wind neutralization. However, *Mann et al.* (2007) say that "the most likely materials to survive in the very vicinity of the Sun are MgO particles from the sublimation of cometary and meteoritic silicates, nanodiamonds originating from meteoroid material, and possibly carbon structures formed by thermal alteration of organics." This once again opens the door for solar wind neutralization.

The primary loss mechanism close to the Sun appears to be sublimation (*Mann et al.*, 2004; *Mann and Murad*, 2005), caused by radiative heating by solar photons. The critical factor determining the heating rate is once again the absorption cross sections (*Draine and Lee*, 1984; *Draine*, 1985), resulting in a radial temperature profile $T(r) = T_0 \, (r/r_0)^{-0.5}$ where $T_0 = 250$ K and r_0 is 1 AU (*Mann and Murad*, 2005). At 2 $R_\odot$, this results in a temperature of approximately 2600 K, which is slightly above the sublimation temperature for MgO and significantly above that of

Si. So it's unlikely that much dust survives inside of 2 Rs, which matches the result of *Mann et al.* (2004).

This is a very complex topic that includes solar photon and particle flux; size, shape, and material properties of dust grains; impact parameters and secondary-electron emission; and much more. The state of the art of near-solar dust populations (*Mann et al.*, 2007; *Mann*, 2008; *Lasue et al.*, 2007; *Levasseur-Regourd et al.*, 2007) is still evolving, and it is likely that nobody will know for certain the composition of the near-solar dust cloud until in-situ measurements are taken and analyzed.

1.2.4 Unanswered Questions

A variety of questions could all be answered or partially answered by in-situ measurements of near-solar neutral atoms and pickup ions. Among them are:

- How close does the interplanetary dust cloud approach the Sun, and what is its radial composition and morphology?
- What is the radial distribution of inner source neutral atoms?
- What are the Si and Mg components, and how do they relate to the local dust population?
- What is the rate of solar wind ion recycling or neutralization by the dust population?
- What is the initial velocity distribution of inner source pickup ions, and how does it evolve after pickup?
- What effect, if any, do the initial velocity distribution and local environment have on cooling?
- Is this cooling adiabatic, or magnetic, or both?
- What effect does the near-solar electron distribution have on electron-impact ionization and dust grain charging?
- What effect does local coronal heating have on charge-exchange ionization?

This dissertation cannot answer all of these questions because most of them require new and unprecedented measurements. However, with the information available from

remote sensing it is possible to develop a predictive model of near-solar dust, neutral atoms, and pickup ions (Chapter II). In addition, the boundaries of micro- and nano-technology have been pushed back in the interests of creating a component for a neutral particle sensor that will help to answer these questions (Chapter V).

1.3 Space Instrumentation

Spaceborne instruments include optical telescopes (X-ray, UV, visible, and infrared), magnetometers, plasma particle sensors, and more. For purposes of this dissertation, the discussion is limited to plasma and neutral particle sensors. Dozens of Sun-observing satellites have taken data from the orbit of Venus (e.g. Pioneer 12) at 0.72 AU to regions beyond the boundaries of the solar system (e.g. Voyager I) and will soon be orbiting Mercury (e.g. the MErcury Surface, Space ENvironment, GEochemistry, and Ranging (MESSENGER) mission), which has an orbit ranging from 66-100 $R_{\odot}$. Many, if not most, of these satellites have carried plasma sensors for purposes of space weather monitoring and forecasting and exploration of planetary environments and the interstellar medium. *Young* (1998) provides a survey of plasma measurement techniques and overview of recent instruments and spacecraft. He defines a particle instrument as "typically made up of a 'sensor', which includes collimators and other optics, 'detectors' that convert particles into electronic signals, and 'electronics' needed to register those signals, control the sensor, and interface commands,data, and electrical power with the spacecraft."

1.3.1 Electrostatic Analyzer

Space plasma instruments that need to survey a wide range of particle energies with a wide field of view often carry electrostatic analyzer (ESA) systems. At its most basic level, the function of an ESA is that of ion-optics band-pass particle filter, with the band in question being a range of energy-per-charge (E/q). A charged particle

in an electrostatic field undergoes acceleration as dictated by the electrostatic force, $F = q\mathbf{E} = m\mathbf{a}$, where $\mathbf{E}$ is the electric field. This acceleration is stronger on particles with smaller mass, and has longer to act on particles moving slower. In essence, the Lorentz force has more effect on particles with lower energy ($E = mv^2$) or higher charge. An ESA using static electric fields generated by charged plates selectively passes ions with a range of E/q given by the analyzer's geometry and the applied field. Periodically stepping the voltage allows particles with different E/q bands to pass.

In order for this to provide meaningful results, however, the particles need to be selected for angle of incidence as well. Thus, a collimator is required either before or after the E/q selection. Then, a position-sensitive detector can further separate the passed band into bins and count the number of hits in each bin. The time allowed at each voltage step depends on the sensitivity of the detector and density of incoming particle flux. Careful tailoring of the geometry and fields is required for any ESA in order to optimize the energy resolution (ΔE/E) of an incoming E/q pass band.

The variety of ESA designs is wide-ranging, as exemplified by the different designs present on the Charge, Element, and Isotope Analysis System (CELIAS) (*Hovestadt et al.*, 1995a,b) on SOHO and the Cassini Plasma Spectrometer Investigation (CAPS) (*Young et al.*, 2004). The basic theory of spherical-plate ESA design is covered by *Paolini* (1967) and *Theodoridis and Paolini* (1969). A toroidal top-hat design is detailed by (*Young et al.*, 1988) and computer simulated by *Sablik et al.* (1988). A similar design was used on the Fast Imaging Plasma Spectrometer (FIPS) (*Zurbuchen et al.*, 1998; *Koehn*, 2002; *Koehn et al.*, 2002; *Andrews et al.*, 2007) on the MESSENGER spacecraft[e] (*Solomon et al.*, 2007; *Leary et al.*, 2007).

[e]http://messenger.jhuapl.edu/

1.3.2 Time of Flight

A particle's mass per charge (m/q) can be determined by a time-of-flight (TOF) system similar to those developed by *Gloeckler and Hsieh* (1979) for a wide range of particle energies. Typically the particle is accelerated by a high static voltage (V) to give it enough energy to transit a carbon foil (*McComas et al.*, 2004). This carbon foil transit causes it to lose energy (*Allegrini et al.*, 2006) and generate on the order of 1-15 secondary electrons (*Allegrini et al.*, 2003) that trigger a start signal detectable by microchannel plate (MCP) (*Wiza*, 1979) or similar sensors. After traversing the TOF system, the particle impacts an MCP, releasing another set of electrons for a stop signal. The time between the two signals (τ) and the distance traversed (d) reveal the m/q of the particle. If the impact is additionally on an energy detector such as a solid-state detector (SSD), the residual energy E_{meas} can be detected. If the E/q is known via ESA or similar technique, the charge (q) can be calculated, and with this charge the mass (m) is also known. *Gloeckler et al.* (1992) derived the following set of equations for particle properties:

$$\begin{aligned} m =& 2\left(\frac{\tau}{d}\right)^2\left(\frac{E_{meas}}{\alpha}\right) \\ \frac{m}{q} =& 2\left(\frac{\tau}{d}\right)^2\left(V+\frac{E'}{q}\right) \approx 2\left(\frac{\tau}{d}\right)^2 V \\ q =& \left(\frac{E_{meas}}{\alpha}\right) / \left(V+\frac{E'}{q}\right) \approx \left(\frac{E_{meas}}{\alpha}\right) / V \\ E =& q\left(\frac{E}{q}\right) \end{aligned} \tag{1.1}$$

where E'/q takes account of the energy loss of ions in the thin foil (*Allegrini et al.*, 2006) and α (<1) represents the nuclear defect in the SSD. Triple-coincidence measurements such as this, requiring both start and stop signals and energy detection, significantly reduce the instrument's background count.

Varieties of TOF systems include the straight-through traversal used on the Solar Wind Ion Composition Spectrometer (SWICS) (*Gloeckler et al.*, 1992, 1998), and also linear-electric-field (LEF) TOF of Cassini-CAPS (*McComas et al.*, 1990; *McComas and Nordholt*, 1990; *Hamilton et al.*, 1990; *Young et al.*, 2004).

1.3.3 Light Traps and Ultraviolet Filters

Instruments measuring low-density plasmas like the solar wind plasma need to be sensitive to individual particle impacts. However, the vast majority of these instruments rely on sensors that are highly vulnerable to energetic ultraviolet photons, which can degrade the instrument performance or lead to noise in the system. Photons energetic enough to be classified as ionizing radiation begin in the extreme ultraviolet (EUV) range. According to *Lean* (1987), "between 120 and 200 nm the [solar] spectrum is primarily continuum emission from the lower chromosphere and upper photosphere, with superimposed chromospheric emission lines and some absorption lines. Hydrogen Lyman-alpha (Ly-α) radiation at 121.6 nm [10.1 eV[f]] can be seen to be emitted from a wide range of heights in the solar chromosphere." Varying by a factor of ~ 3 over the solar cycle (*Lean*, 1987), the Ly-α line has an intensity over a thousand times brighter than the surrounding spectral bands and carries much of the heliospheric background radiation, as can be seen in Figure 1.6.

At one AU the quiet Sun Ly-α solar flux is approximately 2.3×10^{11} cm^{-2} s^{-1} according to (*Lean*, 1987), although more recent numbers by *Tobiska et al.* (1997) put it at 3.0×10^{11} cm^{-2} s^{-1} rising to 7.0×10^{11} cm^{-2} s^{-1} at solar maximum. Anything in that range is enough to produce a signal in an MCP or SSD that is indistinguishable from the particle signal (*Wiza*, 1979; *Hsieh et al.*, 1979, 1980; *Zurbuchen et al.*, 1995; *Curdt et al.*, 2001, 2004). *Young* (1998) says that the key figures of merit for an

[f]The unit eV stands for electron-Volts. 1 eV is the amount of energy gained by a single unbound electron when it is accelerated through an electrostatic potential difference of one Volt, in a vacuum. In other words, it is equal to one Volt multiplied by the (unsigned) charge of a single electron (e = 1.602×10^{-19} C).

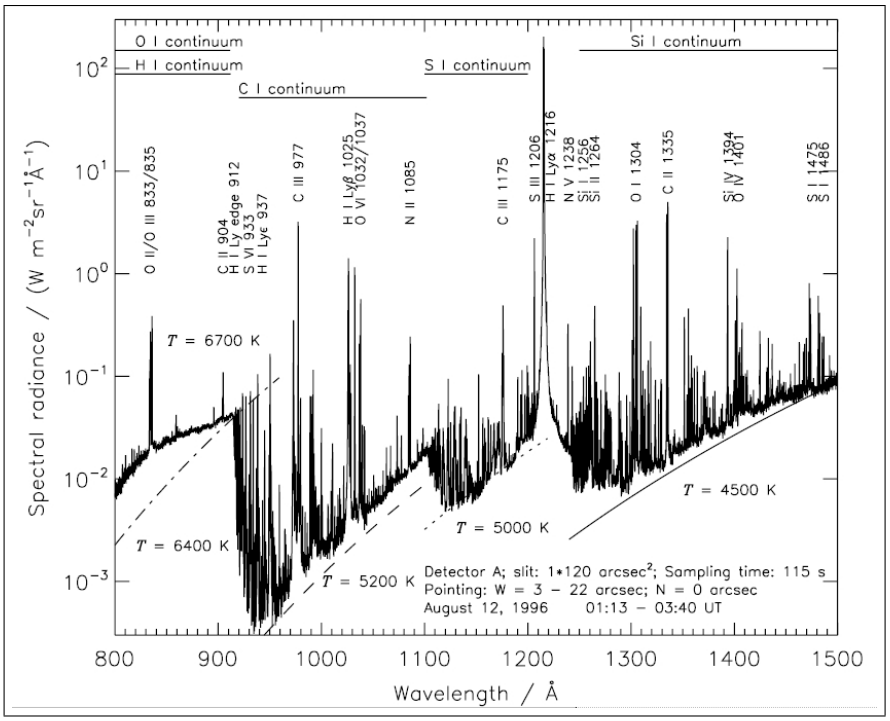

Figure 1.6: Solar extreme ultraviolet spectrum from SOHO-SUMER. The bulk of the energy is carried by the Hydrogen Lyman-alpha line at 121.6nm, 1000 times brighter than nearby wavelengths. Image credit to *Wilhelm* (2006).

instrument are sensitivity, dynamic range, and resolution. A means to reject the UV flux without significantly impeding the ion flow increases signal-to-noise ratio, which in turn affects both sensitivity and dynamic range. This applies throughout the heliosphere, because both the solar wind density and photon counts follow a $1/r^2$ profile.

There are a wide variety of techniques to reject UV. For example, SWICS uses serration, black-coating, and light traps to eliminate reflection of visible and UV radiation into the TOF system (*Gloeckler et al.*, 1998). FIPS uses its collimators along with the hourglass shape of its ESA, similar to the S-shape deflection on the Thermal Ion Dynamics Experiment (*Moore et al.*, 1995). Other techniques viable for highly energetic particles include use of a relatively thick (a few μg cm^{-2}) UV rejecting foil or using an SSD with sufficiently high energy threshold that UV photons cannot

trigger it.

Incidentally, filtration of photons as a pre-measurement step is also of use in studying plasma characteristics in quite a few earth-based applications. For example, on the ground equipment such as plasma etchers, particle accelerators, and tokamaks all contain high-energy plasmas that require careful monitoring. In planetary atmospheres, lightning or aurora studies could also benefit from this technology.

1.3.4 Examples of Modern Plasma Instruments

SWICS and FIPS are two examples of modern plasma spectrometers. Figures 1.7 and 1.8 show schematics of the two instruments. While different in configuration, they both have very similar components. In particular, both have particle collimators, ESA systems, and TOF measurement systems. SWICS also has a SSD and light trap.

SWICS is carried on both the Advanced Composition Explorer (ACE)[g] (*Stone et al.*, 1998; *Chiu et al.*, 1998) and Ulysses[h] (*Wenzel et al.*, 1989, 1992) satellites. SWICS is optimized for measurements of the chemical and isotopic composition and distributions of solar, interplanetary, and interstellar matter (*Gloeckler et al.*, 1998). These measurements include ionic-charge composition of the solar wind and the thermal and mean speeds of all major solar wind ions from H through Fe at a wide range of solar wind speeds. SWICS uses an ESA that scans an E/q range of ~ 0.5 to ~ 100 keV/q in ~ 13 minutes. The following TOF and SSD components determine ion mass and m/q. Post-acceleration between the ESA and TOF components is used in order to measure the mass of ions of solar wind energies which otherwise would fall below the threshold energy of the SSD.

FIPS is carried on MESSENGER. It measures the energy and angular and compositional distributions of the low-energy components of ion distributions (<50 eV/q to 20 keV/q). One of the innovations of FIPS is a new ESA geometry that enables

[g] http://www.srl.caltech.edu/ACE/
[h] http://ulysses.jpl.nasa.gov/

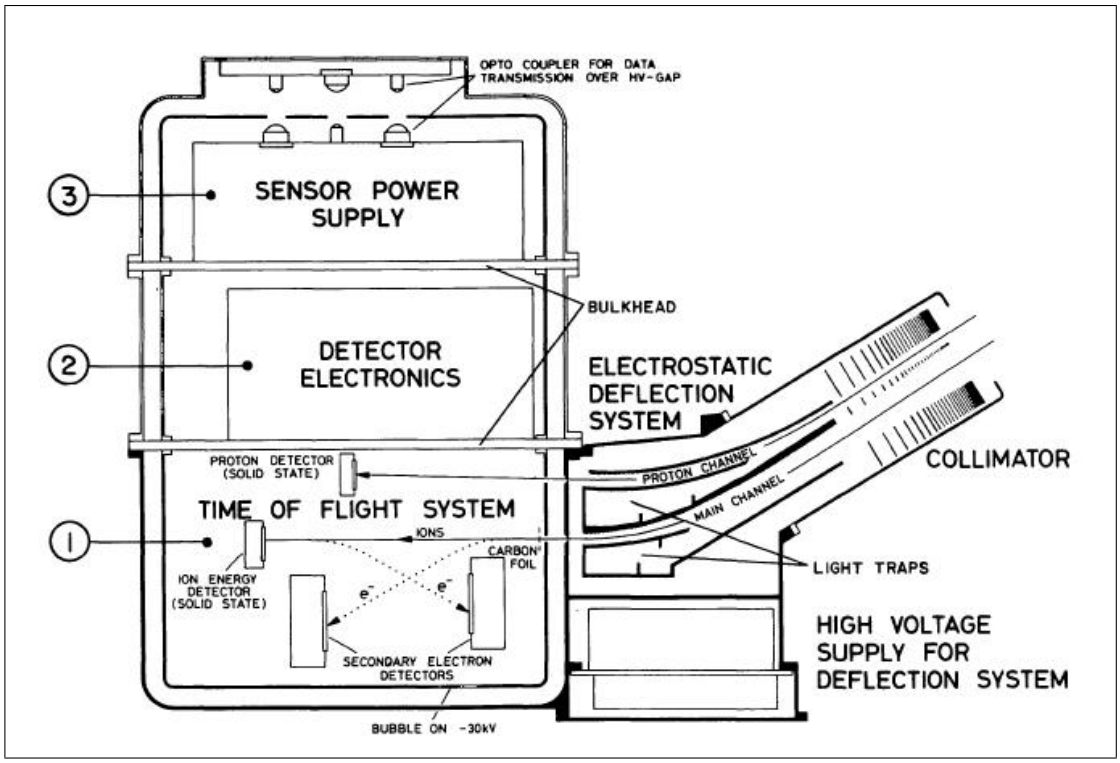

Figure 1.7: Schematic of SWICS instrument showing major functional components. A collimator leads into a two-channel electrostatic deflection system followed by a time-of-flight system. Power supplies and electronics are also shown. Post-acceleration voltage on the three inner compartments are maintained at -15kV to -30kV. Image credit to *Gloeckler et al.* (1992).

an instantaneous field of view around 1.4π steradians. Another innovation is use of the ESA as a UV filter. After ions have passed through the first deflection region and collimator, the ESA has performed its purpose as an E/q filter. However, at this point UV attenuation is not sufficient, so an hourglass-shaped deflection region between the first and second collimators was added to provide the needed UV suppression.

1.4 Miniaturized Sensors for Space Applications

With space launch costs ranging between $10,000 and $50,000 per kilogram depending on the target distance and size of the launch vehicle, and with spending for space launches dropping steadily, interest in miniaturization of payload mass is high.

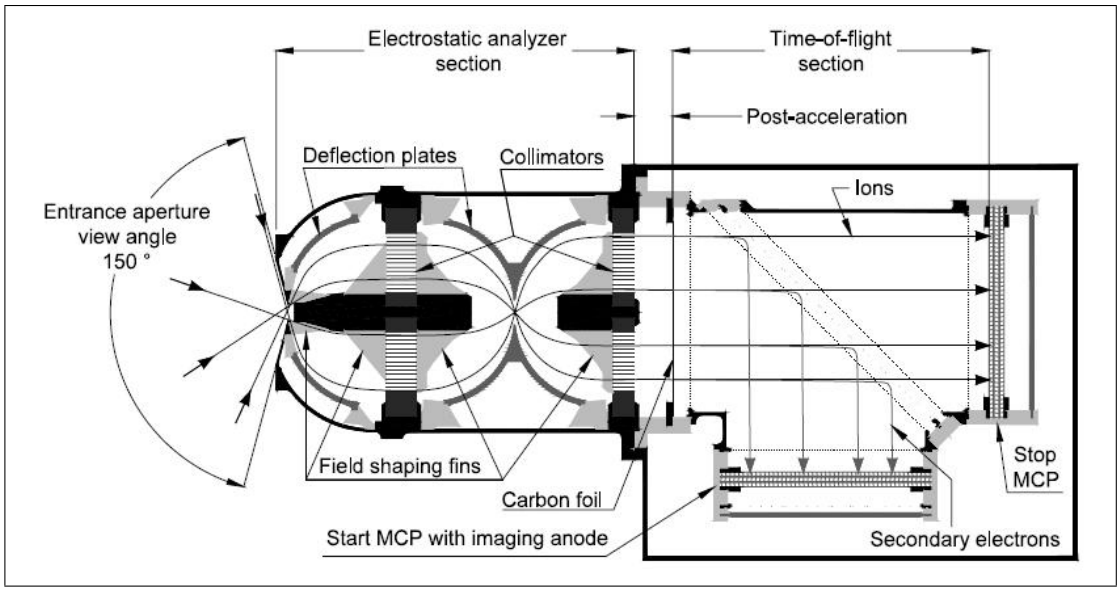

Figure 1.8: Schematic of FIPS instrument showing major functional components. Ions are analyzed by their energy per charge, two-dimensional position, and total time of flight. Image credit to *Andrews et al.* (2007).

Lighter materials are being used for sensor housings, insulators, and even launch vehicles. Sometimes a technological advance allows the swapping of one part for a newer, lighter one (e.g. swapping a chemical laser for a diode laser). In some instances, it may be desirable to exchange added complexity in ground-based data processing for a more compact space instrument, particularly if there is centralized ground processing of the instrument's data stream. The basic physics of photon or ion optics can often limit the amount of miniaturization possible, but in that case there may be a trade-off between size and power or resolution. Reduction in instrument power requirements translates directly to a reduction in cost. Smaller and/or less massive sensors translate to smaller, lighter rockets for additional cost reduction.

An example of this is the MidSTAR-2 mission, integrated by Goddard Space Flight Center (GSFC), which in 2011 will carry "a range of small space experiments and instruments." This includes the Miniature Imager for Neutral Ionospheric atoms and Magnetospheric Electrons (MINI-ME), which is only 6 inches in diameter and 5 inches

in height, 6.6 lbs. This instrument is a successor to the LENA on Imaging from the Magnetopause to the Aurora for Global Exploration (IMAGE), a 44-lb instrument the size of a storage box. Despite being only 15% of LENA's mass, MINI-ME will have 10 times the energy resolution according to the GSFC principal investigator, Michael Collier. In the Summer 2007 issue of Goddard Tech Trends, he says In this current environment, Goddard must be able to produce instruments that have lower mass, consume less power, and are less expensive to build. With MINI-ME, we accomplish all three, plus we offer more performance.

Richard Feynman famously said in 1959 that "there's plenty of room at the bottom," meaning that miniaturization had not nearly reached its limits (*Feynman*, 1992). Making smaller instruments means more than lowered launch costs. It can instead mean more instruments for the same launch cost, in particular distributed arrays of small satellites (*Barnhart et al.*, 2007). Recently there has been great interest in constellations of so-called nanosats, which requires significant reduction in size of individual instruments. For example, *McCann et al.* (2007) demonstrated a 300 gram ion mass analyzer that measures 10 eV to 15 keV ions with sufficient mass resolution to resolve M/q = 1, 2, 4, 8, 16, and >30 with a field of view of 9° × 180°. Like its larger cousins described above, it uses pre-acceleration and ESA and TOF components for E/q and m/q measurements. In addition there are a pair of electrostatic deflection plates to provide angular resolution.

In addition to miniaturizing traditionally machined components to the millimeter scale, one obvious way to accomplish component miniaturization is through micro-electromechanical systems (MEMS) technologies. For example, *Enloe et al.* (2003) has produced a proof-of-concept ESA with micromachining technology and launched it on the Air Force's FalconSAT-2 (*Krause et al.*, 2005). For beam energies of 10-30 eV the device response strongly peaked at a given applied voltage, serving as a bandpass energy filter with energy resolution (ΔE/E) of 0.25 for normal incidence

and 0.37 over the entire field of view ($\sim \pm 30^\circ$ by $\pm 40^\circ$). Other examples include programmable diffraction gratings(*Senturia et al.*, 2005), multispectral imaging systems(*Newman et al.*, 2006), and a full plasma spectrometer (FLAPS)(*Wesolek et al.*, 2005), all built with MEMS technologies. At the 2008 IEEE Aerospace Conference, *Wesolek et al.* (2008) discussed wafer-scale MEMS instrument integration. The technology is there, and applications are being designed and tested faster and faster each year.

1.4.1 Nanogratings

Nanoscale gratings are used for a variety of sensor and instrument applications. Most applications to date have used gold gratings electroplated into pre-formed photoresist patterns (*van Beek et al.*, 1998; *Canizares et al.*, 2005). The high conductivity of gold makes it very absorptive over most of the spectrum, including the deep UV and X-ray. However, gold is relatively weak, requiring support for large-area gratings. For example, NASA's Chandra Space Telescope (*Weisskopf*, 2003) uses 200 and 400 nm period gratings suspended on submicron thickness polyimide membranes (*Canizares et al.*, 2005) for high resolution X-ray spectroscopy. The Medium Energy Neutral Atom (MENA) sensor (*Pollock et al.*, 2000) on the IMAGE satellite (*Burch*, 2000; *Gibson et al.*, 2000) uses 510 nm thick gold gratings with 40 nm slits suspended on nickle support gratings for ultraviolet filtration (*Scime et al.*, 1995; *Gruntman*, 1995, 1997a; *van Beek et al.*, 1998). Similar gratings were used in experiments with EUV diffraction (*McMullin et al.*, 2004) and 0.5 keV electron diffraction (*Gronniger et al.*, 2005; *McMorran et al.*, 2006). A new type of grating for X-ray diffraction has been tested (*Ahn et al.*, 2007), but is not ready.

For UV filtering purposes such as on MENA, the best stand-alone devices to date are perforated foils or gratings. They work on the principle that photons can only pass through a straight channel if the channel width is much smaller than the photon

wavelength, which is on the order of tens or hundreds of nanometers. In contrast, atomic widths are on the order of angstroms with deBroglie wavelengths[i] measured in picometers (*Gronniger et al.*, 2005). For example, the deBroglie wavelength of slow solar wind protons (450 kms^{-1}) is 8.8×10^{-13} meters, or just under one picometer.

In order to be an effective filter, a grating must have a large geometric transparency to pass particles and very narrow, high aspect ratio features to block energetic photons (*Gruntman*, 1995, 1997b; *Balkey et al.*, 1998). For space applications a filter must be light weight and require minimal power. A self-supported structure is ideal since there are no thermal expansion mismatches. To date no prior grating design has provided the all of these desired characteristics.

1.5 Dissertation Overview

This dissertation focuses on the analysis and technology development towards the solution of the science questions in Section 1.2.4.

Chapter II develops a new model for near-solar pickup ions that is used to predict neutrals near the Sun. The basic premise of interstellar pickup ion models is that the ions are for all intents and purposes stationary relative to the solar wind when they are picked up, having only the negligible velocity imparted by the relative motion of the heliosphere through the interstellar medium. While this may be a valid assumption for interstellar pickup ions, inner source pickup ions have a different life cycle. The ions begin as solar wind ions, and as detailed in § 1.2.2, are either recycled or neutralized by near-solar dust grains and then ionized to a singly positive charge state by photoionization, charge-exchange, or electron-impact. This interaction with the dust grains will add a significant azimuthal velocity component not seen in interstellar pickup ions. This azimuthal velocity, along with Alfvén wave scattering, are used in

[i]The equation for deBroglie wavelength is $\lambda = \frac{h}{mv}\sqrt{1-\frac{v^2}{c^2}}$ where h is Planck's constant (6.626 $\times 10^{-34}$ Joule seconds) and m and v are the particle's rest mass (kg) and velocity(m/sec).

a model that attempts to determine the location of peak pickup ion generation, and its effect on adiabatic cooling. Then an instrument is proposed to measure neutral and/or pickup ion fluxes in the near-solar region, possibly to be flown on the Solar Probe Plus mission.

Chapter III introduces the basics of the micromachining technology used in subsequent chapters. All the clean-room technologies used in the rest of the dissertation are covered at a high level, including both photolithography and alternate techniques, thin film growth and deposition, doping, and both chemical and plasma etching. This introduction is intended to serve as a primer for readers unfamiliar with the technology.

Chapter IV covers simulation and modeling of transmission gratings that block ultraviolet and/or broadband light while allowing particles through. Included are both analytical models and results of professional grade simulation tools. Material constraints are also discussed.

Chapter V is an in-depth discussion of grating fabrication techniques, including two unsuccessful technological approaches and the final, successful technique. The first trial was based on femtosecond laser ablation of nanometer-scale trenches in transparent materials. The second was a proof-of-concept process using standard optical lithography, reactive ion etching (RIE), and chemical bulk etching. And the final, successful technique used nanoimprint lithography (NIL) for patterning and deep-reactive ion etch (DRIE) for both bulk and grating etches. This chapter includes process details, optical and scanning electron microscope images of intermediate and final stages, and measured data from fabricated gratings.

Concluding remarks and directions for future work are in Chapter VI.

CHAPTER II

Pickup Ion Profiles

2.1 Introduction

Interplanetary neutral atoms have two major sources: the interstellar medium and the so-called inner-source, which is thought to be solar wind ions recycled or neutralized by dust arising from asteroids, comets, and planets. These neutrals are ionized by electron impact, photoionization, or charge exchange. Once ionized, they are affected by the solar winds magnetic field, thus getting "picked up" and swept outward. This process is covered in more detail in § 1.2.

Pickup ions from the inner source have to date been treated very similarly to those from interstellar space. In particular, the assumption has been made that they are effectively motionless when picked up, and thus in the solar wind frame have a velocity of -U_{SW} which then isotropizes into ring or hemispheric distributions (*Isenberg*, 1987; *Fichtner et al.*, 1996; *Schwadron et al.*, 2000). While this assumption may be valid for interstellar pickup ions, which are generally picked up outside of Earth's orbit, the near-solar environment is home to different physical processes that need to be taken into account, particularly within the solar wind acceleration region.

In the near-solar environment, additional motions or effective motions of these particles need to be considered. Many, if not most, of the neutral particles inside 1 astronomical unit (AU) arise from dust grains spiraling into the Sun in Keplerian

orbits, and thus these neutrals have a large azimuthal velocity perpendicular to the solar wind and the average heliospheric magnetic field. In addition, many of them should be ionized and picked up where the solar wind is sub-Alfvénic. As such, the Alfvén wave velocity needs to be taken into account when finding the effective frame in which ions are picked up, and their thermal velocity should isotropize around a value dependent upon all three major speed contributions. This value, much larger than that of the currently accepted stationary pickup, strongly affects the cooling of pickup ions in the inner heliosphere, and hence the interpretation of inner source pickup ion measurements done to date.

2.2 A Parameterized Model

Dust grains spiral toward the Sun along pseudo-Keplerian orbits influenced by the Poynting-Robertson effect (*Krivov et al.*, 1998; *Mann et al.*, 2004), which for a circular orbit has a velocity of $\sqrt{\frac{GM}{r}}$ where G is the gravitational constant, M is the mass of the Sun, and r is the heliocentric orbital radius. Between grain erosion, sputtering, sublimation, and rotational bursting the dust grain population drops to statistical insignificance before contacting the solar surface, but the radial extent of that dust-free zone could potentially be as small as 1.5–4 $R_\odot$ (*Mann et al.*, 2004).

Since the solar wind accelerates away from the Sun and the dust grain orbital velocities increase closer to the Sun, there is a point at which the grain orbital velocity, and thus the azimuthal velocity of the recycled solar wind, approaches and then exceeds the solar wind radial velocity. At solar minimum, this point is inside 10 $R_\odot$ in the ecliptic plane. *Schwadron et al.* (2000) mention this effect in passing, but only for fast polar wind at 10 $R_\odot$ where the effect resulted in only 19% speed difference and was thus ignored. *Schwadron et al.* (2000) and *Schwadron and Geiss* (2000) used the 10 $R_\odot$ point as the inner cutoff for dust grains and the fast solar wind velocity measured by Ulysses. Thus, the nonlinear increase of the orbital velocity and its effect

on overall speed may not have been noticed. In addition, Alfvén wave speeds close to the Sun follow an r^{-1} profile, and thus surpass the solar wind speed at 10–20 $R_\odot$ as seen in Figure 2.1, rising steeply closer to the Sun. When finding the force-free frame for ion pickup, this effect, potentially even greater than that of azimuthal velocity, needs to be taken into account. Figure 2.1 shows the relative magnitudes of the aforementioned velocity components near the Sun for the equatorial region during solar minimum.

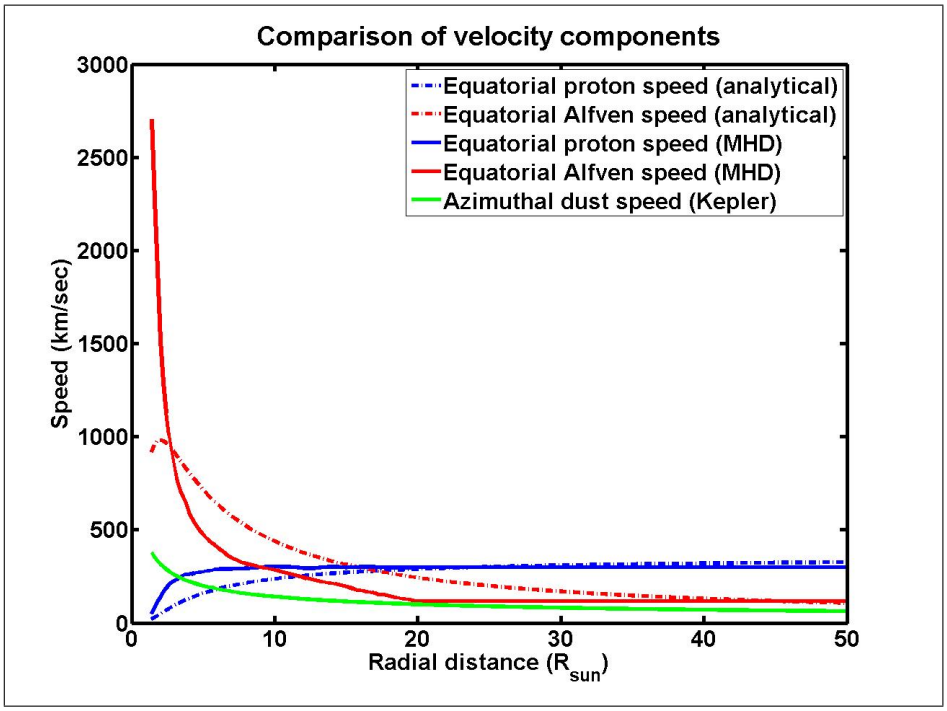

Figure 2.1: Comparison of the velocity components of inner source pickup ions arising from dust in the equatorial plane at solar minimum. The dashed red and blue lines are from an analytical model, and the solid lines from an MHD model (*Cohen et al.*, 2007). The solid green line is for circular Keplerian orbits using the equation $v_{dust} = \sqrt{\frac{GM}{r}}$.

Fichtner et al. (1996) say that pickup ions (PUI) "experience strong and efficient pitch-angle scattering on a time scale short compared to those of momentum and spatial diffusion," and Fahr's 2007 model (*Fahr*, 2007) also allows for rapid pitch angle diffusion, but *Gloeckler et al.* (1995) and *Fisk et al.* (1997) refer to a radial

inward stream of H^+ ions in the solar wind frame that indicates a long mean free path ($\sim$ 1 AU) and weak pitch-angle scattering. For purposes of this model we assume that the PUI isotropize into shell distributions almost immediately. For larger mean free path, the use of hemispheric distributions *Schwadron et al.* (2000) or even kinetic models (*Isenberg and Vasquez*, 2007) might be required.

Pickup ion measurements at 1 AU have never been well matched with model results. It is likely that both model inaccuracies and instrumental factors are involved in this discrepancy. Addition of the velocity of the interstellar neutral stream significantly affected modeling of interstellar pickup ions (*Möbius et al.*, 1999), and it is likely that the addition of the above-mentioned velocity components to inner source models will have an even greater effect. Since measured data of the inner source pickup ion distribution is very scarce, the full effects of such model changes will have to be proven or disproven through measurements in the future, but a model is presented here that begins the journey.

A variety of inputs are required to model the effects of the new velocity components. A simple empirical model of the solar wind and magnetic field was used for this work. The model's analytical elements were validated against published magneto-hydrodynamic (MHD) models for qualitative accuracy, and used for their computational efficiency.

The solar wind speed, Alfvén wave speed, and magnetic field of this model were qualitatively verified against the Block Adaptive-Tree Solar Wind Roe-Type Upwind Scheme (BATSRUS) MHD model (*Powell et al.*, 1999; *Cohen et al.*, 2007, 2008) based on the Wang-Sheeley-Arge empirical model(*Arge and Pizzo*, 2000; *Arge et al.*, 2003; *Arge et al.*, 2004). Electron density was qualitatively verified using a semi-empirical MHD model based on SOHO coronal observations and in-situ measurements by Ulysses (*Sittler and Guhathakurta*, 1999; *Guhathakurta et al.*, 2006). Photoionization and charge-exchange ionization rates were provided by *Ruciński et al.* (1996), and

the aforementioned electron density and temperature measurements combined with cross-sections from *Lotz* (1967) provided the electron-impact ionization rate. The ion density profiles computed by this model were scaled to match existing measured data collected from the Ulysses spacecraft (*Gloeckler et al.*, 2001).

The model is largely unaffected by minor variations in the input velocity and ionization profiles, but the relative variations are important. In particular, the location where the azimuthal dust grain velocity and radial Alfvén wave speeds surpass the solar wind speed are both important, as is the location where the electron-impact ionization rate exceeds the combined photoionization and charge-exchange ionization rates. These "critical points" can significantly affect the results of the model by moving the derived location of peak ion generation, and thus the requisite adiabatic cooling coefficient.

The dust distribution used by *Schwadron et al.* (2000) as the origin for inner source neutrals has the form:

$$n_d(r) = n_d(r_1)\left(\frac{r_1}{r}\right)^{\alpha} \exp\left[-\frac{\lambda}{r_1}\left(\frac{r_1}{r}\right) - 1\right] \tag{2.1}$$

where λ/α sets the location of the dust density peak and α determines the radial spread of the source as shown in Figure 2.2. In the case of solar dust distributions, α can only lie between 1.0 and 1.5 (*Leinert and Grün*, 1990).

The ratio of solar-wind recycled neutral atoms of a given species to their dust source is given by the following:

$$P(r) = P(r_1)\left(\frac{r_1}{r}\right)^{\gamma} \tag{2.2}$$

where γ is assumed to lie between one and two. $\gamma = 2$ would indicate that the production efficiency of neutrals scales to the solar wind density, the most likely case, while γ below two would indicate interference with the solar wind, possibly due to

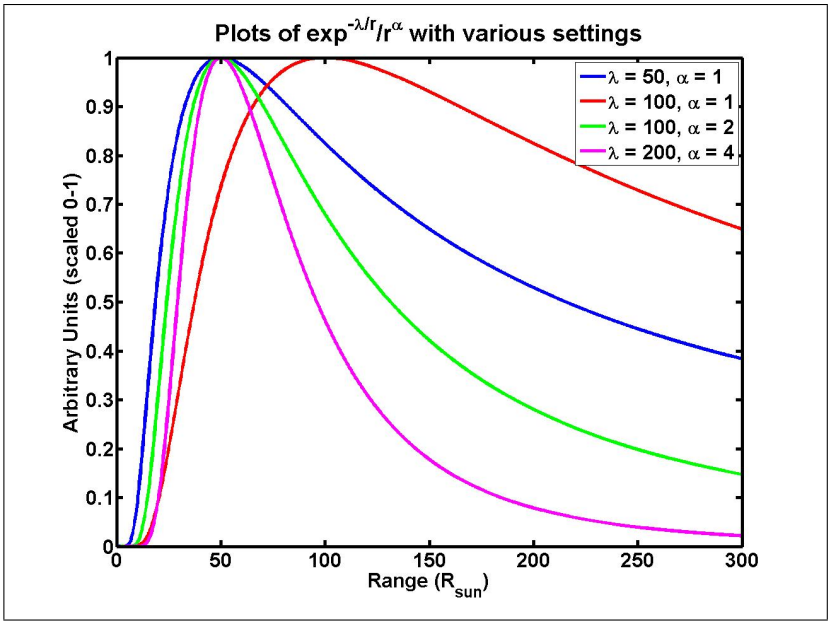

Figure 2.2: Examination of the form of the equatorial dust distribution equation (Eq 2.1). The λ/α sets the peak location, such that 50/1, 100/2, and 200/4 all peak at 50. The α value sets the sharpness of the distribution.

an extended region of nanoscale dust occluding particles farther out. This does not take into account sublimation of the grains themselves, which could be a significant factor for certain elements.

Multiplying Equation 2.1 by Equation 2.2 results in a neutral atom distribution from which ions arise:

$$n_n(r) = C\left(\frac{r_1}{r}\right)^{\alpha+\gamma} \exp\left[\frac{-\lambda}{r}\right] \tag{2.3}$$

where α, γ, and λ are fit parameters and C serves as a scale to match measured data. An implicit assumption is that the dust and neutral distributions are in local equilibrium. This means that dust destruction is balanced by entry of new dust from more distant orbits, and neutral ionization is offset by sputtering of new neutrals from the dust source.

A pickup model can be derived from the continuity equation. The critical com-

ponent for this is the ionization rate, which can be split into three components. The photoionization rate (*Ruciński et al.*, 1996) scales as r^{-2}, the charge-exchange ionization rate (*Ruciński et al.*, 1996) scales by the solar wind proton density, and the electron-impact ionization rate (*Lotz*, 1967) depends upon electron density and temperature. The ionization contributions from each component are mathematically described by Equations 2.4 and shown in Figure 2.3.

$$\begin{aligned}
\beta_{ph}(r) &= \beta_{ph}(r_0)\left(\frac{r_0}{r}\right)^2 \\
\beta_{ce}(r) &= \beta_{ce}(r_0)\left(\frac{n_p(r)}{n_p(r_0)}\right) \\
\beta_{ei}(r) &= S(T_e(r))\, n_e(r) \\
\beta(r) &= \beta_{ph}(r) + \beta_{ce}(r) + \beta_{ei}(r)
\end{aligned} \tag{2.4}$$

where n_p and n_e are the proton and electron densities and T_e is the electron temperature.

The derivation for pickup ion density starts from the steady-state continuity equa-

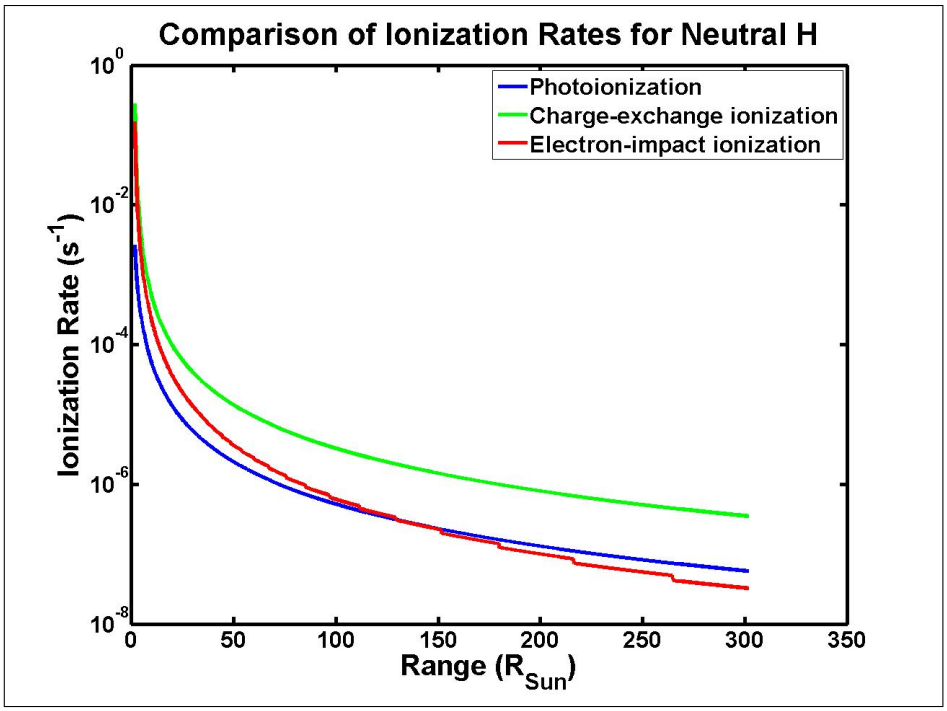

Figure 2.3: Radial profiles of ionization rates for hydrogen via photo-ionization, charge-exchange ionization, and electron-impact ionization. Inside of 20 R_{Sun}, the often-neglected electron-impact ionization becomes a very strong factor.

tion, and assumes spherical symmetry.

$$\nabla \cdot \left(n_{pui}\left(r\right) \mathbf{u} \right) = \text{Sources} = n_{injected}\left(r\right) = n_n\left(r\right) \beta\left(r\right) \quad \text{Cont. eqn.}$$

$$\frac{1}{r^2} \frac{\partial}{\partial r} \left(r^2 n_{pui}\left(r\right) u\left(r\right) \right) = n_n\left(r\right) \beta\left(r\right) \quad \text{Spherical sym.}$$

$$\frac{\partial}{\partial r} \left(r^2 n_{pui}\left(r\right) u\left(r\right) \right) = r^2 n_n\left(r\right) \beta\left(r\right)$$

$$\int \frac{\mathrm{d}}{\mathrm{d}r'} \left(r^2 n_{pui}\left(r\right) u\left(r\right) \right) \, \mathrm{d}r' = \int_1^r r'^2 n_n\left(r\right) \beta\left(r'\right) \, \mathrm{d}r' \tag{2.5}$$

$$r^2 n_{pui}\left(r\right) u\left(r\right) = \int_1^r r'^2 n_n\left(r'\right) \beta\left(r'\right) \, \mathrm{d}r'$$

$$n_{pui}\left(r\right) = \frac{1}{r^2} \frac{1}{u\left(r\right)} \int_1^r r'^2 n_n\left(r'\right) \beta\left(r'\right) \, \mathrm{d}r'$$

$$n_{pui}(r) = \frac{1}{r^2}\frac{1}{u(r)}\int_1^r C\left(\frac{r_1}{r'}\right)^{\alpha+\gamma}\exp\left[\frac{-\lambda}{r'}\right] \left(\beta_{ph}(r_0)\, r_0^2 + r'^2\beta_{ce}(r_0)\left(\frac{n_p(r)}{n_p(r_0)}\right) + r'^2\beta_{ei}(r')\right)\, \mathrm{d}r' \tag{2.6}$$

To find the scaling constant C, Gauss's Theorem was used:

$$\int_V (\nabla\cdot\mathbf{Q})\, \mathrm{d}V = \oint_A \mathbf{Q}\cdot\, \mathrm{d}\mathbf{A} \tag{2.7}$$

So, starting with the integration of the continuity equation:

$$\int_V \nabla\cdot(n_{pui}(r)\, u(r))\, \mathrm{d}V = \int_V n_n(r)\,\beta(r)\, \mathrm{d}V$$

$$\oint_A (n_{pui}(r)\, u(r))\cdot\, \mathrm{d}\mathbf{A} = \int_V n_n(r)\,\beta(r)\, \mathrm{d}V \qquad \text{Use Eq. 2.7} \tag{2.8}$$

$$\cancel{4\pi} r_0^2 n_{pui}(r_0)\, u(r_0) = \int_1^{r_0} \cancel{4\pi} r'^2 n_n(r')\,\beta(r')\, \mathrm{d}r' \quad \text{Assume spherical sym.}$$

$$r_0^2 n_{pui}(r_0)\, u(r_0) = \int_1^{r_0} r'^2 n_n(r')\,\beta(r')\, \mathrm{d}r' \qquad \text{Same finish as Eq. 2.5} \tag{2.9}$$

For a given set of values of $n_{pui}(r_0)$ and $u(r_0)$ at a given radial distance r_0, the scaling constant C can be found using Eqs. 2.9 and 2.3. Figure 2.4 shows the resultant distribution functions for a variety of λ values with γ equal to one and two, while Figure 2.5 shows the location and intensity of the pickup peaks.

$n_{injected}$ is a radial injection rate in $m^{-3}s^{-1}$. To compute the steady-state radial distribution of pickup ions entering the system (m^{-3}) the time it takes the solar wind to cross a given distance is used:

$$n_{in}(r) = n_{injected}(r)\,\frac{dr}{v_{solarwind}} \tag{2.10}$$

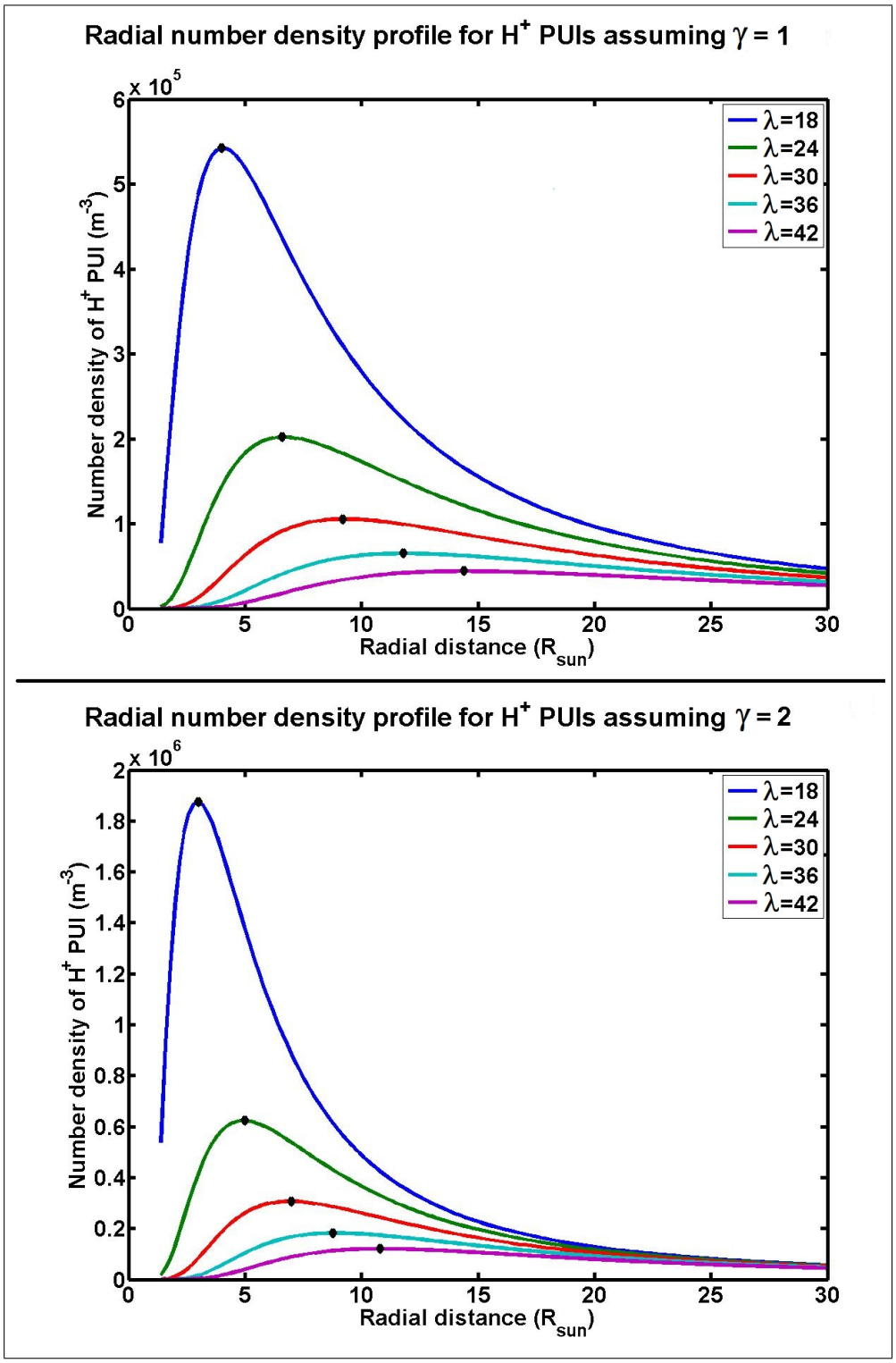

Figure 2.4: Equatorial H^+ ion distributions. The results of Equation 2.6 with $\alpha = 1.5$, $\gamma = 1, 2$, and λ varying from 18-42. The location of each curve's peak is denoted by a black diamond. Clearly, the higher γ value results in curves that peak higher, more sharply, and closer to the Sun.

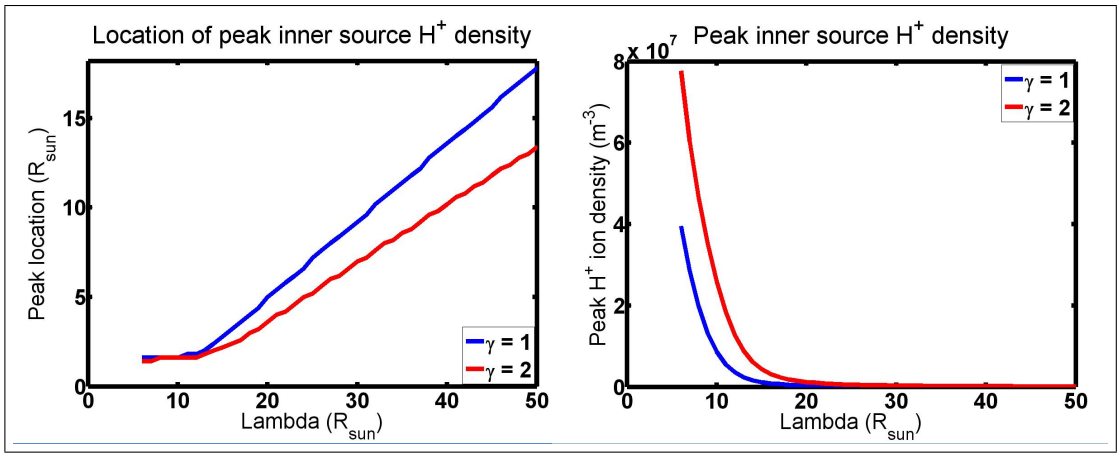

Figure 2.5: Equatorial H^+ pickup ion peak location and intensity for modeled distributions. With higher γ, the peaks are closer to the Sun and sharper, just as would be the case with higher α.

If this is calculated on a small enough distance scale ($dr \rightarrow 0$), a very accurate pickup ion density can be calculated. The accuracy can be tested by radially expanding each "packet" of ions outward, summing them, and comparing to a known data point. From the continuity equation we have $\nabla \cdot (n(r)u(r)) = \text{Sources} = 0$ for each packet, since as they expand there are no additional sources. Thus, $r^2 n(r)u(r) = \text{constant}$ and for each input packet

$$n_{out}(r) = n_{in}(r) \left(\frac{r_{in}^2 u_{in}(r)}{r_0^2 u(r_0)} \right) \tag{2.11}$$

and $n_{out,total}(r) = \sum n_{out}(r) \equiv n_{pui}(r_0)$ from Eq. 2.9.

2.3 Model Results

Radial pickup ion distributions for $\gamma = 1, 2$ and $\lambda = 12$ to 150 are computed, along with the local injection (n_{in}) and velocity profiles for the solar wind (v_{sw}) and thermal pickup temperature with all three major velocity components (v_{full}). Thermal pickup temperature with only the solar wind contribution is identical to the solar wind velocity profile. With these profiles, all the pieces are in place for examining

some emergent behavior. Assuming a polytropic index of 5/3, and assuming that the ion pickup at the peak is much greater than the surrounding locations (i.e. a sharply localized phenomenon), one can calculate the thermal velocity at 1 AU of the resultant ions:

$$\left(\frac{v_{th}\left(r_0\right)}{v_{peak}\left(\lambda\right)}\right)^2 = \left(\frac{n_{pui}\left(r_0\right)}{n_{peak}\left(\lambda\right)}\right) \tag{2.12}$$

where v_{peak} and n_{peak} are the calculated velocity and PUI density at the location of peak pickup. Calculating this v_{th,r_0} over the computed data set, and knowing the thermal velocity of the input data, one can find which value of λ is most likely to provide the correct distribution. The case where thermal velocity includes the new velocity components requires that the distribution travel farther to cool to the measured v_{th,r_0}. This means that the pickup location must be closer to the Sun. For $\gamma = 1$, the difference is between PUI peaks at 32.4 $R_\odot$ for the solar-wind only case versus 9.2 $R_\odot$ for the v_{tot} case, and for $\gamma = 2$ the numbers are 37 $R_\odot$ versus 14.6 $R_\odot$. Figure 2.6 demonstrates this graphically.

The calculation of Equation 2.12 is at best a 0^{th} order estimate, since it does not take into account the acceleration of the solar wind and a majority of the ions are picked up in the acceleration region. However, with a more accurate model the adiabatic expansion of each locally injected packet of particles (Equation 2.10) can be calculated. An algorithm for calculating adiabatic expansion curves based on a spherically-symmetric Fokker-Planck equation (*Fisk et al.*, 1973) was developed.

The adiabatic expansion model begins with the following equation:

$$U_{sw}\left(r\right)\frac{\partial f\left(r,v\right)}{\partial r} - \frac{1}{3}\left[\nabla \cdot U_{sw}\left(r\right)\right] v\left(r\right)\frac{\partial f\left(r,v\right)}{\partial v} = \text{Sources} \tag{2.13}$$

where U_{sw} is the solar wind bulk velocity, r is the heliocentric distance, v is the PUI thermal velocity, and $f\left(r,v\right)$ is the distribution function. The first term of

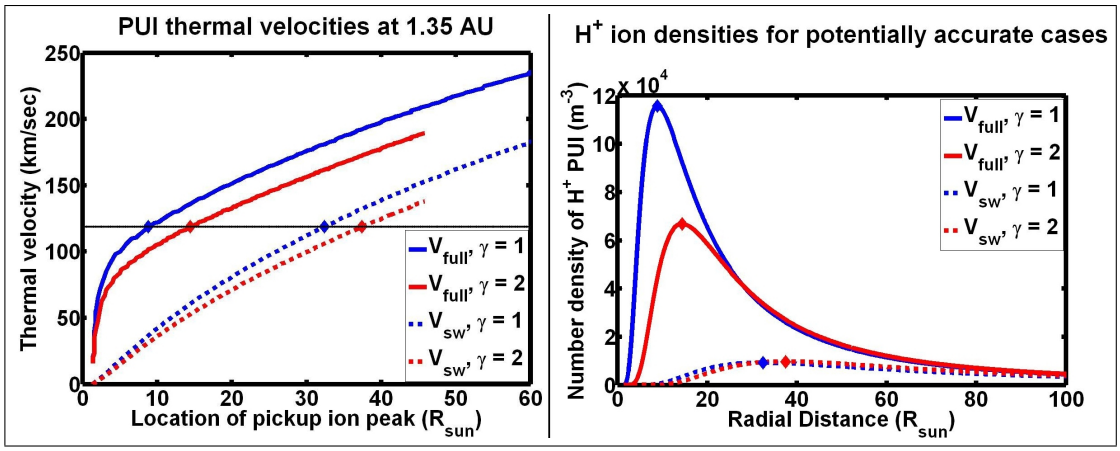

Figure 2.6: Pickup ion dynamic properties under the assumption of simple adiabatic cooling. The graph on the left shows the results of Equation 2.12, with the v_{th} of the measured data shown as a horizontal line. The dotted lines follow curves based on isotropic distributions at the solar wind speed, v_{sw}; the solid lines are for the v_{tot} case. The graph on the right shows the n_{pui} curves from Equation 2.6 corresponding to the dots in the left image, the cases where the calculated and measured thermal velocities match. In the case of both $\gamma = 1$ and $\gamma = 2$ the peaks are sharper and closer to the Sun when all the velocity components are taken into account.

Equation 2.13 represents convection, and the second term adiabatic cooling. Setting the source term to 0 and postulating that r and v can be parameterized as $r(X)$ and $v(X)$, the chain rule allows the following change of variables:

$$\frac{\mathrm{d}f\left(r,v\right)}{\mathrm{d}X} = \frac{\partial f\left(r,v\right)}{\partial r}\frac{\mathrm{d}r}{\mathrm{d}X} + \frac{\partial f\left(r,v\right)}{\partial v}\frac{\mathrm{d}v}{\mathrm{d}X} \tag{2.14}$$

Thus, refering back to Equation 2.13 these definitions can be made:

$$\begin{aligned} \frac{\mathrm{d}r}{\mathrm{d}X} &= U_{sw}\left(r\right) \\ \frac{\mathrm{d}v}{\mathrm{d}X} &= -\frac{1}{3}\left[\nabla \cdot U_{sw}\left(r\right)\right] v\left(r\right) \end{aligned} \tag{2.15}$$

and so

$$
\begin{aligned}
\mathrm{d}X &= \frac{\mathrm{d}r}{U_{sw}(r)} \\
\mathrm{d}X &= \frac{-3\mathrm{d}v(r)}{[\nabla \cdot U_{sw}(r)]\, v(r)} \\
\frac{\mathrm{d}r}{U_{sw}(r)} &= \frac{-3\mathrm{d}v(r)}{[\nabla \cdot U_{sw}(r)]\, v(r)} \\
\frac{\mathrm{d}v(r)}{\mathrm{d}r} &= -\frac{1}{3}\frac{[\nabla \cdot U_{sw}(r)]\, v(r)}{U_{sw}(r)}
\end{aligned}
\tag{2.16}
$$

In spherical coordinates, $[\nabla \cdot U_{sw}(r)] = \frac{1}{r^2}\frac{\mathrm{d}}{\mathrm{d}r}\left(r^2 U_{sw}(r)\right)$, so

$$
\frac{\mathrm{d}v(r)}{\mathrm{d}r} = -\frac{v(r)}{3}\frac{1}{r^2 U_{sw}(r)}\frac{\mathrm{d}\left(r^2 U_{sw}(r)\right)}{\mathrm{d}r} \tag{2.17}
$$

Since radial distributions of U_{sw}, v, and n_{in} are available, one can numerically calculate curves for all (r,v), input n_{in} at the given (r_{in},v_{in}) and follow them down their respective curves to (r_{out},v_{out}) as demonstrated in Figure 2.7.

The radial PUI distributions computed earlier are adiabatically expanded to 1.35 AU using the curves from Figure 2.7. For each input distribution, a vertical cut through the resulting (r, v) curve provides a distribution in (n_{out}, v_{out}). Assuming isotropy of the distribution, and knowing the solar wind speed at r_{out}, one can convert this to a true phase-space distribution. First v_{out} is divided by the solar wind speed to form w_{out}, then converted to a constant bin size (δw). Each bin in w is treated as a spherical shell of radius $w_{out}(i)$ and thickness δw. The ion density (n_{out}) in each shell is divided over the spherical volume of that shell, resulting in an isotropic $f_{sw}(w)$. These distributions are in the solar wind reference frame. The smaller the value of λ, the closer to the Sun the pickup ion peak (as per Figure 2.5), and thus the longer the distributions have had to cool. This means that for small λ the distributions peak close to $w = 0$, meaning that they have nearly thermalized with the solar wind, at least with regard to their speed (i.e. $T_{SW} \approx T_{PUI}$).

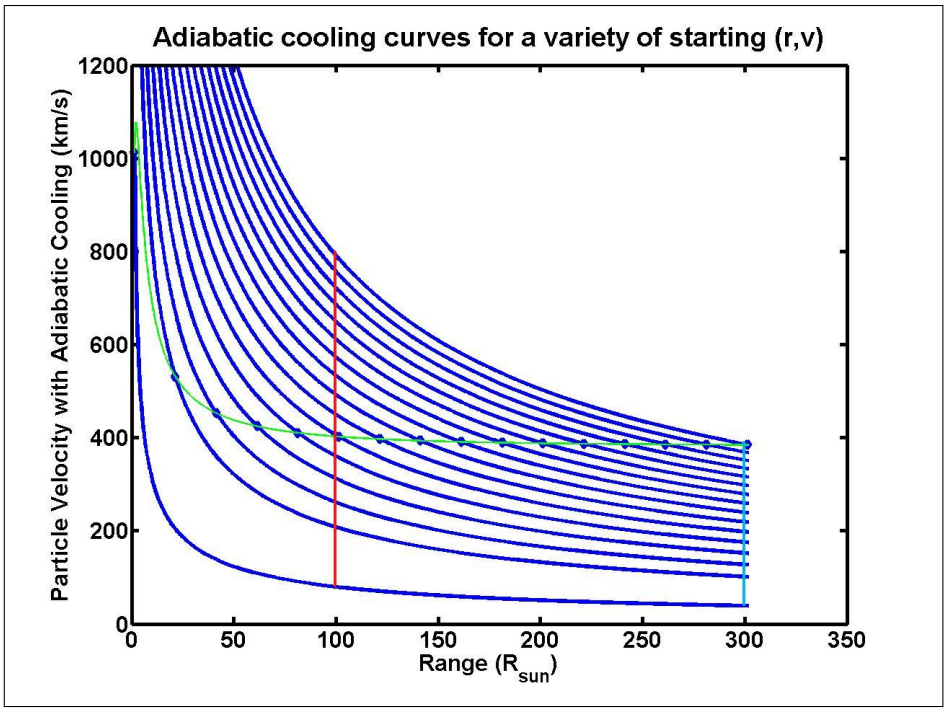

Figure 2.7: Adiabatic cooling of velocity shell distributions. Each "packet" of flux (n_{in} from Eq. 2.10) enters the system at its computed (r_{in}, v_{in}). The green line going through all the dots is the thermal velocity (v_{in}, in this case set to v_{tot}). From that starting point, each packet then moves outward while expanding (as per Eq. 2.11) and cooling. Thus from input (n, r, v) one can find output (n, r, v) for all r. A vertical cut through this graph can be taken as a velocity distribution at a given r_{out} with the y-coordinate being the radius of a spherical shell in velocity phase-space. The distribution narrows (cools) as it propagates outward. At $r = 100$ $R_\odot$ (red line) the distribution is much wider than at $r = 300$ $R_\odot$ (pale blue line).

To convert the distributions from the solar wind frame to the Sun's rest frame, in which an instrument could measure the data, a frame transition has to take place. As mentioned above, the distributions are isotropic nested spherical shells in phase space, each containing a certain amount of ion density (n_{out}) and centered around the origin of a 3-D coordinate system. To move to the Sun's rest frame, the origin needs to shift by the solar wind speed, or $w = 1$. To compute the new distribution, another series of nested shells is formed around the new origin, and the amount of ion density in each shell is the integration of its intersection with the original solar wind

frame distribution. Since ion density is not the desired output, the total ion density of each shell is normalized by dividing by the volume of overlap with the original distribution. This returns a new phase space distribution function $f_{rest}(w)$ that is no longer isotropic. Figure 2.8 demonstrates this process.

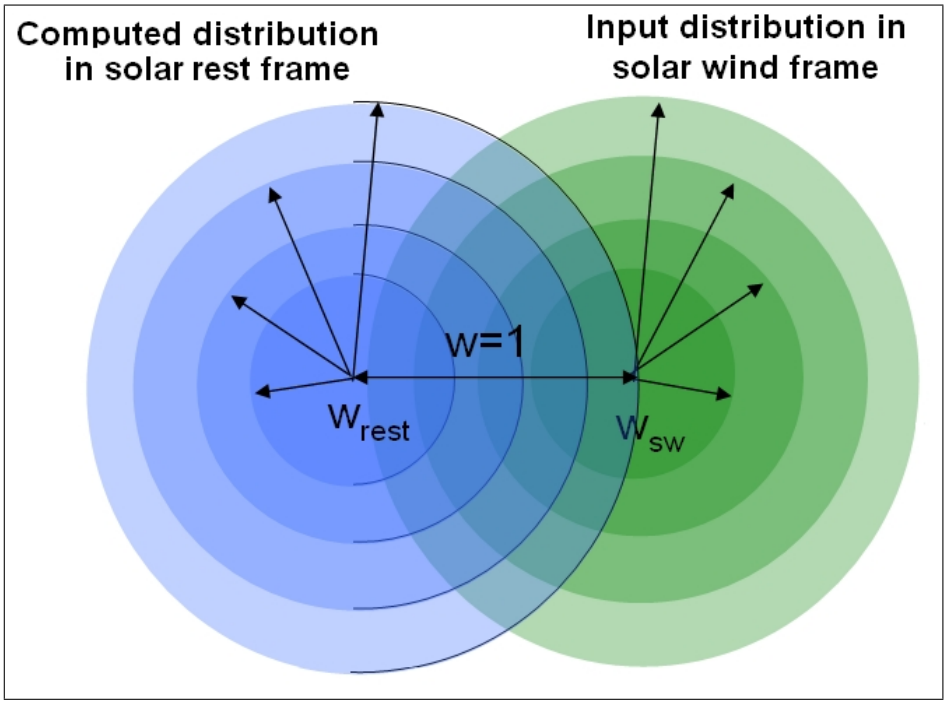

Figure 2.8: Conversion of solar wind frame distributions to the solar rest frame. The green distribution on the right is the original solar wind frame distribution, with the w_{sw} values representing w_{out} from prior calculations. The blue distribution on the left is in the solar rest frame with the w_{rest} values representing the velocities in the new distribution f_{rest}.

An analysis similar to the simple adiabatic case above was undertaken to determine which of the many possible distributions is the most likely. Since this is not just comparison of two numbers, however, it required more complicated data processing. The distribution that best fit the input distribution was determined by least-squares curve fitting, with results as shown in Figure 2.9. Once again, the v_{full} case with all three velocity components results in distributions peaking far closer to the Sun than the v_{sw} case. For $\gamma = 1$, the difference is between PUI peaks at 10.2 $R_{\odot}$ for the

solar-wind only case versus 1.6 $R_\odot$ for the v_{tot} case, and for $\gamma = 2$ the numbers are 13.4 $R_\odot$ versus 1.6 $R_\odot$.

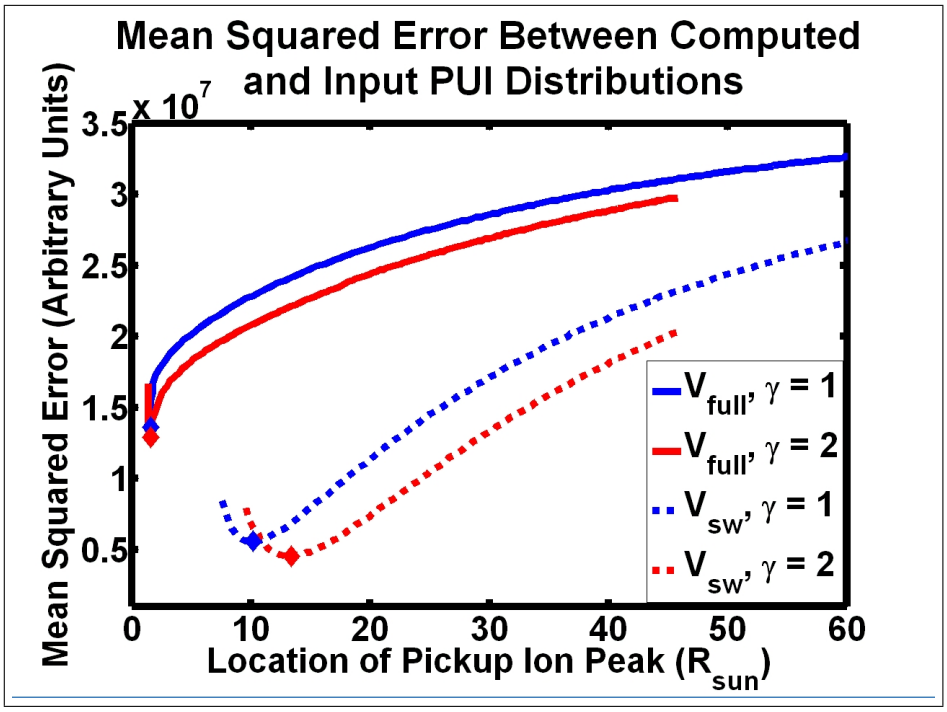

Figure 2.9: Mean-square curve fits between simulated distributions and measured data. The dotted lines follow curves based on isotropic distributions at the solar wind speed, v_{sw}; the solid lines are for the v_{tot} case. As with Figure 2.6, for both $\gamma = 1$ and $\gamma = 2$ the peaks are sharper and closer to the Sun when all the velocity components are taken into account.

The resultant phase-space distributions look similar to the distribution used as an input and scale for the system, but not identical. This is because the model did not include any scattering or thermodynamic calculations aside from the adiabatic cooling. Figure 2.10 shows that the v_{sw} case results in a very good match between measured and simulated data. One important consideration is that in order to get this good of a match the input curve (in red) had to be manually shifted to peak at w=1 rather than w=0.8. In fact, all of the simulated distributions were compared to this shifted input data; if this is not done, the matches are all far worse and, even more notably, the best-fits for the v_{sw} case move outward to 19 $R_\odot$ for $\gamma = 1$ and 24.8

$R_\odot$ for $gamma = 2$.

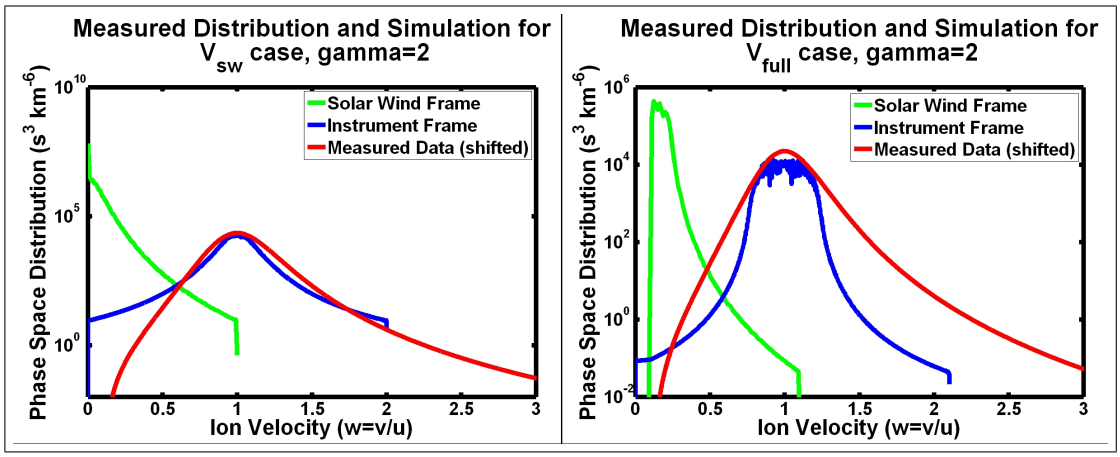

Figure 2.10: Phase-space distributions after adiabatic cooling in both solar wind frame and solar rest frame. The graph on the left shows the results for the v_{sw} pickup case, and the graph on the right shows the v_{full} case using all the velocity components. In both graphs, the red line is the measured data (shifted to peak at w=1), the green and red lines are the simulated distribution in the solar wind and rest frames respectively.

The most obvious deviation remaining in these distributions is that tops of the simulated distributions for v_{tot} are flatter and lower than the peak of the input distribution. This is because the solar wind frame distributions, shown in green in Figure 2.10, begin at some finite w for v_{tot}, often as far from the origin as $w = 0.2$ to 0.3. In the case of v_{sw} pickup velocity, the solar wind frame distribution peak is very close to the Sun. This in essence means that the innermost few green spheres in Figure 2.8 are filled; in the v_{tot} case, with the solar-wind frame distribution dropping to nearly zero at w=0.1, those same parts of the distribution contain zero ions, and thus as the blue shells expand outward they gain nothing from those innermost spheres. As the overlap arc lengths grow with no further contribution, this can flatten the top of the output distributions and, in extreme cases, cause a bow to develop in the flattened top. To partially compensate for the lower, flat peak, the simulated distributions are slightly wider than the input distribution. However, they also lack the long, power-law tail, which is caused by stochastic particle acceleration not taken

into account by this model. The v_{full} distributions thus do not match quite as well, as seen by the higher mean-square errors in Figure 2.9.

2.4 Discussion

This model produces predictions of pickup ion and neutral atom distributions resulting from solar wind ions neutralized by interaction with the interplanetary dust population. This interaction creates an azimuthal velocity component for the neutral atoms that has never before been considered. In addition, upon ionization Alfvén wave scattering adds an additional radial component to the ions' initial pickup thermal velocity.

Both of the adiabatic models used demonstrate that the location of peak ion pickup moves much closer to the Sun when the above two velocity components are included in the pickup thermal velocity. In fact, the more physically accurate adiabatic model resulted in PUI peaks inside of 2.0 $R_\odot$, which are unlikely due to sublimation of the dust grains (*Mann et al.*, 2004). A few factors can be used to explain this. First, the dust population was modeled with a fairly simple parameterized equation, which may need an additional damping factor very close to the Sun to take into account dust losses due to sublimation, β-meteoroids, and sputtering. Second, the production efficiency of neutrals from the dust source was modeled as a $1/r^2$ effect, but there may be additional physical effects that disrupt this efficiency, and they might themselves be radially-dependent. Examples of this include magnetic or thermal changes in the environment or shielding of dust grains by a diffuse cloud of nanoparticles. And third, the addition of the Alfvén wave radial velocity component may not be a 100% efficient process since some of the scattering will isotropize the distribution rather than accelerate the ions. All of these factors indicate that while the pickup peaks do move significantly sunward with the additional pickup thermal velocity components, they may not move in quite as far as the model predicts. The more accurate physics

that can be added to this model, the closer it will come to reality, but this is an iterative process with measurements that have yet to be taken.

2.5 Proposed Neutral Atom Instrument

What was presented above is a model that is underconstrained—only one measured pickup distribution was available for comparison. More data are required to refine this model and fit its novel components into the larger solar weather framework.

The Solar Probe Plus mission is going to fly closer to the Sun than any prior mission (*Solar Probe*, 2008). Figure 2.11 shows the currently planned trajectory of Solar Probe Plus, which goes to an unprecedented 9.5 $R_\odot$ for multiple passes. This mission will be able to answer many of the questions in Section 1.2.4.

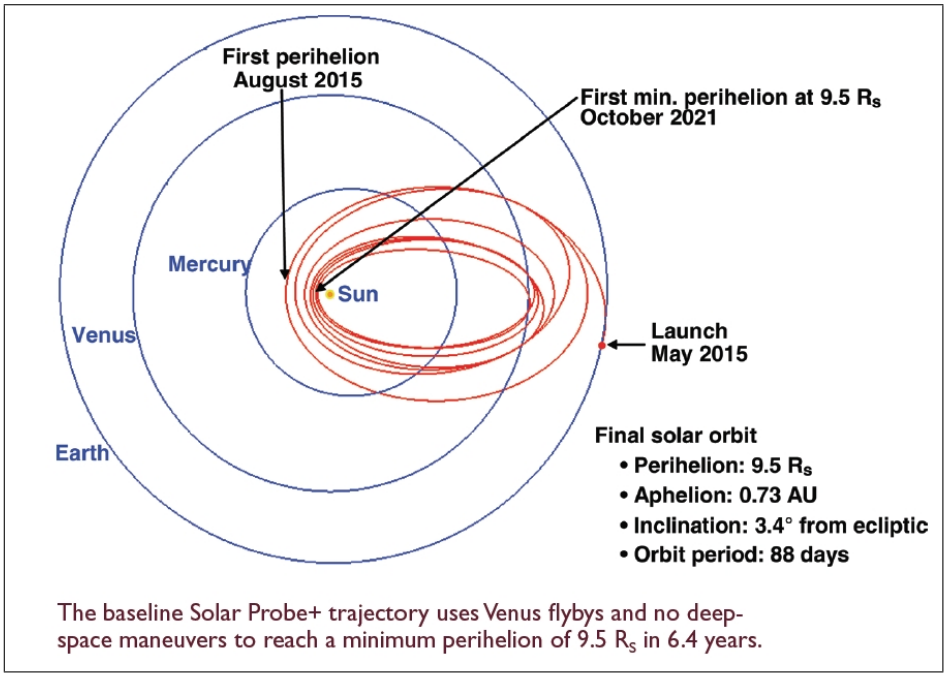

Figure 2.11: Solar Probe Plus trajectory. Image from *Solar Probe* (2008)

An instrument suite capable of measuring pickup ions and neutral atoms in their source region is critical for a wide variety of purposes. Figure 2.12 shows two possible designs for a neutral atom instrument. They borrow heavily from technology devel-

oped for the Fast Imaging Plasma Spectrometer (FIPS) instrument. This new and proposed instrument would fly on the Solar Probe Plus with its aperture facing the direction of flight, also called the ram direction.

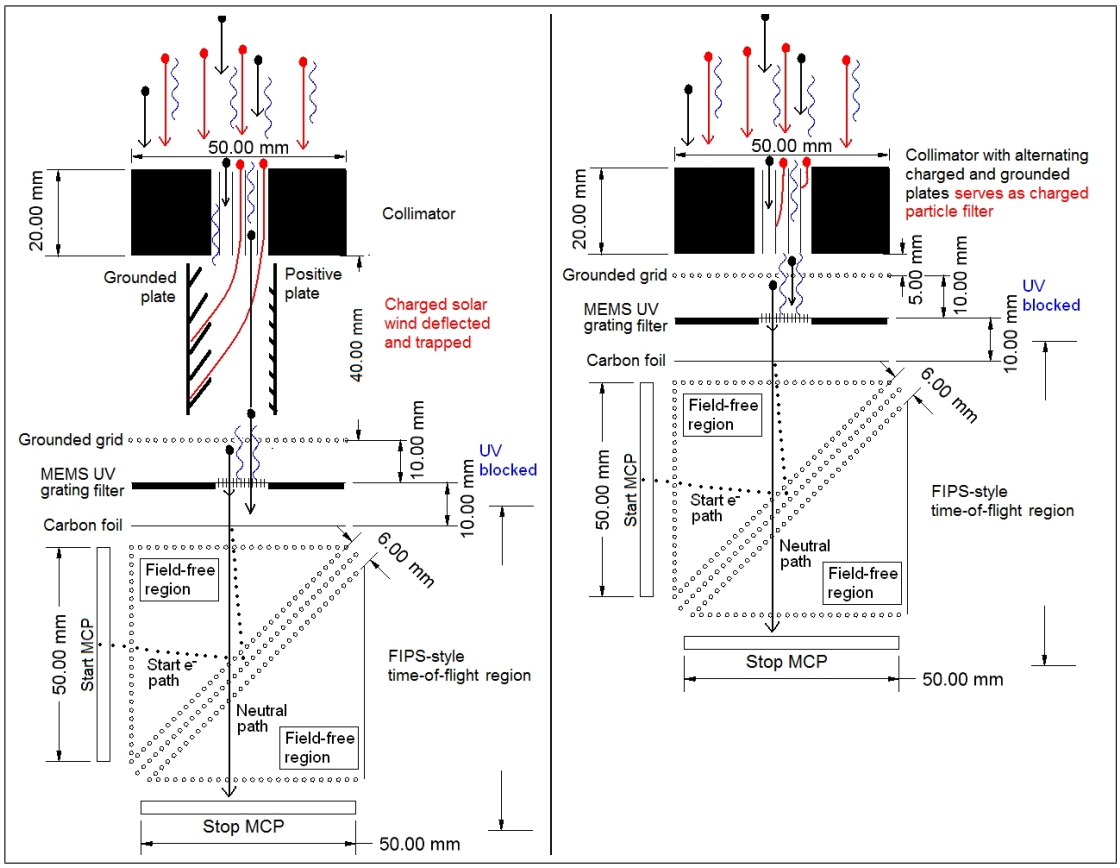

Figure 2.12: Cutaway schematic of two possible configurations for proposed neutral atom instrument. The only difference between the two schematics is the technique for rejection of the charged solar wind (red). In both cases, neutral atoms (black) and photons (blue) pass through; a nanograting blocks UV photons while negatively ionizing a small fraction of neutral atoms. Atoms are analyzed by their two-dimensional position, energy, and total time of flight.

A collimator ensures that incoming particles are a directional beam, and also partially shields the internals of the instrument from solar photons. In one configuration (on the left), this is followed by a solar wind rejection section similar to that used in *Hsieh et al.* (2004). The positive ions are deflected by the potential between two plates and trapped in a metal sawtooth; the smaller mirror sawtooth of the grounded

plate is to trap any electrons sputtered loose by the ions. In the schematic on the right, a design inspired by *Gruntman* (1994b) uses alternating positively-charged and grounded plates as the collimator, and thus the collimator itself serves as a solar wind trap. A grounded grid shields the potentials of either design from the rest of the instrument. Since the collimator is being bombarded with energetic solar photons, which often cause the release of electrons, the collimator plates may draw a significant current to replenish those electrons.

One important point is that while the design on the left may have better rejection of the solar wind ions, it also limits the field of view of the instrument. Shortening the solar wind rejection section would require a higher voltage on the pair of plates, a trade of power for field-of-view. If the entrance aperture is 1 cm x 5 cm, the field of view for the left model is 23° compared to almost 41° for the right model.

Behind the grounded grid is the filter described in Chapters IV and V, which not only rejects energetic ultraviolet (UV) photons, but also should negatively ionize a statistically significant percent of neutral atoms entering the system. The optically-polished tungsten conversion surface used by Low Energy Neutral Atom (LENA) on Imaging from the Magnetopause to the Aurora for Global Exploration (IMAGE) resulted in 1-2% conversion of neutrals to negative ions, with 60-85% of the energy retained after conversion (*Moore et al.*, 2000). A strong potential (∼15-20 kV) between the filter and the carbon foil accelerates these ionized neutrals, which then enter a time-of-flight (TOF) region similar to that of FIPS. Using Equations 1.1, these measurements should be enough to obtain the mass-per-charge of incoming particles with relatively low starting energies such as recycled neutrals, and since the charge is assumed to be one that gives the mass.

A simulation of the Solar Probe Plus trajectory was run through the results of the model above. Particle flux measured by the above instrument was computed with:

$$Flux_{ion} = n_n(r) \times A \times G_{particle} \times I_{eff} \times v_{rel} \tag{2.18}$$

where n_n is the neutral density profile of Equation 2.3; A is the area of the input aperture ($\sim$ 1 cm^2); $G_{particle}$ is the geometric transparency of the collimator, UV filter, and internal harps ($\sim$ 0.15-0.17 m^2/m^2); I_{eff} is the ionization efficiency of the UV filter (1% based on the example of LENA); and v_{rel} is the relative velocity of the spacecraft to the neutral population, the latter being assumed to be moving at the azimuthal velocity of the dust grains. This obviously does not take into account the neutral solar wind, cometary atoms, dust sublimation, the interstellar wind, or any other sources of neutral atoms not mentioned in the model.

Since instruments on Solar Probe Plus are not facing the Sun, but rather facing the ram direction, the UV photons they receive are scattered from dust and the solar wind. Figure 3 of *Romoli et al.* (2003) shows the Lyman-alpha (Ly-α) flux of coronal holes and streamers seen at 1 AU. Looking at a portion of the corona at 2 R$_\odot$, the coronal hole Ly-α flux is 2×10^9 $ph\ cm^{-2}s^{-1}sr^{-1}$ and the streamer flux is 7×10^{10} $ph\ cm^{-2}s^{-1}sr^{-1}$. At the 9.5 R$_\odot$ periapsis of Solar Probe Plus's orbit, these numbers are increased by a factor of upwards of 500, to 1×10^{12} $ph\ cm^{-2}s^{-1}sr^{-1}$ and 4×10^{13} $ph\ cm^{-2}s^{-1}sr^{-1}$ respectively. The latter number serves well as an upper limit for this study.

A grating with 60 nm slits, 2000 nm depth, and 10.75 μm period support grating has acceptance angles of 1.72 degrees in the cross-slit direction and 79.46 degrees along the slit for a total solid angle of 0.0265 steradians. This is of course reduced by the geometry of the instrument, as discussed before, but for now serves as a reasonable starting point. The following equation is used to calculate the total Ly-α flux entering the instrument

$$Flux_{UV} = Ly - \alpha_{Streamer} \times \text{Solid Angle} \times A \times G_{Ly-\alpha} \tag{2.19}$$

where $G_{Ly-\alpha}$ is the same as $G_{particle}$ above except that the internal harps are not considered. With these conditions, and using the best-case solution for neutral density using v_{tot} pickup velocity, the ratio of Ly-α photons to ions is approximately 3×10^9.

The start and stop microchannel plate (MCP)s are far more sensitive to ions than photons, with ion detection efficiency up to 85% and UV (>110 nm) detection efficiency on the order of 1-5%. Figure 3 of *Herrero* (1992) indicates approximately 1.4% MCP quantum efficiency for Ly-α. *Straub et al.* (1999) show that the detection efficiency for ions depends on the MCP bias. Coatings can be applied to MCPs to enhance detection efficiency of specific radiation or particles. For example, magnesium iodide (MgO) coatings are used to improve detection efficiency of ions and electrons, and cesium iodide (CsI), magnesium fluoride (MgF_2), or copper iodide (CuI) coatings enhance detection of UV photons.

The carbon foil also provides some UV rejection. Thinner foils have higher UV transmittance as well as higher electron yields, but are necessary for sensitive measurements of low-energy particles. *Hsieh et al.* (1980) indicate that a 2 μg cm^{-2} carbon foil has Ly-α transmittance of 10^{-1}. These transmitted photons add to the noise level of the stop MCP, and while the slight suppression of the carbon foil is helpful, a more important factor remains. The forward photoelectron yield is $\sim 10^{-3}$ per incident photon. This adds significantly to the noise level of the start MCP, which should have a noise level of only a few counts per second, and thus the UV should be suppressed as much as possible before reaching the carbon foil. *Hsieh et al.* (1991) looked into composite foils (Si/C, Al/C, etc.) and found that they are better than pure carbon foils for particles higher than 5 keV, but for solar wind applications the pure carbon foils are still better.

With the above numbers for the MCP transmittance, and assuming that the UV must be blocked prior to the carbon foil, the desired rejection ratio of photons to negatively-charged ions for the grating is approximately $10^6 - 10^7$. This is a very

high standard to meet, but it should be possible with the technologies explored in Chapters IV and V.

Having the satellite follow a retrograde orbit would be of immense benefit to neutral atom or dust measurements. The particles' velocity would be added to the satellite azimuthal velocity rather than subtracted, which means measurements would be possible throughout the orbit. In addition, the flux of ions rises by 2-4 orders of magnitude, vastly increasing the signal-to-noise ratio.

The critical piece of this design is the silicon nanograting. This not only blocks the vast majority of the UV that gets through the collimator, but also ionizes the incoming neutral particles. The latter ability is as yet only theoretical, but even should tests prove that the grating lacks this quality it would still be of significant use in other plasma instruments since it can replace the bulky and weighty light traps currently used.

The most important specifications of the grating, for it to be useful in an instrument such as the above, are summarized below in Table 2.1.

Table 2.1: Important specifications for nanograting

	Specification	Notes
Rejection ratio (Ly-α/ions)	10^6-10^7	Pinholes must be plugged
Field of View	3°x40°	Can add 2nd instruments at 90° rot.
Area	>1 cm^{-2}	Multiple gratings can be used
Self-supporting		Needs strong support grid

The rest of this dissertation discusses the technological challenges and advances made toward creating such a filter.

CHAPTER III

Introduction to Micromachining

This chapter will cover the basic micromachining technologies, loosely broken down into four major components: lithography, thin film deposition, doping, and etching. The following sections will briefly introduce each component. More in-depth discussion can be found in textbooks such as *Kovacs* (1998), *Senturia* (2001), *Madou* (2002), and others. *Mahalik* (2008) touches briefly upon all relevant subjects and shows examples of microelectromechanical systems (MEMS) devices, and *Najafi* (1991) reviews the application of these technologies to the creation of what he calls "smart sensors" (see also *Najafi and Mastrangelo* (1993)). In recent years the same technologies have been applied to the nanoscale, creating a category of devices known as nanoelectromechanical systems (NEMS) (*Craighead*, 2000; *Ekinci and Roukes*, 2005). *Radelaar* (1993) reviews the problems and technologies for making nanoscale structures and how they differ from microscale structures.

3.1 Lithography

Lithography is, in broadest terms, the transfer of a pattern from a master to another surface, usually a hard surface like a silicon wafer, by using an easily patterned process-resistive material as an intermediate step.

The most common form of lithography is photolithography, which has a long

history in the integrated circuit (IC) industry. Photolithography, a technique very similar to the photographic process of producing a print from a negative, uses light-sensitive polymers called photoresist for pattern transfer. The photoresist is typically spin-coated onto a substrate, resulting in very even thickness except at the substrate edges, which can form edge-beads that need to be removed before further processing. Typically the surface of the substrate is primed with a monolayer of an adhesion promoter such as hexamethyldisilazane (HMDS), either through spin-coating or gas-phase adsorption.

The master pattern is etched into a film of absorptive metal (e.g. chromium) that is coated on a transparent glass plate, called a mask. The mask is put in contact with a surface coated in photoresist, then exposed to ultraviolet (UV) light for a period of time dependent on the thickness and absorption rate of the photoresist. The light thus impinges only on the areas of photoresist not covered in the masking metal. Exposure induces a chemical reaction that changes the photoresist's solubility in a developer solvent. After exposure, a developer is used to remove the photoresist in the exposed areas in the case of positive resist, or the unexposed areas in the case of a negative photoresist. The remaining photoresist is then used to transfer the pattern to the underlying substrate, usually by some form of etching (§3.4). This process is illustrated in Figure 3.1.

Multiple layers of patterns can be photolithographically transfered to the same substrate in sequential fashion through use of alignment marks on each mask. These marks allow pattern registration to an accuracy less than a micrometer[a], enabling exact placement of transistor gates, actuator combs, and other microscopic structures.

The main advantage of photolithography is speed, since an entire wafer can be patterned at the same time so long as the light intensity is constant over the whole mask. In practice, small features tend to be patterned through a step-and-flash

[a]A millionth of a meter, 1 x 10^{-6} meters, is also called a "micron" and is represented by the symbol μm .

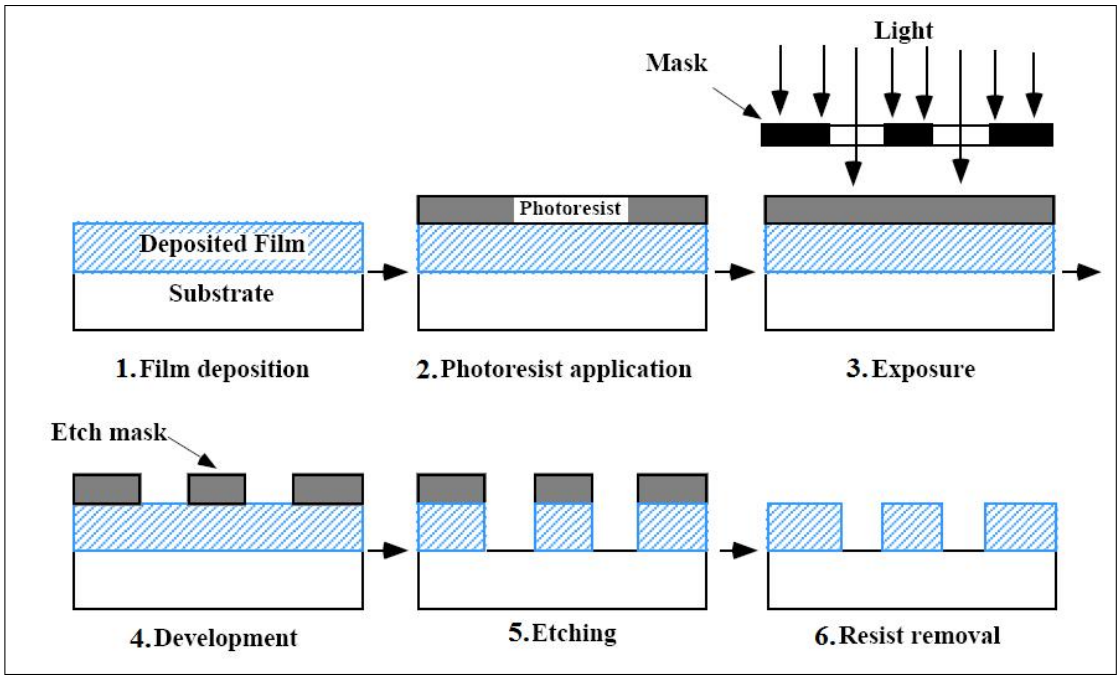

Figure 3.1: Photolithography process steps. For a negative photoresist the inverse image would be developed in Step 4, leaving only the exposed portion. There are some hidden sub-steps that include surface priming, various baking steps, and microscope feature verification steps.

technique that only exposes a portion of a wafer at a time, but even that can transfer many copies of a pattern at once.

The wavelength of the incident light is a limiting factor on pattern features sizes, and the IC industry is currently attempting to find alternative patterning methods that get around this inherent limitation (*Bratton et al.*, 2006; *Gates et al.*, 2004, 2005). Extreme ultraviolet lithography is currently the most promising candidate (*Solak*, 2006; *Wu and Kumar*, 2007).

More fine-grain lithography is possible through the use of lasers (*Tiaw et al.*, 2008) or electron- or ion-beam resist patterning (*Matsui and Ochiai*, 1996). However, in those cases each feature has to be patterned individually, and dense features can take a very long time to pattern. A technique using the standing-wave interference pattern of two coherent beams to pattern photoresist is called laser interference lithography

(LIL) (*van Rijn*, 2006; *Xie et al.*, 2008), with variations including multi-beam LIL (*Su et al.*, 2007) and scanning-beam LIL (*Chen et al.*, 2002a). Very large areas can be patterned this way, but only with periodic line-and-space patterns. Feature sizes from LIL can be as small as half the wavelength of the beams, currently of the order 100 nanometers from UV laser sources.

Soft lithography is a branch of pattern transfer that uses printing or molding rather than light (*Gates et al.*, 2004, 2005; *Rogers and Nuzzo*, 2005). As such, instead of photoresist these techniques use thermal- or UV-curable plastics. Since the wavelength of light is not a limiting factor, soft lithography can transfer features of nearly any size. In addition, the photolithographic limitation of flat surfaces does not apply to soft lithography, allowing pattern transfer through rollers or deformable molds.

The gold standard of soft lithography is nanoimprint lithography (NIL). This technique involves the use of a hard mold to transfer a pattern by mechanically deforming a resist material such as polymethyl methacrylate (PMMA). The resist is then set either through cooling or a reaction to UV light. *Guo* (2007) and *Schift* (2008) provide in-depth reviews of NIL, and *Bao et al.* (2002) demonstrates the creation of 3D structures via multiple imprints. A variant of NIL that uses quartz molds and UV curable resists to allow precise visual pattern registration is step-and-flash imprint lithography (SFIL) (*Resnick et al.*, 2005).

A wide variety of alternative techniques for lithography and direct-building of structures exist, many of them maskless (*Roy*, 2007). Some current examples are scanning tunneling microscope lithography (*Iwasaki et al.*, 2003), direct laser machining (*Webb et al.*, 2008; *Gattass and Mazur*, 2008), microinjection molding (*Giboz et al.*, 2007), and atomic construction with lasers (*Meschede and Metcalf*, 2003) or plasmas (*Ostrikov*, 2005; *Ostrikov and Murphy*, 2007).

3.2 Thin Films

Thin films of dielectrics and metals are critical to many fabrication steps. The uses of thin films include formation of electric circuit components, masking future process steps such as chemical etches (§3.4) or dopanting (§3.3), as an interface between materials (e.g. chromium or titanium as adhesion promoters for other metal films), and as sacrificial layers for MEMS components.

Thin film growth is a very controllable process, but the microphysics is still under investigation (*Venables et al.*, 1984; *Kaiser*, 2002). *Smith* (1995) and *Ohring* (2002) provide in-depth examinations of film deposition ranging from gas kinetics to specific technologies, and *Randhawa* (1991) pays more attention to technologies and applications.

Growth of silicon oxide is perhaps the most well-known and most used thin film growth mechanism in the microelectronics field (*Deal and Grove*, 1965; *Fargeix and Ghibaudo*, 1983; *Watanabe et al.*, 2006). Under high temperature (typically 900-1200° C), silicon can grow an oxide layer that serves as a high quality insulator. Silicon oxide (SiO_2) can be grown under exposure to oxygen ("dry oxide") or water vapor ("wet oxide"). Dry oxide is higher quality than wet oxide, but grows much slower. Growth of very thin oxides for transistor gates is one of the main reasons that silicon is a useful material for the IC industry, which serves to demonstrate how important thin films can be.

Since the oxide layer itself serves as a diffusion barrier for the gas, the growth process is self-limiting. Oxide thickness is proportional to the square root of the oxidation time. One thing worth noting is that since silicon oxide is formed by the addition of oxygen atoms to the silicon matrix, the crystalline silicon is "consumed" during the oxidation process. For every 1 μm of SiO_2 grown, about 0.46 μm of silicon is consumed, resulting in layers that seem to grow both inward and outward from the surface. The thickness of both silicon oxide and silicon nitride can be roughly

determined by eye since they have very deterministic constructive and destructive interference of light (*Huen*, 1979; *Henrie et al.*, 2004). The color depends primarily on thickness and viewing angle, with a secondary dependence on incident light intensity and color. Figure 3.2 demonstrates how a change of even a few nanometers thickness can change the color of the layer.

Film Thickness (Å)	Color of Film (those shown are only indicative
500	tan
700	brown
1000	dark violet to red violet
1200	royal blue
1500	light blue to metallic blue
1700	metallic to very light yellow-green
2000	light gold or yellow - slightly metallic
2200	gold with slight yellow-orange
2500	orange to melon
2700	red-violet
3000	blue to violet-blue
3100	blue
3200	blue to blue-green
3400	light green
3500	green to yellow-green
3600	yellow-green
3700	green-yellow
3900	yellow
4100	light orange
4200	carnation pink
4400	violet-red
4600	red-violet
4700	violet
4800	blue-violet
4900	blue
5000	blue-green
5200	green
5400	yellow-green
5600	green-yellow
5700	yellow to "yellowish" (at times appears light gray or metallic)
5800	light orange or yellow to pink
6000	carnation pink
6300	violet-red
6800	"bluish" (appears between violet-red and blue-green - overall looks grayish
7200	blue-green to green
7700	"yellowish"
8000	orange

Figure 3.2: Color chart for thickness of SiO_2 at vertical viewing under fluorescent light. The color follows a cyclic pattern with a period of approximately 1800-1900 Ångstroms. Image courtesy of ECE444 at the University of Illinois Electrical and Computer Engineering Department, reprinted with permission.

A method for depositing silicon oxide and a wide variety of other materials on

nearly any surface is chemical vapor deposition (CVD). The in-depth review provided by *Choy* (2003) says that CVD involves "the chemical reactions of gaseous reactants on or near the vicinity of a heated substrate surface" to "provide highly pure materials with structural control at atomic or nanometer scale level." A critical part of that description is "heated substrate"; most CVD techniques (and there are many) require heating the substrate to several hundred degrees Celcius. These temperatures can be significantly lower than those in thermal oxide growth, but are still a factor that needs to be taken into account when depositing on partially processed substrates, especially those with metals or polymers on them. The CVD techniques used in this body of work include low pressure chemical vapor deposition (LPCVD) and plasma enhanced chemical vapor deposition (PECVD). LPCVD provides good film quality, but at relatively high temperatures, while PECVD sacrifices quality in favor of lower-temperature processing (*Stoffel et al.*, 1996).

The other major method of thin-film deposition is physical vapor deposition (PVD). This includes such technologies as sputtering tools (*Rossnagel*, 1999; *Helmersson et al.*, 2006) and evaporators. *Rossnagel* (2003) and *Moshfegh* (2004) provide comprehensive reviews of current technologies while *Gilmer et al.* (2000) focus on Monte Carlo modeling of the deposition. *Rossnagel* (2003) says that "PVD processes generically involve individual atoms or perhaps small clusters of atoms which are not normally found in the gas phase. PVD differs from chemical vapor deposition in that the primary source of the depositing species is a solid or liquid, as opposed to a gas, and has a vapor pressure much below the working pressure of the deposition system."

In brief, evaporator tools heat a sample of the material to be deposited until atoms evaporate from the surface and deposit upon the target, and sputter tools use heavy plasma ions (often argon) to physically batter the atoms loose. Evaporation is done in vacuum—typically under 2 x 10^{-6} Torr[b]—because it reduces the boiling point of most

[b]This non-SI unit of pressure equals approximately 133.3 Pascals or 1/760 of an atmosphere, and is commonly used in vacuum engineering.

materials, increases mean free path length of the evaporated atoms, and minimizes the chance of chemical reactions happening between the source and target surfaces. Sputtering is done in low-pressure gas environment.

The primary difference between the two methods is their directionality. Evaporation is a very directional process, which means shadowing effects caused by the topology of the target surface are important. Sputtering is more conformal, able to coat even around corners, since the ions follow a roughly cosine distribution in direction at the substrate. Layer growth rates tend to be significantly higher with sputtering than with evaporation.

One of the key properties of PVD is that the temperature of the source is raised significantly, but generally the substrate is only heated by the incident atoms. This results in far lower temperatures even than CVD processes, temperatures low enough that deposition can even occur on polymers or waxes with relatively low melting points.

Additional methods of depositing films include electroplating (*Gobet et al.*, 1993; *Landolt*, 2002, and references therein) and atomic layer deposition (ALD) (*Leskelä and Ritala*, 2002). Electroplating is an electrochemical process for depositing metal onto a substrate. An electrical current is passed through an electrolyte solution to coat a conductive object (the circuit's cathode) with a thin layer of a material (the circuit's anode) by reducing cations of the material from the electrolyte. Deposition rate of electroplating is controlled by the current density. The ALD process uses saturative adsorption of precursor chemicals to deposit single atomic layers of a material for each pulse, thus giving unmatched control over layer thickness. In addition, it has the advantage of nearly 100% uniformity over very high aspect ratios (over 100:1). The primary interest in those technologies in the context of this work is the conformal deposition of metals (i.e. gold, platinum) in high aspect ratio trenches, an application for which ALD is ideally suited (*Aaltonen et al.*, 2003, 2004; *Leskelä et al.*, 2007).

Virtually all deposited thin films exhibit some amount of planar stress. This stress is divided into intrinsic and extrinsic components. According to *D'Heurle and Harper* (1989), extrinsic stress is caused by thermal expansion mismatch between the film and the substrate, and intrinsic stress is all other stresses, usually caused by film deposition conditions, reactions with the substrate, ion implantation, or other mechanisms. Film stress can be tensile or compressive, and can lead to films peeling loose from substrates, buckling, or otherwise interfering with device functionality.

3.3 Doping

Doping is the addition of a controllable level of impurity atoms into a layer of material to modify its electrical, thermal, and chemical properties. The most common use of doping in the IC industry is the creation of p-n junctions for transistors. This is done through addition of relatively small amounts of substitutional atoms into the crystalline matrix to change the amount of charge carriers.

Charge carriers can be either negatively or positively charged. In silicon and germanium, both group IV semiconductors on the periodic table, elements from group V such as phosphorus, arsenic, and antimony "donate" extra weakly-bound electrons to the crystal matrix to form a predominantly negatively-charged (n-type) substrate. Thus, those elements are called "donors". Group III elements such as boron and aluminum are "acceptors" because they capture weakly-bound outer electrons from nearby silicon atoms, leaving a vacancy called a "hole" and forming a predominantly positively-charged (p-type) substrate. *Chen and Milnes* (1980) explain how doping a semiconductor changes its Fermi level. In brief, n-type substrates have a Fermi level close to the conduction band and use electrons as their primary charge carriers, while p-type substrates have Fermi levels closer to the valence band and use holes as primary charge carriers.

For MEMS, etch stops for bulk micromachining can be created through use of

high concentrations of dopants (as seen in *Steinsland et al.* (1996) and *Huang and Najafi* (2001)) or lower concentrations in a reverse-biased p-n junction configuration (*Kloeck et al.*, 1989). Doping can also change the thermal conduction of the substrate (*Asheghi et al.*, 2002), though in most cases this is not a critical factor.

The two primary methods of doping are thermal diffusion and ion implantation. Both are fairly well-established processes with models and equipment evolving from the 1960s or earlier. *Chason et al.* (1997) and *Dearnaley* (1974) cover the basics of ion implantation and *Current* (1996) looks at beam impurities and how they affect the system. The PhD theses by *Christensen* (2004) and *Silvestri* (2004) together with the articles by *Willoughby* (1978) and *Gösele* (1986) provide a comprehensive look at diffusion. The microphysics of dopant diffusion into a substrate are still not fully understood, and even the most recent models have their flaws.

Thermal diffusion is generally considered the lower-technology option, and operates by a two-stage process of pre-deposition followed by drive-in, as illustrated in Figure 3.3. During the pre-deposition step, the substrate is placed in a high temperature furnace for a short time—around 15 minutes—with a source of the diffusion material. The dopant atoms are transported from the source onto the substrate surface and diffuse into the near-surface region. The drive-in step is an anneal at 950-1280° C that lasts up to a few hours, during which the dopant atoms diffuse deeper into the substrate and take up substitutional positions in the crystal lattice. The diffusion depth and concentration is determined by the temperature and time of the drive-in.

The math governing this diffusive process has evolved from the well-known Fick's Laws (*Fick*, 1855) to more elaborate models incorporating interstitial and vacancy diffusion (*Nichols et al.*, 1989) in two dimensions (*Singh and Das*, 1999) and transient enhanced diffusion (TED) (*Stolk et al.*, 1997; *Theiss et al.*, 2000; *Shao et al.*, 2003). This is especially important given that diffusive drive-in can occur unintentionally

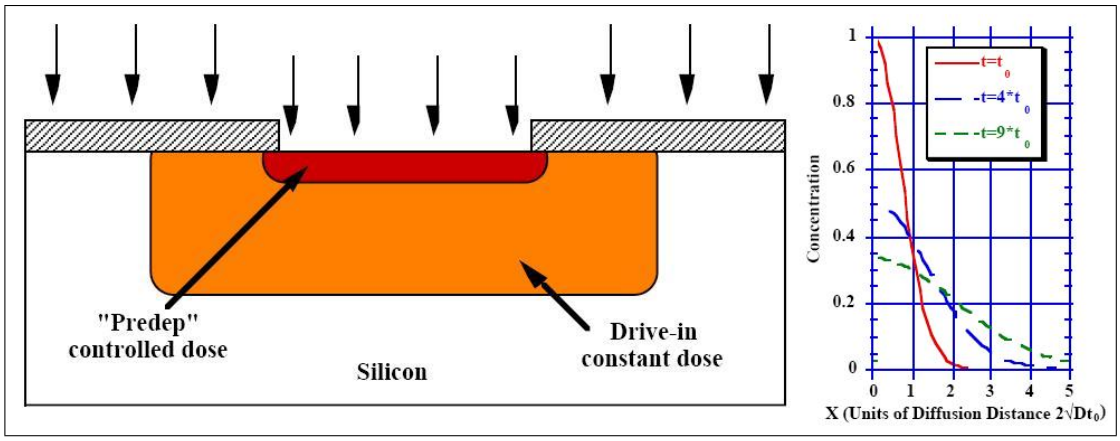

Figure 3.3: Diffusion through pre-deposition and drive-in. The initial dose of dopant slowly diffuses through the solid; in the graph, D is the diffusivity of the dopant.

when performing high-temperature processes such as oxide growth. Heavily-doped layers have internal E-fields that can alter Fick's laws, a fact taken into account only in the more recent models.

One limitation of thermal diffusion doping is the solid solubility limit (approx. 10^{21} cm^{-3} in silicon); this is the thermodynamic limit of the amount of dopant that can be held by the substrate at a given temperature, and thus the maximum amount of dopant the surface can hold before drive-in.

Ion implantation is the introduction of dopant atoms below a wafer's surface via bombardment by an energetic beam (a few keV to MeV) of dopant ions. The ions are slowed down by collisional and stochastic processes in times ranging from femtoseconds (10^{-15}) to picoseconds (10^{-12}). They come to rest at a depth determined by the mass of the ions, the acceleration energy, and the atomic density of the substrate. Since this bombardment can sputter atoms from the surface of a substrate, often a thin protective dielectric layer will be deposited prior to implantation.

Since the ion implant energy is thousands of times the substrate's atomic bond energy, the collisional process also damages the substrate (*Mok et al.*, 2008). A thermal anneal is performed after implantation to repair the damage and incorporate

the implanted ions in the crystal lattice (*Gibbons*, 1972). This anneal will also diffuse the dopant dose as in thermal diffusion. In fact, ion implantation can be considered as a pre-deposition step for diffusion, and thus diffusion is the general term used for doping. Ion implantation, unlike thermal diffusion, can result in peak dopant concentration hundreds of nanometers below the surface. A more recent development is plasma-based ion implantation and deposition (*Pelletier and Anders*, 2005), which uses plasma rather than an ion beam to do implantation and thus is not limited by line-of-sight.

Local substrate doping requires a mask layer to prevent dopants from affecting undesired areas. For silicon processing this is usually accomplished via an oxide layer patterned by photolithography (§3.1). Since the dopant atoms will embed in the surface of the masking layer, a short etch of the masking layer is performed prior to long drive-in or anneal steps to avoid diffusion through the mask into the substrate. During a masked diffusion, there will be lateral diffusion under the mask as well as vertical diffusion (*Kennedy and O'Brien*, 1965); the lateral diffusion rate is 75-85% of the vertical rate for thermal diffusion, and approximately 30-40% for ion implantation.

3.4 Etching

Etching is the selective removal of unwanted portions of a thin film or substrate. This can be done through chemical baths (wet etching, §3.4.1) or through plasma or other non-liquid means (dry etching, §3.4.2). In most cases the material is masked by some means of lithography (§3.1) such that only the undesired portions of the material are removed. Sometimes the masking material is a polymer resist, and sometimes a more durable material like an oxide, nitride, or metallic mask that itself was patterned using resist.

Etching can be broadly grouped into two categories: surface micromachining (*Linder et al.*, 1992; *Bustillo et al.*, 1998) and bulk micromachining (*Kovacs et al.*, 1998).

In surface micromachining, successive layers of thin film materials are patterned and etched to form structures and circuits, sometimes using sacrificial layers to define gaps between the structural layers. In bulk micromachining, the substrate itself (i.e. the "bulk"), usually single crystal silicon (SCS), is etched to form three-dimensional devices. *French and Sarro* (1998) compare and contrast the techniques and provide sample applications of both.

The primary figures of merit for any etching technique are anisotropy and selectivity. An anisotropic etch has a preferred direction, usually vertical, and does not undercut a mask or otherwise remove material outside of the preferred direction. A selective etch is one that removes only the material it is intended to remove, but not the masking material or any underlying layers. The etch rate of the target layer thus must be much higher than that of the other layers.

Comprehensive characterization of etch rates for common materials and processes is provided by *Williams and Muller* (1996) and *Williams et al.* (2003). High selectivity is a primary criterion for masking materials, and also an essential component for stopping an etch at a desired depth. *Collins* (1997) provides a detailed look at a variety of etch-stops for both wet and dry etching as well as an overview of masking and etching techniques.

3.4.1 Wet Etching

Wet etching can be performed with either acids or bases, often with additives to accelerate the process or control selectivity. It is a fairly cheap etching method, because all that is needed is the chemicals, adequate storage and disposal facilities, and a wet bench.

Isotropic etching, typically done with acids, is ideal for some circumstances such as removal of a sacrificial layer, wafer thinning, or surface polishing. Isotropic etching of silicon is commonly done by a mixture of hydrofluoric acid, nitric acid, and acetic

acid (HNA) (*Robbins and Schwartz*, 1959, 1960; *Schwartz and Robbins*, 1961, 1976; *Bogenschütz et al.*, 1967). The most common isotropic etchant of silicon dioxide is hydrofluoric acid (HF) (*Spierings*, 1993). Often a buffered hydrofluoric acid (BHF) solution will be used instead of straight HF in situations where a masking photoresist is present, or where surface roughness or etch rate need stronger control. The solution is a 5:1 to 7:1 mixture of HF and NH_4F with the addition of NH_4OH or HCl for pH control (*Higashi et al.*, 1990).

Even though in ideal circumstances an isotropic etchant can remove material in all directions with equal speed, in practice this is often not the case. Differences in etch profiles can be seen between samples that were agitated in solution and those that were not, as Figure 3.4 shows.

When machining structures with small feature sizes, isotropic etching is often undesirable, so anisotropic wet etches with strongly basic solutions have been devised. They use the crystal planes of semiconductors as etch stops. In the case of SCS, the crystal structure can be represented as two interpenetrating face-centered cubic lattices offset by 1/4 period in each direction (*Madou*, 2002). This crystalline structure results in differences in the surface density of atoms along each crystal plane (*Bean*, 1978).

In crystallography, coordinates in square brackets such as [100] denote a real-space direction. Angle brackets such as <100>denote a family of directions which are equivalent due to symmetry operations. When referring to a cubic system, <100>could mean [100], [010], [001] or the negative of any of those directions. Parentheses such as (100) denote a plane; in a cubic system the normal to the (hkl) plane is the direction [hkl]. And curly brackets such as {100} denote a family of plane normals which are equivalent due to symmetry operations, much the way angle brackets denote a family of directions.

In silicon, the {111} planes have the highest density of atoms, with three out

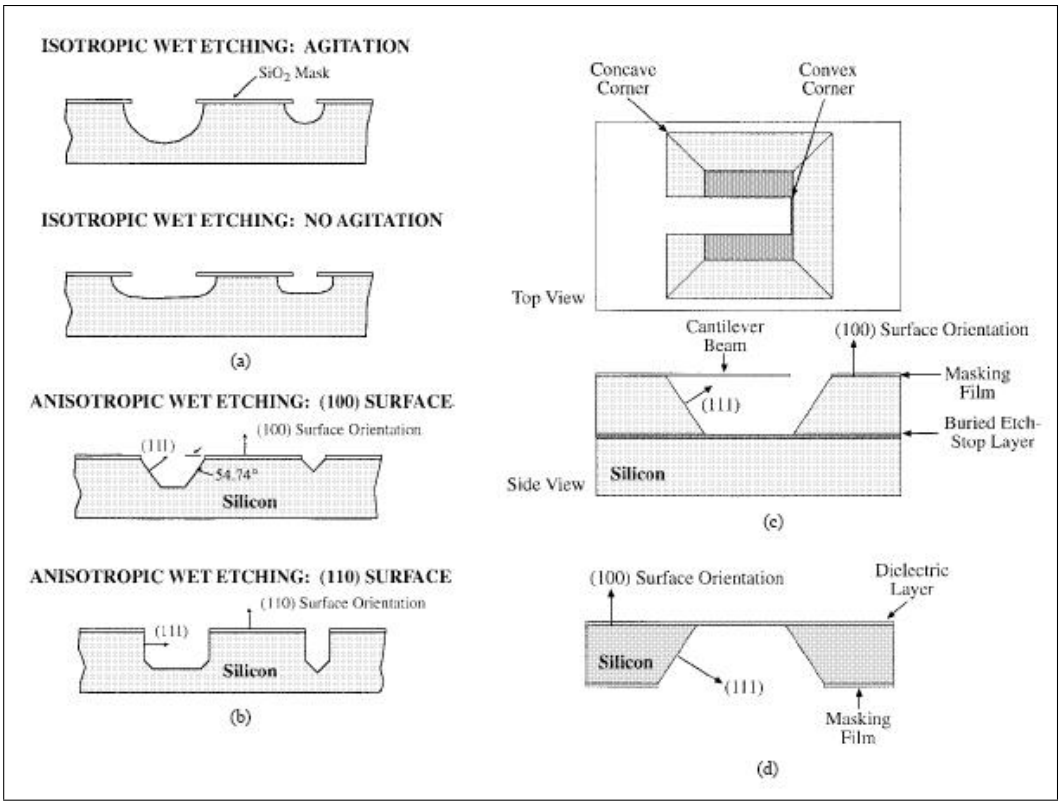

Figure 3.4: Illustration of bulk-micromachined structures.(a) Rounded, isotropically etched pits in a silicon substrate. (b) Pyramidal pits etched into (100) and (110) silicon using anisotropic wet etchants, bounded by (111) crystal planes. (c) A pyramidal pit etched down to a buried etch-stop layer in (100) silicon, with an undercut cantilever beam. (d) An undercut dielectric membrane released by back-side bulk etching with anisotropic wet etchants. Image adapted from *Kovacs et al.* (1998), copyright of IEEE.

of the four covalent bonds below the surface. This property makes them very resistant to a variety of strong bases, notably alkaline hydroxides such as potassium hydroxide (KOH), alkaline organics such as ethelene-diamine pyrocatechol (EDP), and ammonium hydroxides such as tetramethylammonium hydroxide (TMAH). *Seidel et al.* (1990a) detail silicon etch rates and activation energies for <100>, <110>, and <111> oriented silicon for KOH and EDP. Temperature, concentration, solution constituents, and agitation all directly affect etch rate, selectivity, and feature smoothness. Depending on process parameters, it is possible to get selectivities of up

to 600:1 with wet etching.

Stopping a wet etch at a desired location is critical to many applications. This can be done by as simple a means as stopping on a layer of material that will not etch, or etches very slowly. An example of this is use of the buried oxide (BOX) layer of silicon-on-insulator (SOI) wafers to stop anisotropic etchants, a *dielectric etch stop*. The bulk dopant level (§3.3) is very important to both isotropic and anisotropic etching. Heavy boron doping ($> 2 \times 10^{19}$ cm^{-3}) can drastically slow down alkali etches (*Seidel et al.*, 1990b), EDP far moreso than KOH. Conversely, low dopant levels ($< 10^{17}$ cm^{-3}) will slow the isotropic HNA etch rate by a factor of up to 150. Thus doping is often used as a *concentration etch stop* (*Steinsland et al.*, 1996; *Huang and Najafi*, 2001) in cases where electronics are not required. The concentration etch stop works as a strong p-n junction, an effect that can be mimicked by an *electrochemical etch stop* (*Kloeck et al.*, 1989) by biasing one side of a lightly-doped wafer relative to the etching solution.

Which etchant to use depends on the process, etchant characteristics, and available masking materials and etch-stopping techniques. For example, since complementary metal oxide semiconductor (CMOS) is very sensitive to alkali ions, KOH and EDP are not compatible, but TMAH, lacking alkali ions, is. A KOH solution etches silicon with far better selectivity and smoothness than EDP or TMAH, but it etches oxide quickly and causes lots of H_2 bubbles that may damage thin films. These sorts of trade-offs are critical to successful process development.

The most common substrate is still the (100) silicon wafer. The {111} planes meet the <100> surfaces at a 54.74° angle, resulting in significantly slanted sidewall features and thus relatively large real-estate requirements for bulk micromachining. On (110) wafers the {111} planes are vertical which, with correct mask alignment, can result in atomically smooth vertical features (*Kaminsky*, 1985; *Hölke and Henderson*, 1999; *Ahn et al.*, 2007).

For MEMS structures, it is often necessary to undercut features such as bridges or struts, which can be done through careful application of anisotropic etchants. The primary difficulty is in maintaining corner integrity (*Pal et al.*, 2007). Some interesting devices can be fabricated under these conditions, as demonstrated by *Bassous* (1978), *Kaminsky* (1985), and *Bäcklund and Rosengren* (1992). Figure 3.4 shows the results of a variety of wet etches, both isotropic and anisotropic.

3.4.2 Dry Etching

Dry etching covers a wide variety of techniques, and is generally far more expensive than wet etching due to the cost of tools. Most dry etches are by their nature highly anisotropic, though there are exceptions. Their accurate control over feature shape, independent of the crystal orientation used by anisotropic wet etches, is offset by the loss of selectivity compared to wet chemistry.

Most dry etches are performed by plasmas, so many that the terms "dry etch" and "plasma etch" are often interchangeable. However, dry etching also includes other methods (*Rajurkar et al.*, 2006) such as vapor-phase etching (*Chang et al.*, 1995; *Chu et al.*, 1997; *Chan et al.*, 1999), direct-writing via laser ablation (*Holmes*, 2002; *Rizvi*, 2003; *Joglekar et al.*, 2004; *Wang et al.*, 2007) or focused ion beam (FIB) milling (*Vasile et al.*, 1994; *Matsui and Ochiai*, 1996; *Tseng*, 2004), electro-discharge machining (EDM) (*Ho and Newman*, 2003; *Morgan et al.*, 2006; *Mohd Abbas et al.*, 2007), and ultrasonic drilling (*Taniguchi*, 1983; *Sun et al.*, 1996; *Thoe et al.*, 1998).

Even the sub-field of plasma etching includes a continuum of techniques (*Oehrlein and Rembetski*, 1992; *Cardinaud et al.*, 2000), as seen in Figure 3.5, including physical sputtering, chemical etching, and a combination of the two called reactive ion etching (RIE), also called "reactive sputter etching" or "chemical sputtering". *Winters and Coburn* (1992) model the plasma-surface interactions of these techniques, using silicon and fluorine as representative species.

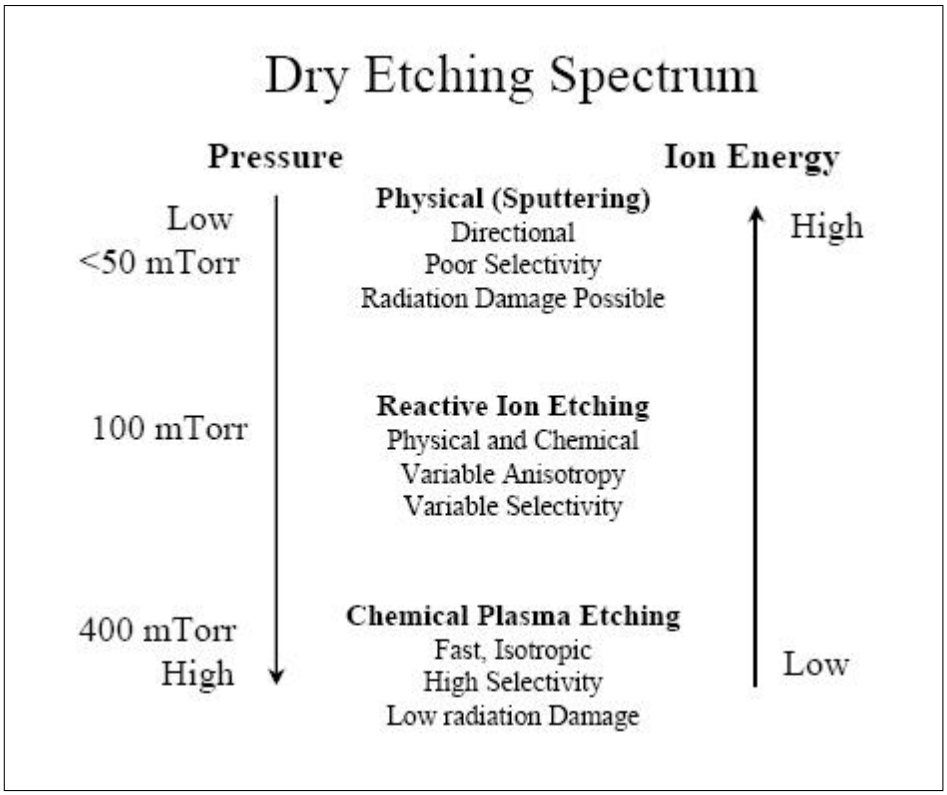

Figure 3.5: Continuum of dry etching techniques. Based on *Madou* (2002), pg 98.

The simplest technique is sputter etching, also called plasma ion milling, a purely physical mechanism relying on energetic ion bombardment of a substrate to remove material. This results in strongly anisotropic etching, but with fairly low selectivity since the sputter yield difference between the masking material and material being etched is the sole determinant of selectivity. According to *Carter* (2001), the sputter yield can depend on "incident ion mass, species, energy, azimuthal and polar angles with respect to the surface normal and a specified surface crystallographic direction, flux density and fluence and substrate mass, species, crystallographic orientation and temperature." Since the ejected species are non-volatile, redeposition can occur. Sputter etching is done at relatively low pressure but with highly energetic ions, usually noble gas ions such as Ar^+.

The opposite end of the spectrum is chemical etching, a plasma process carried

out at higher pressure and relying on reactive gases rather than momentum transfer to enact surface removal. It is 10-1000 times faster than physical sputtering and highly selective with regard to mask and substrate layers. Since it is a chemical process, it results in isotropic profiles, making it unsuitable for structures with lateral dimensions under one micron. The process comprises the following steps: 1) generation of reactive species in a plasma; 2) diffusion of these species to the surface of the material being etched; 3) adsorption of these species on the surface; 4) occurrence of chemical reactions between the species and the material being etched, forming volatile byproducts; 5) desorption of the byproducts from the surface; and 6) diffusion of the desorbed byproducts into the bulk of the gas.

While chemical etching lacks the level of anisotropy required for etching small features and physical sputtering lacks selectivity, a balance between anisotropy and selectivity can be reached by using reactive gases along with physical bombardment. This is called RIE (*Jansen et al.*, 1996), and follows the same process steps as chemical etching. The only difference is that desorption of the byproducts is enhanced by the physical bombardment of the plasma ions, resulting in significantly increased anisotropy. Figure 3.6 demonstrates the sequence of events in a typical RIE tool.

To create deep, narrow features (high aspect ratio), a deep-reactive ion etch (DRIE) is used. The primary requirement for DRIE is directionality, which means that the sidewalls of features cannot etch. This requirement is met in one of two ways: cooling the substrate to inhibit chemical reactions, thus enhancing the effect of the physical component of the etch (*de Boer et al.*, 2002); and using gas-chopping methods to successively etch and passivate (*Lärmer and Schilp*, 1996; *Volland et al.*, 1999). This will be covered in greater detail in Chapter V.

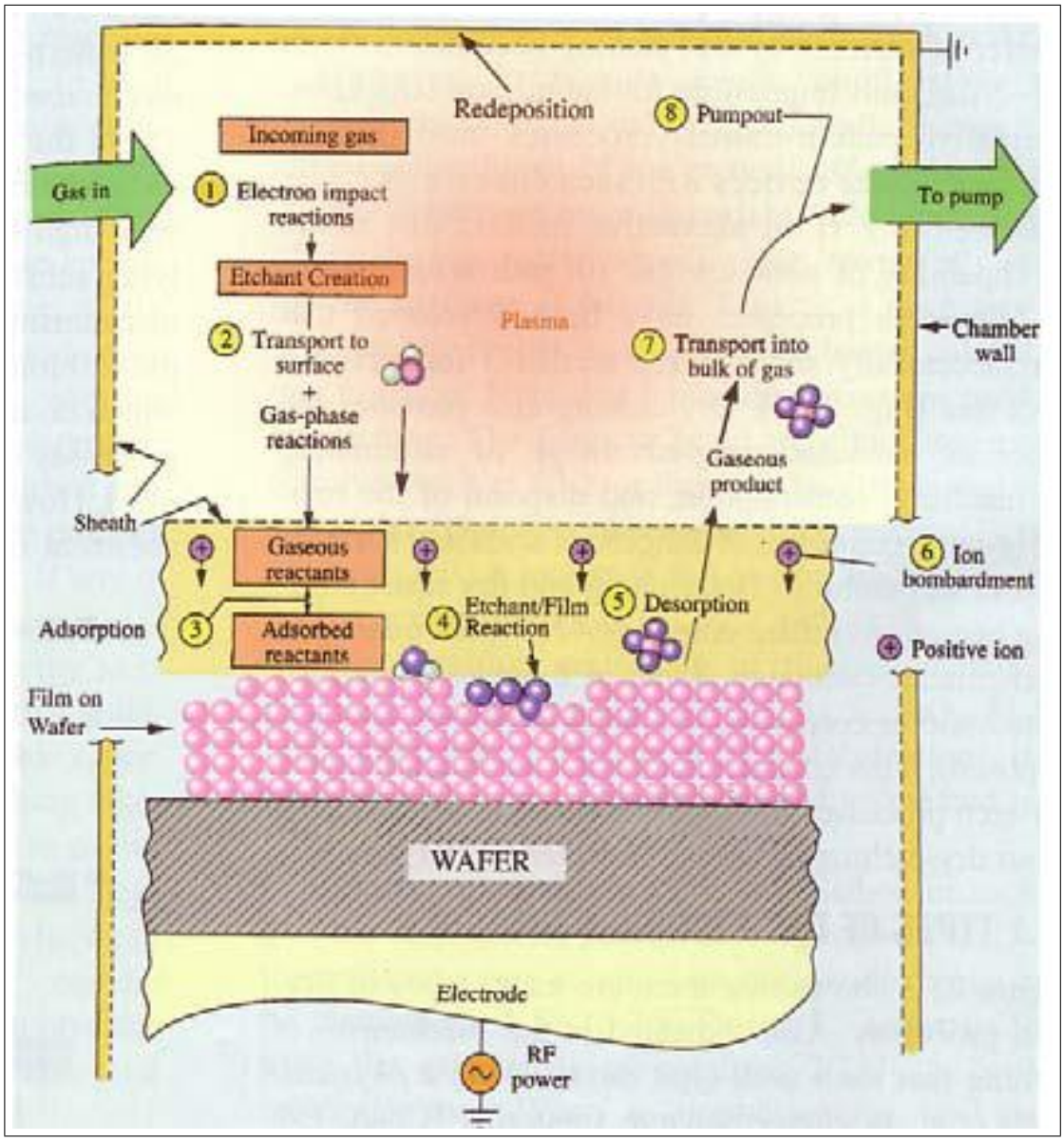

Figure 3.6: Reactions inside an RIE reactor

CHAPTER IV

Modeling and Simulations

The transmission grating design of this dissertation is based on the fact that light can not easily propagate in a waveguide narrower than half of its wavelength. It is either reflected or absorbed in evanescent fashion. Its transmitted intensity falls off as $e^{-\alpha z}$ where z is the length of the transit and α is dependent on the shape of the waveguide. Narrower features result in a higher α value, and thus more rapid attenuation of the wave intensity. Thus thin, deep waveguides serve as very efficient polarizers or filters of incoming light.

Pollock et al. (2000) indicate that this type of transmission grating was the sole component dedicated to ultraviolet (UV) rejection on the Medium Energy Neutral Atom (MENA) instrument, and met mission goals. The gold gratings they used had a period of 200 nm, geometrical transparency g = d/p = 0.31, and grating thickness 494 nm, and had transmission 121.6 nm of 3×10^{-5}. At 30.4 nm (He-II) and 58.4 nm (He I) the transmission was 5×10^{-2} and 1×10^{-2}, respectively.

This chapter covers the modeling and simulation of a variety of grating materials and geometries prior to the fabrication detailed in Chapter V. Section 4.1 discusses material properties and the trade-offs of various materials, and § 4.2 details the modeling of gratings including the effects of geometry and single or layered grating materials.

4.1 Material Properties

Before simulating a grating, it is illustrative to examine some of the properties of materials. Since the primary concern of the grating is filtration of photons, electromagnetic properties such as dielectric constant, complex refractive index, and skin depth are important. For a strong grating that will let particles through only in the slotted areas, the values of import are Young's modulus, yield strength, and density. When energy is absorbed, thermal considerations such as specific heat and thermal conductivity are important.

4.1.1 Electromagnetic Properties

The primary electromagnetic properties of a material are the dielectric constant, ϵ, and the magnetic permeability, μ. The dielectric constant, or permittivity, of a material represents the material's ability to polarize in response to an electric field, thereby reducing the total electric field inside the material. Magnetic permeability is the degree of magnetization of a material that responds linearly to an applied magnetic field.

The electric constant, ϵ_0, and magnetic constant, μ_0, are respectively the permittivity and permeability of free space, or vacuum. They are defined constants that relate mechanical and electromagnetic units. In the International System of Units (SI), $\epsilon_0 = 8.854 \times 10^{-12}$ Farads/meter and $\mu_0 = 4\pi \times 10^{-7}$ Henries/meter. These constants are related to the material properties such that $\epsilon = \epsilon_r \epsilon_0$ and $\mu = \mu_r \mu_0$ where the relative values ϵ_r and μ_r are material-specific, generally frequency-dependent, and often complex. ϵ_0 and mu_0 relate directly to the speed of light in vacuum, c, as $c^2 = (\epsilon_0 \mu_0)^{-1}$.

For optical purposes, a more useful material property is refractive index, defined by *Hecht* (1990) as the ratio of c to the speed of an electromagnetic wave in a material. The speed in this case is the phase velocity, defined as

$$\nu = \frac{\omega}{k_\omega} = \frac{1}{\sqrt{\epsilon\mu}} \tag{4.1}$$

where k_ω is the frequency-dependent complex wavenumber

$$k_\omega = \omega\sqrt{\epsilon\mu} = \beta + i\frac{\alpha}{2}. \tag{4.2}$$

In a medium, since ϵ_r and μ_r are frequency specific the speed of each frequency may vary. Mathematically, the complex refractive index is written as

$$n_c = n + ik = \frac{c}{\nu} = \sqrt{\frac{\epsilon\mu}{\epsilon_0\mu_0}} = \sqrt{\epsilon_r\mu_r} \tag{4.3}$$

where n and k (not to be confused with k_ω, the wavenumber) are real values. Determination of those values is a non-trivial process (*Alenkowicz and Levitas*, 1998). Appendix A contains plots of the complex indices and broadband optical penetration for a variety of materials.

The refractive index is related to the dielectric constant in one-to-one fashion. With either pair the other can be calculated. Calculating the index of refraction from the dielectric constant can be accomplished in the following manner (*Gruntman*, 1995):

$$n^2 = \frac{\epsilon_1}{2}\left\{\sqrt{1+\left(\frac{\epsilon_2}{\epsilon_1}\right)^2}+1\right\} \; and \; k^2 = \frac{\epsilon_1}{2}\left\{\sqrt{1+\left(\frac{\epsilon_2}{\epsilon_1}\right)^2}-1\right\}. \tag{4.4}$$

And given the index of refraction, the dielectric constant is:

$$\epsilon = n_c^2 = \epsilon_1 + i\epsilon_2 \; where \; \epsilon_1 = n^2 + k^2 \; and \; \epsilon_2 = 2nk. \tag{4.5}$$

Skin depth is an emergent property typically defined as the depth in a material at which the electric and magnetic field strengths will drop to $1/e$ of the initial value.

The formula for skin depth depends on the imaginary portion of the refractive index and the angular frequency *Hecht* (1990), is:

$$\delta = \frac{1}{\alpha};\ \alpha = \frac{2\omega k}{c};\ I(z) = I_0 e^{-\alpha z} \tag{4.6}$$

where ω is the incident wave's angular frequency ($2\pi f$) and α is not the same as that in Equation 4.2.

At the Lyman-alpha (Ly-α) frequency ($\omega = 2\pi f = 15.5 \times 10^{15} s^{-1}$), for gold $k = 0.967$, which gives a skin depth of 10×10^{-9} meters from (4.6). Platinum has $k = 1.18$ at Ly-α, resulting in a skin depth of 8.2×10^{-9} meters. Both of these match up very well with simulated transmissions from §4.2.2 shown in Table 4.2 on page 92. For silicon and SiO_2, $k = 1.32$ and 0.715, which provide skin depths of 7.33×10^{-9} and 13.54×10^{-9} meters respectively, which do not match the simulated 12.6×10^{-9} and 9.8×10^{-9} meters. This is because skin depth is a term usually applied to so-called "good conductors". It doesn't apply as well to semiconductors and dielectrics, since in those media the free carriers required for skin depth to be relevant are created by the photoelectric effect and thus are dependent upon the intensity of incident radiation. Other definitions for skin depth depend on the frequency of incident light and conductivity and magnetic permeability of the material.

The skin depth is important to the grating design since smaller skin depth means less thickness of a given material necessary to make the waveguides "opaque" enough to be functional. This has a direct effect on the geometric transparency of the grating, depending on the material used.

4.1.2 Physical Properties

The purpose of the gratings is to enable measurements of neutrals atoms and ions that pass through unimpeded, not ions that are slowed and scattered by penetration

of the grating material. In order to determine whether or not this device would work in the solar wind, a Monte Carlo simulation (*Reiter*, 2008) of ion penetration through solid silicon was performed using the program Stopping Range of Ions in Matter (SRIM)[a] (*Ziegler*, 2004). Since SRIM only allows for "layer" geometry, a solid sheet of Si was used for the model rather than a grating. Particle penetration depends on layer density and thickness, and particle size and energy.

A sheet thickness of 15,000 Ångstroms was chosen for the Monte Carlo simulation, and 10,000 ions were simulated for a given energy and particle type as shown in Figure 4.1. Since the grating should be $\sim$ 30-50% open area, all of the penetration figures from the model should be doubled to be safe, possibly even tripled. Even doubling the penetration depth values it is clear that anything under 20 keV/nucleon will be stopped within the grating. If we triple the depth numbers, the safety limit is 10-15 keV/nucleon. Since the solar wind is typically in the range of 1-2 keV/nucleon, only high-energy particles will penetrate. Larger ions penetrate deeper than smaller ions with the same energy since they are less affected by scattering, a case made very strongly by the example of hydrogen, which is strongly scattered even at very high energies.

In 1982 Kurt Petersen wrote a paper entitled Silicon as a Mechanical Material (*Petersen*, 1982) that summarized the reasons why silicon was not just useful as a semiconductor, but also as a mechanical substrate. This has since become one of the most cited papers in the field of microelectromechanical systems (MEMS), and by some is given credit for kick-starting the field.

The elementary material properties used in material deformation are stress and strain. Stress is defined as "the force per unit area acting on the surface of a differential volume element of a solid body" and strain is "the differential deformation expressed as change in length per unit length." (*Senturia*, 2001) While detailed materials science

[a] http://www.srim.org

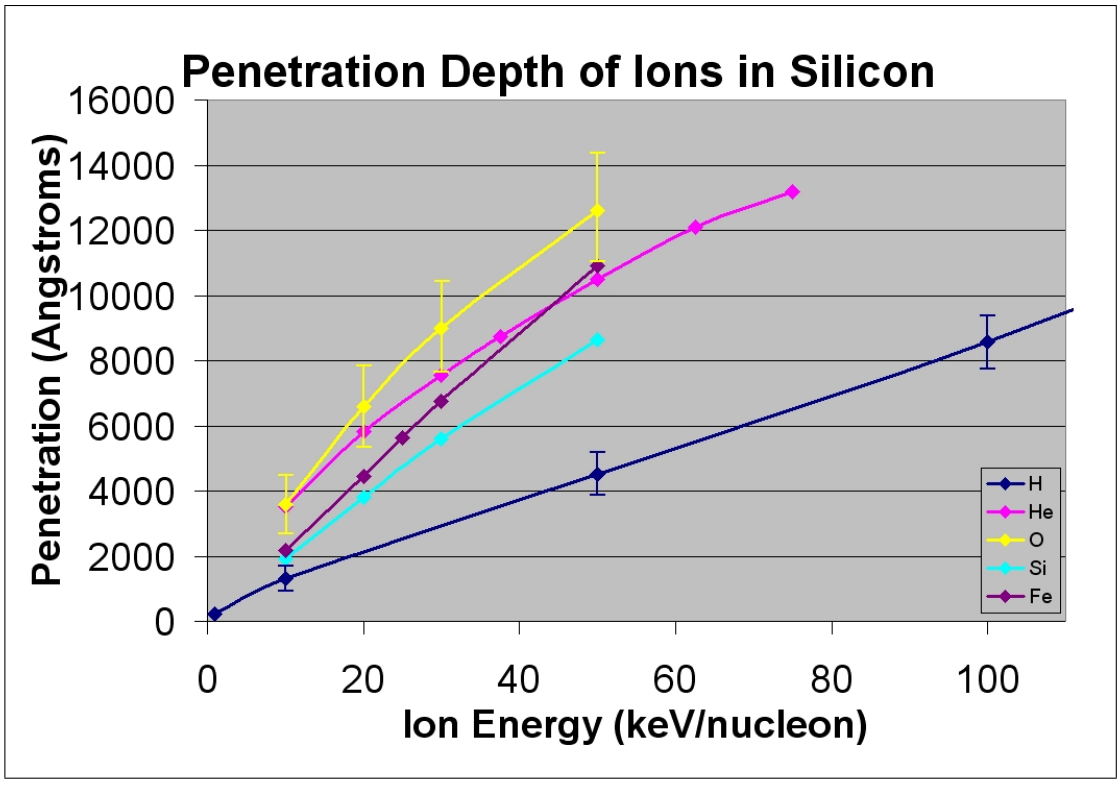

Figure 4.1: Ion penetration depth through solid silicon for incoming particles. Error bars were provided for H and O to demonstrate that heavier particles have wider straggle within the material.

considerations are beyond the scope of this dissertation, the relative strength and stiffness of materials is an important consideration when choosing a freestanding material. The properties of interest are the Youngs modulus and yield strength.

Young's modulus is a measure of the stiffness of a material defined as the ratio of stress (which has units of Pascals) to linear strain (which is dimensionless) for the material. It can be experimentally determined from the slope of a stress-strain curve created during tensile tests conducted on a sample of the material. The Young's modulus allows the behavior of a material under load to be calculated. For instance, it can be used to predict the amount a wire will extend under tension or buckle under compression. In anisotropic materials such as silicon, the Young's modulus will change depending on which direction the force is applied from. As a result, these

anisotropic materials have different mechanical properties when load is applied in different directions. For purposes of this dissertation, Young's modulus is relevant because the grating must be self-supporting (i.e. not bend or buckle under its own weight).

Yield strength is a term with many definitions in materials science. It can mean the minimum stress which produces permanent plastic deformation, the minimum stress that is necessary to ensure the failure of a material, the load at fracture divided by the cross sectional area of the sample, or a wide variety of other definitions.

Since the results of stress/strain curves, and thus the material constants that arise from them, are dependent on both the state of the material (anneal state, crystalline configuration, etc.) and the conditions of the test (temperature, rate of deformation), the utility of these data are in the relative values rather than the absolute numbers.

When energy is absorbed, thermal considerations such as expansion coefficients and thermal conductivity are important. The thermal expansion coefficient is a measure of the expansion undergone by a material as it is heated. As such, it is defined in terms of strain per Kelvin, with values on the order of 10^{-6}. Mismatch in thermal expansion coefficient at the interface between two layers of films is a primary cause of stress. Thermal conductivity is similar to electrical conductivity in that it is defined as the rate of heat transmission through a given thickness of material in a direction normal to a surface of unit area due to a temperature difference. The definition applies under steady state conditions and when the heat transfer is dependent only on the temperature gradient. The thermal conductivity of a material is itself temperature-dependent (*Glazov and Pashinkin*, 2001), but generally the value at room temperature is used. Thermal conductivity is important when any process step that requires heating of a substrate, which includes most non-wet processing.

The material properties listed above are tabulated for a variety of materials in Table 4.1. The data were collected from a number of sources (*Senturia*, 2001; *Ko-*

vacs, 1998; *Stark*, 1999; *Madou*, 2002, and others), and in some cases varied over a significant range, illustrating the difficulty in determining true constants rather than relative values.

Table 4.1: Physical properties of a variety of common materials

	Density kg/m^3	Yield Strength GPa	Young's Modulus GPa	Thermal Conductivity $W/(m*K)$	Thermal Exp. Coeff $10^{-6}/K$
Si	2,331	7	162-190	149-157	2.33
SiO_2	2,500	8.4	69-73	1.4	0.35-1.6
Si_3N_4	3,000	14	130-385	18.5	0.8-2.8
Steel	7,900	4.2	210	97	12
Au	19,400		80	315-318	14.2

Some of the advantages of using single crystal silicon (SCS) as a structural material are made clear by the values in Table 4.1. In particular, silicon is very strong, with a higher yield strength than steel and Young's modulus approaching that of steel. It is also a fair thermal conductor, better than steel but worse than gold. Unfortunately, the thermal expansion coefficient of silicon does not match well with that of either of the most common deposited dielectrics, SiO_2 and Si_3N_4, resulting in thermal stress. The thermal expansion coefficients of deposited materials depend very strongly upon deposition technique and temperature, leading to a wide variance.

4.2 Grating Modeling

4.2.1 Introduction

From *Jackson* (1998), the equation for electromagnetic wave propagation in a dispersive and/or dissipative medium is

$$E = E_0 e^{ik_\omega z} e^{-i\omega t}\,, \tag{4.7}$$

where the second exponential indicates a simple harmonic time-dependence and k_ω is from Eq. 4.2.

Plugging Eq. 4.2 into Eq. 4.7, the traveling-wave equation becomes

$$E = E_0 e^{-\frac{\alpha}{2}z} e^{-i(\omega t - \beta z)}\,, \tag{4.8}$$

where the α-term is an absorption term and the β-term is indicative of wave dispersion, an alteration of the phase velocity of each frequency element. The wave intensity is the square of the wave's magnitude:

$$I = |E|^2 = |E_0 e^{-\frac{\alpha}{2}z} e^{-i(\omega t - \beta z)}|^2 = |E_0|^2 e^{-\alpha z} = I_0 e^{-\alpha z}. \tag{4.9}$$

Intensity falls off as $e^{-\alpha z}$, much faster than the falloff of the field strength. A large, real α-term indicates that the wave will be damped very quickly, which is desirable in a filter. There is no harmonic (imaginary) term in intensity since intensity isn't concerned with the phase of a wave. This means that the β-term, though important to phase velocity, is irrelevant in intensity calculations.

While an isotropic medium allows a complete spectrum of wavenumbers (k_ω) as in Eq. 4.2, waveguides only allow propagation of specific modes. The wavenumbers of electromagnetic waves propagating through a waveguide are restricted to the eigenmodes set by the waveguide's boundary conditions. In general, either the electric component, the magnetic component, or both are transverse, measured in a plane perpendicular to the propagation direction of the beam with zero field component in the direction of propagation. If a mode has no electric field in the direction of propagation, it is called a transverse electric (TE) mode. Similarly, transverse magnetic (TM) modes have no magnetic field in the direction of propagation and transverse electromagnetic (TEM) modes have neither electric nor magnetic field in the direction of propagation.

For gratings, the direction of primary polarization is also important. When referring to polarization states, p- and s-polarization refer to the plane in which the electric field of a light wave is oscillating. For TE waves (s-polarization), the principal E-field is normal to the plane of incidence defined by k and the z-axis as seen in Figure 4.2, meaning it oscillates along the grating direction. For TM waves (p-polarization), the principal E-field is in the plane of incidence, and for normal incidence is perpendicular to the slit direction.

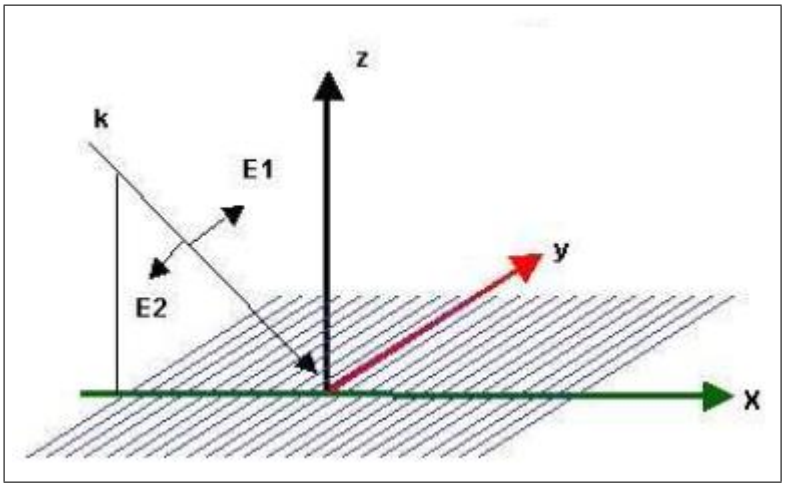

Figure 4.2: Coordinate system for light impinging on polarized gratings. Image from page 36 of the GSOLVER online user manual, available at http://www.gsolver.com/UserManual.pdf

Each allowed mode in a waveguide has a critical frequency based on the geometry and mode numbers. For frequencies higher than the critical frequency the mode will propagate with minimal losses, meaning the α in Eq. 4.2 becomes imaginary or close to zero.

Below the critical frequency (i.e. waves larger than the critical wavelength) the mode is considered to be evanescent, which means it disappears quickly due to absorption into the medium (large, real α), causing Joule heating. An attenuation factor for a waveguide can be considered as the ratio of transmitted intensity to incident

intensity at a given frequency. From Eq. 4.9, this attenuation factor would be

$$A_\omega = \frac{I}{I_0} = e^{-\alpha z}. \tag{4.10}$$

where α, the absorption constant, depends upon the waveguide geometry and material properties.

Gratings are different than singular waveguides in a few important ways. A grating has multiple channels for light to go through, which results in more complicated interference patterns as each point of each slit acts as a point-source for a spherical wavefront. Transmissions of higher diffracted orders can interfere, both constructively and destructively, with lower orders based on the path-length difference traveled by the light from successive grating slits. This means that the periodicity of the grating is important in determining the pattern of transmitted light. Also, the grating walls can, if conductive, allow TEM modes to propagate, which cannot happen in single-slit waveguides.

4.2.2 Maxwell's Equations Simulations

Simulations were performed using a professional Maxwell's equation solver called GSOLVER, from the Grating Solver Development Company[b]. From their product statement, "GSOLVER solves Maxwells equations within an arbitrary periodic grating structure at the interface of two semi-infinite half-spaces: the superstrate, and the substrate. GSOLVER assumes that the grating structure is determined by a piecewise constant construction (of arbitrary spatial resolution) wherein each region is assigned a homogeneous isotropic material–a constant index of refraction. [It] solves the full vector Maxwell's equations for each layer of a grating. The fields are then matched across each boundary giving the fields in the superstrate and substrate. The diffraction efficiency is then determined for each real propagating order." The simulations

[b]http://www.gsolver.com

can result in transmission well under 10^{-10}, which in practical circumstances is meaningless, but the results of the program have been retained to demonstrate trends if not measurable phenomena.

The first basic analysis was attenuation of Ly-α light through single-material gratings as a function of depth, slit width, and period. Figure 4.3 shows that polarization is very important as well, with TM mode blocked far more strongly than TE mode at this wavelength and material. The simulation covers depths ranging from 500 nm to 3000 nm. Gratings with depth less than 500 nm would be too fragile and not attenuate the UV nearly enough to be useful, and those deeper than 3000 nm would be prohibitively difficult to manufacture due to the extreme aspect ratio. Figure 4.3 also shows that TE mode transmission is dominated by slit width, with grating periodicity being a secondary effect. This is true for TM mode for wider slits only.

Figure 4.4 demonstrates the effect of slit width on broadband UV transmission through a 240 nm period silicon grating of 2000 nm depth. TM mode is again strongly blocked between 75-125 nm, but TE mode is not. TE mode falls off even more strongly, but depending on the slit width it can happen between 150-250 nm. The shape of the TE transmission compares favorably with silicon's base transmission, shown on page 153, which in turn follows the inverse shape of the absorptive portion of the index of refraction. The TM transmission more closely follows the real portion of the index.

The material a grating is made of is probably the most important consideration, because the absorption is largely dependent on the material's complex index of refraction, most notably the imaginary (absorptive) component. The figures in Appendix A show broadband transmission through solid 100 nm thick films of a variety of materials. These transmission spectra in many cases show dramatic anti-correlation to the imaginary (k) part of the refractive index, as well as interactions between the real and imaginary components.

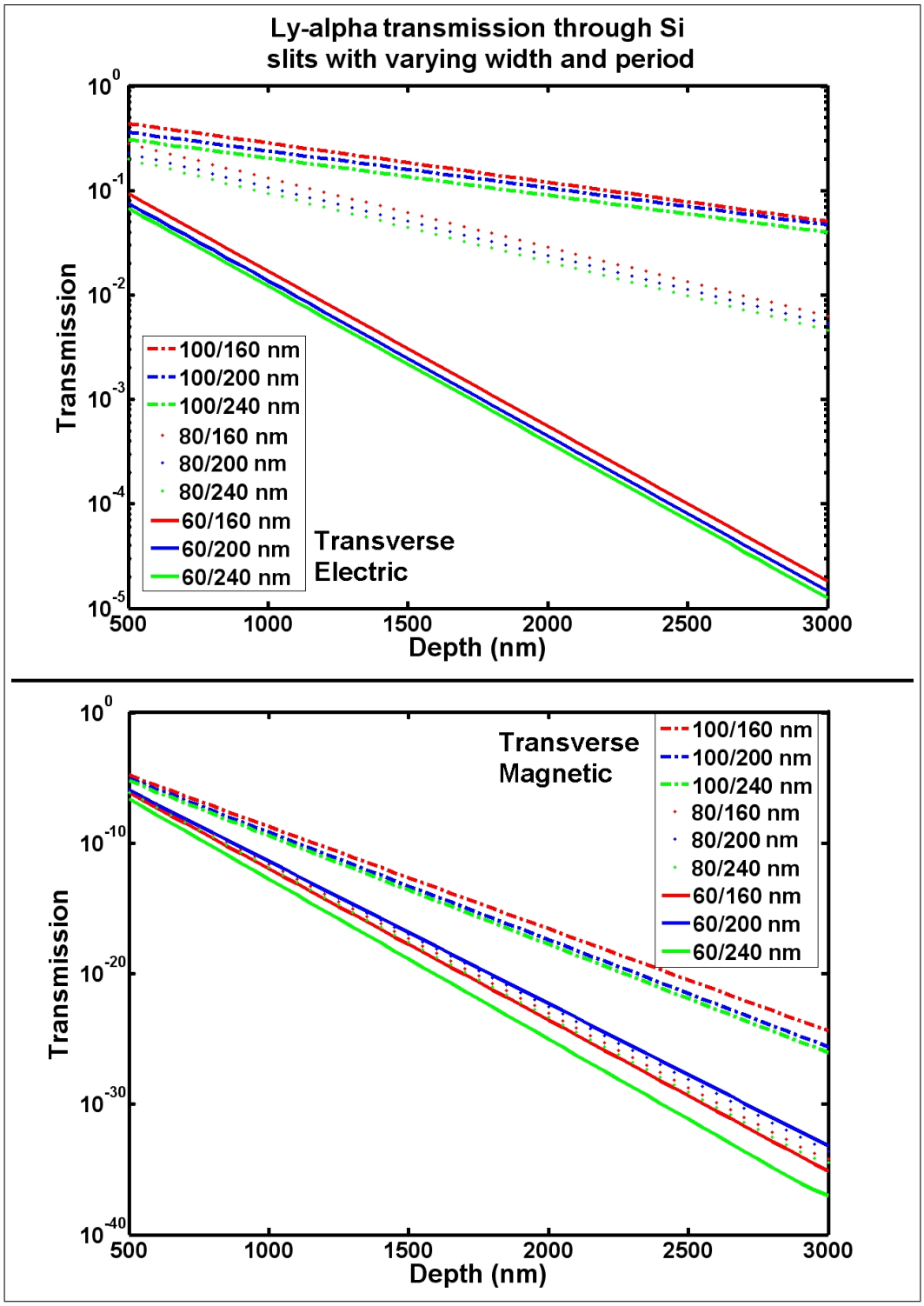

Figure 4.3: Attenuation calculations for Lyman-alpha light normal to gratings with a variety of slit widths and periods (noted by width/period in the legend). The depth scale was chosen based on machining constraints.

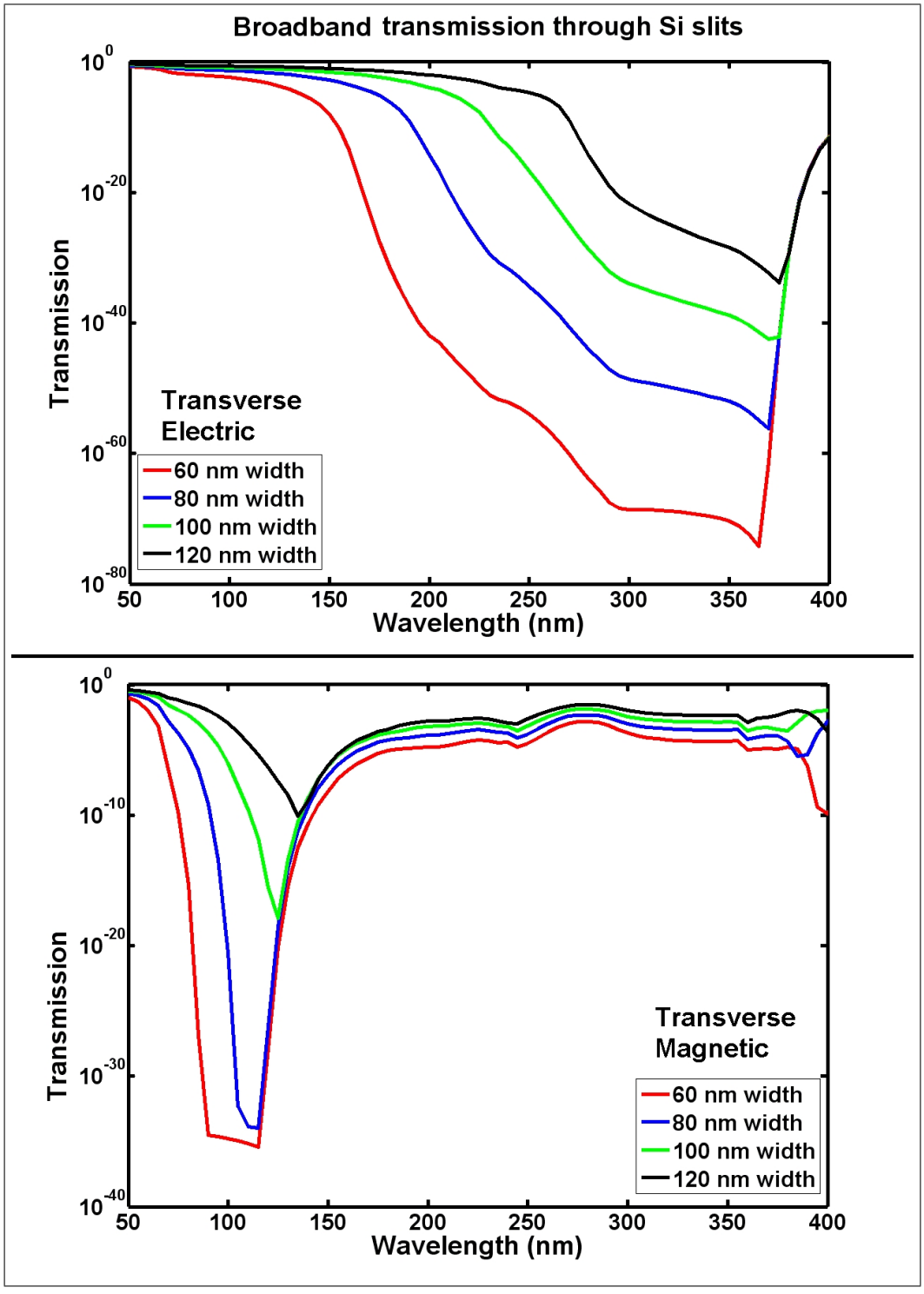

Figure 4.4: Ultraviolet transmission through silicon grids with 240 nm period, 2000 nm depth, and a variety of slit widths.

The effect of grating morphology can be seen in Figures 4.3 and 4.4, but are not as clear as they would be if the imaginary portion of silicon's refractive index did not drop sharply in the ultraviolet (Figure A.9). For example, in gold the transmission normally drops sharply around 80 nm (Figure A.2), but a gold grating with the same geometry as those modeled above sees a sharp rise in transmission toward the lower wavelengths, an effect entirely dependent upon the grating dimensions rather than a property of the material.

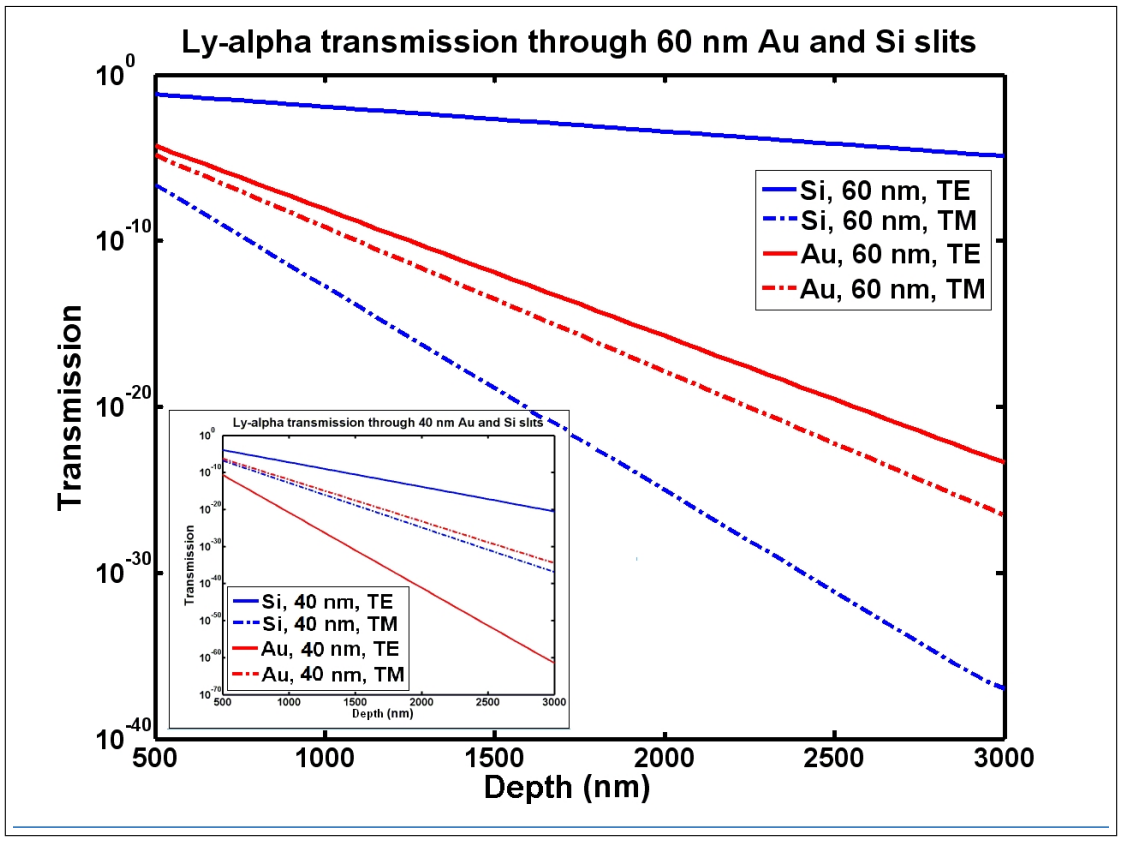

Figure 4.5: Comparison of Lyman-alpha transmission through 2000 nm deep Si and Au gratings with 240 nm period and 60 nm slits. The inset shows that the polarization of the grating reverses if the slits are only 40 nm wide.

This material effect is graphically demonstrated Figure 4.5. The silicon (semiconductive) grating preferentially blocks TM mode light. While the gold (conductive) grating does the same, albeit less strongly, with 60 nm slits, the inset shows that with 40 nm slits the gold grating preferentially blocks TE mode by many orders of

magnitude.

One thing that this shows us is that the material properties (optical and structural) are as important as the geometry. In § 4.1.1 the skin depth, the depth at which transmitted intensity drops to $1/e = 0.36787$ of the incoming intensity, was explained. Table 4.2 demonstrates clearly the wavelength and material dependence of skin depth. As can be seen here, the skin depth of many important solar physics wavelengths is shorter in either dielectrics or metals than in a semiconductor.

Table 4.2: Skin Depths of of Important Solar Physics Wavelengths in Easily Micromachined Materials. All wavelengths and skin depths are in nm.

	19.5 (Fe XII)	28.4 (Fe XV)	30.4 (He II)	58.4 (He I)	121.6 (H I)
Si	401.4	246.2	233.9	63.1	12.6
Au	9.6	7.8	7.8	6.5	10.8
Pt	no data	10.3	9.7	6.6	8.6
SiO2	no data	27	24.9	11.1	9.8
Al2O3	31.4	17.8	15.5	13.4	8.2

Given the demonstrated importance of material properties to the transmission and polarization of light, an exploration of layered gratings was undertaken in order to minimize the total transmission, defined here as the average of TE and TM modes. One immediate discovery was that strong dielectrics such as SiO_2 and Al_2O_3 are very strongly absorbing in the far UV, which was surprising given how transparent they are to visible and infrared light. Figures A.12 and A.16 in Appendix A demonstrate strong optical cutoffs under 200 nm wavelength. Strong conductors such as Au and Pt exhibit similar cutoffs (Figures A.2 and A.6).

It is highly desirable to have a conductive layer coating the inside of the channels in order to act as conversion surfaces for neutral atoms (*Scheer et al.*, 2006; *Novikov et al.*, 2007; *Wurz et al.*, 2008). Appendix A of *Moore et al.* (2000) provides an overview of the conversion surface technology used on the Low Energy Neutral Atom (LENA) instrument on Imaging from the Magnetopause to the Aurora for Global

Exploration (IMAGE). In the case of the gratings modeled here, the electron cloud of a conductor may induce resonant electron ionization of neutral atoms passing through the grating slits. It is possible that a dielectric layer alone can serve as a conversion surface (*Scheer et al.*, 2007), but this is a less-studied phenomenon than metallic conversion surfaces.

Since SiO_2, Al_2O_3, and Pt are easily deposited via atomic layer deposition (ALD), models using thin conformal layers on achievable grating geometries were run. Figure 4.6 demonstrates the transmission of Ly-α through silicon gratings with conformal coatings. In all cases the period is 240 nm, the gap is fixed at 60 nm, and the depth variable, with either 5 or 20 nm conformal coatings. In these simulations, the coatings replace sidewall silicon rather than narrow the gap, so the effect on transmission is material-related rather than geometry-related. These graphs show how even very thin layers of conformal coatings can have a huge effect on Ly-α attenuation. Since the interest is reduction of total transmission rather than polarization, the best case is where both TE and TM modes are minimized, as is the case with 5 nm of Al_2O_3 or 20 nm of Pt. As the two graphs show, too much of a given coating can simply reverse the transmission of the two polarities rather than block both. For example, 5 nm of SiO_2 greatly reduces both TE and TM transmissions, but 20 nm blocks TE but lets TM through, the opposite of what would happen with no coating. Careful tailoring of material layers is critical.

The realities of plasma etching of high aspect ratio freestanding gratings, detailed in Chapter V, dictate further limitations on grating geometry. In particular, it is extremely difficult to etch 40, 50, or 60 nm wide gratings that are 2000 nm deep. While the lithography technology is available to pattern to such specifications, the diffusion limitation of plasma etch tools do not allow for such high aspect ratio etching without causing a bowing effect. A more realistic goal was to etch grating slits of 100-130 nm and use ALD coatings to narrow the slits down to the desired range.

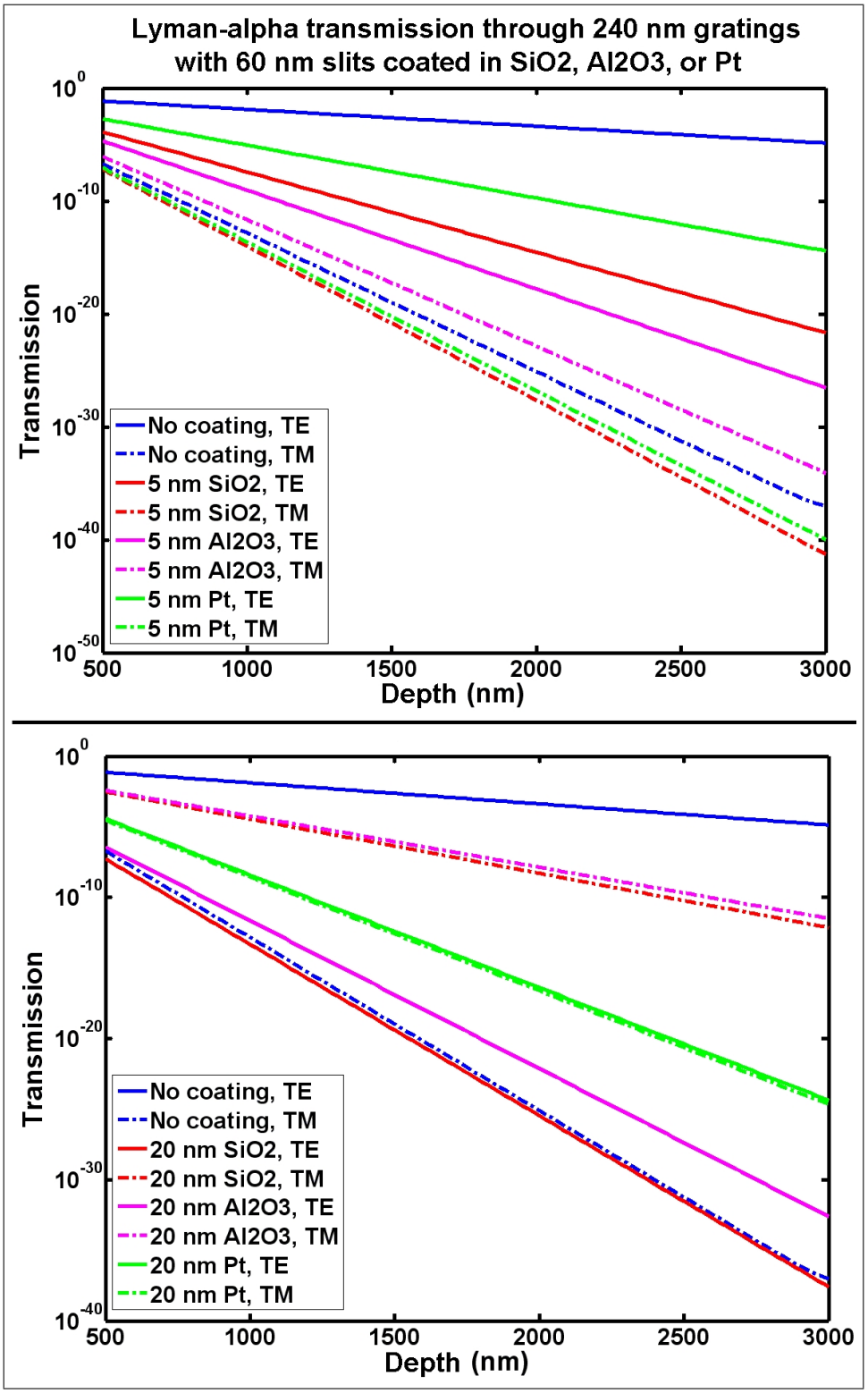

Figure 4.6: Transmission of Lyman-alpha light through silicon gratings of 240 nm period with fixed 60 nm gaps and conformal 5 nm or 20 nm sidewall coatings.

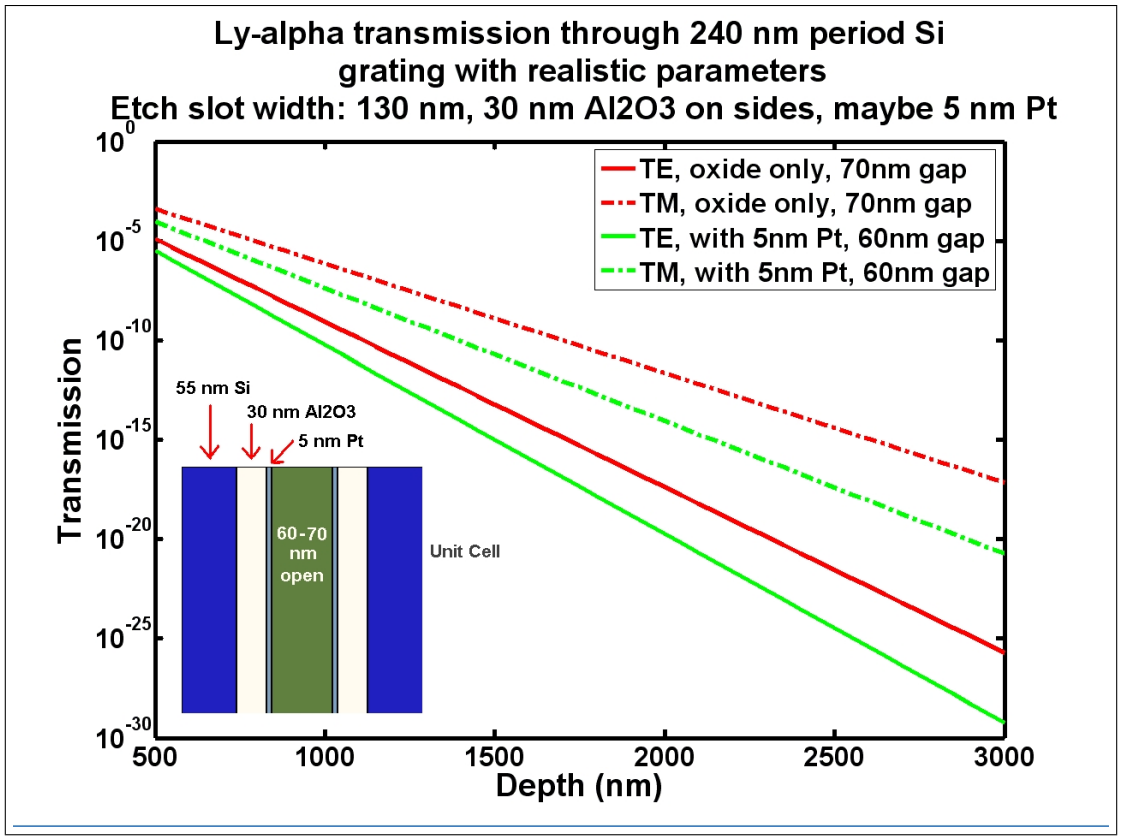

Figure 4.7: Transmission of Lyman-alpha through realistic layered grating structure. The inset shows a top-down image of a unit-cell of the grating.

Since tools capable of depositing coatings of Pt are far more rare, Figure 4.7 shows the transmission of such a grating with and without a thin Pt layer. Even with just the aluminum oxide layer, the total Lyman-alpha transmission is under 10^{-10} at a depth of 2000 nm. Addition of the Pt layer drops the total transmission by another 4-5 orders of magnitude. This shows the effectiveness of layered gratings in stark relief.

The addition of multiple layers of material to a grating have effects beyond simply affecting one wavelength. As each material has its own resonances and absorption cross sections, the layering effect has additional refractive and absorptive effects. Figure 4.8 shows broadband transmission through the same grating modeled in Figure 4.7. There are far more peaks and valleys present than in single-material grating

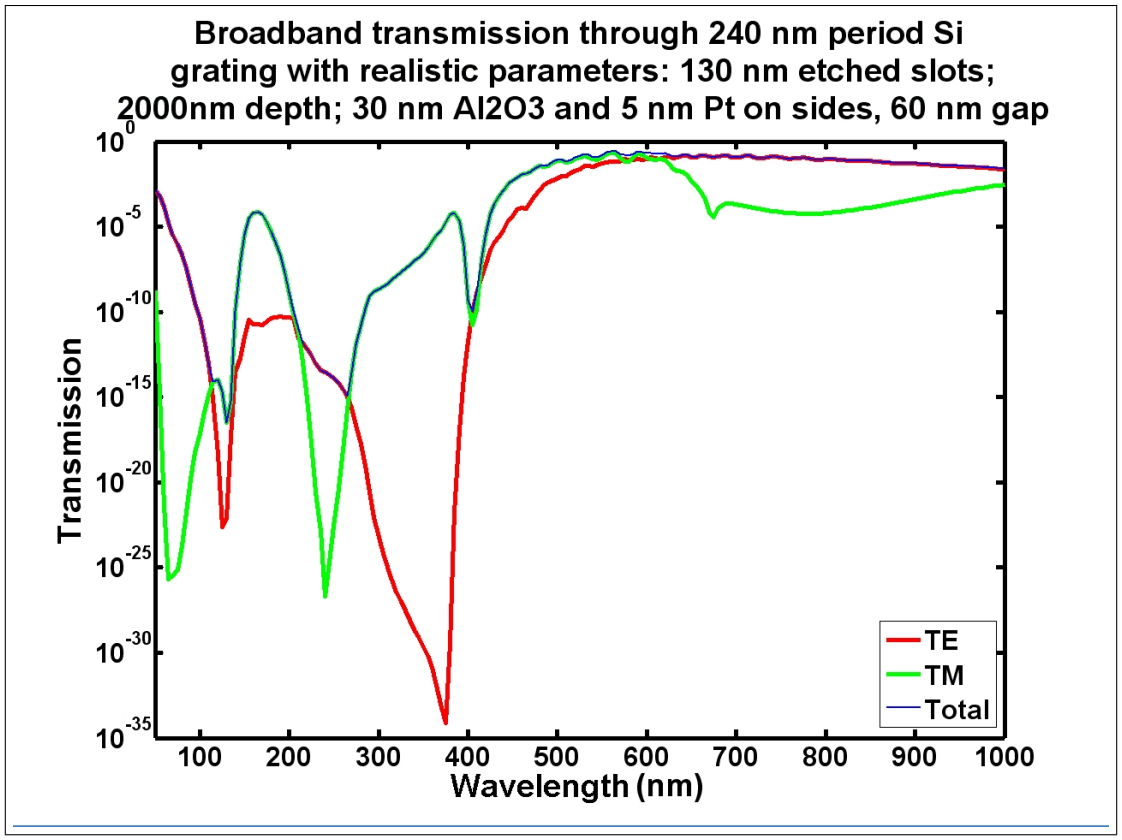

Figure 4.8: Broad-band transmission through realistic layered grating structure. The blue line traces the sum of TE and TM transmission, which is essentially the higher of TE and TM modes at any given wavelength.

simulations. This is only to be expected, and nearly the entire energetic UV spectrum transmits at under 10^{-5}.

The prior graphs are all for light normally incident on the gratings, but simulations indicate angular variation as well. As seen in Figure 4.9, this is clearly more relevant for the TE mode since TM mode is well below the noise floor, but the $\sim 64^{\circ}$ peak of the latter is interesting, though not of extreme importance in this case.

All of the above simulations were done with the same software. To verify that the software was functioning correctly, a simulation of a simple grating structure was performed using a separate software package called FullWave. This software models 3D high-frequency structures with access ports through which energy enters and leaves. A time-domain simulation was done of a 240 nanometer period silicon

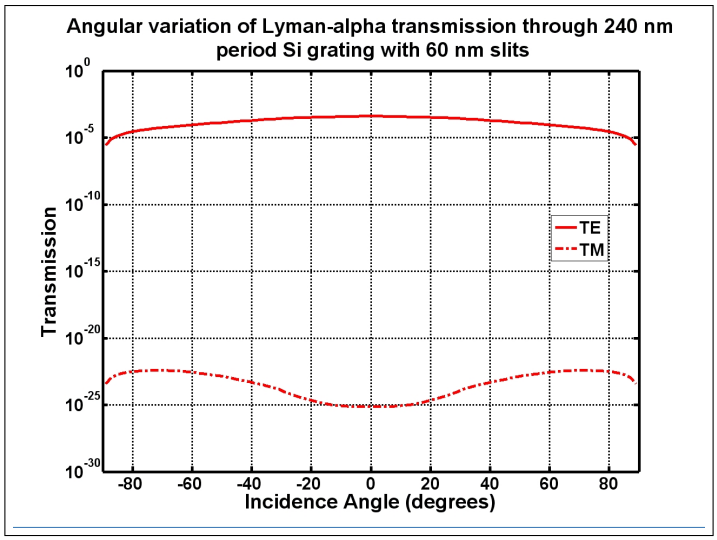

Figure 4.9: Angular dependence of Lyman-alpha transmission through a 2000 nm deep silicon grating with 240 nm period and 60 nm slits in the range of +/- 89 degrees. At +/- 90 degrees the transmission drops to zero, and cannot be simulated with GSOLVER.

grating of 2000 nm depth and 60 nm slit width illuminated by continuous-wave 121 nm light at normal incidence. The electric and magnetic fields of TE light were modeled as they propagated through the grating, as shown in Figure 4.10. The peak field strength seen from the far side (top) of the grating was approximately 4×10^{-4}. A simulation of the same structure in GSOLVER resulted in 4.7×10^{-4}, a very close match.

4.3 Discussion

The major challenge in creating a grating such as those modeled above is the size scale. While it is relatively simple to pattern features greater than a micrometer (micron), fabrication of submicron features is more difficult and when the feature size is under 200 nanometers it is extremely difficult. The second major challenge is the aspect ratio. Not only do the features have to be very narrow and very dense, but also very deep. The only technology capable of attaining the required depth on features

so small is deep-reactive ion etch (DRIE), and there are many pitfalls to overcome even with that. The final challenge is making the grating freestanding. All of these challenges are addressed in Chapter V.

The simulations in this chapter are for "perfect" gratings, in other words gratings whose geometry and illumination can be exactly modeled in GSOLVER or similar programs. In reality, there are effects due to the processing that cannot be fully modeled such as sidewall scalloping from DRIE, wearing away of the etch mask and possible redeposition of its material inside the grating, and pinhole flaws in the grating due to nonuniformities in the etch plasma. In addition, materials do not remain pristine during processing. They oxidize, become locally doped by plasma processing, retain residue from passivation, and so on, all of which can change their optical properties in potentially significant ways. These processing artifacts can have a major effect on the transmission characteristics of the grating.

However, despite all of the above effects, GSOLVER has been used in the past to model fairly accurately the UV transmission of the gold gratings used on MENA. The transmission through the MENA gratings was actually slightly less than that modeled by GSOLVER. The above simulation results should be fairly reliable for the silicon grating constructed in Chapter V.

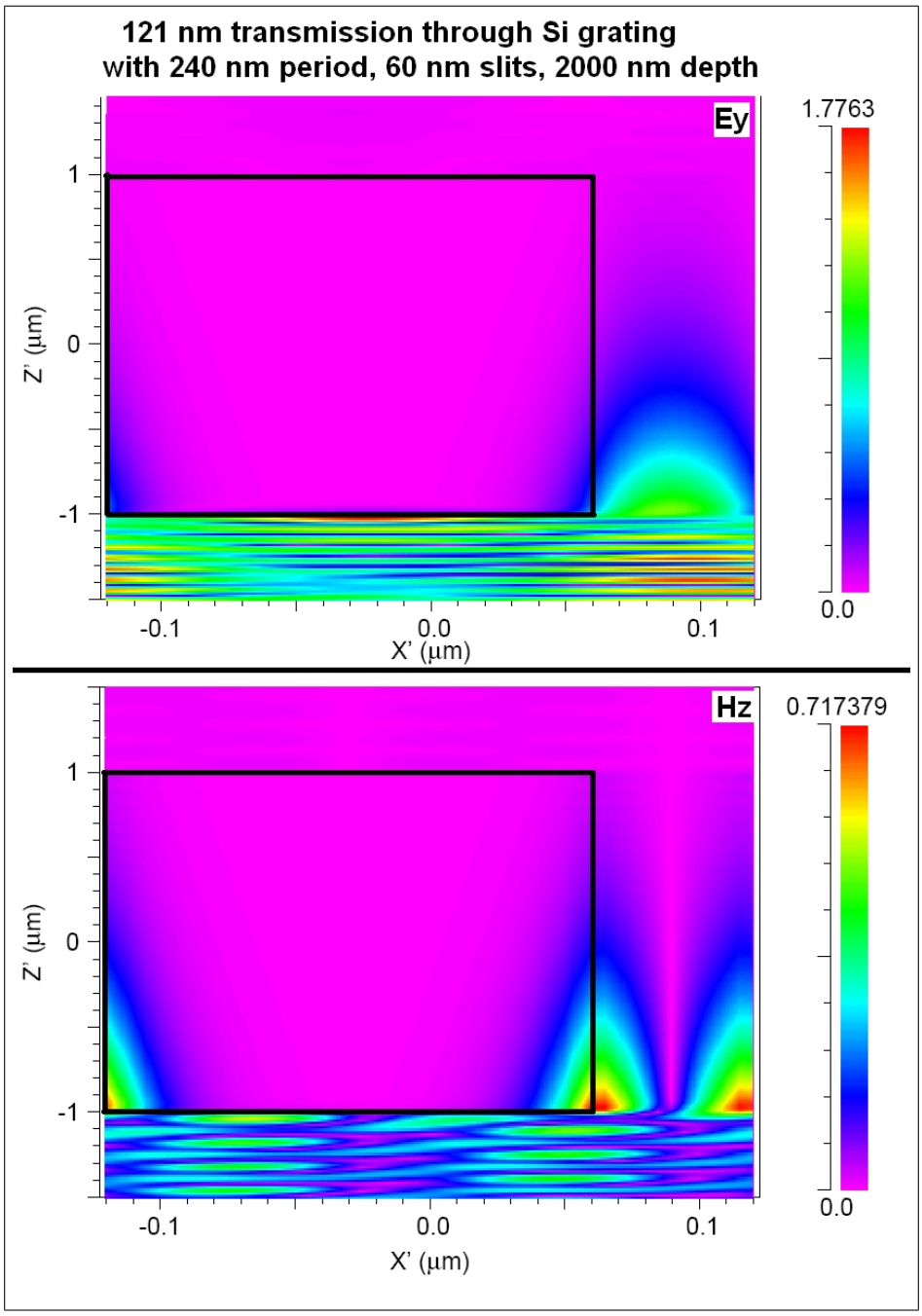

Figure 4.10: Electric and magnetic fields of 121 nm light propagating through silicon grating. The top image shows transverse electric field strength (E_y) and the bottom image shows the magnetic field strength (H_z). The black boxes in each image outline the silicon portion of the grating as seen from a cutaway. The illumination was from the bottom of each image, which shows the strong fields due to incoming and reflected waves, and both E and H quickly dissipate within the grating slits.

CHAPTER V

Grating Fabrication and Testing

This chapter covers the fabrication of the optical filter grating modeled in Chapter IV. Three techniques were attempted. The first, detailed in Section 5.1, was a trial based on femtosecond laser ablation of nanometer-scale holes or trenches in transparent materials such as glass or silicon nitride. The second (§ 5.2) was a proof-of-concept process using standard optical lithography, reactive ion etching (RIE), and chemical bulk etching. And the final, successful technique (§ 5.3) used nanoimprint lithography (NIL) for patterning and deep-reactive ion etch (DRIE) for both bulk and grating etches.

Unless otherwise specified, all scanning electron microscope (SEM) imagery was taken on an FEI NOVA Nanolab Dualbeam focused ion beam (FIB) Workstation and SEM (henceforth, NOVA)[a] at 10 kV acceleration and 0.13 nA beam current, using sample holders angled at 45 degrees. Optical microscopy was performed on a Nikon Dual Scope DME. Tools used in the lab are listed in Appendix B.

[a]Provided by the support of NSF grant #DMR-0320740.
http://www.fei.com/uploadedFiles/Documents/Content/2006_06_Nova_family_Semi_fb.pdf

5.1 Laser-etched Grid

5.1.1 Review of Femtosecond Laser Ablation

Lasers have been used for a number of different applications (*Phipps*, 2003). New hybrid technologies take advantage of lasers in ways never before imagined, such as laser microjet machining (*Mai et al.*, 2007) which may replace deep-reactive ion etching for certain applications. Femtosecond lasers in particular have promise across the spectrum of applications. Their recent development is reviewed with an eye on technology by *Keller* (2003) in Nature magazine, and *Rizvi* (2003) reviews the applications.

Unlike the longer pulses used for typical laser micromachining (*Holmes*, 2002), the nature of the laser-induced optical breakdown caused by femtosecond pulses allows for better control of pulse energy deposition, and therefore what portion of the target material is ablated (*Joglekar et al.*, 2004; *Gattass and Mazur*, 2008). *Webb et al.* (2008) say that "the advantage of ultra fast [laser] processing is that a broad range of materials can be processed with minimal heat transfer to the material." It is even possible to machine metals with femtosecond pulses (*Ostendorf et al.*, 2003; *Rizvi*, 2003), though possibly not with very fine features. The issue of heat transfer has been disputed (*Tran et al.*, 2007), especially in the case of fast lasers (*Eaton et al.*, 2005) but the controllability of machining with femtosecond pulses is universally accepted.

The process of laser ablation begins with the generation of free carriers in the target material through photoionization. At lower electromagnetic field strengths the dominant mode is multiphoton ionization (MPI) (*Gattass and Mazur*, 2008). In this regime an electron absorbs multiple photons, eventually raising its energy into the material's conduction band. At the higher field strengths associated with ultrashort pulses, it has been proposed that the dominant mode is tunneling ionization, also known as Zener ionization (*Joglekar et al.*, 2004). Changes in the band struc-

ture of the material allow electrons and holes to tunnel directly into the conduction band. *Fedosejevs et al.* (2007) examine the two modes in detail, and *Hwang et al.* (2006) investigate energy coupling and ablation efficiency in silicon under both modes. *Schaffer et al.* (2001) look at the mechanisms of ablation, including measurements of ionization and damage thresholds of a range of materials with differing band-gaps.

Whichever method begins the ionization, the result is an avalanche ionization that turns a portion of the target material into a micro-bubble of high pressure plasma. This plasma bubble cools primarily by expanding, heating the surrounding material, though emission of light is a secondary cooling mechanism. The initial high pressure in the plasma causes a shock wave to form and propagate. For pulses of picosecond or longer duration, the plasma bubble absorbs a great deal of energy and the few oscillations it goes through before collapsing damage a significant region of the target. For femtosecond pulses, the amount of damage is quite low since the amount of energy absorbed is small.

Uniform, repeatable ablations are enabled by machining just above a material's damage threshold, also called the optical breakdown threshold (OBT). In order to damage a material, a pulse requires a certain amount of energy. As pulses become shorter, both the energy threshold and threshold uncertainty decrease. Thus, femtosecond pulses have very clear damage thresholds at relatively low energies and can produce very reproducible cuts. Figure 5.1 shows the effects of decreasing pulse energy on the size of trenches etched in glass. Rather than using single pulses, it is possible to machine materials with bursts of multiple pulses as well. *Gattass et al.* (2006) examine the effects of laser repetition rate and burst pulse size on heat diffusion and machined feature size and *Deng et al.* (2005) explore the optical breakdown threshold of silicon with double pulses. *Crawford et al.* (2005) provide details on femtosecond laser etching of grooves in silicon, but on the scale of micrometers rather than nanometers. On the nano-scale, damage mechanisms and feature morphology

have been examined in detail for transparent dielectrics (*Kudryashov et al.*, 2007a,b).

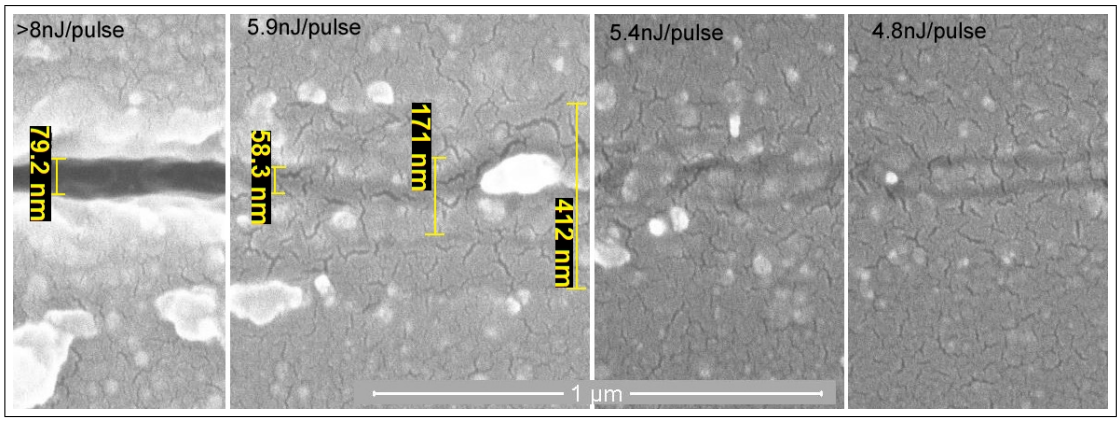

Figure 5.1: Femtosecond laser ablation of glass trenches at pulse energies of 4-8 nJ. Even at low energies the damaged region around each trench interferes with trench density, thus limiting grating fill factor.

The energy distribution of the laser footprint follows a Gaussian pattern, and thus only a small portion of the focus spot of the pulse exceeds the OBT. Because of this, visible-light lasers can etch regions only a few dozen nanometers wide. When applied to optically transparent materials, this even allows for machining inside the material. The plasma produced by the avalanche ionization will essentially shatter the material *inside* the bubble, leaving gritty sand that is easily removed once an opening is bored.

5.1.2 Fabrication Problems and Future Considerations

Fabrication by this technique follows a five-step process. First, 200 μm wide support lines with a pitch of 1 mm are diffused into bulk silicon. Then a layer of low-stress silicon nitride is deposited by low pressure chemical vapor deposition (LPCVD) and covered with an oxide protective layer. The bulk silicon is chemically etched from the back side using potassium hydroxide (KOH) masked by silicon nitride, stopping on the diffused lines to leave a membrane, and the protective oxide is removed with buffered hydrofluoric acid (BHF). Then the nitride membrane is etched by femtosecond laser to form an array of nanometer-scale holes or grooves, and gold is

sputtered into the grid.

This fabrication technique contains significant technical challenges. The primary challenge is with the grating etch itself, specifically the required etch time. To etch patterns of usable size (a square on the order of 2 centimeters on a side), a very fast laser is required. Since the etched region for each laser shot is roughly spherical, the smaller the feature size the more shots it takes to etch both horizontally and vertically. For example, assuming a desired array of 50 nanometer holes separated by 50 nanometers, and 500 nanometer depth, each shot will ablate a spheroid of approximately 50 nm diameter and thus the required number of shots is approximately 4×10^{11}. This research used a diode-pumped Nd:glass chirped pulse amplification (CPA) laser system (Intralase Corp., Irvine, CA) that generates 600 to 800 fs pulses at a repetition rate of up to 3 kHz. Manufacturing a single grating using this laser would have required an unreasonable 4.2 years of continuous operation, and thus fabrication with this technique was canceled prior to full process integration.

However, high repetition-rate extended cavity Ti:sapphire lasers (e.g. *Dantan et al.* (2007)) and fiber lasers(e.g. *Dupriez et al.* (2006) and *Chen et al.* (2007)) can reach repetition rates of up to 200 MHz with reasonable power throughput. *Shah et al.* (2005) and *Eaton et al.* (2005) have written waveguides using a 1 MHz Yb-fiber laser, and *Osellame et al.* (2005) with a 26 MHz stretched-cavity Ti:sapphire laser. In addition, ongoing work to diffract the beams into multiple parallel beams (*Li et al.*, 2005) may enable ablation of up to 10^4-10^6 holes or lines simultaneously depending on the power of the laser. External repetition rate multiplication can increase the writing speed of an individual beam (*Chen et al.*, 2008). Shot rates of up to 2 GHz are achievable, which would allow an array of holes such as that mentioned above to be machined on glass substrates in under five minutes of laser operation. This, of course, does not take into account alignment time or any required cooling time during etching.

The above numbers are relevant to any kind of direct-writing, whether it be via laser or ion beam or electron beam. Since each feature of each pattern is written individually, the speed of that writing becomes of paramount importance.

In the interests of maintaining diaphragm structural integrity it is required to leave the bulk back-etch until the end of the process. However, machining via femtosecond laser usually requires high numerical aperture lenses, often a drop of oil in contact with the surface of the substrate. This means that gratings must be machined from the bottom up, and since there needs to be a path for machined material to be ejected the substrate must be removed to provide that path.

The original fabrication method had two other minor challenges, both with fairly simple solutions. First, the issue of stopping a back-side etch on a thin nitride membrane without damaging the membrane can be solved through use of a sacrificial etch stop layer, probably an oxide layer, that can be removed either by a short BHF immersion or selective plasma etch. If the sacrificial oxide is deposited at low temperature, and the device layer is a low-stress nitride, there should not be a problem with stress either before or after the oxide removal. The second problem is the deposition of a metal layer in small, high aspect-ratio features. Sputter deposition is not entirely directional, and thus has good step coverage, but can not deposit on narrow vertical features. However, as mentioned in § 3.2, atomic layer deposition (ALD) can do so.

With the newer tools, it is likely that a re-visitation of this process could result in a successful optical filter.

5.2 Optical Lithography and Reactive Ion Etching

In contrast to the above technique, optical lithography allows the creation of multiple sets of an entire pattern in a single exposure. Using the standard techniques described in Chapter III, a double-sided bulk silicon process was used to test lithography and etch steps, determine optimal feature length-to-width ratio, and gain

experience with the lab tools. The process steps are detailed in Appendix B.2, and briefly summarized below:

1. Ion implant a high density of boron ions ($> 10^{12}$ cm^{-3}) on one side of a double-polished (100) wafer
2. Front-side photolithography of multiple instances of the desired pattern
3. Plasma etch the gratings into the doped silicon
4. Back-etch, stopping on boron concentration etch-stop

Only the most advanced photolithography tools can pattern the required 50-100 nm features. Limitations of the available tools (Appendix B) required much larger feature sizes. Optical mask creation was accomplished on an ElectroMask II pattern generator using both 1.5 μm and 2.0 μm half-pitch grating features. Optimization of exposure and development parameters over the 33% variance in feature size proved impossible. For features over 10 μm , a 0.5 μm variance is relatively simple to accomodate, but at the tool limit the exposure and development times are very sensitive. Optimization for 2.0 μm features proved to be the most convenient. The gratings were etched 500 nm deep into the doped silicon by a Trion Oracle III RIE tool.

The back side etch was broken into a two-step process, a plasma etch followed by a chemical etch. The reasons for this were the relatively low selectivity of the boron etch stop (approximately 80:1 according to *Petersen* (1982)) and the footprint of the 54.74° angle caused by the <111>planes. The masking layers for this two-stage etch were a 1 μm plasma enhanced chemical vapor deposition (PECVD) silicon oxide and a 10 μm layer of AZ-9260 photoresist. Back-side pattern alignment and resist exposure were done with a Suss MA-6 tool and a short BHF dip patterned the oxide.

After lithography, DRIE in an STS MESC Multiplex inductively coupled plasma (ICP) etcher removed $\sim$ 420 μm of the bulk silicon. Most of the available STS etches were optimized for approximately 20% open area, but the test pattern had 70% open area. Since the STS is gas-flow limited in SF_6, the process had to be re-optimized for

the wider open area. A Zygo NewView 5000 profilometer was used to determine etch depth. The remaining 80-100 μm of bulk silicon were removed by a soak in ethelene-diamine pyrocatechol (EDP) that stopped on the grating's boron concentration. The EDP etch was only slowed by the ion implant rather than stopped entirely, so it had to be carefully monitored toward the end.

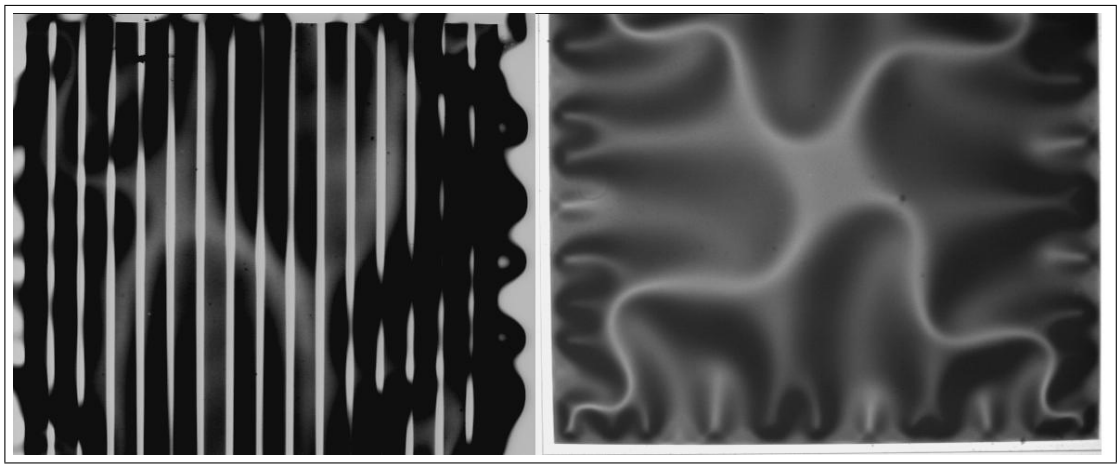

Figure 5.2: Optical microscope imagery of 2 mm diaphragms after EDP etch. On the left are a series of 2 μm half-pitch gratings with 100 μm long slits under a 1 μm thick protective oxide layer, and on the right is a window of equal size with only the oxide layer. It is clear from these images that the compressive stress of the oxide caused significant rippling of the windows with the maximum stress around the window edges.

The 500 nm thick gratings were protected from the EDP by a 1 μm PECVD oxide layer on the front side. The oxide layer caused significant bowing of the grating windows, as seen in Figure 5.2. The final step of this process was a BHF dip to remove the oxide and leave the diaphragm freestanding. Due to the fragility of the gratings, the BHF dip was performed very carefully, and the usual vigorous post-BHF rinse was replaced with a series of seven five-minute dips separate beakers of clean de-ionized water.

This process was a partial success. The wet steps, both in lithography and etching, caused problems with feature size, diaphragm stability, and stiction. The low selectivity of the boron etch-stop required removal of the chips from the EDP bath

every few minutes to rinse and examine them. In addition, the EDP etch could not be allowed sufficient over-etch time to guarantee complete clearance of all windows. Since each entry to and removal from a liquid involves liquid resistance, a few diaphragms broke toward the end of the EDP etch. The same problem was evident during the BHF dip and rinse. Final yield for this process was approximately 5-10%, largely due to the post-EDP fragility of the membranes.

However, in addition to the process experience one very useful result was obtained. A primary purpose of this test was determination of how long the lines could be relative to their width before stiction became a problem (*Tas et al.*, 1996; *Maboudian and Howe*, 1997). Figure 5.3 shows that approximately 30:1 is a reasonable limit if wet processing is involved. Stiction effects become evident at 45:1 and dominate beyond that; stiction can be controlled by critical-point drying (*Jafri et al.*, 2003).

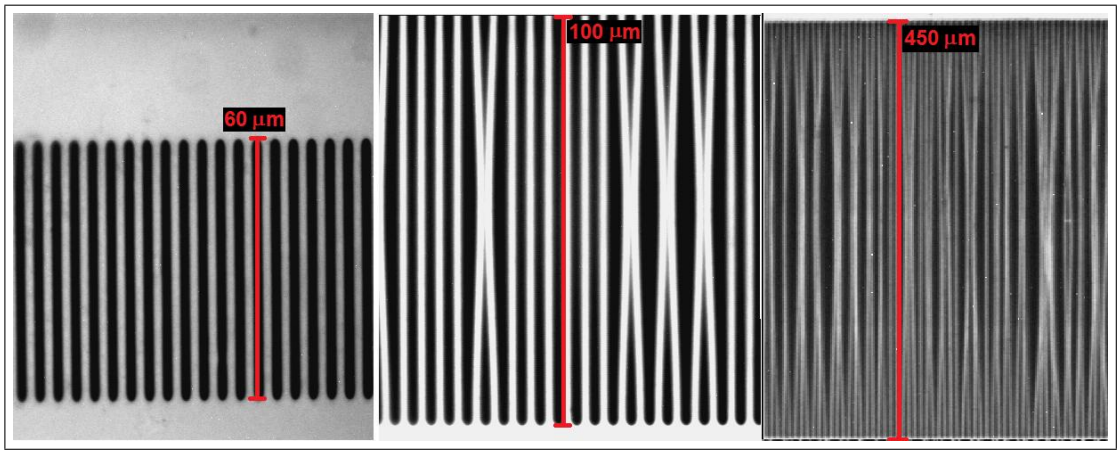

Figure 5.3: Optical microscope imagery of freestanding 2 μm half-pitch gratings. The grating lines on the left are 60 μm long (length-to-width ratio 30:1) at 100x magnification. The middle set of lines are 100 μm long (ratio of 50:1), also at 100x. On the right are 450 μm lines at 20x magnification. Stiction effects are due to surface tension while drying after the BHF removal of the protective resist layer.

In order to strengthen the diaphragms, support lines could be added through deep boron diffusion into the bulk silicon prior to the surface ion implantation. This was part of the initial process flow, but was skipped for the first trial. In order to not cut

the diffused lines, the entire release would be via wet-etch, which would likely require using a silicon-on-insulator (SOI) wafer for the strong dielectric etch stop.

The last few steps of this process, sputter-deposition of a conductive seed layer followed by gold electroplating to narrow the grating slots, were never performed due to time pressure, lack of sufficient yield, and the fact that the fill factor would be a mere 2% even with complete success. Also, narrowing the grating slots via electroplating has diffusion limitation problems as one approaches the desired 10:1 aspect ratio. Using a pulsed source rather than constant-current may mitigate that effect, but it was not available in the lab.

The problems with this technique—in particular the wet etch fragility, electroplating, and low fill factor—far outweigh the advantages, even if better lithography tools were to become available. With top-of-the-line photolithography tools and carefully-tailored RIE it would be possible to achieve much greater fill factor, but the cost of such tools is prohibitive.

5.3 Nanoimprint Lithography and Deep-Reactive Ion Etch

Complete process integration for fabricating sturdy, self-supported transmission gratings in silicon was achieved with a new technique using NIL and DRIE. Gratings are patterned with NIL and aluminum liftoff on SOI wafers. Front side DRIE creates the 120 nm half-pitch, 2000 nm depth gratings with scalloping under 10 nm. Back side through-wafer DRIE produces a 1 mm pitch support structure. Full process details can be found in Appendix B.3.

5.3.1 Review of Reactive Ion Etch Technologies

Reactive ion etch tools come in a variety of forms. A DC glow discharge is the most basic, but under DC conditions a dielectric will become charged and the etch rate will drop to zero. Plasmas operating at radio frequency (RF) can avoid this problem;

at frequencies greater than 100 kHz electrons respond and ions do not. Typical RF plasmas operate at 13.56 MHz by designation of the FCC. The methods of generating the plasma can also vary. *Lill and Joubert* (2008) say that "Process engineers have preferred capacitively coupled plasmas (CCP) for oxide etch, but ICP or electron-cyclotron resonance (ECR) plasmas for conductor etch. However, the lines are now blurred and both types (CCP and ICP) can be used for a variety of applications." Magnetic neutral loop discharge plasma is a new technique with two advantages: high ionization rates (high-density plasmas, low electron temperatures and gas pressures) and field controllability (*Uchida and Hamaguchi*, 2008). *Jansen et al.* (1996) explain a wide range of etch reactors, chemistries, and masking techniques.

The research in this dissertation used primarily an STS MESC Multiplex ICP tool, shown in Figure 5.4, for DRIE along with a variety of tools for surface RIE processes. Oxygen plasmas were used for ashing (the isotropic removal of polymer layers) and residual layer etching (anisotropic removal of thin layers of polymer at the bottom of patterned features). Fluorocarbon plasmas were used for etching of silicon oxide and deposition of passivation layers. And sulfur hexafluoride (SF_6), a fluorine-based plasma, was used for deep silicon etching (*Lii et al.*, 1990).

Gas chemistry is of course of critical importance. *Gleizes et al.* (2005) provide a detailed look at the modeling of thermal plasmas, and *Murphy* (2001) models plasmas with multiple gases. *Tian et al.* (2000) compare the etching of high aspect-ratio silicon structures with Cl_2- and F-based chemistries and find that when large portions of the substrate must be etched, the F-based etching provides high etch rate and high mask selectivity, but for smaller features without sidewall roughness Cl_2 etching is better. Oxide etching in fluorocarbon plasmas such as carbon tetrafluoride (CF_4), trifluoromethane (CHF_3), and octafluorocyclobutane (C_4F_8) is particularly tricky. This is because it is a race between etch rate and polymer deposition rate (*Oehrlein et al.*, 1994a,b; *Rueger et al.*, 1997; *Standaert et al.*, 2003), because the fluorocarbons

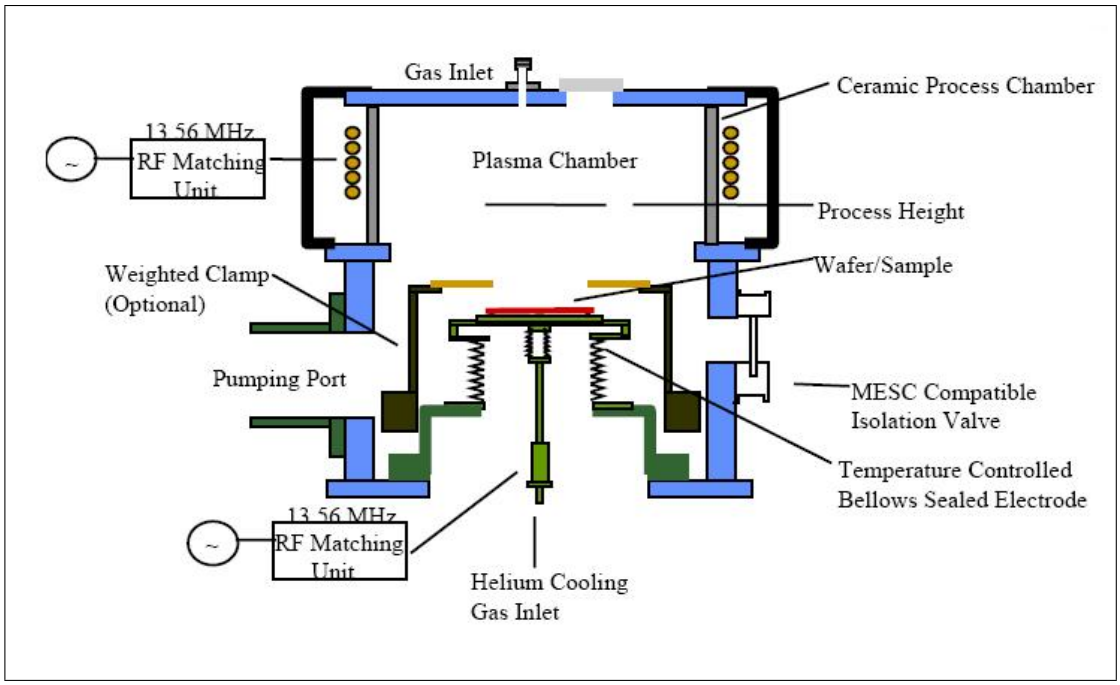

Figure 5.4: Schematic of STS ICP plasma etcher. Image credit to *Bhardwaj et al.* (1997).

used also etch silicon (*Standaert et al.*, 1998; *Humbird and Graves*, 2004), and because they deposit on the sidewalls, thus changing the etch conditions (*Schaepkens et al.*, 1998).

As mentioned in Chapter III, DRIE is a repeated two-step process of passivation and isotropic etch. It is called by a variety of names, including Bosch process after the patent by Robert Bosch GmbH (*Lärmer and Schilp*, 1996), gas-chopping, and time multiplexed deep etching (TMDE). In DRIE, as in standard RIE, there are trade offs between etch characteristics—such as pressure and power—and the etch rate, selectivity, and uniformity of the resultant features (*Ayón et al.*, 1999a,b). *O'Brien et al.* (2001) characterized the tradeoffs between etch cycle time, passivation cycle time, and RF coil power for etching deep submicron structures. *Chen et al.* (2002b) did similar work in process parameter optimization. *Blauw et al.* (2000) looked into the effects of crystal orientation and aspect-ratio dependent etching (ARDE), the tendency of larger or shallower features to etch faster. ARDE is a very important

phenomenon to understand, and was also examined by *Cardinaud et al.* (2000) and others in the last few years. Research has also been put into straightening and smoothing feature sidewalls (*Oehrlein and Kurogi*, 1998; *Liu et al.*, 2001) and tailoring etch directionality (*Ayón et al.*, 2000). In the cases of low gas flows, the amount of exposed surface area is also a factor since the chamber is gas-limited. *Zhou et al.* (2004) present an accurate computer model of the Bosch process that takes into account many of the effects just mentioned.

DRIE has been used for fabrication of deep nanolines on solid substrates by others. The line buckling strength for high aspect ratio silicon gratings has been examined (*Kang et al.*, 2008; *Li et al.*, 2008). *Marty et al.* (2005) achieved aspect ratios of 107 with 374 nm wide channels in silicon using aluminum masking. *Woldering et al.* (2008) demonstrated tightly packed arrays of 300-500 nm wide nanopores with aspect ratios of 16 using Cr masking. A significant portion of the research for this dissertation involved pushing the boundaries of the STS tool's SF_6/C_4F_8 Bosch process in order to create high aspect ratio nanogratings in silicon, but without any remaining substrate. The removal of the substrate is as challenging of a problem as the high aspect ratio grating etch, and the two technologies have never before been paired.

Reactive ion etching is as much art as it is science. There are a wide variety of controllable parameters, but despite perfect optimization a process may not be uniform across the surface of a wafer or from run to run. The tools are affected by power fluctuations or outages in the lab and other day-to-day events which may require resetting of coolant systems, initialization of the tools, and so on. The robots that control the movement of wafers, activation and de-activation of pumps and valves, gas flows, and more can sometimes malfunction, often resulting in wafers getting stuck inside the tools and occasionally broken. However, despite all of this, an optimized recipe and a little luck can provide phenomenal results.

5.3.2 Review of Nanoimprint Lithography Technologies

Fabrication at the nanoscale is rife with challenges that have only begun to be met in recent years. Nanoimprint lithography is a relatively new technology first demonstrated by Dr. Stephen Chou at the University of Minnesota in 1995 (*Chou et al.*, 1995, 1996a,b, 1997). It is viewed by the International Technology Roadmap for Semiconductors (ITRS)[b] as one of the front-runners for next-generation lithography due to its simplicity, high fidelity, throughput speed, and repeatability, its capability for submicron features, and its cost compared to the other options. It compares well with other technologies at the nanoscale. *Marrian and Tennant* (2003) review nanofabrication from top-down methods such as beam and imprint lithography to bottom-up methods like block copolymer self-assembly. From macroscopic injection molding to state-of-the-art hot embossing and NIL, *Heckele and Schomburg* (2004) review the history and current status of micromolding, including a table of the tradeoffs between some of the most commonly used thermal plastic polymers. In similar vein, *Cross* (2006) examines the nanoscale mechanical phenomena and design space, including flow phenomenology and issues with mold geometry. *Hirai et al.* (2004) study polymer deformation during imprinting, including for high aspect-ratio imprints.

The in-depth reviews by *Guo* (2007) and *Schift* (2008) describe in detail the current state of NIL. Many process variants are being tested, but as a general rule they all are descendants of either hot embossing or UV curing. Some interesting variants include low pressure NIL (*Khang et al.*, 2004) and ultrasonic NIL (*Lin and Chen*, 2006). One of the most popular variants is step-and-flash imprint lithography (SFIL) (*Colburn et al.*, 1999, 2000) which, according to *Resnick et al.* (2005), uses "a transparent fused silica template, facilitating the viewing of alignment marks on the template and wafer simultaneously." To facilitate alignment accuracy, *Mühlberger et al.* (2007) present a Moiré pattern alignment technique that provides < 100 nm

[b] http://www.itrs.net/

accuracy. *Lan et al.* (2007) describe a six degree of freedom, actively controlled substrate stage that enables parallel surface contact between mold and wafer and minimizes relative lateral motions during imprinting. Some advantages of NIL include the ability to fabricate nanostructures on non-flat surfaces (*Sun et al.*, 1998) and to use industrial roll-to-roll printing (*Tan et al.*, 1998).

One of the difficulties in imprint lithography is that of resist adhesion to the mold rather than the substrate during mold separation. This is usually solved by adjusting the surface energy of the mold and/or substrate. Molds are often treated with a fluorinated self-assembling monolayer surfactant, and substrates can be treated with spin-cast or evaporated adhesion promoters. *Jung et al.* (2005) conclude that vapor-phase surfactant monolayer formation is superior to liquid-phase. *Bailey et al.* (2000) examine a variety of surfactant types with an eye to SFIL defect characterization.

Another difficulty is attaining large grating molds with very small features. If one has a mold with relatively large, periodic features, it is possible to create finer-grain molds via frequency doubling processes, which have been demonstrated to create gratings with periods of 100 nm (*Yu et al.*, 2001) and 50 nm (*Cui et al.*, 2007).

In this dissertation, thermal plastic resists were imprinted with nanogratings as a primary lithography step on the device layer of SOI wafers. This enabled large areas to be patterned in a matter of minutes rather than the days or weeks it would have taken with e-beam patterning.

5.3.3 Fabrication

The fabrication of a freestanding, self-supported nanograting can be divided into three major components: grating lithography, back-side support lithography and through-wafer etch, and grating etch. These components, while related in the final process integration, were developed independently.

Each sample starts as an approximately 1.5 inch square (100) SOI chip with a

2 μm top silicon device layer, 250 nm buried oxide (BOX), and 500-520 μm thick Si substrate which is refered to as the handle layer. Device layer patterning is accomplished by two successive NIL imprints and metal liftoff processes. First the samples are thoroughly cleaned, and a 3-5 nm Cr layer is evaporated on them to promote resist adhesion. Then they are nanoimprinted using a 140 nm layer of mr-I 8030, a thermal plastic resist from Micro Resist Technology[c]. Imprinting is done for five minutes at 600 PSI and 180° C by a Nanonex[d] NX-2000 Imprintor. After imprint, 5 nm of aluminum is shadow-evaporated from both sides with a shadow angle of approximately 75°. Figure 5.5 demonstrates the mechanism of shadow evaporation.

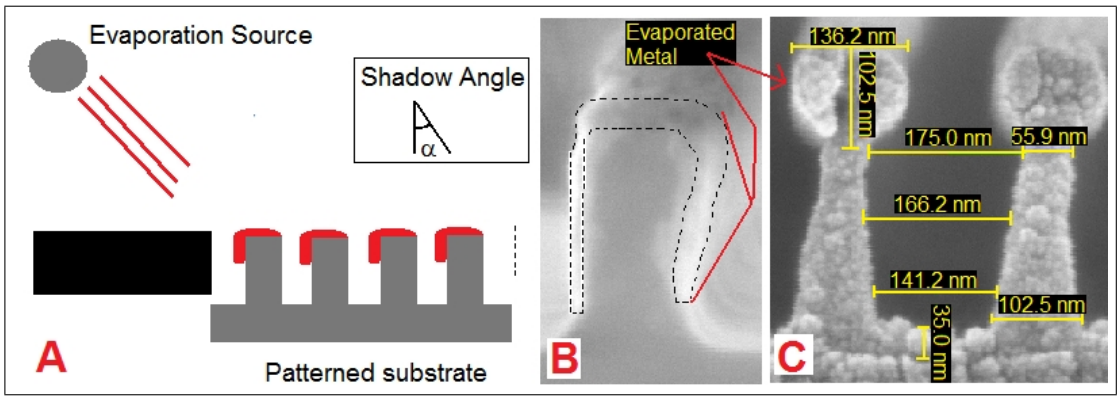

Figure 5.5: Shadow evaporation process and examples. A) If the substrate is angled with regard to the evaporation target, the periodic lines shadow one another such that only the tops are coated. If samples are coated from both directions, the coating is symmetrical. With low shadow angle (B) the evaporated material (outlined by dotted line) coats farther down the sidewalls than with high shadow angle (C).

After shadow evaporation, the residual polymer layer was removed by plasma etching in a Plasmatherm 790 at 20 mT, 20 sccm[e] O_2, and 50 W RF power for 105 seconds. The resist trenches themselves are protected by the shadow-evaporated metal layer, with only slight undercutting to facilitate subsequent liftoff. Next is direct deposition of a 70 nm thick aluminum hard-mask; in this case the shadow

[c] http://www.microresist.de/home_en.htm
[d] http://www.nanonex.com/
[e] "sccm" is measure of gas flow that stands for Standard Cubic Centimeters per Minute

angle is zero, indicating normal incidence such that the metal coats between the lines and atop them. The slight widening caused by the shadow evaporation keeps the metal from touching the resist sidewalls, which would interfere with liftoff. Lift-off of the resist and metal caps is performed in an ultrasound-agitated acetone bath for approximately 20 minutes. Figure 5.6 shows SEM imagery of the process up to the direct-evaporation stage of a 240 nm period 1-D grating with 50% duty cycle.

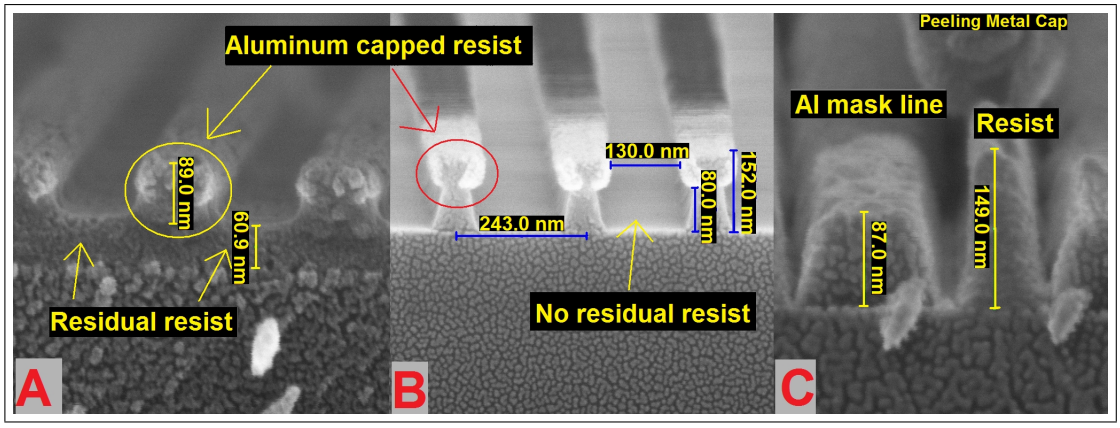

Figure 5.6: Cutaway SEM imagery of front-side lithography process. The edge-on shots are of the same sample after A) imprint and dual shadow-evaporation of 5 nm Al, B) residual resist etch, and C) direct-evaporation of 70 nm Al.

After the first aluminum liftoff patterning, an 11 μm period grating with 300 nm lines is deposited at 90° to the fine grating and using the same process. This thicker grating enhances the rigidity of the long, thin grating lines and assists in avoiding stiction problems. The device layer is then spin-coated with a protective layer of photoresist and hard-baked at 110° C for a half-hour. Figure 5.7 shows a schematic of the whole grating lithography process.

Back side handle layer patterning is performed by standard photolithography. First a 2 μm layer of aluminum is evaporated on the back side of the sample. A 5 μm layer of Shipley 1827 photoresist is spin-cast, then soft-baked on a hotplate at 115° for 90 seconds. An MA-6 mask aligner is then used for back-side alignment and 20

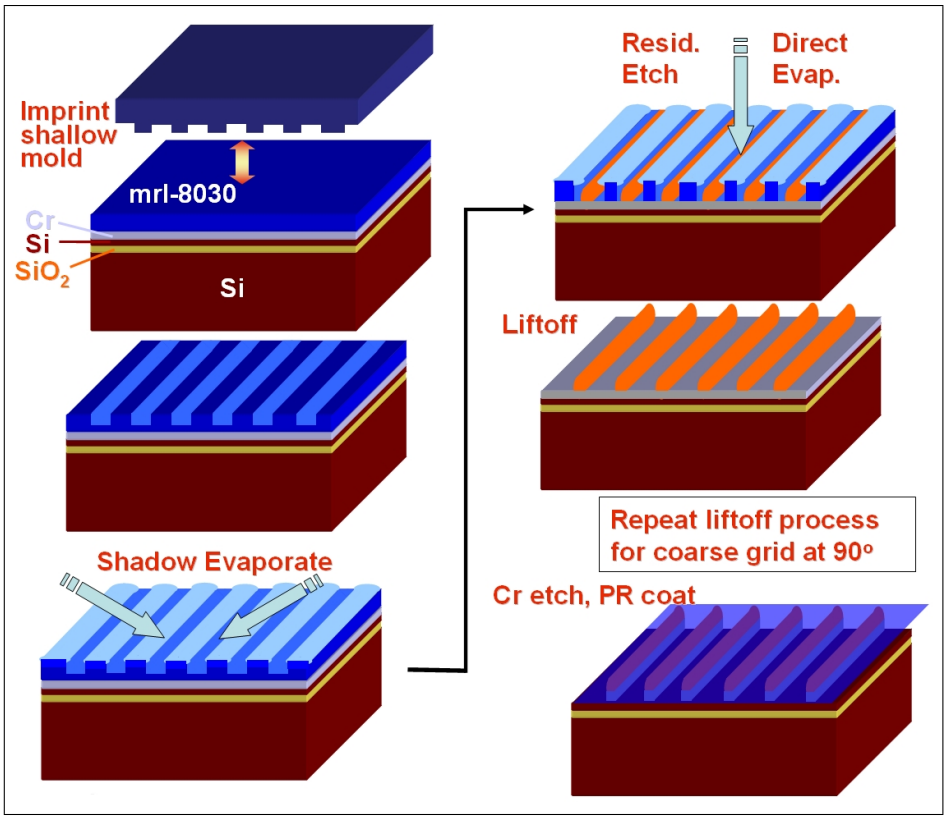

Figure 5.7: Grating lithography process. An SOI chip with mr-I 8030 thermal plastic resist is imprinted with a 120 nm half-pitch mold and 5 nm Al is shadow-evaporated from both sides. Next is residual layer removal, direct deposition of 70 nm Al hard-mask, and acetone lift-off. A second 11 μm imprint at 90° follows the same procedure. Then the surface is protected with photoresist during back-side processing.

second exposure. The pattern is a 1 mm period 2-D grating with 150 μm support lines. A four minute dip in Transene Aluminum Etchant A transfers the pattern from the photoresist to the aluminum mask layer.

One unexpected process requirement is removal of the protective photoresist on the front device layer between aluminum patterning and DRIE steps. This is because exposure to the aluminum etchant changes the characteristics of the photoresist such that the heat of a subsequent through-wafer etch will bond it permanently to the substrate, ruining the grating pattern.

After patterning both sides of the chip, the handle layer is etched from the back

using the STS tool shown in Figure 5.4 running an SF_6/C_4F_8 Bosch process. The etch stops on the BOX layer after approximately three hours. A slight overetch is necessary to ensure that the edges of the revealed windows are thoroughly etched. During this 3-10 minute overetch it is important to watch the color of the oxide (Figure 3.2) to avoid penetration to the underlying device layer. The BOX is removed in a LAM 9400 ICP tool and the sample is removed from its carrier wafer by an acetone soak. All subsequent steps must be performed very carefully due to the fragility of the patterned 2 μm silicon device layer. An O_2 plasma ash of the device layer removes resist residue from between the aluminum grating mask lines, and then high aspect ratio grating etch is performed in the STS, resulting in freestanding, self-supported gratings as shown schematically in Figure 5.8.

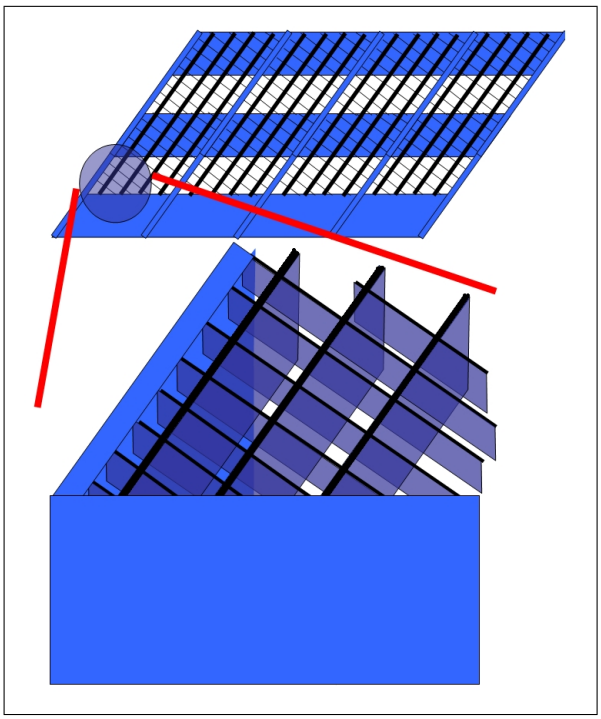

Figure 5.8: Freestanding grating structure. The 240 nm pitch grating is stabilized by an 11 μm pitch grating. The whole structure is supported by a 500 μm deep bulk silicon mesh of 150 μm wide lines on a 1 mm pitch.

The three critical steps in this process are the through-wafer handle layer etch that

stops on the BOX, removal of the BOX, and the grating etch itself. The considerations to develop an integrated process that is compatible among these critical steps are detailed below.

5.3.3.1 Grating Lithography

The grating lithography has in the past been accomplished with laser interference patterning of photoresist (*van Beek et al.*, 1998; *Canizares et al.*, 2005). Though this is a wafer-scale process, it requires careful optical matching of a multi-layer stack of materials and the resultant patterned material does not have the selectivity necessary to withstand a deep grating etch.

A similar pattern density is achievable with single-layer nanoimprint lithography, facilitating a liftoff process. The advantages of a liftoff process are twofold. It allows separate patterning of a fine-grain grating and a 90° crossed stabilization grating as detailed above, and the metal deposition step automatically plugs flaws in the lithography process.

To enhance resist adhesion to the silicon substrate, a three to five nanometer chromium layer is deposited by an Enerjet e-beam evaporator. This is removed by a 30 second plasma etch after the aluminum pattern is complete. For the fine grating a thin resist layer (140 nm) and shallow mold (90 nm) result in very easy mold release after imprinting and an easily removable residual layer of 60-70 nm. For the crossed grating a thicker resist (350 nm) and very low duty cycle mold result in equal ease of separation, and thicker shadow-evaporations enable longer residual etches.

A simple conservation of mass equation can be used for rough calculations of resist residual layer thickness: $r = h - d\left(\frac{o}{p}\right)$, where r is the residual thickness, h is the height (thickness) of the initial resist, d is the depth of the mold, o is the open area of the mold (i.e. line width of the imprinted sample), and p is the period. However, the layer thicknesses computed with this equation are often significantly different than

the reality, so the only accurate way to determine residual layer thickness is by taking a SEM image of a cleaved dummy sample.

Before arriving at the two-stage grating lithography, attempts were made to use a single, 2-D grating lithography step. Though a mold was successfully created, it did not result in a viable process. The reason for this is that shadow-evaporation did not function as expected with the 2-D imprinted features. Shadow-evaporation at 90° to the main grating direction will deposit metal along the crosshatched support lines. However, shadow-masking at 45° rather than 90°, with a shadow-angle of >70° was expected to use the resist pillars themselves to mask the lines in both directions. Figure 5.9 shows the results, which were not the desired clean rectangles necessary for successful direct evaporation and liftoff. Thus, this process was replaced.

5.3.3.2 Grating Etch

The most challenging task in creating the grating structure is etching the densely packed Si trenches with high aspect ratio and very smooth sidewalls. Characterization of a high aspect-ratio grating etch began with 2 μm half-pitch photolithographic features, then migrated to NIL at 350 nm half-pitch followed by 120 nm. Using an oxygen-rich DRIE process (*Kawata et al.*, 2006) as a starting point, a silicon etch recipe was developed on the STS tool for grating sidewalls with scalloping under 7 nm, as can be seen in Figure 5.10 (*Mukherjee et al.*, 2007). This etch recipe was used to fabricate a silicon grating with aspect ratio 8.5 and depth 1.27 μm . Figure 5.11 shows the process flow for this.

Further experimentation with etch parameters resulted in the following observations, which were valuable for maximization of etch rate and selectivity while maintaining straight sidewalls.

1. The ratio of etch time versus passivation time affects feature profiles (i.e. the verticality of the etched slits), but not scalloping. Overpassivation results in

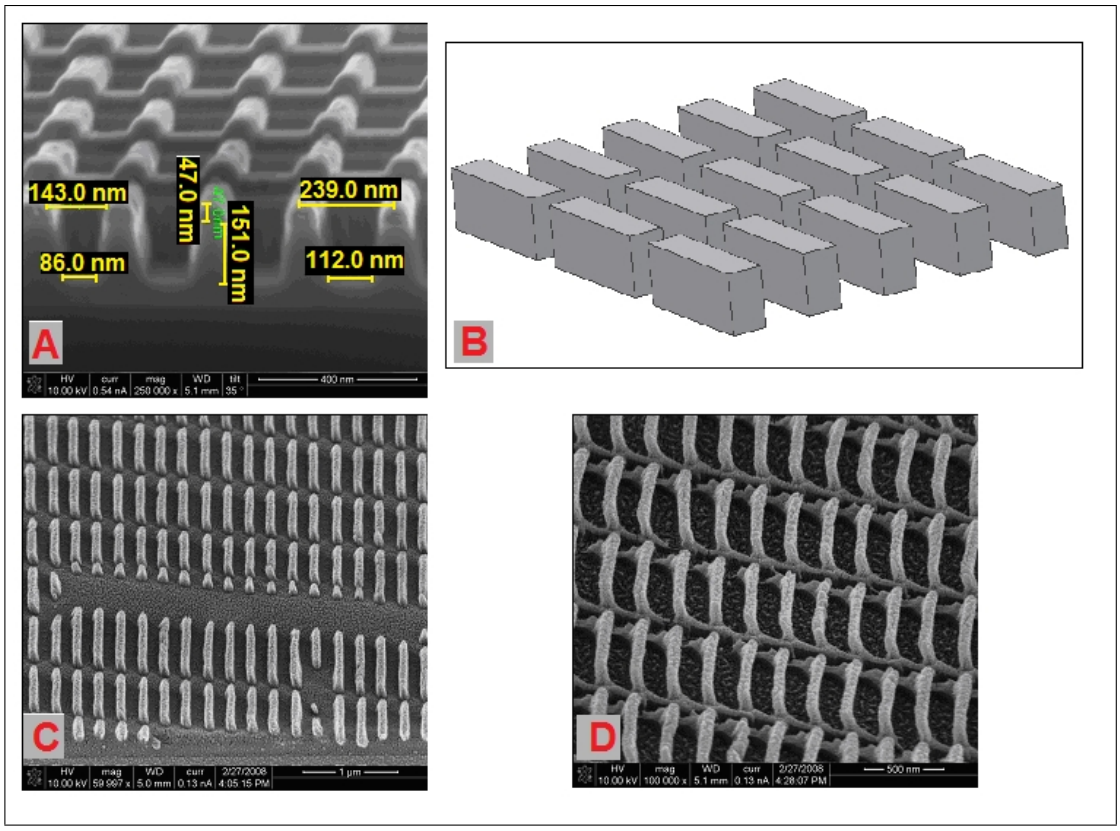

Figure 5.9: Crosshatched mold evaporation. A) SEM of the mold, with 240 nm pitch grating crosshatched with by a 700 nm pitch grating. B) Model of a view of resist pillars created with this mold, viewed at 45 degree rotation and shadow angle of 75°, such that the lines in both directions are occluded. After shadow-evaporation (C), metal is seen between the lines, and after residual etch (D) the pattern is not clean.

features narrowing toward the bottom since the etch fails to completely remove the passivation layer, and underpassivation results in widening features as the plasma etches past the passivation a little more each cycle.

2. Absolute gas pressures during etching affect feature profiles significantly since it is one of the primary determinants of chamber pressure, but scalloping is only minimally affected. During the etch step the amount of oxygen in the mixture determines the self-passivation rate (i.e. sidewall oxidation). The oxidation has a higher efficiency than the SF_6 etch. In addition, higher chamber pressure

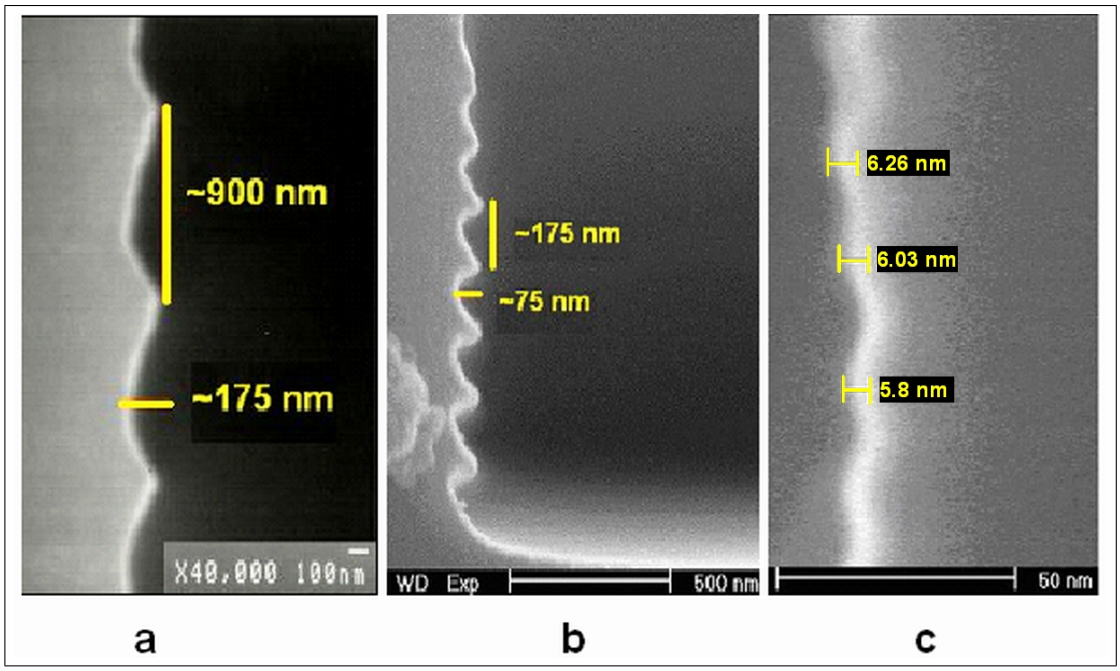

Figure 5.10: Reduction of scalloping from DRIE. Addition of oxygen and reduction of etch cycle time reduced both scalloping and etch rate. a) The standard Bosch process results in large, deep scallops. b) Initial tests with SF_6 + 60% O_2 etch chemistry reduced scalloping depth from 175 nm to 75 nm. c) Current process chemistry results in less than 7 nm scalloping over a vertical etch of 15 nm. Image from (*Mukherjee et al.*, 2007).

results in smaller mean free paths for the ions, and thus less control over the etch toward the bottom of the slits. So, for example, doubling both SF_6 and O_2 gas flow rates will result in overpassivation and features will narrow as they go deeper.

3. Gas ratio during etch affects scalloping, but not feature profiles. This is because the gas ratio determines the rate that the self-passivation is removed. An ideal gas mixture will self-passivate the sidewalls exactly as fast as it etches them to maintain smoothness but not overpassivate. The primary etching should be downward, not sideways. It should be noted that the gas ratio seems to primarily affect the bottom of the features (i.e., the portion immediately being etched) whereas absolute gas pressure and etch/passivation time ratio seem to

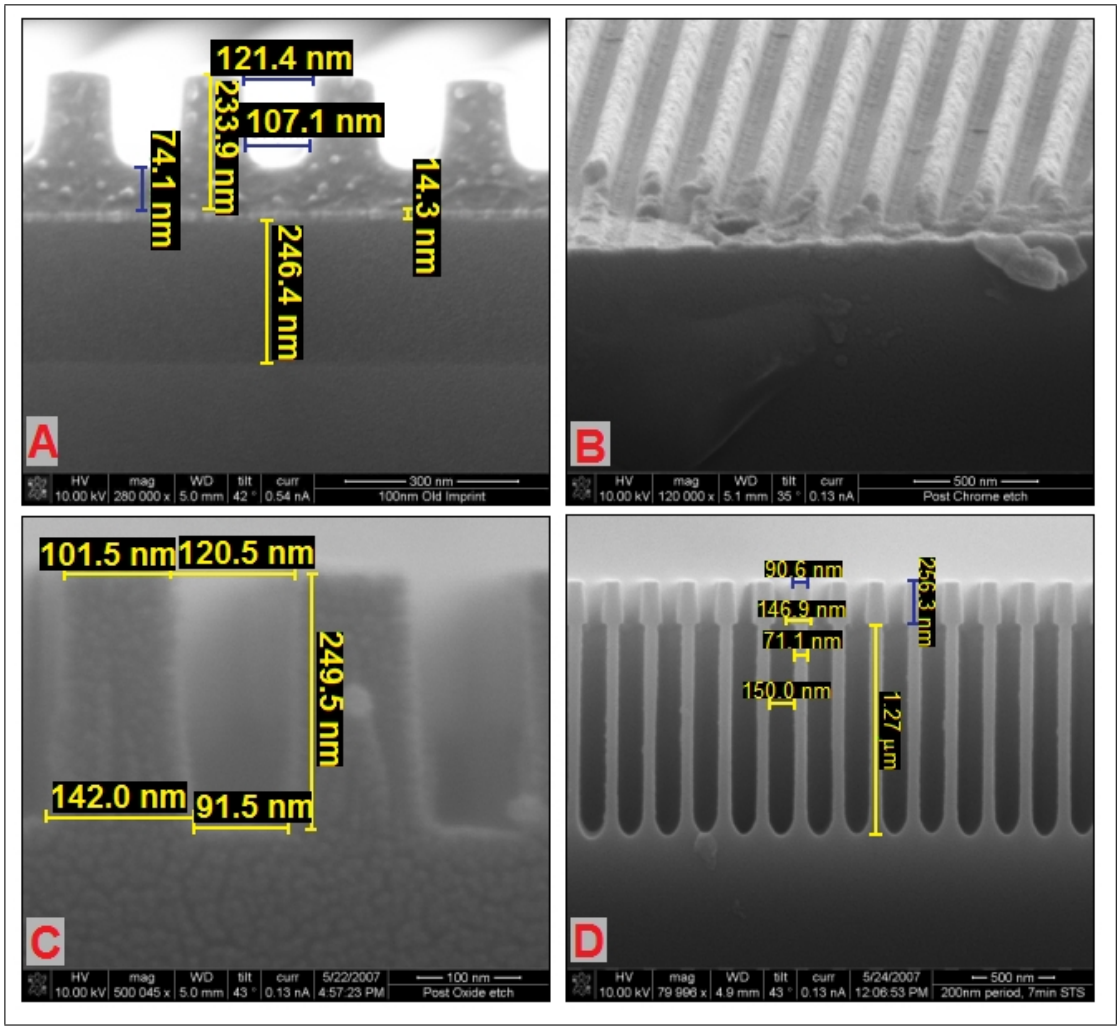

Figure 5.11: First successful Si DRIE grating. A silicon wafer with 250 nm thermal SiO_2, 15 nm evaporated Cr, and 200 nm mr-I 8030 resist was imprinted with a 240 nm period mold (A). Panel B shows the sample after a 2 minute residual layer etch (20 mT, 20 sccm O_2, 50 W) and 1 minute Cr etch (200 mT, 8 sccm O_2, 40 sccm Cl_2, 200 W). After this, the oxide was etched (20 mT, 20 sccm CHF_3, 150 W) for 11.7 minutes (C) and then the silicon was etched for 7 minutes in the STS (D), resulting in 1.27 μm deep grating lines (etch rate: 0.18 μm /min). The early 35 nm mask undercut widened the initial lines to 150 nm, leaving an aspect ratio of 8.5:1. The STS recipe used was: 50% APC, 0.7 mT base pressure, etch first; 9 seconds etch with 20 sccm SF_6, 80 sccm O_2, 550 W coil, 15 W platen; 12 second passivation with 100 sccm C_4F_8, 3 sccm SF_6, 500 W coil, 0 W platen. The SF_6 valve was left slightly open during passivation to keep it from sticking during the first few seconds of the etch phase. citepMukherjee07

affect the entire feature.

4. Absolute etch time per cycle affects scalloping; lower etch times per cycle result in smaller scallops.

5. The SF_6 valve must remain slightly open at all times, even during passivation, since otherwise the low flow during the etch stage results in the valve occasionally sticking between passivation and etch steps, causing non-deterministic etch profiles.

The mask undercut seen in Figure 5.11 resulted in significantly wider grating lines than intended, drastically reducing the projected ultraviolet (UV) blocking efficacy of the grating. The undercut was caused by an aggressive initial etch stage with no passivation layer to etch through, and positively-charged plasma ions embedding in the oxide hard-mask. The embedded ions caused a positive sheet charge that induced a negative mirror charge at the oxide/silicon interface. This negative charge acted on plasma ions inside the slits, pulling them toward the side-walls.

To minimize the undercut, the recipe was switched to a passivate-first mode with a higher percentage of the cycle spent on passivation, the SF_6 component of the etch chemistry was reduced by 40% (from 20 sccm to 12 sccm), and metal masks were tested to reduce or eliminate the mask charging effect. *Marty et al.* (2005) indicate that reduction of the platen voltage below the metal's sputtering threshold can result in successful masking of very high aspect ratio (depth-to-width ratio 107) nanostructures. Testing in the STS with chromium and nickel masks resulted in ubiquitous grassy silicon caused by sputtering and re-deposition of the masking metal even at very low (5 W) platen power, but aluminum masking was a success.

The most important change for undercut minimization was the reduction in SF_6, followed by the metal masking and the changes to passivation order and time fraction. In all, the undercut seen in Figure 5.11 was successfully removed. Figure 5.12

demonstrates the evolution of the mask undercut mitigation on oxide masks.

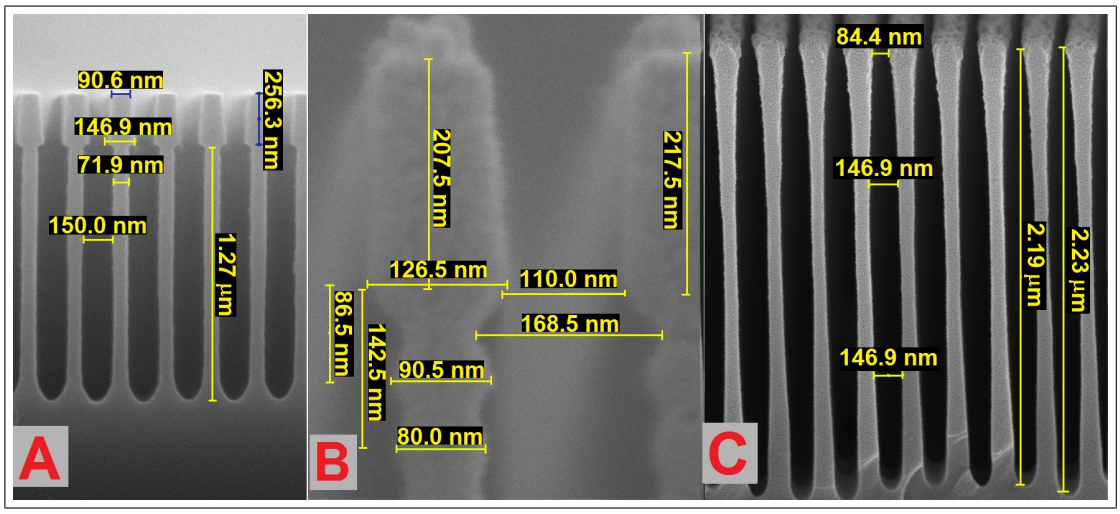

Figure 5.12: Mask undercut reduction. Oxide-masked samples. A) 20/80 sccm SF_6/O_2, 9/12 seconds etch/passivation, resulting in significant undercut; B) same as (A) with 5/10 second etch/passivation, undercut scalloping is less; C) 12/80 sccm SF_6/O_2, 5/10 second etch/passivation, minimal undercut, but lines bowed. Aspect ratio improves from 8.5 in (A) to 14.9 in (C). Etch rate of (A) and (B) is 0.18 μm /minute, but lower SF_6 flow for (C) drops the rate to 0.10 μm /minute.

Even without the mask undercut, the etched profiles initially showed significant concave bowing. Ramping down the passivation time for each cycle helped straighten out the bottom portion of the grating slits, but did not affect the bow in the middle. The solution to that was to lower the pressure in the STS etch chamber from 12 mT to 9 mT by opening the automatic pressure control (APC) butterfly valve from 50% to 65% (or 35% closed, as read by the tool). Opening the valve any further had no effect, nor did lowering the absolute gas flows by as much as 25%. The final etch chemistry is:

> *passivate*: 12 seconds ramped down by 0.1 second per minute of etch, 100 sccm C_4F_8, 3 sccm SF_6, 500 W coil power, 0 W platen bias power
>
> *etch*: 5 seconds, 12 sccm SF_6, 80 sccm O_2, 550 W coil power, 15 W platen bias power

passivate first, base pressure 0.7 mT, keep butterfly valve at 35%

Figure 5.13 shows the evolution of the bowing mitigation culminating in the final recipe, albeit on samples with remaining underlying substrate. One thing worth noting is that the final etch chemistry uses 2.9% SF_6 during the passivation cycle and only 13% during the etch. This is similar to other etch recipes that use SF_6+O_2 without gas chopping and find that higher percentages of SF_6 result in worse anisotropy (*Liang et al.*, 2004).

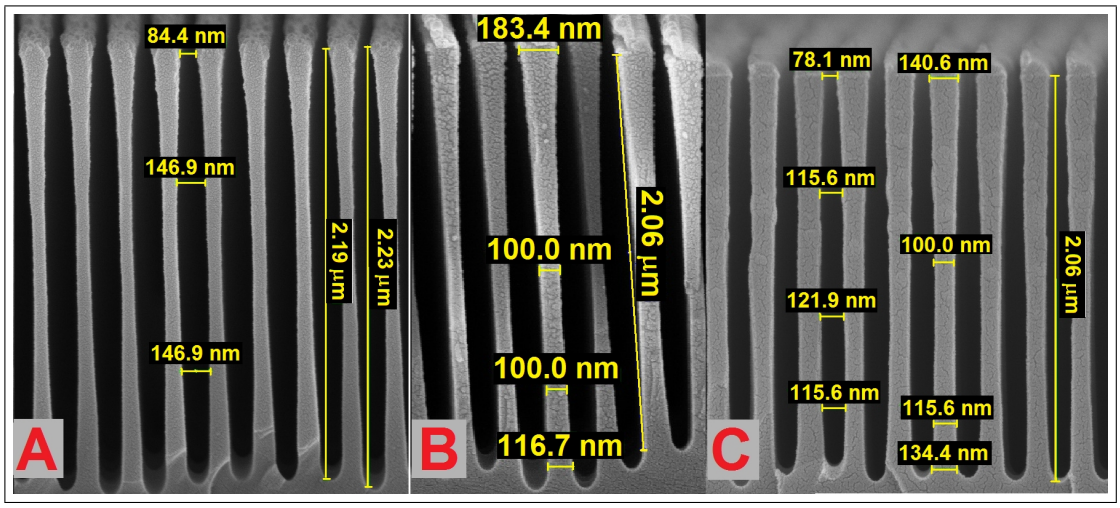

Figure 5.13: Front-side grating bow mitigation. A) Same as 5.12.A: 20 minute oxide-masked etch with 12/80 sccm SF_6/O_2, 5/10 second etch/passivation; B) 20-minute Al-masked etch with same chemistry as (A), ramping passivation time from 12 sec to 10 sec; C) 20-minute Al-masked etch same recipe as (B), butterfly valve at 35%, very minimal bowing. Aspect ratios range from 14.9 to 16.9 across this series.

Since DRIE uses relatively dense plasmas, a significant amount of heat is transfered from the plasma to the substrate. The STS tool utilizes an electrostatic chuck with helium cooling of the back side of the wafer, but for suspended structures there needs to be a thermal path to the bulk. The 150 μm support grating helps with this, but even that is suspended over the recess in the custom carrier wafer. To enable additional cooling, the grating etch was broken up into 2 minute segments separated by 5 minutes of cool-down.

5.3.3.3 Etch Step Order

A great deal of work went into the decision of which side of the wafer to etch first. Since a carrier wafer is required for chip processing in the STS tool, there are problems either way. If the handle layer is etched first, attachment to a carrier for the front-side DRIE will trap air in the etched gaps in the handle. Upon vacuum pump-down, this air would rapidly expand and burst the diaphragms. However, if the device layer is etched first, the grating would need to be protected for the remainder of the process, especially during the through-wafer etch and subsequent wet carrier separation. In addition to that, the bottom of the grating lines would be notched due to charging of the underlying BOX layer (*Ayón et al.*, 1999c).

For the case of the grating being etched first, a variety of wet through-wafer etch techniques were considered, but each had problems. One viable option is to use a chip carrier with a protected recess on one side and opening on the other, such that the etched grating is not touched by chemicals. Advanced Micromachining Tools GmBH[f] in Germany makes such carriers for either full wafers or chips. However, this would leave a single large, unsupported membrane with a compressive stress load from the BOX layer.

Doing the handle layer etch first—and doing it with DRIE—was deemed the best choice. The largest advantage provided by dry etching is that it allows a back-side support grating, which is essential for a large diaphragm. The supports also provide additional paths for thermal bleed from the suspended diaphragm during the grating etch. To avoid the problem of trapped air during the grating etch, a custom carrier wafer was designed with a recessed cavity and grooves to allow air in and out. Figure 5.14 shows schematics of the back-side support grating and the chip carrier.

After the through-wafer etch of the back-side support grating, the BOX removal provided an additional challenge. Removal of the BOX via BHF dip proved unsuc-

[f] http://www.ammt.de

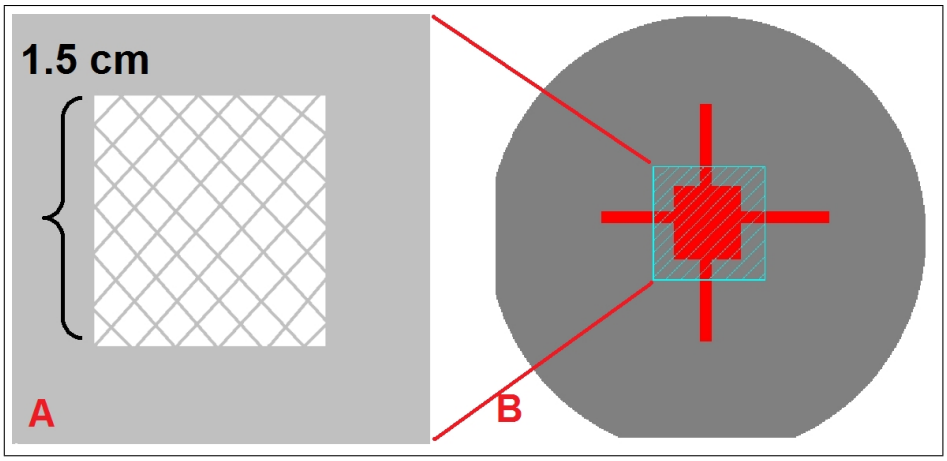

Figure 5.14: Schematics of back side support grating structure and grooved carrier wafer. A) Schematic of back side support grating. The support lines, at 45° to the fine-grain front-side gratings, are 150 μm wide with a period of 1 mm in both directions. B) Schematic of grooved carrier for vacuum processing after through-wafer etching. The red area is etched 70-100 μm deep, allowing air to flow freely underneath the sample (teal).

cessful since the surface tension of the liquid and the hydrophobic nature of the silicon sidewalls resulted in air bubble formation atop the structure, preventing BHF penetration to the BOX. Agitation was of some assistance, but could not be performed with vigor due to the fragility of the membranes. The solution to the bubble formation was pre-wetting of the sample with a low surface-tension liquid such as isopropanol. However, the wet etch step was deemed too dangerous to the membranes since many broke during either the etch or the post-etch clean.

Selective oxide etching using a CF_4+H_2 plasma was undertaken with some success. The free H and F ions combine to form HF, which etches oxide and leaves less free fluorine to etch the silicon. In addition, protective polymer formation by the plasma is primarily on the silicon while the oxygen in SiO_2 prevents the polymer from forming on that layer. Adding O_2 instead of H_2 to the CF_4 plasma will increase the silicon etch rate, since the C and O ions combine to form CO_2, leaving more free fluorine to etch silicon. This chemistry of this selective oxide etch resulted in unpredictable etch rates, and was thus abandoned despite its promise. Since the BOX layer is only 250

nm thick, a well-characterized oxide plasma etch was used with 3:1 selectivity over silicon, such that even a significant over-etch would not notably affect the 2000+ nm device layer.

The final challenge in the double-sided process was bonding and separation of the chip and the recessed carrier wafer shown in Figure 5.14B. Photoresist can not be used as a bonding agent since separation would require chemical processing such as an acetone dip, and wet steps after the grating etch can cause collapse of the freestanding grating lines. An additional factor is that the silicon carrier needs to be protected from the etch plasma due to chamber loading effects of the low SF_6 flow process.

A two-layer coating solved both problems. A 5 μm layer of PECVD oxynitride protects the carrier, and a 5 μm layer of photoresist prevents charging effects that may otherwise cause damage to the back side of the grating after breakthrough. The photoresist is hard-baked prior to application of the chip. A synthetic oil, perfluoropolyether (PFPE), is used to bond the chip to the carrier atop the photoresist. This provides suitable thermal contact and bond strength in the vertical direction. A single drop can be spread over the non-etched portion of the back side of the chip to bond it to the carrier, and separation is accomplished using a razor blade.

Figure 5.15 shows the final etched grating from the top. A nice feature of SEM imagery is that the acceleration voltage of the incident electrons determines their penetration depth, and thus the depth from which electrons can be scattered. This means that by upping the voltage, one can see deeper into the target. The inset of Figure 5.15 was taken with 30kV acceleration rather than 10kV, allowing the underlying backside support grating to be seen through the fine grating.

Figure 5.16 shows 45° cutaway views of the final grating. The grating was etched in three stages to ensure the etch proceeded correctly. The bowing problem from before has been completely resolved, and if anything the lines narrow toward the bottom. This can be resolved in future production by slightly more aggressive downward

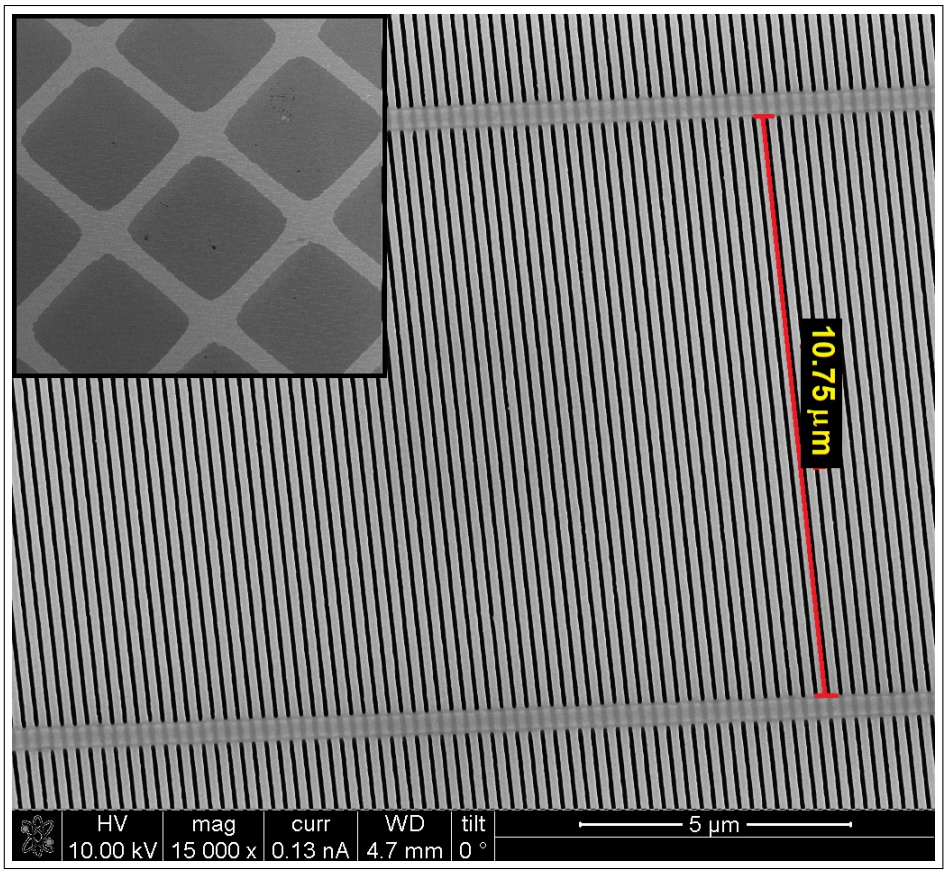

Figure 5.15: Top-view 15k magnified SEM image of the final etched grating. Slit length is 10.75 μm between the 90° stabilization grid lines. Inset: 65x magnification image of the backside support grating seen through the fine grating. Pinholes caused by the etch process are evident.

ramping of the passivation time as the etch proceeds.

5.4 Testing and Discussion

5.4.1 Test Setup and Results

Tests of the broadband optical transmission of the grating were performed with a xenon arc lamp for the UV (188–385 nm) and near IR (775–870 nm). The beam from the lamp was narrowed by an iris, then focused to a $\sim$ 3 mm point by a lens, and a second iris held the filter. A UV-Vis capable optical fiber was placed $\sim$ 7 mm from the filter to collect the transmitted light. The fiber led to a spectrometer with gratings

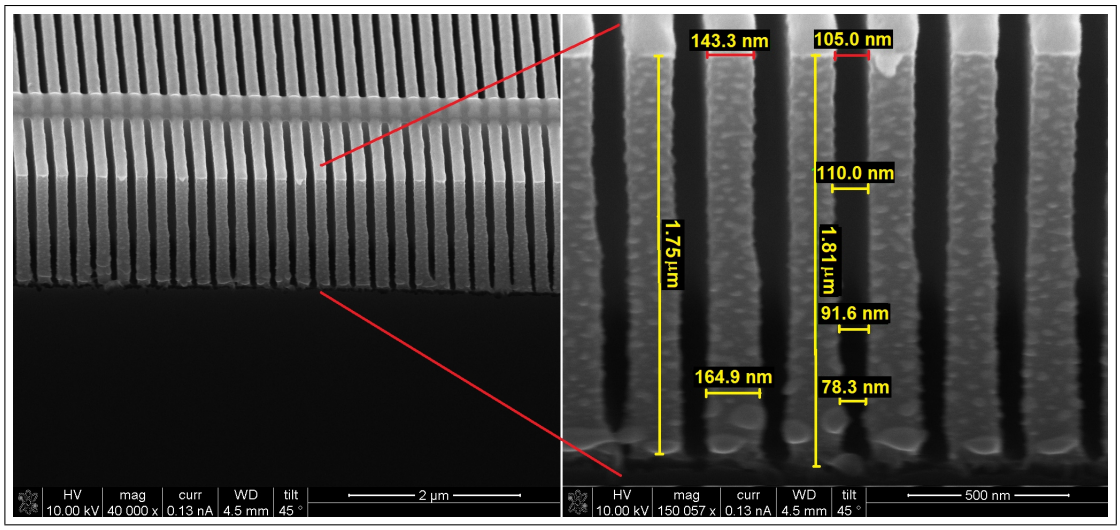

Figure 5.16: 45-degree angled SEM image of freestanding grating. The left image is at 40k magnification, showing the edge of a hole in the grating. The right image is a 150k zoom of the same section.

having 600 blazes per millimeter and peak sensitivity at 400 nm. The measurement integrated over 25 milliseconds and averaged 100 spectra over a boxcar smoothing of 10 bins. A filter was used to flatten the UV portion of the lamp's emitted spectrum, but the visible portion saturated the spectrometer and was not usable. A second measurement was taken without the filter, but most of the spectrum was saturated even at low beam power. One thing worth noting is that the beam intensity fluctuated over a time scale of approximately one to two minutes, so it was essential to take a reference spectrum, dark spectrum, and transmitted spectrum as quickly as possible.

A deuterium arc lamp was used to measure the visible portion of the spectrum (400–800 nm) and. This lamp setup used a microscope that collected light from a region $\sim$ 900 μm in diameter and fed it into a spectrometer with peak sensitivity at 800 nm. This measurement integrated over 15 milliseconds with the same averaging and smoothing as the xenon lamp measurement. The resultant composite spectrum can be seen in Figure 5.17.

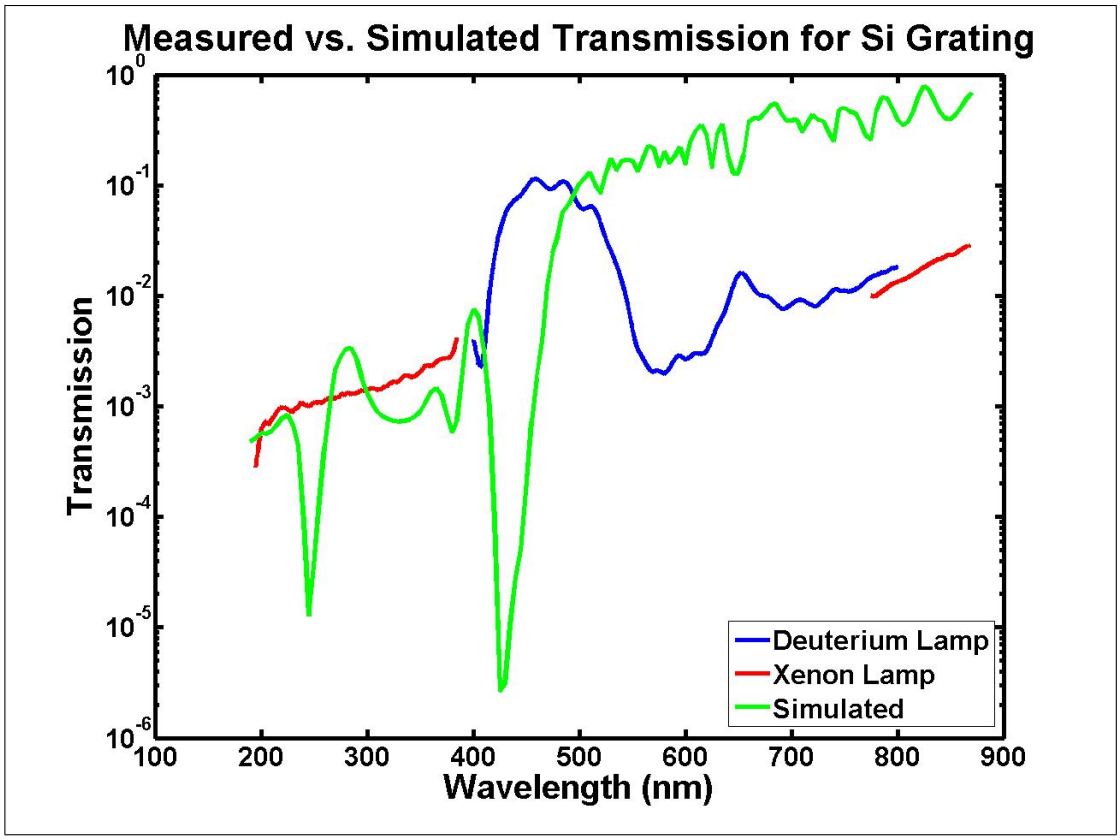

Figure 5.17: Broadband transmission through fabricated grating filter.

5.4.2 Discussion of Simulated and Measured Data

This fabricated grating is very promising. The measured transmission indicates that the UV is blocked with significant strength down to 195 nm. A strong positive result is that the measured transmission peak at 455 nm matches visible inspection; a white light source seen through the device has blue transmission. However, there are some obvious anomalies between the measured and simulated data. In particular, there are sharp transmission dips at 250 nm and 430 nm in the simulated data, and the transmission from 550 nm up is off by a factor of 100. These data anomalies will be addressed below.

The anomalous downward spikes in the simulated distribution have a variety of sources. To examine them in detail it is necessary to decouple the transverse electric

(TE) and transverse magnetic (TM) modes. Figure 5.18 shows the transmission of both modes and the total transmission through the grating, with the addition of 70 nm Al on the surface. One immediately noteworthy result is that the transmission drops to around the measured value at 800 nm as a result of the Al addition. The region of 550-800 nm still needs explanation, though.

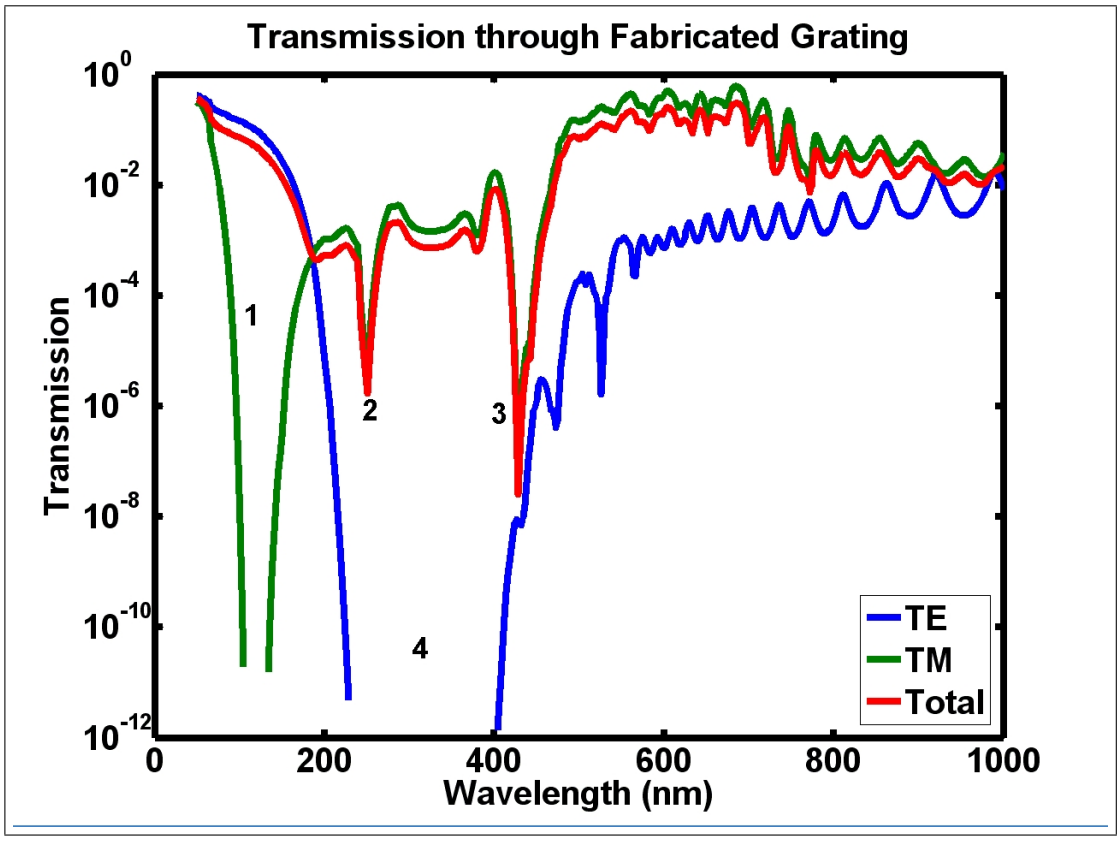

Figure 5.18: Simulated TE and TM broadband transmission through fabricated grating filter. The peaks are labeled for subsequent reference.

The first sharp drop in simulated TM transmission (Location 1 in Figure 5.18) is completely canceled out by the rise of the TE mode, and also beyond the range of the measurement spectrometer. However, the TM drops at 2 and 3 are within the same region as the strong TE drop 4, and thus their absence in the measured data require explanation. Location 2 is at 250 nm, which is very close to the period of the simulated grating. This transmission drop is entirely dominated by the TM mode. It

is caused by surface plasmon polaritons (SPP), which are "localized electromagnetic waves at a dielectric-metal interface, formed by a single evanescent plane-wave on the dielectric side of the interface, and a single inhomogeneous plane-wave on the metal side." (*Raether*, 1988) They are caused by excitation near the entrance aperture of a metallic slitted grating, and carry energy tangential to the surface, thus reducing transmitted intensity. These are normally only studied in metals due to very sharp changes in transmission, but a semiconductor has enough free carriers to create a similar effect.

The SPP is associated with another phenomenon called the Wood Anomaly (*Wood*, 1902, 1935), which results in a sharp rise in transmitted intensity. The coupling betweeen these two grating phenomena is not fully understood as yet (*Kihm et al.*, 2005; *Xie et al.*, 2006a,b). Section 4 of *Xie et al.* (2006b) says that "the SPP anomaly occurs when a diffracted order m acquires the SPP wavelength of $\lambda_0/Re\left[n_{spp}\right]$, where $n_{spp} = \sqrt{\epsilon_m \epsilon_d / \left(\epsilon_m + \epsilon_d\right)}$." ϵ_m and ϵ_d are defined respectively as the complex dielectric constants of the metal (or in this case semiconductor) and the dielectric (in this case 1.0 for free space). Thus, θ_{Wood} and θ_{spp} are:

$$\begin{aligned} sin\left(\theta_{Wood}\right) + m\left(\lambda_0/p\right) &= \pm 1 \\ sin\left(\theta_{spp}\right) + m\left(\lambda_0/p\right) &= \pm Re\left[n_{spp}\right] \end{aligned} \tag{5.1}$$

where λ_0 is the wavelength of incoming light, m is an integer, p is the grating period, and n_{spp} is the complex index of refraction of the SPP.

The same simulation as in Figure 5.18 was performed with the incident light at 0, 5, and 10 degrees, and the results are shown in Figure 5.19. As the figure shows, for m=1 in all cases the SPP dip is preceded by a sharp rise in transmission at the Wood Anomaly location. Aside from the difference in peak sharpness, this matches

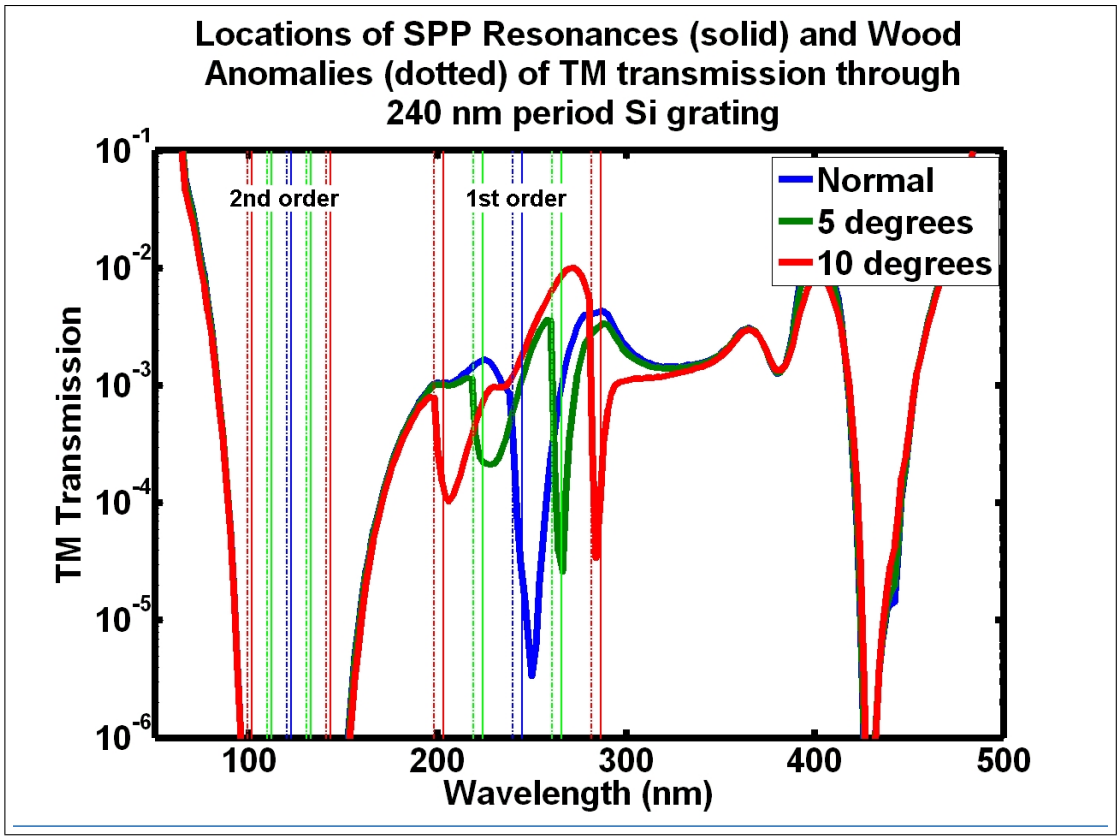

Figure 5.19: Predicted wavelengths for surface plasmon polariton resonance and Wood's Anomaly for TM light incident at 0, 5, and 10 degrees on a 240 nm period Si grating. The solid vertical lines are the predicted locations of the SPP, and the dotted lines correspond to Wood's Anomaly, both using Eqs. 5.1.

the infrared results that *Xie et al.* (2006a) obtained for silver. The peaks and dips in a silicon spectrum are not nearly as sharp as they are in the case of a metal because silicon's dielectric constant is changing fairly rapidly over the full spectrum, resulting in wider anomalous regions. This is also why the locations are not quite perfect, since Equations 5.1 were intended for use with a metal. However, within these limits the match is quite good, and the bifurcation of the peak caused by non-normal light incidence is very clearly seen. Since the light source used in the testing was not fully collimated, the SPP resonance and Wood anomaly would not be in one specific set of wavelengths, and thus the angular variance of the incident light results in a smoother

measured distribution. All of the m=2 locations fall within the sharp drop at location 1, as expected.

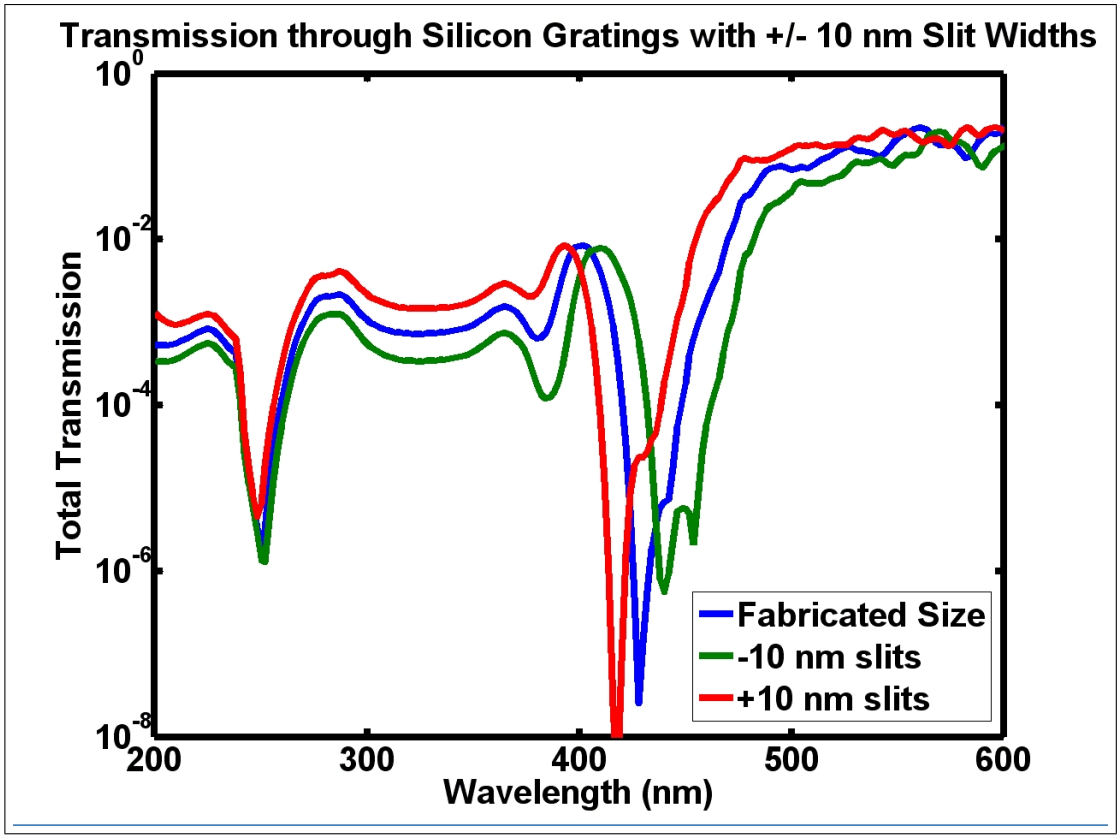

Figure 5.20: Simulated effect of slight slit-width variation on broadband transmission through fabricated grating.

The dip at location 3 from Figure 5.18 is not caused by SPP or Wood's Anomaly since the wavelength is significantly larger than the period rather than the period divided by an integer. Thus, changing the angle of incident light does not have much effect on this feature, as seen in Figure 5.19. However, this feature is very sensitive to slit width and the refractive index of the matial, neither of which affect the SPP location much, as shown in Figures 5.20 and 5.21.

The slit width can vary significantly from slit to slit due to plasma uniformities during the etch process. In addition, there are small line drop-outs scattered over the surface. These are not considered on the same level as the larger pinholes because

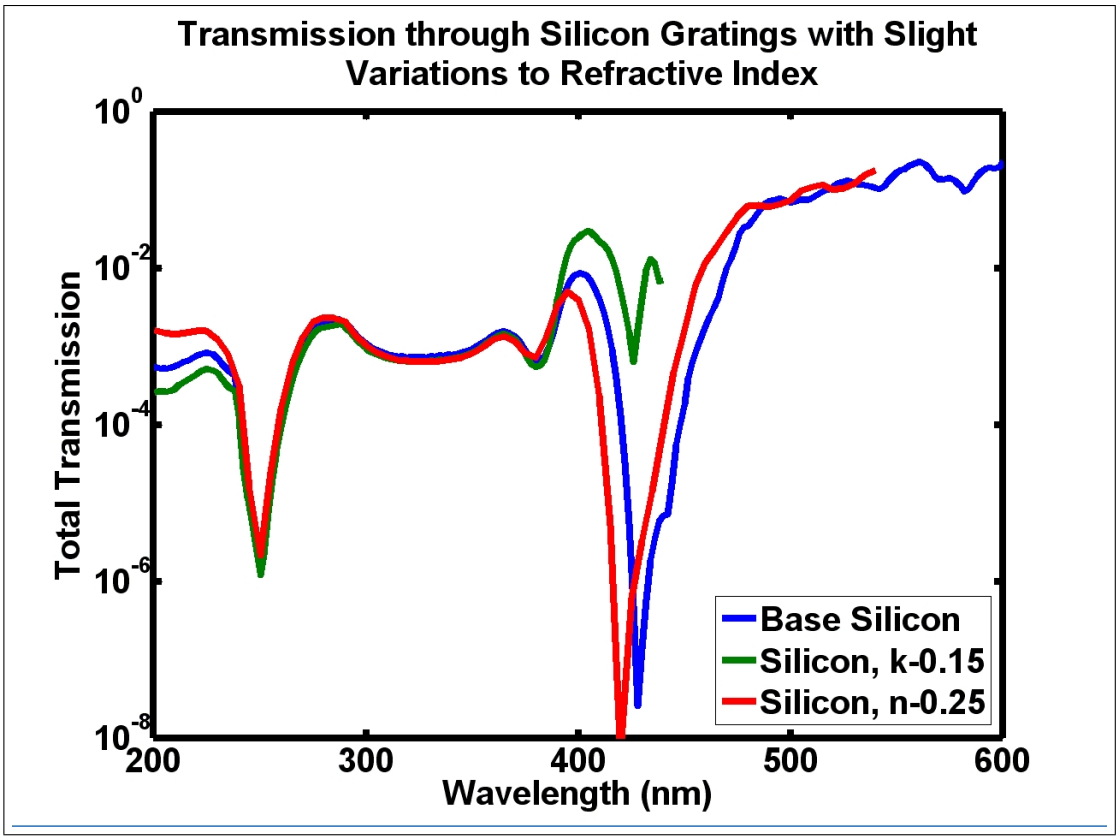

Figure 5.21: Simulated effect of slight refractive index variation on broadband transmission through fabricated grating.

they only affect a region of a few hundred nanometers, but are not uncommon and can smooth out this anomaly region. The plasma process can also change the index of the material, primarily through doping effects. As shown in Figure 5.21, changing the absorptive portion of the refractive index (k) has a much larger effect than changing the real portion (n). Simulations using different materials for the grating still had the SPP dip at 250 nm, but the location of the #3 dip varied significantly between gratings made of metal, semiconductor, and dielectic material.

The prior mentioned effects serve to smooth out the transmitted spectrum such that the two spikes of interest disappear, as in the measured data. Figure 5.22 demonstrates this clearly by averaging over variations from Figures 5.19-5.21. Those variations were chosen simply to demonstrate the effects, but are definitely within

the realm of possible variations within the tool and measurement apparatus.

The dip in measured transmission above 600 nm in Figure 5.17 is partially caused by the residual aluminum mask lines on the surface of the grating structure. Addition of a 70 nm Al layer in subsequent simulations resulted in a significant drop in simulated transmission around 800 nm, as seen in Figure 5.22, bringing it into line with measured data. The difference between measured and simulated data at 600-800 nm is caused by geometric effects such as slight variations in the periodicity of the grating and sidewall roughness. Since the visible portion of the spectrum would be very strongly blocked in a real instrument by the measurement microchannel plate (MCP) (*Herrero*, 1992), this region is of less concern than the UV spikes explained above.

One noteworthy design constraint discovered in the above analysis is that it is important to avoid building gratings with a period close to an integer multiple of the wavelength intended to be blocked. While creation of a grating with perfect geometry might allow strong blocking of the target wavelength by the SPP effect, the above-mentioned uncertainties in fabrication and measurement configuration make it equally likely that the target wavelength would land in the Wood Anomaly region of enhanced transmission.

This design space is further complicated by the fact that below 200 nm the SPP resonance for silicon is not determined solely by incidence angle and grating period, but also by effects unique to the material. Figure 5.23 shows that while a change in incidence angle or period results in easily-predicted resonances, the wide variation in n_{spp} below 200 nm cause rapid changes in the SPP resonance wavelength that need to be taken into account. Coating of the grating sidewalls with an ALD metal layer would of course result in much sharper, easily predicted anomaly regions, and thus provide easier control of where the anomalies lie, but for a grating intended to block 121 nm light it would still be better to use a grating with a periodicity of, for example,

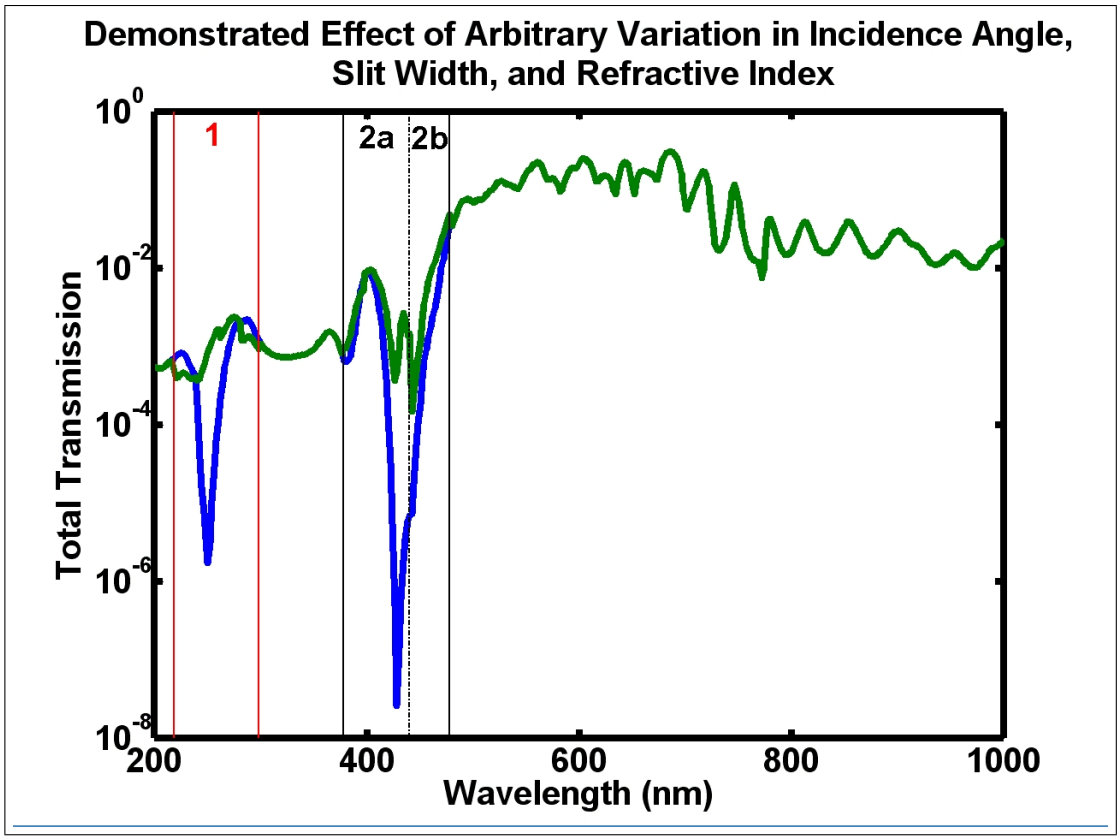

Figure 5.22: Aggregate effects of simulated variations in incidence angle, slit width, and refractive index on broadband transmission through fabricated grating. The blue line is the total transmission from Figure 5.18 used as a reference. The green line in region 1 is averaged over light incident at 0, 5, and 10 degrees as in Figure 5.19. In region 2a it is averaged over slits ±10 nm from the default and refractive index variance, specifically reduction of n by 0.25, and reduction of k by 0.15. Region 2b is the same as 2a without the k reduction, since that would reduce k below 0.

190 or 280 nm in order to better control the location of the second-order resonance peak (Location 1 in Figure 5.18, 2nd order in Figure 5.19).

5.4.3 Discussion of Grating Functionality and Design

This type of grating is a significant step forward for neutral spectroscopy. There are some important differences between doing UV filtering with gold gratings such as those used on Medium Energy Neutral Atom (MENA) and using a silicon structure. The most important difference is that the silicon structure is self-supporting without

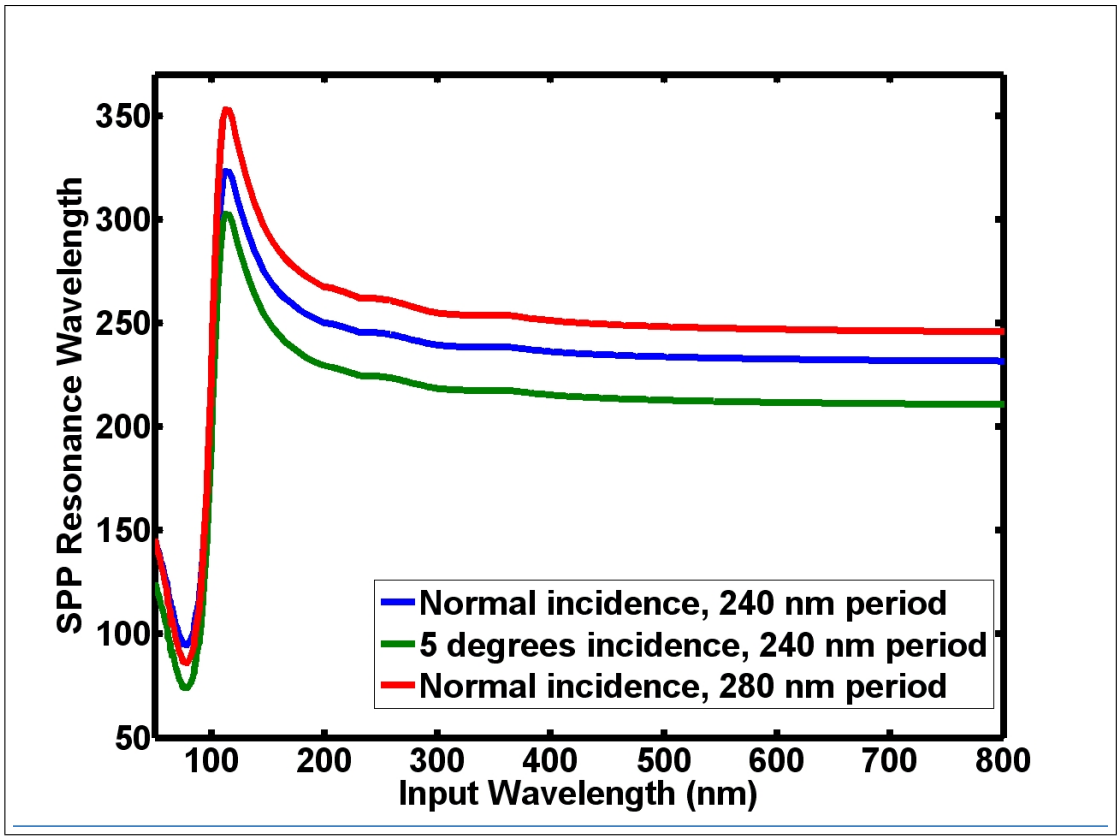

Figure 5.23: SPP resonance wavelength as a function of input wavelength, and effects of varying periodicity and incidence angle. Below 200 nm the SPP wavelength is not trivially determined. Changing incidence angle or grating period does not change this effect, since it is based on the material properties of silicon.

need for further nickel supports or glued-on handles. The grating is a self-contained, self-supported chip with a wide handle region that can be used to attach it to an instrument. In addition, the silicon grating's lack of a need for elaborate support grating structure results in a much wider open area than the gold grating, 20% compared to 10% even after application of the proposed ALD coatings, which should let a much larger number of particles through. Silicon has a much higher heat tolerance than gold. Conformally coated oxide and/or metal layers could experience thermal stress due to expansion coefficient mismatch at high temperatures, deforming the structure or delaminating the layers, but since the stress is experienced on both sides

of grating lines it should cancel out.

In addition, the technique applied above can be used to create gratings with even higher aspect ratio if desired, resulting in even better blockage of UV. The gold technique was limited by the mechanical strength of the metal, and the grating lines became wavy if the depth was increased (*van Beek et al.*, 1998). The variable depth of the silicon technique, the ability to add conformal layers to tailor the optical properties and aspect ratio, and the additional depth serving as a conversion surface all make the silicon technique more adaptable than the gold technique. However, the electroplating of the gold technique allows for plugging of fabrication holes with much more ease than the silicon technique. In the case of silicon, the liftoff process used for patterning the grating automatically plugs flaws caused by resist adhesion to the mold, but flaws caused by the plasma etching process are more difficult to address and could seriously limit the efficacy of the grating. After ALD coating with a metal layer, it should be possible to use a similar technique as that used by the Massachusetts Institute of Technology (MIT) group to plug the pinholes, which uses the grating itself as a mask for standard photolithography and electroplating to plug the open areas.

CHAPTER VI

Conclusions and Future Work

6.1 Conclusions

This dissertation has covered the modeling of near-solar populations of dust, neutral atoms, and pickup ions, the design and simple simulation of an instrument to measure those populations, and the design, fabrication, and test of a critical component of such an instrument. The major successes achieved include a demonstration that pickup ion generation may peak far closer to the Sun than formerly expected, and the fabrication and analysis of the first freestanding, self-supported silicon nanofilter.

Chapter I introduced the Sun and solar environment, including the solar wind, dust populations, and pickup ions. It then introduced space plasma instrumentation, concentrating on the various parts of standard instruments with a particular focus on light traps and instrument miniaturization. A few as-yet unanswered questions were introduced in Section 1.2.4. The remainder of this dissertation is the creation of tools to help answer those questions.

In Chapter II a new model of near-solar pickup ions (inner source) proved that they play a more important role close to the Sun than previously thought. The parameterized inputs of this model allowed the prediction of a wide variety of potential radial distributions of dust, neutral atoms, and pickup ions, and adiabatic models were used both to select the most likely distribution and to demonstrate that the neutrals

are ionized and picked up far closer to the Sun than expected. The reason for this is higher than expected pickup thermal speed caused by the azimuthal velocity of the neutrals' dust source, and the scattering caused by Alfvén waves in the sub-Alfvénic near-solar region.

This additional pickup thermal speed requires more cooling range in order to match the measured data, which in turn implies the presence of neutrals and pickup ions near the Sun that can be directly measured. For that purpose, a neutral instrument meant to fly on the Solar Probe Plus mission was designed, and photon and particle fluxes calculated for the closest portion of Solar Probe's orbit. This set a constraint for a ultraviolet (UV) blocking filter of 10^6-10^7 rejection of solar UV compared to particles. This filter has utility for many applications other than measurement of space plasmas, such as X-ray diffraction, collimators, and UV polarizers.

Chapter III introduced the topic of micromachining, and Chapter IV modeled the optical transmission of uniform freestanding nanogratings. This modeling verified that the efficacy of a grating in blocking UV light depends not only on the grating geometry, but also the material or materials it is built with and the polarization of the incoming light. Pure gold gratings can strongly block transverse electric (TE) light, but not transverse magnetic (TM), and are mechanically flimsy. Silicon is the opposite in polarization preference, and far stronger as a mechanical material. The best gratings, however, are composites of multiple materials that can offset the weakness of any one material. Silicon gratings with a conformal coating of oxide and/or metal block *both* TE and TM light, and are possible to manufacture thanks to the emerging technology of atomic layer deposition (ALD).

Chapter V demonstrated the successful fabrication of the first freestanding, self-supported, high aspect ratio nanograting in bulk silicon. Patterning of the fine grating lines was accomplished with nanoimprint lithography (NIL), and deep-reactive ion etch (DRIE) was used for both bulk and grating etches. A process meeting all

the desired characteristics (§ 1.4.1) was designed after a comprehensive study of tool capabilities, mold configurations, and etch parameters. The slit widths of the fabricated grating are still not quite narrow enough for the target application, but the measured transmission of the grating in the UV between 200-250 nm is still on the order of $10^{-}4$.

6.2 Future Work

The model demonstrated in Chapter II is capable of handling a variety of solar wind models. The components of the model can be changed with relative ease. An interesting test of its capabilities would be to swap the analytical solar wind model with a complete magneto-hydrodynamic (MHD) model and see how the results compare. An important factor in doing so would be to make sure that all of the required inputs are available from the model in question, since using pieces of one model with pieces of another provide inconsistent results. It would also be interesting to swap the adiabatic cooling component with a more accurate cooling model such as that used by *Fahr* (2007).

Another good test would be to change the assumptions in the model, in particular the assumption of instantaneous isotropization of picked up ions. The hemispherical distributions modeled by *Schwadron* (1998) might be an alternative approach. Accurate modeling of a variety of different ions rather than just hydrogen will only be possible when measured data exist for use as a scaling standard and output comparitor. Generation of unscaled curves can be done for any ion, but without both a scaling factor and thermal velocity there would be no way to choose the most accurate. The same applies to models at non-ecliptic latitudes.

This model was meant to examine the effect of additional velocity components on the evolution of inner source pickup ions (PUI) distributions, which it successfully did. Addition of wave-particle interactions, stochastic acceleration, and the interaction of

PUIs with solar wind proton heating would bring this model into further agreement with state-of-the-art models and measurements. The distributions resulting from this model may be used as predictions for instruments intended for taking in-situ data close to the Sun, including possibly the instrument presented in Section 2.5 or some variation on that design. The evolution of this model, as with all others, will be a symbiotic process with the collection of further data.

The grating modeled in Chapter IV and fabricated in Chapter V is a significant step toward the realization of such an instrument, but it is as yet imperfect. It still needs to be tested for transmission in the far UV (50-200 nm), and likely does not meet the specifications arrived at in Section 2.5. The grating lines, shrinking from 105 nm to 70nm, are still not small enough to adequately block the Lyman-alpha (Ly-α), but that can be solved by an ALD coating of SiO_2, Al_2O_3, or Pt as demonstrated in Chapter IV. The oxide layer will have the added advantage of significantly increasing the absorption of energetic photons in the 50-150 nm wavelength band.

A thicker ALD coating of a metal, probably platinum, might enable the negative ionization of neutral atoms in transit through the slits due to the metal's surface electron cloud. These ionized atoms can then be accelerated and measured as detailed in Section 2.5. This would revolutionize neutral atom spectroscopy, since traditional methods involve far larger plates with grazing-angle incidence.

Another step toward perfecting the grating would be the plugging of the pinholes caused by the final grating etch. The pinholes caused by the lithography were automatically plugged by the liftoff process, as intended, but the plasma etch caused an unexpected second set of pinholes that, while only occupying on the order of 10^{-4} ($1/100^{th}$ of a percent) of the surface area, will yet be an upper limit on the efficacy of the grating. A grating such the one fabricated in Chapter V, with nominal attenuation of 10^{-4} and $G_{holes} = 10^{-4}$, would have a combined attenuation factor of 2×10^{-4}, so twice as times as much light gets through as would without the pinholes. This only

gets worse as the grating efficacy improves. A grating with nominal attenuation factor of 10^{-8} would, with the same 0.01% pinholes, have a combined attenuation factor of 1.0001×10^{-4}, which is totally dominated by the pinholes rather than the grating geometry. Thus, for any highly effective grating the pinholes must be plugged.

Whether or not the pinholes are plugged, a very interesting measurement would be the transmission of ions and neutral atoms through the grating, both in terms of measuring its geometric factor and for determining whether or not it does ionize neutral atoms, and to what extent. These measurements, while beyond the scope of this dissertation, are a critical test of the effectiveness of the grating for its intended application, and the obvious next step in furthering its development.

APPENDICES

APPENDIX A

Materials Information

The following pages contain optical data on a variety of materials ranging from metals (Au, Ag, Pt, Ni) to semiconductors (Si) to dielectrics (SiO_2, Si_3N_4, Al_2O_3). Each page has graphs for one material; the top graph is the complex refractive index (n, k) and the bottom graph is the transmission of broadband light from 50-1000 nm wavelength through a 100 nm solid sheet of the material. The optical constants were collected from E. Palik's Handbook of Optical Constants of Solids, Vol. I and II (*Palik*, 1985, 1991) and used as table-lookups for simulations in the Grating Solver Development Company's[a] GSolver package. The more complicated simulations in Chapter IV use the same materials data as that used for the following figures.

[a] http://www.gsolver.com

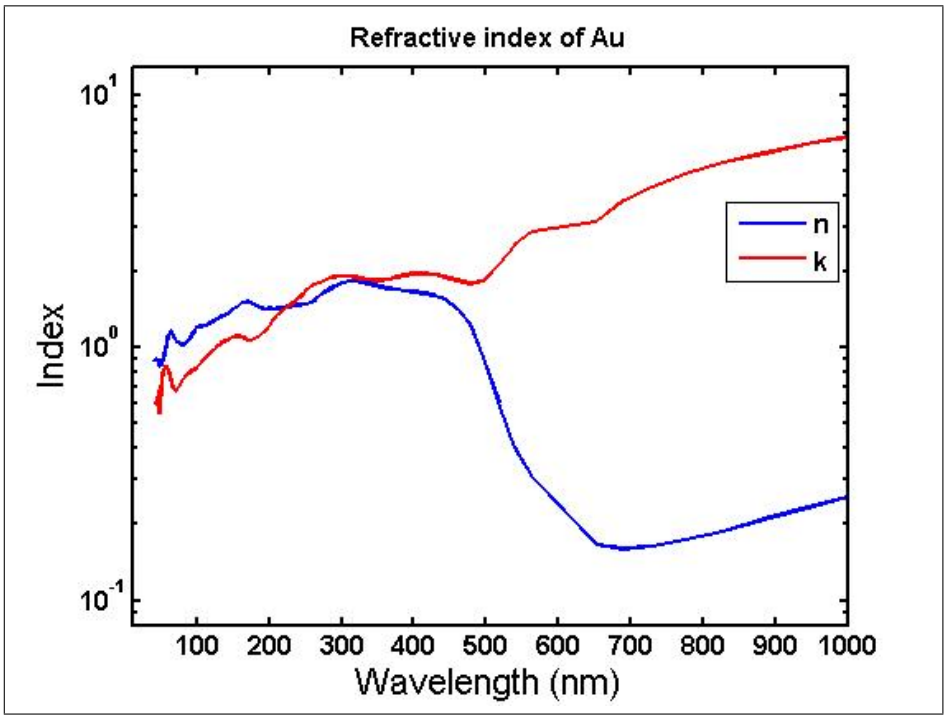

Figure A.1: Refractive indices for Au

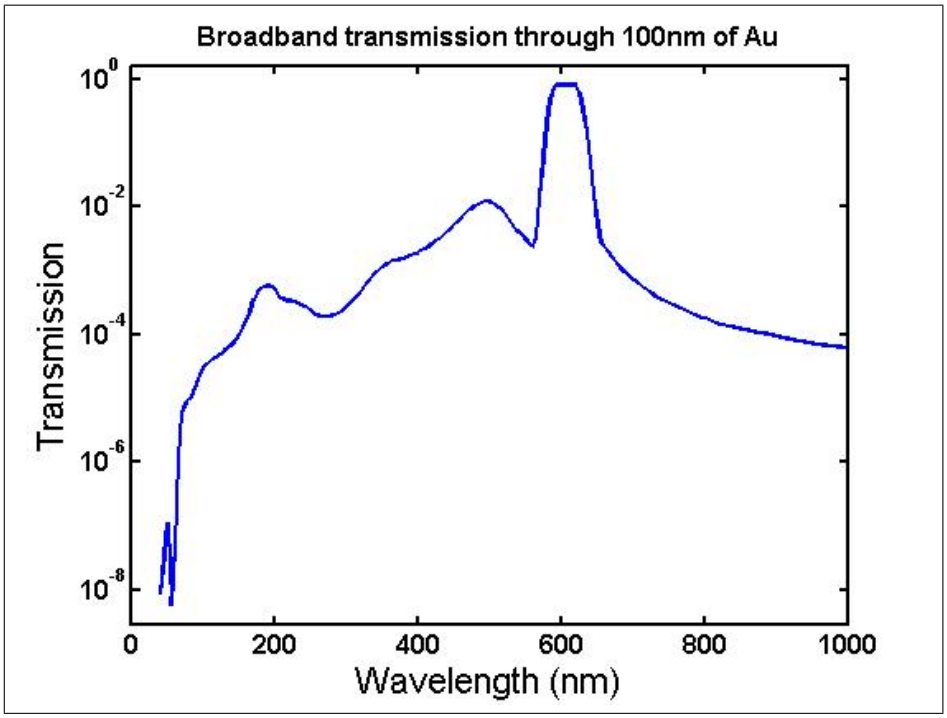

Figure A.2: Broadband transmission through 100nm of Au

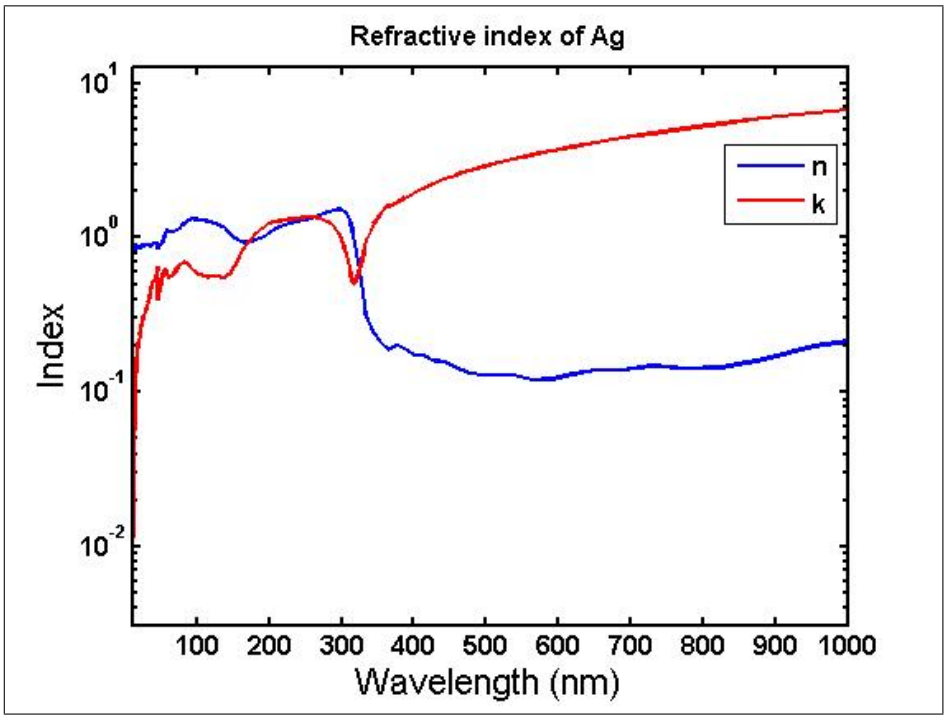

Figure A.3: Refractive indices for Ag

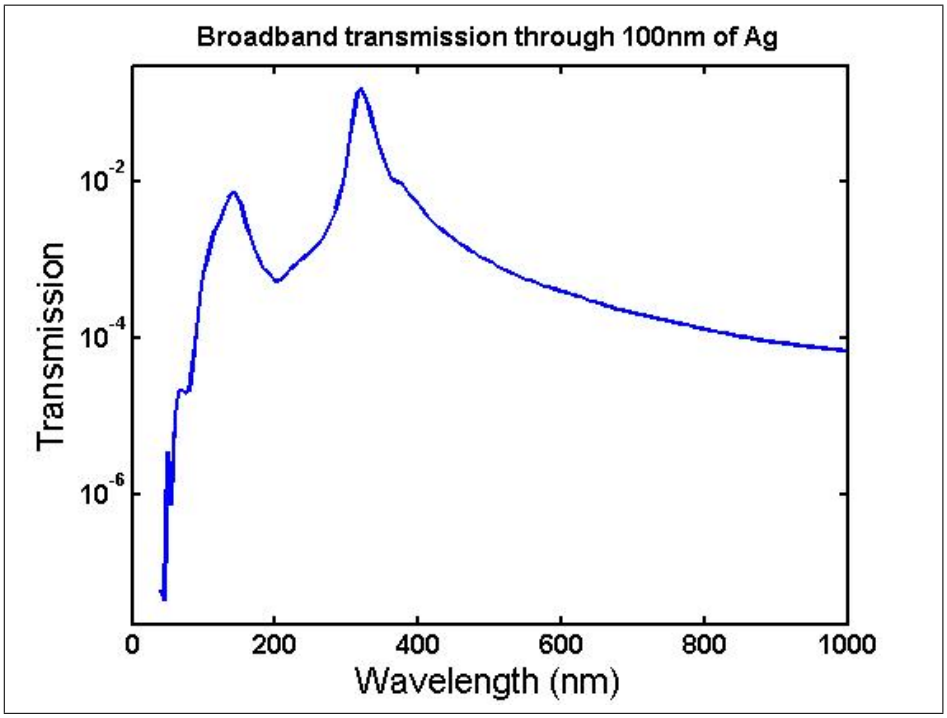

Figure A.4: Broadband transmission through 100nm of Ag

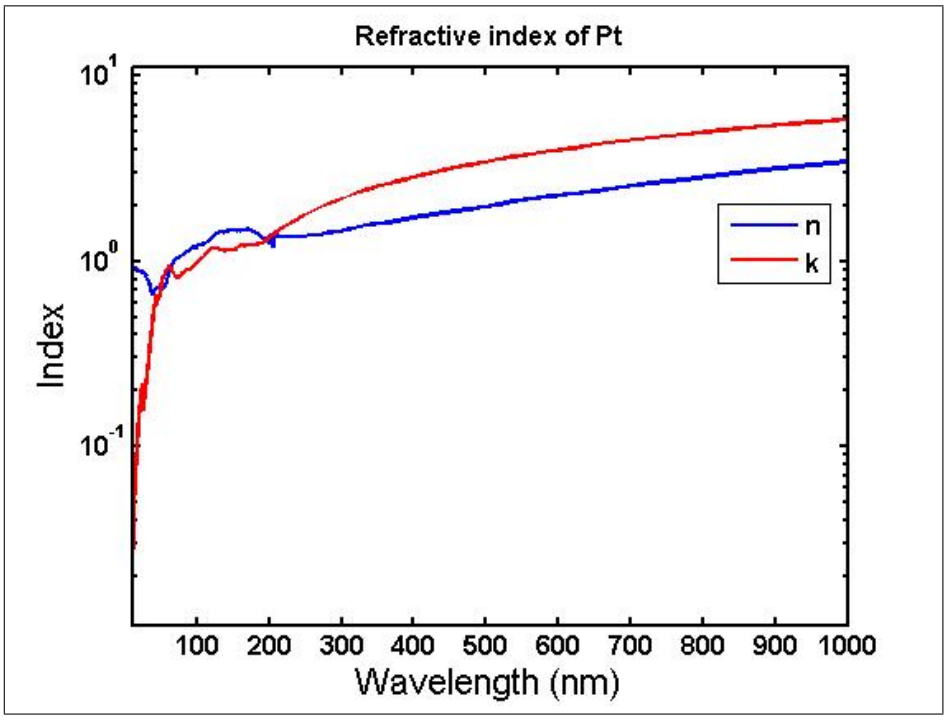

Figure A.5: Refractive indices for Pt

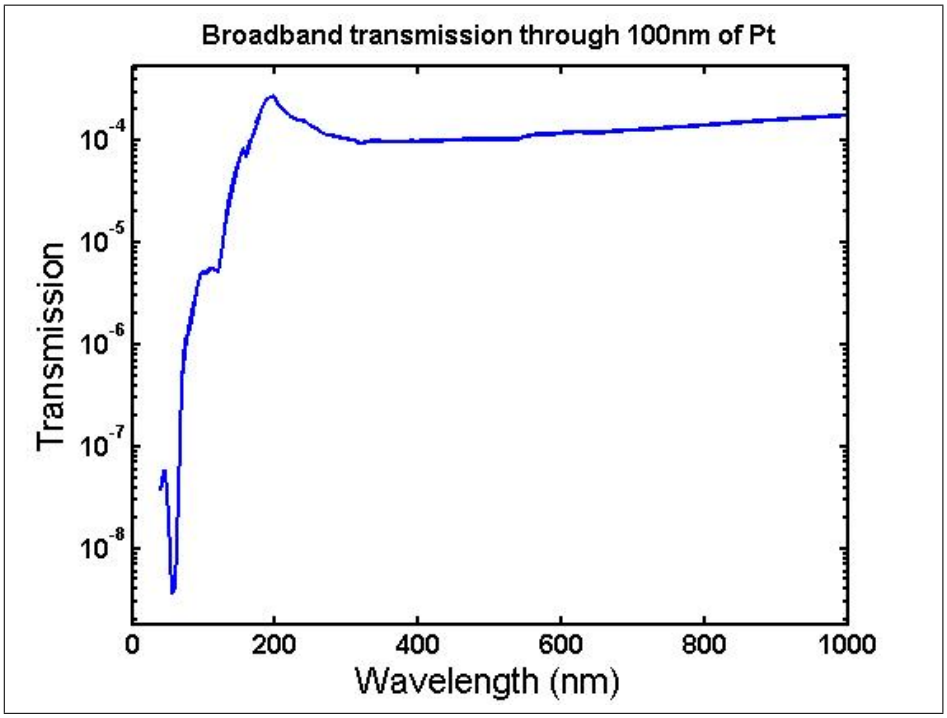

Figure A.6: Broadband transmission through 100nm of Pt

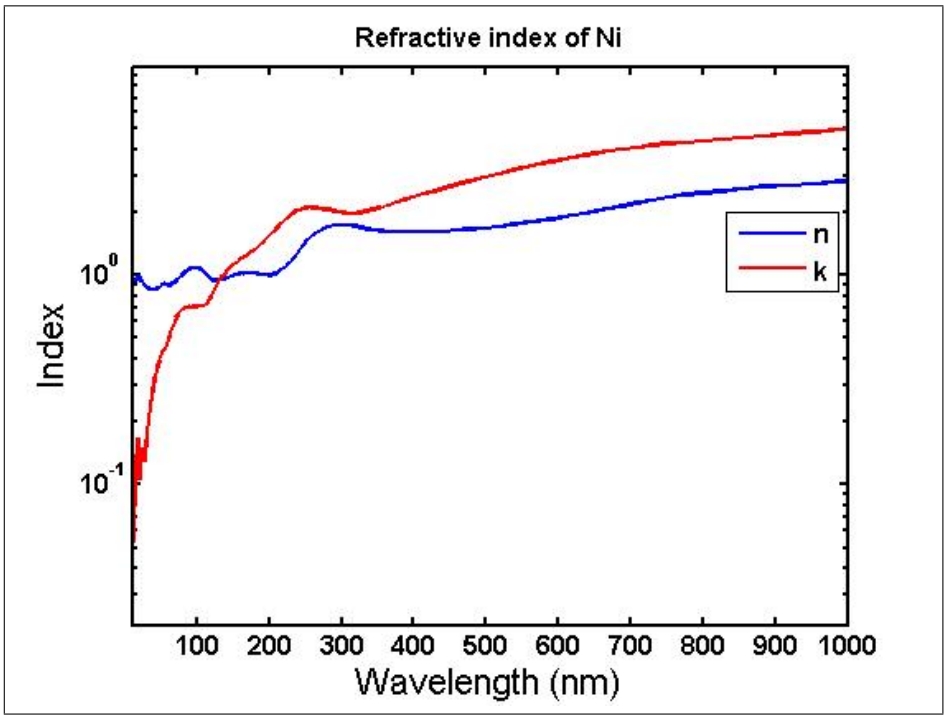

Figure A.7: Refractive indices for Ni

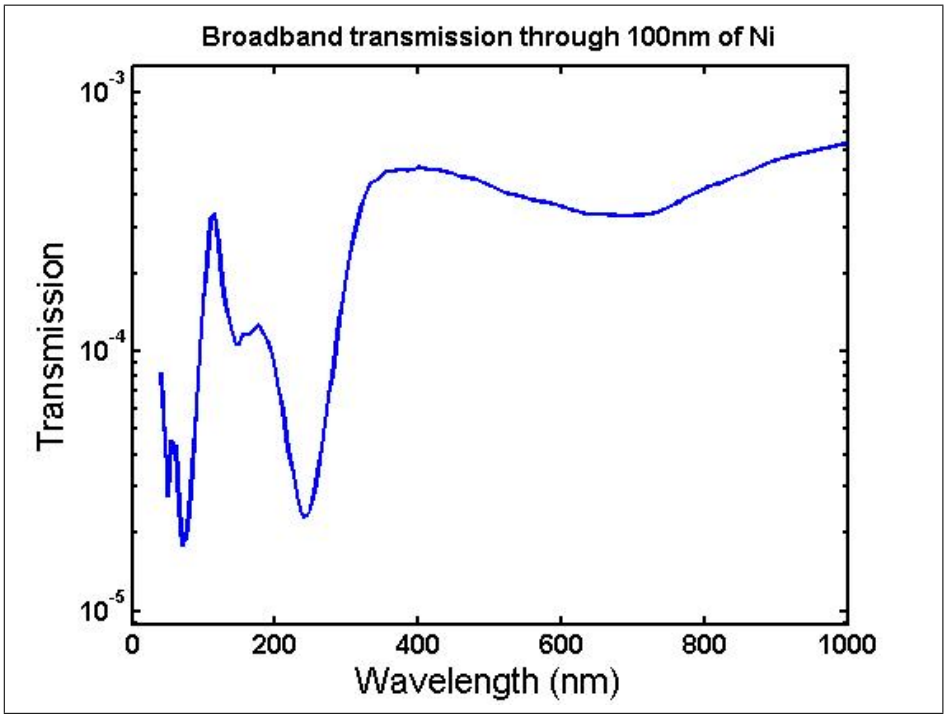

Figure A.8: Broadband transmission through 100nm of Ni

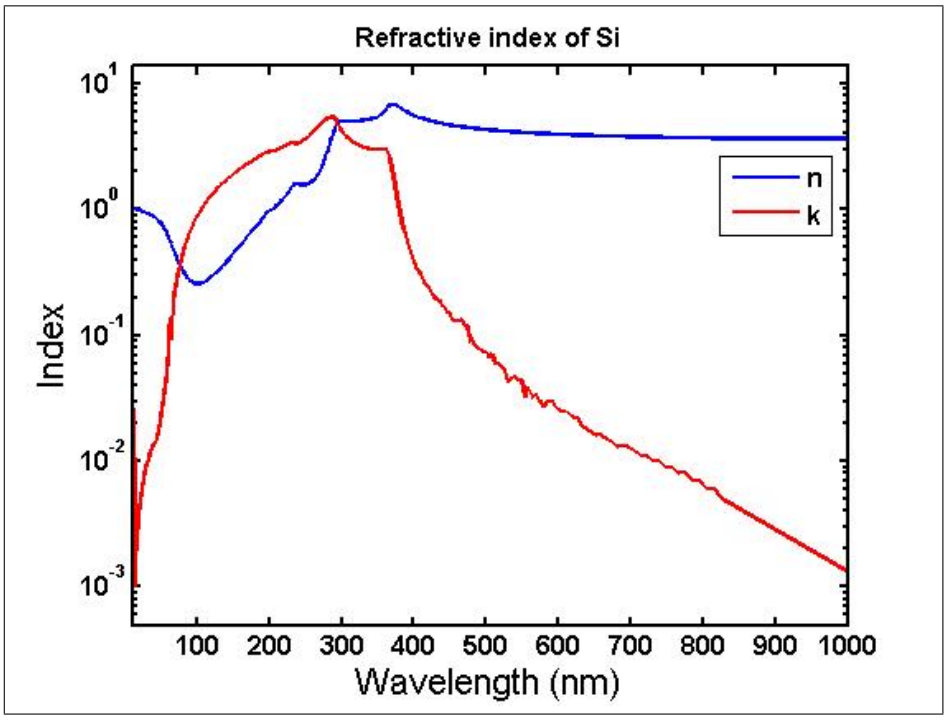

Figure A.9: Refractive indices for Si

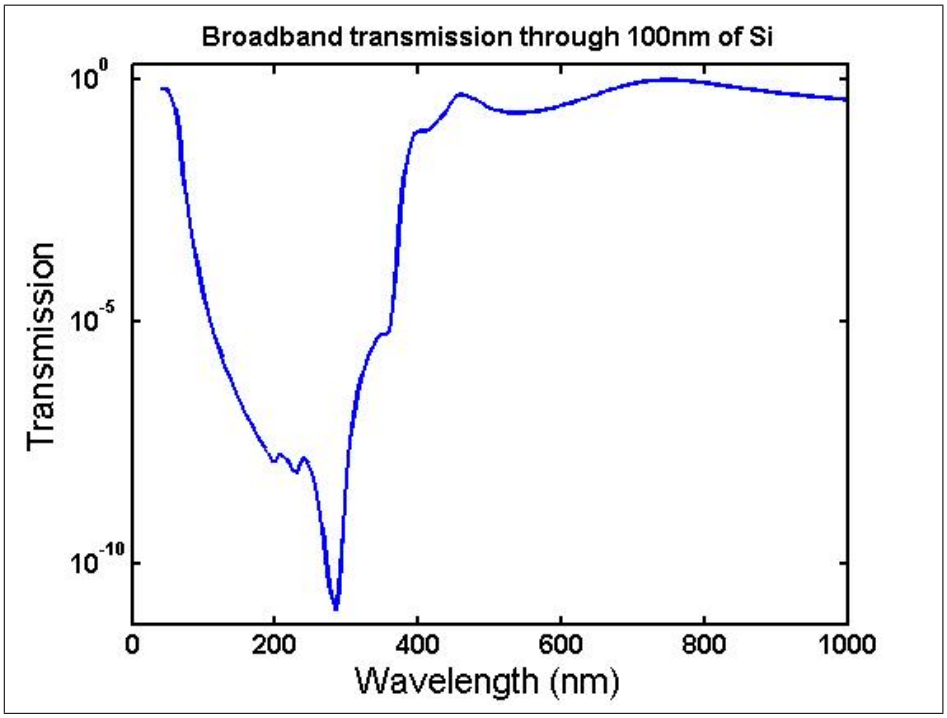

Figure A.10: Broadband transmission through 100nm of Si

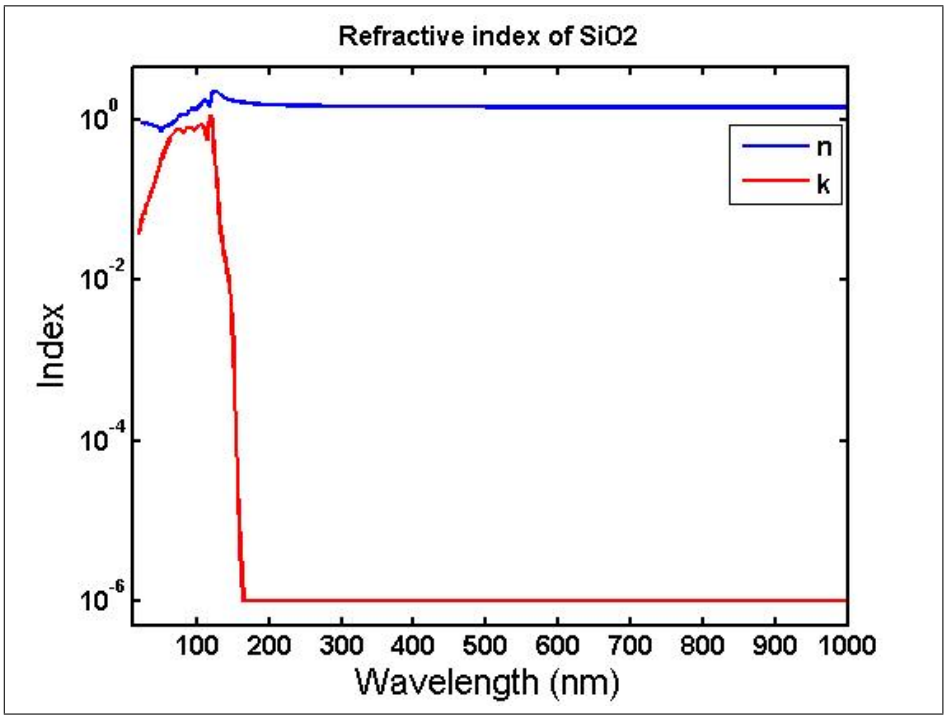

Figure A.11: Refractive indices for SiO_2

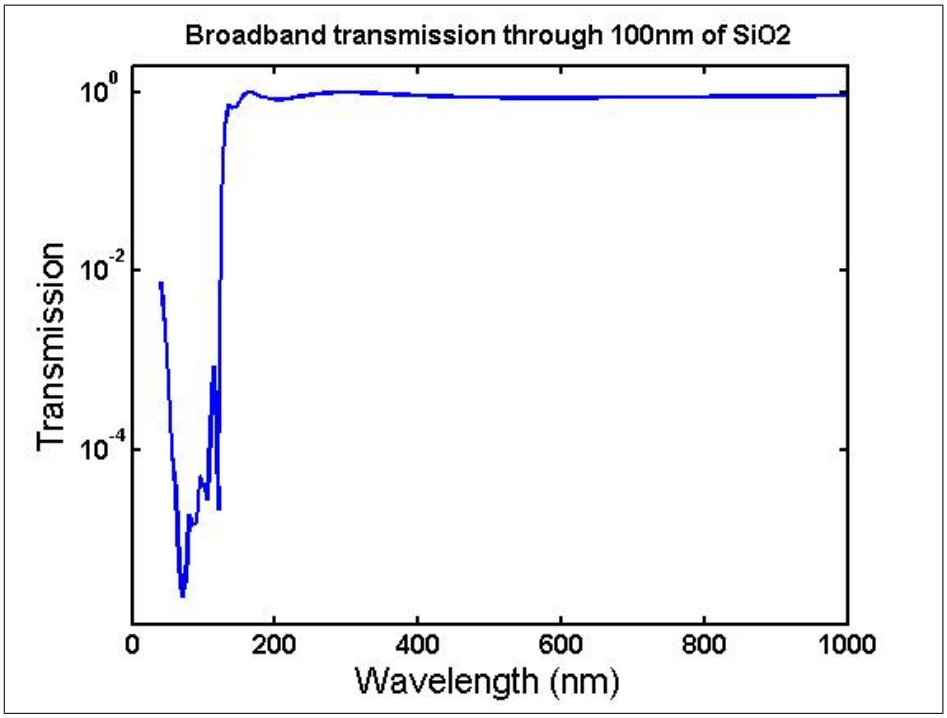

Figure A.12: Broadband transmission through 100nm of SiO_2

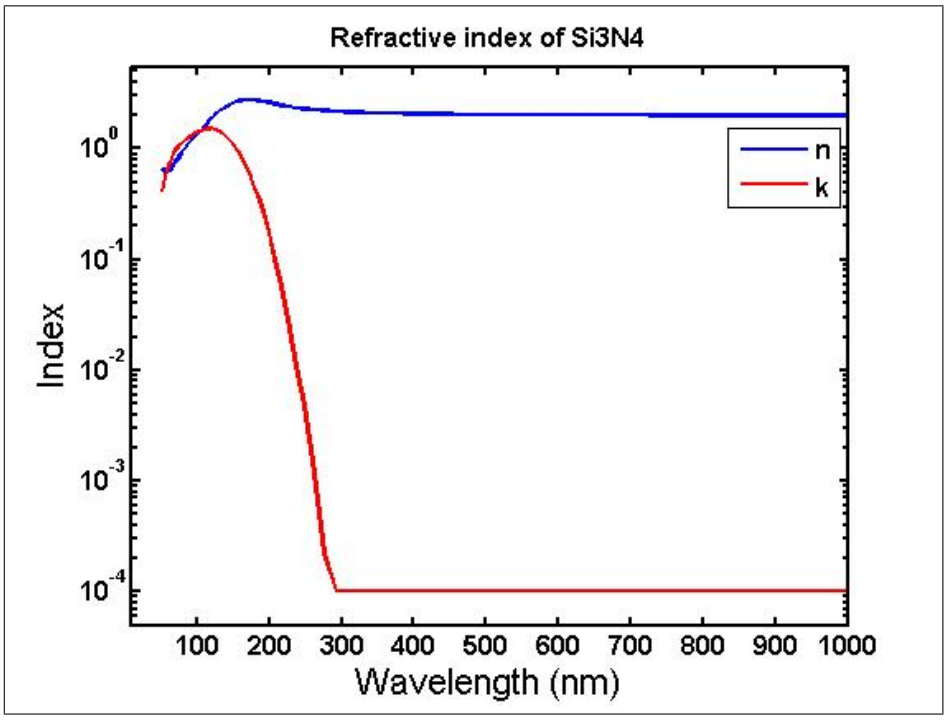

Figure A.13: Refractive indices for Si_3N_4

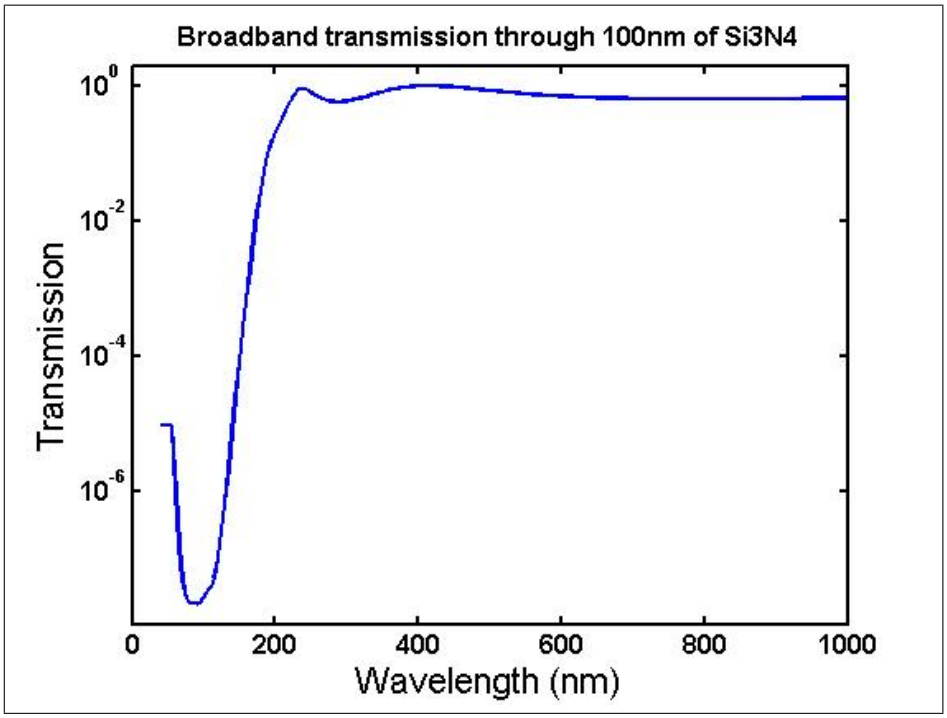

Figure A.14: Broadband transmission through 100nm of Si_3N_4

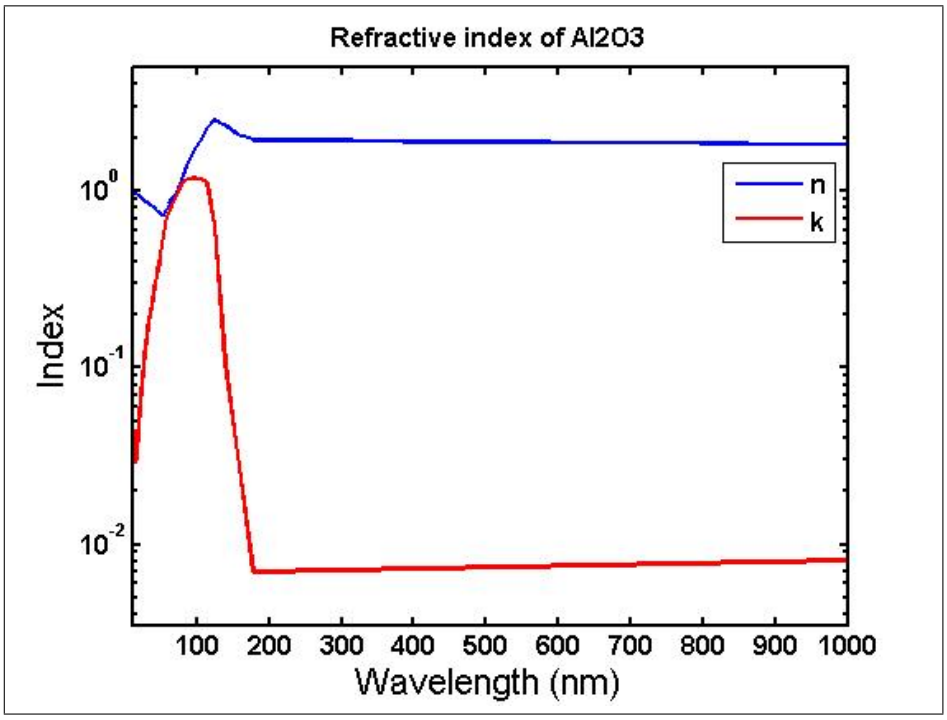

Figure A.15: Refractive indices for Al_2O_3

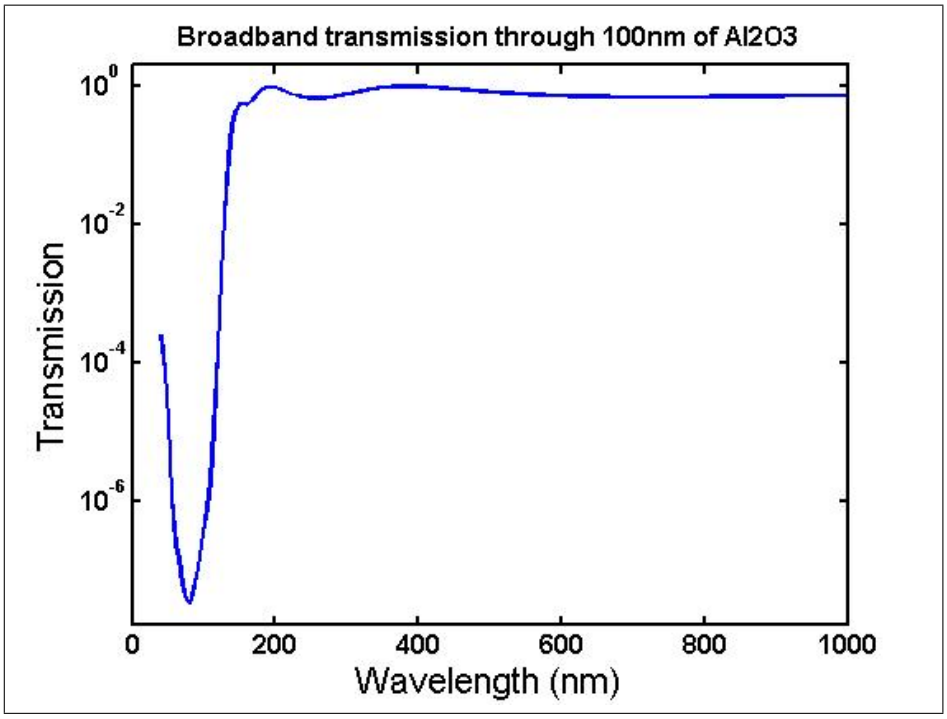

Figure A.16: Broadband transmission through 100nm of Al_2O_3

APPENDIX B

Lab Tools and Recipes

B.1. Lab Tools

The tools used in the lab include the following:

- Lithography
  - ElectroMask II 4" pattern generator, minimum feature 1500 nm
  - Suss MA-6 4" double-sided contact alignment/lithography, minimum feature 1500 nm
  - Suss MJB-3 4" contact alignment/lithography, minimum feature 2000 nm
  - Suss 4" ACS-200 C-to-C coater-developer
- PVD tools
  - Enerjet E-beam Evaporator for depositions of Al, Cr, Au, Pt, and Ti
  - SJ-20 E-beam Evaporator for depositions of Ge, Au, Ni, and Ti
  - Cooke E-beam Evaporator for depositions of Ni, NiCr, Au, Pd, Sn, In, Ag, and Zn
- Plasma tools
  - GSI PECVD
  - LAM 9400 Transformer Coupled Plasma Tool[a]
  - Plasmatherm 790 Series RIE
  - Trion Oracle III RIE[b]

[a] http://www.lamresearch.com/
[b] http://www.triontech.com/oracle.htm

- Metrology
  - NanoSpec 6100
  - Zygo NewView 5000
  - Dektak 6M Surface Profilometer by Veeco Metrology Group[c]
- Other
  - Xactix X3B XeF_2 gas-phase silicon etcher[d]
  - Thermco 9K 4" auto-load high temperature furnaces, anneal/sinter (Si, contacts)
  - JetFirst 150 rapid thermal process tool
  - Intralase diode-pumped Nd:glass chirped pulse amplification (CPA) laser system

[c] http://www.veeco.com
[d] http://www.xactix.com

B.2. Optical Lithography Process

The optical lithography process of Section 5.2 is as follows:

1. Front side high density implant of boron ions ($> 10^{12}$ cm^{-3})
2. Front side lithography and etch
   (a) ACS-200: Spin-coat 1.5 μm of Shipley 1813 positive photoresist
   (b) MA-6: Expose to 20 mW/cm^2 405 nm light for 6.5 seconds in hard-contact mode
   (c) Develop in fresh tank of MicroPosit MF-319 developer for 75 seconds with gentle agitation
   (d) Oven: Bake at 110° C for 20 minutes
   (e) Trion: Silicon grating etch for 245 seconds
   (f) Strip resist in Baker PRS-2000 Positive Resist Stripper for 3 hours with ultrasound assist
   (g) Rinse with acetone, isopropanol, and water
   (h) Plasmatherm: Ash in 100 sccm O_2 at 250 mTorr for 15 minutes
   (i) GSI: Deposit 1 μm SiO_2 for protection from the back-etch
3. Back side lithography and etch
   (a) GSI: Deposit 1 μm SiO_2 on back side
   (b) Spin-coat hexamethyldisilazane (HMDS)
   (c) Spin-coat 10 μm of Microchem AZ-9260 positive photoresist; 1800 RPM, 30 seconds
   (d) Wait 20 minutes with wafer horizontal in carrier with moist napkin
   (e) Oven: Bake at 90° C for 10 minutes
   (f) Wait 20 minutes with wafer horizontal in carrier with moist napkin
   (g) MA-6: Expose to 20 mW/cm^2 405 nm light for 40 seconds in hard-contact mode
   (h) Wait 20 minutes with wafer horizontal in carrier with moist napkin
   (i) Develop in 3:1 mixture of H_2O and Clariant AZ400K developer for approximately 1 minute
   (j) Rinse in de-ionized water for 2 minutes, blow-dry
   (k) Soak in BHF for 5 minutes
   (l) Rinse in de-ionized water for 5 minutes, blow-dry
   (m) ACS-200: Spin 2 μm Shipley 1827 positive photoresist on blank carrier wafer

(n) Attach wafer to carrier, bake on hotplate at 90° C for 3 minutes

(o) STS: Etch through 420 μm in STS[e], 2:30:00

(p) Zygo: Check etch depth, continue STS etch as needed

(q) Separate from carrier in acetone soak

(r) Cleave along etched scribe lanes

(s) Soak in EDP until etch stops on concentration stop; carefully check multiple times during etch by removing from solution, dipping in multiple clean beakers of H_2O, and examining under microscope

(t) Strip resist in Baker PRS-2000 Positive Resist Stripper for 3 hours with ultrasound assist

(u) Rinse with acetone, isopropanol, and water

(v) Plasmatherm: Ash in 100 sccm O_2 at 250 mTorr for 15 minutes

(w) Soak in BHF for 5 minutes

(x) Gently immerse in seven successive beakers of de-ionized water for five minutes each

[e]Back-side etch parameters: 65% APC, 0.7 mT base pressure, etch first; 12 second etch with 130 sccm SF_6 and 13 sccm O_2, 800 W TCP and 10 W coil power; 6 second passivation with 85 sccm C_4F_8, 800 W coil, 0 W platen

B.3. Nanoimprint lithography and DRIE

Notes for this process: Be VERY careful of any kind of dust on the samples, especially before spin-coating the first thermal resist layer. A single grain of dust can ruin a sample. Blow absolutely everything clean before using it.

1. CLEAVE AND CLEAN SAMPLES
   (a) Spin-coat a thick layer of any photoresist to protect from dust
   (b) Soft-bake for 2-3 minutes on hotplate at 115°
   (c) Etch 1 mm or smaller mark with diamond-tip scribe tool at desired location on edge of (100) surface
   (d) Grip with fingers at edge of wafer, spanning the scribed mark, exert small pressure to cleave wafer along <110>plane
   (e) Repeat scribe-and-cleave until wafer(s) reduced to desired size chips
   (f) Spray chip surfaces with acetone, then isopropanol, blow-dry with N_2 gun
   (g) Piranha-clean (1:1 mixture of H_2SO_4:H_2O_2) batches of chips for 20 minutes
   (h) Rinse in N_2-agitated de-ionized water for 10 minutes or more; this is to remove any residue of the Piranha etch that could interfere with the Cr deposition
2. Enerjet: Deposit 3 nm Cr adhesion layer at 2Å/sec; the low deposition rate is to ensure control of layer thickness since low thickness depositions usually deposit 2x - 3x the desired amount if using high deposition rate
3. FIRST IMPRINT
   (a) Blow any dust free of chip surface with N_2
   (b) Attach chip to spinner
   (c) Blow any dust free of pipette with N_2
   (d) Pipette thermal plastic resist (50:50 mixture of mrI-8030 and Propylene Glycol Methyl Ether Acetate (PGMEA)) on chip
   (e) Spin-coat for 30 seconds at 3000 (CHECK THIS) RPM, target thickness 140 nm
   (f) Bake on hotplate for 5 minutes at 140 ° to remove solvents
   (g) Blow clean chip surface and mold surface
   (h) Attach 240 nm period, 50% duty-cycle mold to chip, press with fingers or tweezers to ensure good contact
   (i) Assemble in Nanonex imprinter: bottom silicone sheet, carrier wafer, chip-and-mold stack, aluminum, and top silicone sheet

(j) Run imprint recipe: 180°C at 600 PSI for 5 minutes, ramp down pressure when temp reaches 40∘C

(k) Remove from imprinter, hold stack upside down over clean wipe and carefully slide razor blade between to separate; mold falls face-up to wipe

4. Enerjet: Shadow-evaporation at high shadow-angle from both sides, 50Å Al at 2Å/second; be certain chips are angled properly!

5. Residual etch

   (a) Mount chip on center of 6" carrier using poly-tetrafluoroethelene (PTFE)

   (b) Plasmatherm: Chamber conditioning run (20 mT, 20 sccm O_2, 50 W, 10 minutes)

   (c) Plasmatherm: Residual etch at same conditions as above, for 0:01:45

6. Enerjet: Direct deposition of 700Å Al

7. LIFTOFF

   (a) Soak in warm methanol for 20 minutes

   (b) Acetone liftoff with ultrasound agitation, chip flat in beaker

   (c) Soak chip in acetone overnight; spray chips with acetone as they're removed from soak

   (d) Methanol and isopropanol rinse, N_2 blow-dry

   (e) March Asher: Ash chip to remove residual resist (250 mT, 150 W, 17% O_2, 5 minutes)

8. SECOND IMPRINT

   (a) Spin thick polystyrene (7% mixture in Toluene) with same procedure as above, targeting 310 nm or thicker

   (b) Imprint with 10 μm period 5% duty-cycle mold at 90° across prior imprint

9. Enerjet: Shadow-evaporation at high shadow-angle from both sides, 200Å Al at 2Å/second

10. Plasmatherm: Chamber conditioning and residual etch as above, 4 minutes for significant over-etch)

11. Enerjet: Direct deposition of 700Å Al

12. Liftoff as above, except in Xylene

13. LAM: Ash to remove residual resist (60 mT, 400 W ICP, 0 W bias, 100 sccm O_2, 3 minutes)

14. LAM: Cr etch (10 mT, 100 W TCP, 5 W bias, 25 sccm Cl_2, 5 sccm O_2, 30 seconds)

15. Spin 3-4 micron protective resist on front side, hard-bake at 110°C for 10 minutes

16. BACK-SIDE PATTERNING

    (a) Enerjet: Deposit 20,000Å Al on back side of chip at 15Å/second

    (b) Spin-coat 3 μm Shipley 1827 photoresist (2000 RPM) on backside, softbake at 110°C for 90 seconds

    (c) MA-6: Back-side alignment of 1 mm period support grating and exposure to 20 mW/cm^2 405 nm light for 20 seconds (significant over-exposure)

    (d) MF319 tank develop until pattern is clear, DI rinse, N_2 blow-dry

    (e) Aluminum Etchant A dip for 3-4 minutes until silicon surface is revealed, add 30 second over-etch

    (f) Remove resist with acetone dip, rinse with ipa, blow-dry. THIS IS CRITICAL! The Al etchant changes the chemistry of the resist such that the heat of a through-wafer etch will cross-link it, leaving unremovable sludge on chip surface

17. BACK-SIDE ETCH

    (a) GSI: Deposit 4-5 μm PECVD oxynitride on blank Si carrier wafer

    (b) Spin-coat 5 μm Shipley 1827 photoresist (1400 RPM) on carrier as adhesion layer

    (c) Attach chip to carrier grating-side down

    (d) Soft-bake on hotplate at 115° for 2-3 minutes

    (e) STS: Etch $\sim$ 2:45:00 until oxide layer revealed[f], then 5 minutes over-etch

    (f) LAM: Etch buried oxide layer; for 5:30, check with Nikon to verify removal of oxide layer Acetone soak to separate from carrier, rinse with methanol and IPA, hotplate dry Attach to recessed carrier with LAM grease

18. FRONT-SIDE ETCH

    (a) GSI: Prepare recessed carrier as in B.7

    (b) Spin-coat 5 micron layer of Shipley 1827 resist on carrier to prevent charging, hard-bake in oven at 110° for 20 minutes

    (c) "Paint" bottom side corners of chip with PFPE using foam pad

    (d) Attach to carrier, with back-side etched region over the recess

[f]Back-side etch parameters: 65% APC, 0.7 mT base pressure, etch first; 12 second etch with 130 sccm SF_6 and 13 sccm O_2, 800 W TCP and 10 W coil power; 6 second passivation with 85 sccm C_4F_8, 800 W coil, 0 W platen

(e) STS etch front side grating for 10 minutes[g]

(f) Separate chip from carrier by putting razor blade flush with a corner and pushing the chip with tweezers onto blade; this minimizes the force required for separation

(g) SEM chip to ascertain etch depth, repeat etch as needed to finish etching through, re-setting passivation times as needed

[g]Front-side etch parameters: 35% APC, 0.7 mT base pressure, passivate first; 12 second passivation -0.1 second per minute of etch; 100 sccm C_4F_8 and 3 sccm SF_6 (to keep the flow valve from sticking), 500 W coil, 0 W platen; 5 second etch with 12 sccm SF_6 and 80 sccm O_2, 550 W TCP and 15 W coil power; after every two minutes, pause for 5 minutes with 13 sccm Ar and 0 power to cool chip

B.4. Surfactant coating

1. Set hotplate temperature at 130° C
2. Place Petri dish on hotplate with cover canted to side
3. Place glass slide in Petri dish
4. Place mold(s) on slide
5. Drip 5-6 drops of fluoro-surfactant liquid into Petri dish next to slide, cover dish
6. Wait for 30-60 minutes; cover or Petri dish will slowly become foggy
7. Remove mold(s) and slide from Petri dish and *immediately* swab dish and cover with acetone and isopropanol

B.5. Mold duplication in oxide

1. Ash oxide-coated chips (250 mT, 100 W, 17% O_2, 3 minutes)
2. Enerjet: Deposit 10-20 nm Cr
3. Spin mr-I 8030 resist
4. Bake at 140°C for 5 minutes
5. Imprint mold as in B.3 (Figure B.1A)
6. Enerjet: dual shadow-evaporate 5 nm Al at 2Å/sec
7. LAM: Residual etch (10 mT, 100 W TCP, 30 W bias, 20 sccm O_2, 180 nm/min etch rate), time dependent upon residual layer thickness
8. LAM: Cr etch (10 mT, 100 W TCP, 5 W bias, 25 sccm Cl_2, 5 sccm O_2, $\sim$ 15 nm/min etch rate), time dependent upon Cr thickness
9. LAM: Oxide etch (10 mT, 500 W TCP, 100 W bias, 50 sccm each of C_2F_6, He, 60 sccm Ar, 10 sccm O_2, $\sim$ 192 nm/min etch rate), time dependent upon desired mold depth (Figure B.1B)
10. Rinse with acetone, methanol, and isopropanol, N_2 blow dry
11. Plasmatherm: plasma surface treatment (20 mT, 20 sccm O_2, 50 W, 5 minutes)
12. Coat with surfactant as in B.4

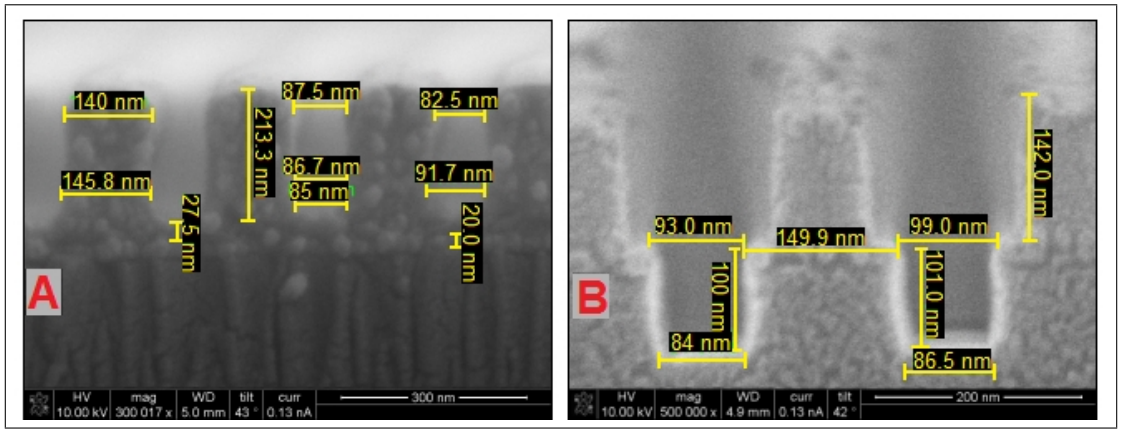

Figure B.1: Fabrication of oxide molds via RIE. This is a visible walkthrough of recipe B.5. The mold used had period 240 nm, 42% duty cycle, depth 200 nm.

B.6. Mold duplication in silicon

1. Cleave and clean chips as in B.3
2. Enerjet: Deposit 3-5 nm Cr as in B.3
3. Spin mr-I 8030 resist
4. Bake at 140°C for 5 minutes
5. Imprint mold as in B.3 (Figure B.2A)
6. Enerjet: dual shadow-evaporate 5-10 nm Al and 5 nm Ti at 2Å/sec; the Ti has a lower sputter yield than Al, but high tensile stress
7. LAM: Residual etch (10 mT, 100 W TCP, 30 W bias, 20 sccm O_2, 180 nm/min etch rate), time dependent upon residual layer thickness (Figure B.2B)
8. LAM: Cr etch (10 mT, 100 W TCP, 5 W bias, 25 sccm Cl_2, 5 sccm O_2, $\sim$ 15 nm/min etch rate), 30 sec
9. STS: Mold etch with front-side grating etch of B.3 except no cooling steps; time dependent upon desired depth, with $\sim$ 50-100 nm per minute depending on mask geometry, particularly width of opening between shadow-masked features (Figure B.2C and D)
10. Rinse with acetone, methanol, and isopropanol, N_2 blow dry
11. Plasmatherm: plasma surface treatment (20 mT, 20 sccm O_2, 50 W, 5 minutes)
12. Coat with surfactant as in B.4

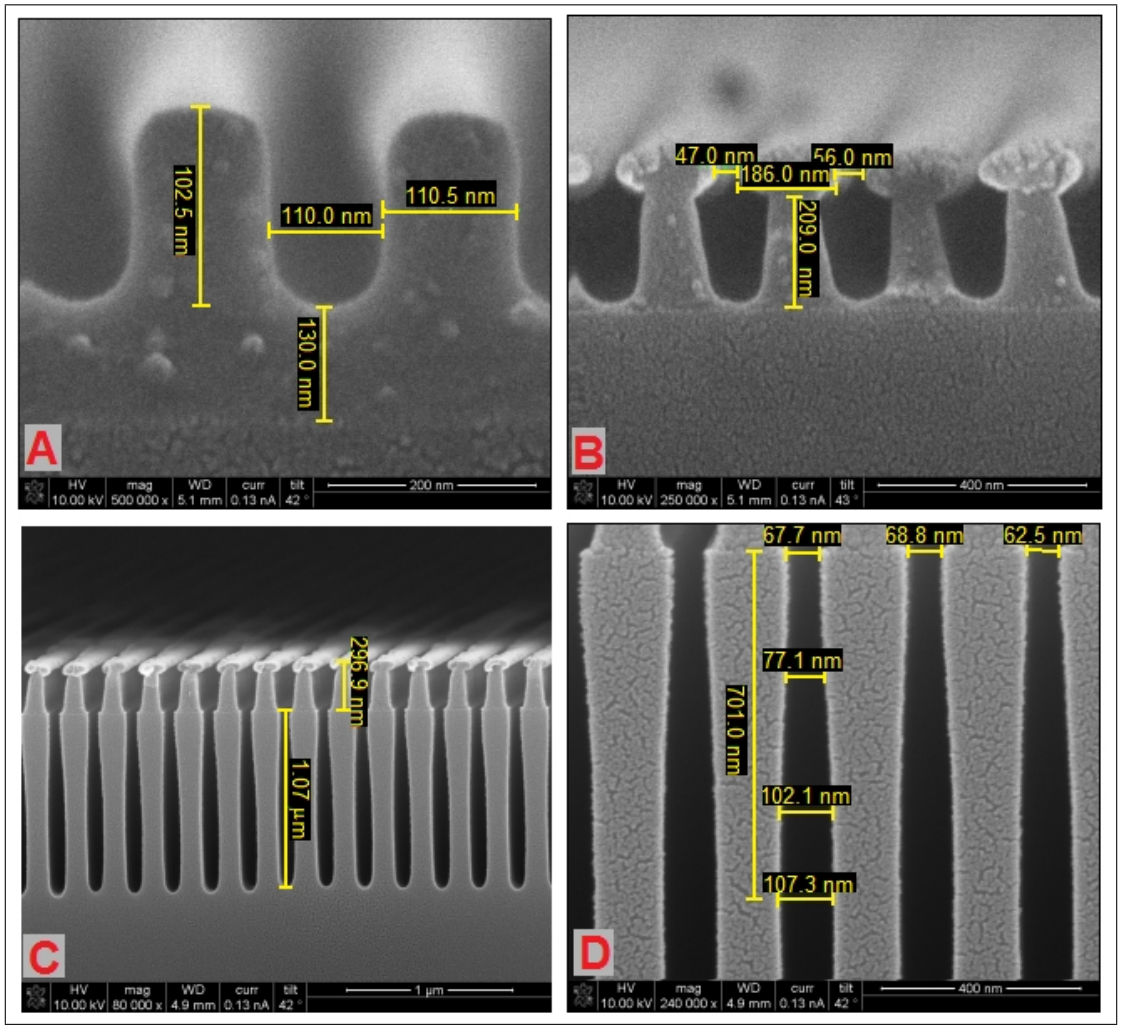

Figure B.2: Fabrication of silicon molds via DRIE. This is a visible walkthrough of recipe B.6. The mold used had period 240 nm, 50% duty cycle, depth 110 nm. The shadow evaporation was 15 nm Al and 5 nm Ti, significantly closing the imprinted gaps. This had the effect of reducing the silicon etch rate by approximately half. Though the 20 minute etch laterally removed some of the masking photoresist, the underlying Cr mask maintained the features. However, there was relatively large bowing of the features which should be mitigated by either reducing the pressure or increasing passivation.

B.7. Recessed Carrier Wafer

1. GSI: deposit 2 μm PECVD oxide on bare Si wafer
2. Spin 3 μm Shipley 1827 photoresist (2000 RPM), soft-bake on hotplate at 115° for 90 seconds
3. Cut sheet of aluminum with razor blade into shape of desired recess, attach to wafer
4. MJB-3: Flood-expose for 20 seconds
5. Remove aluminum mask, develop in MF319 for 2 minutes
6. BHF: 20-30 minutes (until hydrophobic)
7. STS: etch recess using back-side etch recipe from B.3, (2.5-3.5 μm /minute); if desired etch depth over 100 μm , attach to carrier wafer first using PFPE
8. Remove resist with PRS2000 or acetone
9. GSI: PECVD 3 microns oxide on back side, 2 microns on front

BIBLIOGRAPHY

BIBLIOGRAPHY

Aaltonen, T., M. Ritala, T. Sajavaara, J. Keinonen, and M. Leskelä (2003), Atomic Layer Deposition of Platinum Thin Films, *Chem. Mater.*, *15*(9), 1924–1928.

Aaltonen, T., M. Ritala, Y.-L. Tung, Y. Chi, K. Arstila, K. Meinander, and M. Leskelä (2004), Atomic layer deposition of noble metals: Exploration of the low limit of the deposition temperature, *J. Mater. Res.*, *19*(11), 3353–3358.

Adelberger, E. G., et al. (1998), Solar fusion cross sections, *Rev. Mod. Phys.*, *70*, 1265–1291.

Ahn, M., R. K. Heilmann, and M. L. Schattenburg (2007), Fabrication of ultrahigh aspect ratio freestanding gratings on silicon-on-insulator wafers, *J. Vac. Sci. Technol. B*, *25*(6), 2593–2597.

Alenkowicz, H., and B. Levitas (1998), Measurement of complex permittivity and complex permeability of materials, in *12th International Conference on Microwaves and Radar*, *IEEE Conference Proceeding*, vol. 2, pp. 668–671.

Allegrini, F., R. F. Wimmer-Schweingruber, P. Wurz, and P. Bochsler (2003), Determination of low-energy ion-induced electron yields from thin carbon foils, *Nucl. Inst. Meth. Phys. Res., B*, *211*(4), 487–494.

Allegrini, F., N. A. Schwadron, D. J. McComas, G. Gloeckler, and J. Geiss (2005), Stability of the inner source pickup ions over the solar cycle, *J. Geophys. Res.*, *110*, A05,105.

Allegrini, F., D. J. McComas, D. T. Young, J. J. Berthelier, J. Covinhes, J. M. Illiano, J. F. Riou, H. O. Funsten, and R. W. Harper (2006), Energy loss of 1–50 keV H, He, C, N, O, Ne, and Ar ions transmitted through thin carbon foils, *Rev. Sci. Inst.*, *77*, 044,501.

Andrews, G. B., et al. (2007), The Energetic Particle and Plasma Spectrometer Instrument on the MESSENGER Spacecraft, *Space Sci. Rev.*, *131*, 523–556.

Arge, C. N., and V. J. Pizzo (2000), Improvement in the prediction of solar wind conditions using near-real time solar magnetic field updates, *J. Geophys. Res*, *105*, 10,465–10,480.

Arge, C. N., D. Odstrcil, V. J. Pizzo, and L. R. Mayer (2003), Improved Method for Specifying Solar Wind Speed Near the Sun, in *Solar Wind Ten*, *American Institute of Physics Conference Series*, vol. 679, edited by M. Velli, R. Bruno, F. Malara, and B. Bucci, pp. 190–193.

Arge, C. N., J. G. Luhmann, D. Odstrcil, C. J. Schrijver, and Y. Li (2004), Stream structure and coronal sources of the solar wind during the May 12th, 1997 CME, *J. Atmos. Terr. Phys.*, *66*(15-16), 1295–1309.

Asheghi, M., K. Kurabayashi, R. Kasnavi, and K. E. Goodson (2002), Thermal conduction in doped single-crystal silicon films, *J. Appl. Phys.*, *91*(8), 5079–5088.

Asplund, M., N. Grevesse, and A. Jacques Sauval (2006), The solar chemical composition, *Nucl. Phys. A*, *777*, 1–4.

Ayón, A. A., R. Braff, C. C. Lin, H. H. Sawin, and M. A. Schmidt (1999a), Characterization of a Time Multiplexed Inductively Coupled Plasma Etcher, *J. Electrochem. Soc.*, *146*, 339.

Ayón, A. A., R. A. Braff, R. Bayt, H. H. Sawin, and M. A. Schmidt (1999b), Influence of Coil Power on the Etching Characteristics in a High Density Plasma Etcher, *J. Electrochem. Soc.*, *146*, 2730.

Ayón, A. A., K. Ishihara, R. A. Braff, H. H. Sawin, and M. A. Schmidt (1999c), Microfabrication and testing of suspended structures compatible with silicon-on-insulator technology, *J. Vac. Sci. Technol. B*, *17*, 1589.

Ayón, A. A., S. Nagle, L. Fréchette, A. Epstein, and M. A. Schmidt (2000), Tailoring etch directionality in a deep reactive ion etching tool, *J. Vac. Sci. Technol. B*, *18*, 1412.

Bäcklund, Y., and L. Rosengren (1992), New Shapes in (100) Si Using KOH and EDP Etches, *J. Micromech. Microeng.*, *2*(2), 75–79.

Bailey, T., B. J. Choi, M. Colburn, M. Meissl, S. Shaya, J. G. Ekerdt, S. V. Sreenivasan, and C. G. Willson (2000), Step and flash imprint lithography: Template surface treatment and defect analysis, *J. Vac. Sci. Technol. B*, *18*, 3572.

Balkey, M. M., E. E. Scime, M. L. Schattenburg, and J. van Beek (1998), Effects of gap width on vacuum-ultraviolet transmission through submicrometer-period, freestanding transmission gratings, *Appl. Opt.*, *37*(22), 5087–5092.

Bandyopadhyay, A., S. Choubey, R. Gandhi, S. Goswami, and D. P. Roy (2003), The solar neutrino problem after the first results from KamLAND, *PhysLett. B*, *559*(3-4), 121–130.

Bao, L. R., X. Cheng, X. D. Huang, L. J. Guo, S. W. Pang, and A. F. Yee (2002), Nanoimprinting over topography and multilayer three-dimensional printing, *J. Vac. Sci. Technol. B*, *20*, 2881–2886.

Barnhart, D. J., T. Vladimirova, and M. N. Sweeting (2007), Very-Small-Satellite Design for Distributed Space Missions, *J. Spacecraft Rockets*, *44*(6), 1294–1306.

Bassous, E. (1978), Fabrication of novel three-dimensional microstructures by the anisotropic etching of (100) and (110) silicon, *IEEE Trans. Electr. Dev.*, *25*(10), 1178–1185.

Basu, S., and H. M. Antia (2008), Helioseismology and solar abundances, *Phys. Rep.*, *457*, 217–283.

Baumjohann, W., and R. A. Treumann (1996), *Basic Space Plasma Physics*, World Scientific Publishing Company.

Bean, K. E. (1978), Anisotropic Etching of Silicon, *IEEE Trans. Electr. Dev.*, *ED-25*(10), 1185–1193.

Bhardwaj, J., H. Ashraf, and A. McQuarrie (1997), Dry Silicon Etching for MEMS, *Electrochem. Soc. Proc.*, pp. 118–130.

Bhardwaj, J. K., and H. Ashraf (1995), Advanced silicon etching using high-density plasmas, *Proc. SPIE*, *2639*, 224.

Blauw, M. A., T. Zijlstra, R. A. Bakker, and E. van der Drift (2000), Kinetics and crystal orientation dependence in high aspect ratio silicon dry etching, *J. Vac. Sci. Technol. B*, *18*, 3453.

Bochsler, P., E. Möbius, and R. F. Wimmer-Schweingruber (2006), On the velocity distributions of dust-related inner-source pickup ions, *Geophys. Res. Lett.*, *33*, 6102–+.

Bogenschütz, A. F., W. Krusemark, K. H. Löcherer, and W. Mussinger (1967), Activation Energies in the Chemical Etching of Semiconductors in HNO_3-HF-CH_3COOH, *J. Electrochem. Soc.*, *114*(9), 970–973.

Bratton, D., D. Yang, J. Dai, and C. K. Ober (2006), Recent progress in high resolution lithography, *Polymers Adv. Technol.*, *17*(2), 94–103.

Burch, J. L. (2000), IMAGE mission overview, *Space Sci. Rev.*, *91*, 1–14.

Burns, J. A., P. L. Lamy, and S. Soter (1979), Radiation forces on small particles in the solar system, *Icarus*, *40*(1), 1–48.

Bustillo, J. M., R. T. Howe, and R. S. Muller (1998), Surface micromachining for microelectromechanical systems, *Proc. IEEE*, *86*(8), 1552–1574.

Bzowski, M., and M. Królikowska (2005), Are the sungrazing comets the inner source of pickup ions and energetic neutral atoms?, *Astron. Astrophys.*, *435*, 723–732.

Bzowski, M., H. J. Fahr, D. Rucinski, and H. Scherer (1997), Variation of bulk velocity and temperature anisotropy of neutral heliospheric hydrogen during the solar cycle., *Astron. Astrophys.*, *326*, 396–411.

Canizares, C. R., et al. (2005), The Chandra High-Energy Transmission Grating: Design, Fabrication, Ground Calibration, and 5 Years in Flight, *Publ. Astro. Soc. Pacific*, *117*(836), 1144–1171.

Cardinaud, C., M.-C. Peignon, and P.-Y. Tessier (2000), Plasma etching: principles, mechanisms, application to micro-and nano-technologies, *Appl. Surf. Sci.*, *164*(1-4), 72–83.

Carter, G. (2001), The physics and applications of ion beam erosion, *J. Phys. D: Appl. Phys.*, *34*, R1–R22.

Chalov, S. V., and H. J. Fahr (2006), Pickup interstellar helium ions in the region of the solar gravitational cone, *Astron. Lett.*, *32*(7), 487–494.

Chan, I. W. T., K. B. Brown, R. P. W. Lawson, A. M. Robinson, Y. Ma, and D. Strembicke (1999), Gas Phase Pulse Etching of Silicon For MEMS With Xenon Difluoride, *Proc. IEEE Canadian Conf. Elec. Comp. Engin.*, *3*, 1637–1642.

Chang, F. I., R. Yeh, G. Lin, P. B. Chu, E. G. Hoffman, E. J. Kruglick, K. S. J. Pister, and M. H. Hecht (1995), Gas-phase silicon micromachining with xenon difluoride, *Proc. SPIE*, *2641*(1), 117–128.

Chason, E., et al. (1997), Ion beams in silicon processing and characterization, *J. Appl. Phys.*, *81*, 6513–6561.

Chen, C. G., P. T. Konkola, R. K. Heilmann, C. Joo, and M. L. Schattenburg (2002a), Nanometer-accurate grating fabrication with scanning beam interference lithography, *Proc. SPIE*, *4936*, 126.

Chen, F. (1984), *Introduction to Plasma Physics and Controlled Fusion*, Plenum Publishing Corporation.

Chen, J., J. Sickler, E. Ippen, and F. Kärtner (2007), High repetition rate, low jitter, low intensity noise, fundamentally mode-locked 167 fs soliton Er-fiber laser, *Opt. Lett.*, *32*(11), 1566–1568.

Chen, J., J. Sickler, P. Fendel, E. Ippen, F. Kärtner, T. Wilken, R. Holzwarth, and T. Hänsch (2008), Generation of low-timing-jitter femtosecond pulse trains with 2 GHz repetition rate via external repetition rate multiplication, *Opt. Lett.*, *33*(9), 959–961.

Chen, J. W., and A. G. Milnes (1980), Energy Levels in Silicon, *Ann. Rev. Mater. Sci.*, *10*, 157–228.

Chen, K. S., A. A. Ayon, X. Zhang, and S. M. Spearing (2002b), Effect of process parameters on the surface morphology and mechanical performance of silicon structures after deep reactive ion etching, *J. Microelectromech. Syst.*, *11*(3), 264–275.

Chiu, M. C., et al. (1998), ACE Spacecraft, *Space Sci. Rev.*, *86*, 257–284.

Chou, S. Y., P. R. Krauss, and P. J. Renstrom (1995), Imprint of sub-25 nm vias and trenches in polymers, *Appl. Phys. Lett.*, *67*, 3114.

Chou, S. Y., P. R. Krauss, and P. J. Renstrom (1996a), Imprint Lithography with 25-Nanometer Resolution, *Science*, *272*(5258), 85.

Chou, S. Y., P. R. Krauss, and P. J. Renstrom (1996b), Nanoimprint lithography, *J. Vac. Sci. Technol. B*, *14*(6).

Chou, S. Y., P. R. Krauss, W. Zhang, L. Guo, and L. Zhuang (1997), Sub-10 nm imprint lithography and applications, *J. Vac. Sci. Technol. B*, *15*(6), 2897–2904.

Choy, K. L. (2003), Chemical vapour deposition of coatings, *Prog. Mater. Sci.*, *48*(2), 57–170.

Christensen, J. S. (2004), Dopant diffusion in Si and SiGe, Ph.D. thesis, KTH, Microelectronics and Information Technology, Stockholm, Sweden.

Christensen-Dalsgaard, J. (2003), Lecture Notes on Stellar Oscillations, 5th ed, available at http://whome.phys.au.dk/ jcd/oscilnotes/index.html/.

Chu, P. B., J. T. Chen, R. Yeh, G. Lin, J. C. P. Huang, B. A. Warneke, and K. S. J. Pister (1997), Controlled pulse-etching with xenon difluoride, *Proc. Intl. Conf. Solid State Sensors and Actuators (TRANSDUCERS) '97*, *1*(16-19), 665–668.

Cohen, O., I. V. Sokolov, I. I. Roussev, and T. I. Gombosi (2008), Validation of a synoptic solar wind model, *J. Geophy. Res.*, *113*(A12), 3104–+.

Cohen, O., et al. (2007), A Semiempirical Magnetohydrodynamical Model of the Solar Wind, *Astrophys. J. Lett.*, *654*, L163–L166.

Colburn, M., A. Grot, M. N. Amistoso, B. J. Choi, T. C. Bailey, J. G. Ekerdt, S. V. Sreenivasan, J. Hollenhorst, and C. G. Willson (2000), Step and flash imprint lithography for sub-100-nm patterning, *Proc. SPIE*, *3997*, 453.

Colburn, M., et al. (1999), Step and flash imprint lithography: a new approach to high-resolution patterning, *Proc. SPIE*, *3676*, 379–389.

Collier, M. R., et al. (2001), Observations of neutral atoms from the solar wind, *J. Geophys. Res. A*, *106*, 24.

Collins, S. D. (1997), Etch Stop Techniques for Micromachining, *J. Electrochem. Soc.*, *144*(6), 2242–2262.

Consolmagno, G. (1979), Lorentz scattering of interplanetary dust, *Icarus*, *38*(3), 398–410.

Couvidat, S., S. Turck-Chièze, and A. G. Kosovichev (2003), Solar Seismic Models and the Neutrino Predictions, *Astrophys. J.*, *599*, 1434–1448.

Craighead, H. (2000), Nanoelectromechanical Systems, *Science*, *290*(5496), 1532–1535.

Cranmer, S. (2005), Why is the Fast Solar Wind Fast and the Slow Solar Wind Slow? A Survey of Geometrical Models, *Proc. Solar Wind 11/SOHO 16*, p. 159.

Cranmer, S., A. van Ballegooijen, and R. Edgar (2007), Self-consistent Coronal Heating and Solar Wind Acceleration from Anisotropic Magnetohydrodynamic Turbulence, *Astrophys. J. Suppl. Ser.*, *171*(2), 520–551.

Cranmer, S. R. (2008), On Competing Models of Coronal Heating and Solar Wind Acceleration: The Debate in '08, *ArXiv e-prints*, *804*.

Cranmer, S. R., et al. (1999), An Empirical Model of a Polar Coronal Hole at Solar Minimum, *Astrophys. J.*, *511*, 481–501.

Crawford, T. H. R., A. Borowiec, and H. K. Haugen (2005), Femtosecond laser micromachining of grooves in silicon with 800 nm pulses, *Appl. Phys. A: Mat. Sci. Proc.*, *80*(8), 1717–1724.

Cross, G. L. W. (2006), The production of nanostructures by mechanical forming, *J. Phys. D: Appl. Phys*, *39*, 20.

Cui, B., Z. Yu, H. Ge, and S. Y. Chou (2007), Large area 50 nm period grating by multiple nanoimprint lithography and spatial frequency doubling, *Appl. Phys. Lett.*, *90*, 043,118.

Curdt, W., P. Brekke, U. Feldman, K. Wilhelm, B. N. Dwivedi, U. Schuhle, and P. Lemaire (2001), The SUMER spectral atlas of solar-disk features, *Astron. Astrophys.*, *375*, 591–613.

Curdt, W., E. Landi, and U. Feldman (2004), The SUMER spectral atlas of solar coronal features, *Astron. Astrophys.*, *427*, 1045–1054.

Curdt, W., E. Landi, T. Wang, and U. Feldman (2005), In-Situ Heating in Active Region Loops, *Hvar Observatory Bulletin*, *29*, 157–165.

Current, M. (1996), Ion implantation for silicon device manufacturing: A vacuum perspective, *J. Vac. Sci. Technol. A*, *14*, 1115–.

Czechowski, A., and I. Mann (2003), Penetration of interstellar dust grains into the heliosphere, *J. Geophys. Res.*, *108*, 8038–+.

Dantan, A., J. Laurat, A. Ourjoumtsev, R. Tualle-Brouri, and P. Grangier (2007), Femtosecond Ti: sapphire cryogenic amplifier with high gain and MHz repetition rate, *Opt. Exp.*, *15*(14), 8864–8870.

de Boer, M. J., J. G. E. Gardeniers, H. V. Jansen, E. Smulders, M. J. Gilde, G. Roelofs, J. N. Sasserath, and M. Elwenspoek (2002), Guidelines for etching silicon MEMS structures using fluorine high-density plasmas at cryogenic temperatures, *J. Microelectromech. Syst.*, *11*(4), 385–401.

Deal, B. E., and A. S. Grove (1965), General Relationship for the Thermal Oxidation of Silicon, *J. Appl. Phys.*, *36*(12), 3770–3778.

Dearnaley, G. (1974), Ion implantation, *Ann. Rev. Mat. Sci.*, *4*(1), 93–123.

Delaboudinière, J.-P., et al. (1995), EIT: Extreme-Ultraviolet Imaging Telescope for the SOHO Mission, *Sol. Phys.*, *162*, 291–312.

Delanoye, S. N., and J. de Keyser (2007), Comets and Chemical Composition, *Space Sci. Rev.*, *130*, 73–78.

Deng, Y. P., X. H. Xie, H. Xiong, Y. X. Leng, C. F. Cheng, H. H. Lu, R. X. Li, and Z. Z. Xu (2005), Optical breakdown for silica and silicon with double femtosecond laser pulses, *Opt. Exp.*, *13*(8), 3096–3103.

D'Heurle, F. M., and J. M. E. Harper (1989), Note on the origin of intrinsic stresses in films deposited via evaporation and sputtering, *Thin Solid Films*, *171*, 81–92.

Domingo, V., B. Fleck, and A. I. Poland (1995), The SOHO Mission: an Overview, *Sol. Phys.*, *162*, 1–37.

Draine, B. T. (1985), Tabulated optical properties of graphite and silicate grains, *Astrophys. J. Suppl. Ser.*, *57*, 587–594.

Draine, B. T., and H. M. Lee (1984), Optical properties of interstellar graphite and silicate grains, *Astrophys. J.*, *285*, 89.

Dupriez, P., C. Finot, A. Malinowski, J. K. Sahu, J. Nilsson, D. J. Richardson, K. G. Wilcox, H. D. Foreman, and A. C. Tropper (2006), High-power, high repetition rate picosecond and femtosecond sources based on Yb-doped fiber amplification of VECSELs, *Opt. Exp.*, *14*(21), 9611–9616.

Eaton, S., H. Zhang, P. Herman, F. Yoshino, L. Shah, J. Bovatsek, and A. Arai (2005), Heat accumulation effects in femtosecond laser-written waveguides with variable repetition rate, *Opt. Exp.*, *13*(12), 4708–4716.

Ekinci, K. L., and M. L. Roukes (2005), Nanoelectromechanical systems, *Rev. Sci. Inst.*, *76*, 061,101.

Enloe, C., L. Krause, R. Haaland, T. Patterson, C. Richardson, C. Lazidis, and R. Whiting (2003), Miniaturized electrostatic analyzer manufactured using photolithographic etching, *Rev. Sci. Inst.*, *74*, 1192.

Fahr, H. J. (1968), On the Influence of Neutral Interstellar Matter on the Upper Atmosphere, *Astrophys. Space Sci.*, *2*, 474–495.

Fahr, H. J. (2007), Revisiting the theory of the evolution of pick-up ion distributions: magnetic or adiabatic cooling?, *Ann. Geophys*, *25*, 2649–2659.

Fargeix, A., and G. Ghibaudo (1983), Dry oxidation of silicon: A new model of growth including relaxation of stress by viscous flow, *J. Appl. Phys.*, *54*(12), 7153–7158.

Fedosejevs, R., S. E. Kirkwood, R. Holenstein, N. Young, and Y. Y. Tsui (2007), Femtosecond interaction processes near threshold: damage and ablation, *Proc. SPIE*, *6403*, 640,302.

Feynman, R. P. (1992), There's plenty of room at the bottom [data storage], *Microelectromech. Syst.*, *1*(1), 60–66, reprinted from the 1959 annual meeting of the American Physical Society.

Fichtner, H., J. A. Le Roux, U. Mall, and D. Rucinski (1996), On the transport of pick-up ions in the heliosphere., *Astron. Astrophys.*, *314*, 650–662.

Fick, A. (1855), On liquid diffusion, *Phil. Mag. and Jour. Sci.*, *10*, 31–39, reprinted in J. Membr. Sci. 100 (1995) 33-38.

Fisk, L. A. (2003), Acceleration of the solar wind as a result of the reconnection of open magnetic flux with coronal loops, *J. Geophys. Res*, *108*, 1157.

Fisk, L. A., M. A. Forman, and W. I. Axford (1973), Solar modulation of galactic cosmic rays 3. Implications of the Compton-Getting coefficient, *J. Geophys. Res*, *78*(7).

Fisk, L. A., N. A. Schwadron, and G. Gloeckler (1997), Implications of fluctuations in the distribution functions of interstellar pick-up ions for the scattering of low rigidity particles, *Geophys. Res. Lett*, *24*(1), 93–96.

Fisk, L. A., N. A. Schwadron, and T. H. Zurbuchen (1998), On the Slow Solar Wind, *Space Sci. Rev.*, *86*(1), 51–60.

Fogli, G. L., E. Lisi, A. Marrone, D. Montanino, A. Palazzo, and A. M. Rotunno (2003), Solar neutrino oscillation parameters after first KamLAND results, *Phys. Rev. D*, *67*(7), 73,002.

French, P. J., and P. M. Sarro (1998), Surface versus bulk micromachining: the contest for suitable applications, *J. Micromech. Microeng.*, *8*, 45–53.

Gates, B. D., Q. Xu, J. C. Love, D. B. Wolfe, and G. M. Whitesides (2004), Unconventional nanofabrication, *Ann. Rev. Mater. Res.*, *34*, 339–372.

Gates, B. D., Q. Xu, M. Stewart, D. Ryan, C. G. Willson, and G. M. Whitesides (2005), New approaches to nanofabrication: Molding, printing, and other techniques, *Chem. Rev.*, *105*, 1171–1196.

Gattass, R. R., and E. Mazur (2008), Femtosecond laser micromachining in transparent materials, *Nature Photonics*, *2*(4), 219–225.

Gattass, R. R., L. R. Cerami, and E. Mazur (2006), Micromachining of bulk glass with bursts of femtosecond laser pulses at variable repetition rates, *Opt. Exp.*, *14*(12), 5279–5284.

Geiss, J., G. Gloeckler, L. A. Fisk, and R. von Steiger (1995a), C^+ pickup ions in the heliosphere and their origin, *J. Geophys. Res.*, *100*, 23,373–23,378.

Geiss, J., G. Gloeckler, and R. von Steiger (1995b), Origin of the Solar Wind From Composition Data, *Space Sci. Rev.*, *72*, 49–60.

Gibbons, J. F. (1972), Ion implantation in semiconductors–Part II: Damage production and annealing, *Proc. IEEE*, *60*(9), 1062–1096.

Giboz, J., T. Copponnex, and P. Mele (2007), Microinjection molding of thermoplastic polymers: a review, *J. Micromech. Microeng.*, *17*(6), R96–R109.

Gibson, W. C., et al. (2000), The IMAGE Observatory, *Space Sci. Rev.*, *91*, 15–50.

Gilmer, G. H., H. Huang, T. Diaz de la Rubia, J. Dalla Torre, and F. Baumann (2000), Lattice Monte Carlo models of thin film deposition, *Thin Solid Films*, *365*, 189–200.

Glazov, V. M., and A. S. Pashinkin (2001), The Thermophysical Properties (Heat Capacity and Thermal Expansion) of Single-Crystal Silicon, *High Temperature*, *39*(3), 413–419.

Gleizes, A., J. J. Gonzalez, and P. Freton (2005), Thermal plasma modelling, *J. Phys. D: Appl. Phys*, *38*, R153–R183.

Gloeckler, G., and J. Geiss (1998), Interstellar and Inner Source Pickup Ions Observed with SWICS on ULYSSES, *Space Sci. Rev.*, *86*, 127–159.

Gloeckler, G., and J. Geiss (2004), Composition of the local interstellar medium as diagnosed with pickup ions, *Adv. Space Res.*, *34*, 53–60.

Gloeckler, G., and K. C. Hsieh (1979), Time-of-flight technique for particle identification at energies from 2 to 400 keV/nucleon, *Nucl. Instrum. Methods*, *165*, 537–544.

Gloeckler, G., N. A. Schwadron, L. A. Fisk, and J. Geiss (1995), Weak pitch angle scattering of few MV rigidity ions from measurments of anisotropies in the distribution function of interstellar pickup H+, *Geophys. Res. Lett.*, *22*(19), 2665–2668.

Gloeckler, G., L. A. Fisk, J. Geiss, N. A. Schwadron, and T. H. Zurbuchen (2000a), Elemental composition of the inner source pickup ions, *J. Geophys. Res.*, *105*, 7459–7464.

Gloeckler, G., J. Geiss, N. A. Schwadron, L. A. Fisk, T. H. Zurbuchen, F. M. Ipavich, R. von Steiger, H. Balsiger, and B. Wilken (2000b), Interception of comet Hyakutake's ion tail at a distance of 500 million kilometres, *Nature*, *404*, 576–578.

Gloeckler, G., J. Geiss, and L. A. Fisk (2001), Heliospheric and interstellar phenomena revealed from observations of pickup ions., in *"The heliosphere near solar minimum. The Ulysses perspective"*, edited by A. Balogh, R. G. Marsden, and E. J. Smith, pp. 287–326, Springer-Praxis Books, London.

Gloeckler, G., F. Allegrini, H. A. Elliott, D. J. McComas, N. A. Schwadron, J. Geiss, R. von Steiger, and G. H. Jones (2004a), Cometary Ions Trapped in a Coronal Mass Ejection, *Astrophy. J. Lett.*, *604*, L121–L124.

Gloeckler, G., et al. (1992), The Solar Wind Ion Composition Spectrometer, *Astron. Astrophys. Suppl. Ser.*, *92*, 267–289.

Gloeckler, G., et al. (1998), Investigation of the composition of solar and interstellar matter using solar wind and pickup ion measurements with SWICS and SWIMS on the ACE spacecraft, *Space Sci. Rev.*, *86*, 497–539.

Gloeckler, G., et al. (2004b), Observations of the helium focusing cone with pickup ions, *Astron. Astrophys.*, *426*, 845–854.

Gobet, J., F. Cardot, J. Bergqvist, and F. Rudolf (1993), Electrodeposition of 3D microstructures on silicon, *J. Micromech. Microeng.*, *3*, 123–130.

Gombosi, T. (1998), *Physics of the space environment*, Cambridge University Press.

Gösele, U. M. (1986), Point defects and diffusion mechanisms in crystalline semiconductors, in *Festkörperprobleme 26, Advances in Solid State Physics*, pp. 89–112, Springer Berlin/Heidelberg.

Grevesse, N., M. Asplund, and A. J. Sauval (2007), The Solar Chemical Composition, *Space Sci. Rev.*, *130*, 105–114.

Gronniger, G., B. Barwick, H. Batelaan, T. Savas, D. Pritchard, and A. Cronin (2005), Electron diffraction from free-standing, metal-coated transmission gratings, *Appl. Phys. Lett.*, *87*, 124,104.

Grün, E., and M. Landgraf (2001), Fast Dust in the Heliosphere, *Space Sci. Rev.*, *99*(1), 151–164.

Gruntman, M. (1995), Extreme-ultraviolet radiation filtering by freestanding transmission gratings, *Appl. Opt.*, *34*(25), 5732–5737.

Gruntman, M. (1997a), Energetic neutral atom imaging of space plasmas, *Rev. Sci. Inst.*, *68*, 3617–3656.

Gruntman, M. (1997b), Transmission grating filtering of 52–140-nm radiation, *Appl. Opt*, *36*, 2203–2205.

Gruntman, M., and V. Izmodenov (2004), Mass transport in the heliosphere by energetic neutral atoms, *J. Geophys. Res.*, *109*, A12,108.

Gruntman, M. A. (1994a), Neutral solar wind properties: Advance warning of major geomagnetic storms, *J. Geophys. Res.*, *99*(A10), 19–213.

Gruntman, M. A. (1994b), A new collimator design for energetic neutral atom instruments, *Rev. Sci. Inst.*, *65*(3), 758.

Guenther, D., P. Demarque, Y. Kim, and M. Pinsonneault (1992), Standard solar model, *Astrophys. J.*, *387*, 372.

Guhathakurta, M., E. C. Sittler, and L. Ofman (2006), Semiempirically derived heating function of the corona heliosphere during the Whole Sun Month, *J. Geophys. Res.*, *111*(A10), 11,215–+.

Guo, L. J. (2007), Nanoimprint Lithography: Methods and Material Requirements, *Adv. Mater.*, *19*, 495–513.

Hamilton, D. C., G. Gloeckler, F. M. Ipavich, R. A. Lundgren, R. B. Sheldon, and D. Hovestadt (1990), New high-resolution electrostatic ion mass analyzer using time of flight, *Rev. Sci. Inst.*, *61*, 3104.

Hecht, E. (1990), *Optics*, Addison-Wesley, Reading, MA.

Heckele, M., and W. K. Schomburg (2004), Review on micro molding of thermoplastic polymers, *J. Micromech. Microeng*, *14*(3), 1–14.

Helmersson, U., M. Lattemann, J. Bohlmark, A. P. Ehiasarian, and J. T. Gudmundsson (2006), Ionized physical vapor deposition (IPVD): A review of technology and applications, *Thin Solid Films*, *513*, 1–24.

Henrie, J., S. Kellis, S. M. Schultz, and A. Hawkins (2004), Electronic color charts for dielectric films on silicon, *Opt. Express*, *12*(7), 1464–1489.

Herrero, F. (1992), Light-trap design using multiple reflections and solid-angle attenuation-Application to a spaceborne electron spectrometer, *Appl. Opt.*, *31*(25), 5331–5340.

Higashi, G. S., Y. J. Chabal, G. W. Trucks, and K. Raghavachari (1990), Ideal hydrogen termination of the Si (111) surface, *Appl. Phys. Lett.*, *56*(7), 656–658.

Hirai, Y., T. Konishi, T. Yoshikawa, and S. Yoshida (2004), Simulation and experimental study of polymer deformation in nanoimprint lithography, *J. Vac. Sci. Technol. B*, *22*, 3288.

Ho, K. H., and S. T. Newman (2003), State of the art electrical discharge machining (EDM), *Int. J. Mach. Tools Manuf.*, *43*(13), 1287–1300.

Hölke, A., and H. T. Henderson (1999), Ultra-deep anisotropic etching of (110) silicon, *J. Micromech. Microeng*, *9*, 51–57.

Hollenstein, C. (2000), The physics and chemistry of dusty plasmas, *Plasma Phys. Control. Fus.*, *42*(10), 93–104.

Holmes, A. S. (2002), Laser processes for MEMS manufacture., *Riken Rev.*, *43*, 63–69.

Holzer, T. (1977), Neutral hydrogen in interplanetary space, *Rev. Geophys*, *15*, 467–490.

Holzer, T. E. (2005), Heating and acceleration of the solar plasma, *Proc. Solar Wind 11/SOHO 16*.

Hovestadt, D., et al. (1995a), CELIAS - Charge, Element and Isotope Analysis System for SOHO, *Solar Physics*, *162*, 441–481.

Hovestadt, D., et al. (1995b), The Charge, Element, and Isotope Analysis System CELIAS on SOHO, in *Coronal Magnetic Energy Releases*, *Lecture Notes in Physics, Berlin Springer Verlag*, vol. 444, edited by A. O. Benz and A. Krüger, pp. 271–278.

Hsieh, K. C., E. Keppler, and G. Schmidtke (1979), Forward photoemission from thin carbon foils, *Appl. Opt.*, *18*(22), 3732–3733.

Hsieh, K. C., E. Keppler, and G. Schmidtke (1980), Extreme ultraviolet induced forward photoemission from thin carbon foils, *J. Appl. Phys.*, *51*, 2242.

Hsieh, K. C., B. R. Sandel, V. A. Drake, and R. S. King (1991), H Lyman a transmittance of thin C and Si/C foils for keV particle detectors, *Nucl. Inst. Meth. Phys. Res., B*, *61*, 187–193.

Hsieh, K. C., T. H. Zurbuchen, J. Orr, G. Gloeckler, and M. Hilchenbach (2004), A collimator design for monitoring heliospheric energetic neutral atoms at 1 AU, *Adv. Space Res.*, *34*(1), 213–218.

Huang, C., and K. Najafi (2001), Fabrication of Ultrathin p++ Silicon Microstructures Using Ion Implantation and Boron Etch-Stop, *J. Microelectromech. Syst.*, *10*(4), 532–537.

Huen, T. (1979), Reflectance of thinly oxidized silicon at normal incidence, *Appl. Opt.*, *18*(12), 1927–1932.

Humbird, D., and D. B. Graves (2004), Fluorocarbon plasma etching of silicon: Factors controlling etch rate, *J. Appl. Phys.*, *96*, 65.

Hwang, D. J., C. P. Grigoropoulos, and T. Y. Choi (2006), Efficiency of silicon micromachining by femtosecond laser pulses in ambient air, *J. Appl. Phys.*, *99*, 083,101.

Isenberg, P. A. (1987), Evolution of interstellar pickup ions in the solar wind, *J. Geophys. Res.*, *92*, 1067–1073.

Isenberg, P. A., and B. J. Vasquez (2007), Preferential Perpendicular Heating of Coronal Hole Minor Ions by the Fermi Mechanism, *Astrophys. J.*, *668*, 546–556.

Ishihara, O. (2007), Complex plasma: dusts in plasma, *J. Phys. D.*, *40*(8).

Issautier, K. (2006), Some basic aspects of the solar wind, *Lecture notes in physics*, *699*, 25–52.

Iwasaki, H., T. Yoshinobu, and K. Sudoh (2003), Nanolithography on SiO_2/Si with a scanning tunnelling microscope, *Nanotechnology*, *14*(11), R55–R62.

Jackson, J. D. (1998), *Classical Electrodynamics*, third ed., John Wiley & Sons Inc., Hoboken, New Jersey.

Jafri, I. H., H. Busta, and S. T. Walsh (2003), Critical point drying and cleaning for MEMS technology, *Proc. SPIE*, *3880*, 51.

Jansen, H., H. Gardeniers, M. de Boer, M. Elwenspoek, and J. Fluitman (1996), A survey on the reactive ion etching of silicon in microtechnology, *J. Micromech. Microeng.*, *6*(1), 14–28.

Joglekar, A. P., H. Liu, E. Meyhöfer, G. Mourou, and A. J. Hunt (2004), Optics at critical intensity: Applications to nanomorphing, *Proc. Natl. Acad. Sci.*, *101*, 5856–5861.

Jokipii, J. R., and B. Thomas (1981), Effects of drift on the transport of cosmic rays. IV- Modulation by a wavy interplanetary current sheet, *Astrophys. J.*, *243*, 1115.

JPL (1993), Proc. Workshop on Microtechnologies and Applications to Space Systems held at the Jet Propulsion Laboratory 27-28 May 1992, JPL Publ. 93-8; NASA-CR-195688.

Jung, G. Y., Z. Li, W. Wu, Y. Chen, D. L. Olynick, S. Y. Wang, W. M. Tong, and R. S. Williams (2005), Vapor-Phase Self-Assembled Monolayer for Improved Mold Release in Nanoimprint Lithography, *Langmuir*, *21*(4), 1158–1161.

Kaiser, N. (2002), Review of the fundamentals of thin-film growth, *Appl. Opt.*, *41*, 3053–3060.

Kallenbach, R., J. Geiss, G. Gloeckler, and R. von Steiger (2000), Pick-up Ion Measurements in the Heliosphere - A Review, *Astrophys. and Space Sci.*, *274*, 97–114.

Kallenbach, R., K. Bamert, and M. Hilchenbach (2007), Isotopic Composition of the Solar Wind Inferred from In-Situ Spacecraft Measurements, *Space Sci. Rev.*, *130*, 173–182.

Kaminsky, G. (1985), Micromachining of silicon microstructures, *J. Vac. Sci. Technol. B*, *3*(4), 1015–1024.

Kang, M. K., B. Li, P. S. Ho, and R. Huang (2008), Buckling of Single-Crystal Silicon Nanolines under Indentation, *J. Nanomat.*

Kawata, H., M. Yasuda, and Y. Hirai (2006), Si Etching with High Aspect Ratio and Smooth Side Profile for Mold Fabrication, *Jpn. J. Appl. Phys.*, *45*(6B), 5597–5601.

Keller, U. (2003), Recent developments in compact ultrafast lasers, *Nature*, *424*, 831–838.

Kennedy, D. P., and R. R. O'Brien (1965), Analysis of the Impurity Atom Distribution Near the Diffusion Mask for a Planar p-n Junction, *IBM J. Res. Dev.*, *9*(3), 179–186.

Khang, D. Y., H. Kang, T. Kim, and H. H. Lee (2004), Low-pressure nanoimprint lithography, *Nano Lett.*, *4*(4), 633–637.

Kihm, J. E., Y. C. Yee, K. G. Park, D. J. Kim, D. S. Ropers, C. Lienau, C. Park, J. W. Kim, and J. Q. H. Park (2005), Positive and negative band gaps, Rayleigh-Wood's anomalies in plasmonic band-gaps structures, *Quantum Electronics and Laser Science Conference, 2005. QELS'05*, *1*.

Kimura, H., and I. Mann (1998), The Electric Charging of Interstellar Dust in the Solar System and Consequences for Its Dynamics, *Astrophys. J.*, *499*(1), 454–462.

Kimura, H., H. Ishimoto, and T. Mukai (1997), A study on solar dust ring formation based on fractal dust models, *Astron. Astrophys*, *326*, 263–270.

Kimura, H., H. Okamoto, and T. Mukai (2002), Radiation Pressure and the Poynting–Robertson Effect for Fluffy Dust Particles, *Icarus*, *157*(2), 349–361.

Kloeck, B., S. D. Collins, N. F. De Rooij, and R. L. Smith (1989), Study of Electrochemical Etch-Stop for High-Precision Thickness Control of Silicon Membranes, *IEEE Trans. Electron Dev.*, *36*(4), 663–669.

Koehn, P. L. (2002), The development and testing of the fast imaging plasma spectrometer and its application in the plasma environment at Mercury, Ph.D. thesis, Univ. of Mich., Ann Arbor.

Koehn, P. L., T. H. Zurbuchen, G. Gloeckler, R. A. Lundgren, and L. A. Fisk (2002), Measuring the plasma environment at Mercury: The fast imaging plasma spectrometer, *Meteoritics and Planetary Science*, *37*, 1173–1189.

Kohl, J., G. Noci, S. Cranmer, and J. Raymond (2006), Ultraviolet spectroscopy of the extended solar corona, *Astron. Astrophys. Rev.*, *13*(1), 31–157.

Kovacs, G. T. A. (1998), *Micromachined Transducers Handbook*, Mcgraw-Hill.

Kovacs, G. T. A., N. I. Maluf, and K. E. Petersen (1998), Bulk micromachining of silicon, *Proc. IEEE*, *86*(8), 1536–1551.

Krause, L. H., C. L. Enloe, R. K. Haaland, and P. Golando (2005), Microsatellite missions to conduct midlatitude studies of equatorial ionospheric plasma bubbles, *Adv. Space Res.*, *36*(12), 2474–2479.

Krivov, A., H. Kimura, and I. Mann (1998), Dynamics of Dust near the Sun, *Icarus*, *134*, 311–327.

Krüger, H., M. Landgraf, N. Altobelli, and E. Grün (2007), Interstellar Dust in the Solar System, *Space Sci. Rev.*, *130*, 401–408.

Kudryashov, S. I., A. Joglekar, G. Mourou, A. A. Ionin, V. D. Zvorykin, and A. J. Hunt (2007a), Mechanisms of femtosecond laser nanomachining of dielectric surfaces, *Proc. SPIE*, *6459*, 64,590N.

Kudryashov, S. I., A. Joglekar, G. Mourou, A. A. Ionin, V. D. Zvorykin, and A. J. Hunt (2007b), Femtosecond laser surface ablation of transparent solids: understanding the bulk filamentation damage, *Proc. SPIE*, *6733*, 67,332H.

Lallement, R., J. C. Raymond, J.-L. Bertaux, E. Quémerais, Y.-K. Ko, M. Uzzo, D. McMullin, and D. Rucinski (2004a), Solar cycle dependence of the helium focusing cone from SOHO/UVCS observations. Electron impact rates and associated pickup ions, *Astron. Astrophys.*, *426*, 867–874.

Lallement, R., J. C. Raymond, J. Vallerga, M. Lemoine, F. Dalaudier, and J. L. Bertaux (2004b), Modeling the interstellar-interplanetary helium 58.4 nm resonance glow: Towards a reconciliation with particle measurements., *Astron. Astrophys.*, *426*, 875–884.

Lallement, R., J. R. Raymond, and J. Vallerga (2004), Diagnostics of the Local Interstellar Medium using particles and UV radiation, *Adv. Space Res.*, *34*(1), 46–52.

Lan, H., Y. Ding, H. Liu, and B. Lu (2007), Review of the wafer stage for nanoimprint lithography, *Microelectronic Eng.*, *84*(4), 684–688.

Landi Degl'Innocenti, E. (2003), The Zeeman effect: applications to solar physics, *Astronomische Nachrichten*, *324*(4), 393–394.

Landolt, D. (2002), Electrodeposition Science and Technology in the Last Quarter of the Twentieth Century, *J. Electrochem. Soc.*, *149*(3), S9–S20.

Lärmer, F., and A. Schilp (1996), Method for anisotropic plasma etching of substrate, *USA Patent*, *5501893*, Robert Bosch GmbH.

Lasue, J., A. C. Levasseur-Regourd, N. Fray, and H. Cottin (2007), Inferring the interplanetary dust properties. from remote observations and simulations, *Astron. Astrophys.*, *473*, 641–649.

Lean, J. (1987), Solar ultraviolet irradiance variations- A review, *J. Geophys. Res.*, *92*, 839–868.

Leary, J. C., et al. (2007), The MESSENGER Spacecraft, *Space Sci. Rev.*, *131*, 187–217.

Leinert, C., and E. Grün (1990), *Interplanetary Dust*, pp. 207–282, Physics of the Inner Heliosphere I: Large-scale Phenomena.

Leinert, C., et al. (1998), 1997 reference of diffuse night sky brightness, *Astron. Astrophys. Suppl. Ser.*, *127*, 1–99.

Lepri, S. T., T. H. Zurbuchen, L. A. Fisk, I. G. Richardson, H. V. Cane, and G. Gloeckler (2001), Iron charge distribution as an identifier of interplanetary coronal mass ejections, *J. Geophys. Res*, *106*(A12), 29,23129,238.

Leskelä, M., and M. Ritala (2002), Atomic layer deposition (ALD): from precursors to thin film structures, *Thin Solid Films*, *409*, 138–146.

Leskelä, M., M. Kemell, K. Kukli, V. Pore, E. Santala, M. Ritala, and J. Lu (2007), Exploitation of atomic layer deposition for nanostructured materials, *Mater. Sci. Eng. C*, *27*, 1504–1508.

Levasseur-Regourd, A. C., T. Mukai, J. Lasue, and Y. Okada (2007), Physical properties of cometary and interplanetary dust, *Planetary and Space Science*, *55*, 1010–1020.

Li, B., M. K. Kang, K. Lu, R. Huang, P. S. Ho, R. A. Allen, and M. W. Cresswell (2008), Fabrication and Characterization of Patterned Single-Crystal Silicon Nanolines, *Nano Lett.*, *8*(1), 92–98.

Li, G., C. Zhou, and E. Dai (2005), Splitting of femtosecond laser pulses by using a Dammann grating and compensation gratings, *J. Opt. Soc. Amer. A*, *22*(4), 767–772.

Liang, E. Z., C. J. Huang, and C. F. Lin (2004), 20 nm silicon nanorods fabricated by reactive ion etch, *IEEE Conf. Nanotechnol.*, pp. 482–484.

Lii, Y. J., J. Jorné, K. C. Cadien, and J. E. Schoenholtz Jr (1990), Plasma Etching of Silicon in SF, *J. Electrochem. Soc.*, *137*, 3633.

Lill, T., and O. Joubert (2008), MATERIALS SCIENCE: The Cutting Edge of Plasma Etching, *Science*, *319*(5866), 1050.

Lin, C. H., and R. Chen (2006), Ultrasonic nanoimprint lithography: a new approach to nanopatterning, *J. Microlith. Microfab. Microsys.*, *5*, 011,003.

Linder, C., L. Paratte, M. A. Gretillat, V. P. Jaecklin, and N. F. de Rooij (1992), Surface Micromachining, *J. Micromech. Microeng.*, *2*, 122–132.

Liu, H.-C., Y.-H. Lin, B. C. S. Chou, Y.-Y. Hsu, and W. Hsu (2001), Parameters study to improve sidewall roughness in advanced silicon etch process, *Proc. SPIE*, *4592*, 503–513.

Lodders, K. (2003), Solar System Abundances and Condensation Temperatures of the Elements, *Astrophys. J.*, *591*(2), 1220–1247.

Lotz, W. (1967), Electron-Impact Ionization Cross-Sections and Ionization Rate Coefficients for Atoms and Ions, *Astrophys. J. Suppl. Ser.*, *14*, 207–+.

Maboudian, R., and R. T. Howe (1997), Critical Review: Adhesion in surface micromechanical structures, *J. Vac. Sci. Technol. B*, *15*, 1–20.

Madou, M. J. (2002), *Fundamentals of Microfabrication*, second ed., CRC Press.

Mahalik, N. (2008), Principle and applications of MEMS: a review, *Int. J. Manufac. Technol. and Management*, *13*(2-4), 324–343.

Mai, T. A., B. Richerzhagen, P. C. Snowdon, D. Wood, and P. G. Maropoulos (2007), The Laser MicroJet (LMJ): a multi-solution technology for high quality micromachining, *Proc. SPIE*, *6459*, 64,590.

Mann, I. (1998), Zodiacal Cloud Complexes, *Earth, Planets, and Space*, *50*, 465–471.

Mann, I. (2008), Interplanetary medium: A dusty plasma, *Adv. Space Res.*, *41*, 160–167.

Mann, I., and H. Kimura (2000), Interstellar dust properties derived from mass density, mass distribution, and flux rates in the heliosphere, *J. Geophys. Res.*, *105*, 10,317–10,328.

Mann, I., and E. Murad (2005), On the Existence of Silicon Nanodust near the Sun, *Astrophys. J. Lett.*, *624*, L125–L128.

Mann, I., H. Okamoto, T. Mukai, H. Kimura, and Y. Kitada (1994), Fractal aggregate analogues for near solar dust properties, *Astron. Astrophys.*, *291*(3), 1011–1018.

Mann, I., A. Krivov, and H. Kimura (2000), Dust Cloud near the Sun, *Icarus*, *146*, 568–582.

Mann, I., E. Murad, and A. Czechowski (2007), Nanoparticles in the inner solar system, *Planetary and Space Science*, *55*(9), 1000–1009.

Mann, I., et al. (2004), Dust Near The Sun, *Space Sci. Rev.*, *110*, 269–305.

Marrian, C. R. K., and D. M. Tennant (2003), Nanofabrication, *J. Vac. Sci. Technol. A*, *21*, S207.

Marty, F., B. Saadany, T. Bourouina, Y. Mita, and T. Shibata (2005), High aspect ratio nano-structures (HARNS) for photonic MEMS based on vertical DBR architecture, *Proc. 13th Intl. Conf. Solid-State Sens. Act. Microsys. TRANSDUCERS'05.*, *1*.

Matsui, S., and Y. Ochiai (1996), Focused ion beam applications to solid state devices, *Nanotechnology*, *7*(3), 247–258.

McCann, D., S. Barabash, H. Nilsson, and A. Bhardwaj (2007), Miniature ion mass analyzer, *Planet. Space Sci.*, *55*(9), 1190–1196.

McComas, D. J., and J. E. Nordholt (1990), New approach to 3-D, high sensitivity, high mass resolution space plasma composition measurements, *Rev. Sci. Inst.*, *61*, 3095.

McComas, D. J., J. E. Nordholt, S. J. Bame, B. L. Barraclough, and J. T. Gosling (1990), Linear electric field mass analysis: a technique for three-dimensional high mass resolution space plasma composition measurements., *Proc. Natl. Acad. Sci.*, *87*(15), 5925.

McComas, D. J., F. Allegrini, C. J. Pollock, H. O. Funsten, S. Ritzau, and G. Gloeckler (2004), Ultrathin (10 nm) carbon foils in space instrumentation, *Rev. Sci. Inst.*, *75*, 4863.

McComas, D. J., et al. (2007), Understanding coronal heating and solar wind acceleration: Case for in situ near-Sun measurements, *Rev. Geophys.*, *45*, G1004+.

McDonald, A., J. Klein, and D. Wark (2003), Solving the Solar Neutrino Problem, *Scientific American*, *288*(4), 22–31.

McMorran, B., J. D. Perreault, T. A. Savas, and A. Cronin (2006), Diffraction of 0.5 keV electrons from free-standing transmission gratings, *Ultramicroscopy*, *106*(4-5), 356–364.

McMullin, D. R., D. L. Judge, C. Tarrio, R. E. Vest, and F. Hanser (2004), Extreme-Ultraviolet Efficiency Measurements of Freestanding Transmission Gratings, *Appl. Opt.*, *43*(19), 3797–3801.

McMullin, D. R., et al. (2004), Heliospheric conditions that affect the interstellar gas inside the heliosphere, *Astron. Astrophys.*, *426*, 885–895.

Meschede, D., and H. Metcalf (2003), Atomic nanofabrication: atomic deposition and lithography by laser and magnetic forces, *J. Phys. D*, *36*(3), R17–R38.

Michels, J. G., et al. (2002), The Helium Focusing Cone of the Local Interstellar Medium Close to the Sun, *Astrophys. J.*, *568*, 385–395.

Minato, T., M. Köhler, H. Kimura, I. Mann, and T. Yamamoto (2004), Momentum transfer to interplanetary dust from the solar wind, *Astron. Astrophys.*, *424*, L13–L16.

Miralles, M. P., S. R. Cranmer, and J. L. Kohl (2006), Coronal Hole Properties During the First Decade of UVCS/SOHO, in *SOHO-17. 10 Years of SOHO and Beyond*, *ESA Special Publication*, vol. 617.

Möbius, E., et al. (1999), Direct evidence of the interstellar gas flow velocity in the pickup ion cut-off as observed with SOHO CELIAS CTOF, *Geophys. Res. Lett.*, *26*, 3181–3184.

Möbius, E., et al. (2004), Synopsis of the interstellar He parameters from combined neutral gas, pickup ion and UV scattering observations and related consequences, *Astron. Astrophys.*, *426*, 897–907.

Mohd Abbas, N., D. G. Solomon, and M. Fuad Bahari (2007), A review on current research trends in electrical discharge machining (EDM), *Int. J. Mach. Tools Manuf.*, *47*(7-8), 1214–1228.

Mok, K. R. C., F. Benistant, M. Jaraiz, J. E. Rubio, P. Castrillo, R. Pinacho, and M. P. Srinivasan (2008), Comprehensive model of damage accumulation in silicon, *J. Appl. Phys.*, *103*, 014,911.

Moore, T. E., et al. (1995), The Thermal Ion Dynamics Experiment and Plasma Source Instrument, *Space Sci. Rev.*, *71*, 409–458.

Moore, T. E., et al. (2000), The low-energy neutral atom imager for IMAGE, *Space Sci. Rev.*, *91*, 155–195.

Morgan, C. J., R. R. Vallance, and E. R. Marsh (2006), Micro-machining and micro-grinding with tools fabricated by micro electro-discharge machining, *Int. J. Nanomanuf.*, *1*(2), 242–258.

Moshfegh, A. Z. (2004), PVD Growth Method: Physics and Technology, in *Proc. Int. Workshop Physics and Technol. Thin Films*, edited by A. Z. Moshfegh, H. V. Känel, S. C. Kashyap, and M. Wuttig, p. 28, World Scientific Publishing Co, Singapore.

Mühlberger, M., et al. (2007), A Moiré method for high accuracy alignment in nanoimprint lithography, *Microelectronic Eng.*, *84*(5-8), 925–927.

Mukai, T., and T. Yamamoto (1982), Solar wind pressure on interplanetary dust, *Astron. Astrophys.*, *107*, 97–100.

Mukherjee, P., M.-G. Kang, T. H. Zurbuchen, L. J. Guo, and F. A. Herrero (2007), Fabrication of high aspect ratio nanogratings with smooth sidewalls for a deep uv-blocking filter, *J. Vac. Sci. Technol. B*, *25*(6), 2645–2648.

Muller, L. (1995), Microelectromechanical Systems(MEMS) technology integration into microspacecraft, *AIAA/Utah State 9th Univ. Ann. Conf. Small Satellites*.

Muller, L., M. H. Hecht, L. M. Miller, H. K. Rockstad, and J. C. Lyke (1996), Packaging and qualification of MEMS-based space systems, *IEEE Proc. 9th Ann. Int. Workshop on MEMS, MEMS'96*, pp. 503–508.

Murphy, A. B. (2001), Thermal plasmas in gas mixtures, *J. Phys. D: Appl. Phys.*, *34*(20), R151–R173.

Najafi, K. (1991), Smart sensors, *J. Micromech. Microeng.*, *1*(2), 86–102.

Najafi, K., and C. Mastrangelo (1993), Solid-state microsensors and smart structures, *Proc. IEEE Ultrasonics Symp.*, pp. 341–350.

Newman, J. D., M. W. Kowarz, J. G. Phalen, P. P. K. Lee, and A. D. Cropper (2006), MEMS programmable spectral imaging system for remote sensing, *Proc. SPIE*, *6220*, 622,006.

Nichols, C. S., C. G. Van de Walle, and S. T. Pantelides (1989), Mechanisms of dopant impurity diffusion in silicon, *Phys. Rev. B*, *40*(8), 5484–5497.

Novikov, N. V., Y. A. Teplova, and V. V. Bondurko (2007), Energy and charge distributions of fast nitrogen ions reflected from metal surface at grazing incidence, *Nucl. Inst. Meth. Phys. Res., B*, *256*(1), 21–23.

O'Brien, G., D. J. Monk, and K. Najafi (2001), Sub-micron high aspect ratio silicon beam etch, *Proc. SPIE*, *4592*, 315–325.

Oehrlein, G. S., and Y. Kurogi (1998), Sidewall surface chemistry in directional etching processes, *Mat. Sci. Eng. R*, *24*(4), 153–183.

Oehrlein, G. S., and J. F. Rembetski (1992), Plasma-based dry etching techniques in the silicon integrated circuit technology, *IBM J. Res. Dev.*, *36*(2), 140–157.

Oehrlein, G. S., Y. Zhang, D. Vender, and M. Haverlag (1994a), Fluorocarbon high-density plasmas. I. Fluorocarbon film deposition and etching using CF and CHF, *J. Vac. Sci. Technol. A*, *12*, 323.

Oehrlein, G. S., Y. Zhang, D. Vender, and O. Joubert (1994b), Fluorocarbon high-density plasmas. II. Silicon dioxide and silicon etching using CF and CHF, *J. Vac. Sci. Technol. A*, *12*, 333.

Ohring, M. (2002), *Materials Science of Thin Films*, second ed., Academic Press.

Osellame, R., et al. (2005), Optical properties of waveguides written by a 26 MHz stretched cavity Ti: sapphire femtosecond oscillator, *Opt. Exp.*, *13*(2), 612–620.

Ostendorf, A., G. Kamlage, and B. N. Chichkov (2003), Precise deep drilling of metals by femtosecond laser pulses, *Riken Rev.*, *50*, 87–89.

Ostrikov, K. (2005), Reactive plasmas as a versatile nanofabrication tool, *Rev. Mod. Phys.*, *77*(2), 489–511.

Ostrikov, K., and A. B. Murphy (2007), Plasma-aided nanofabrication: where is the cutting edge?, *J. Phys. D: Appl. Phys.*, *40*(8), 2223–2241.

Pal, P., K. Sato, and S. Chandra (2007), Fabrication techniques of convex corners in a (1 0 0)-silicon wafer using bulk micromachining: a review, *J. Micromech. Microeng*, *17*, R111–R133.

Palik, E. D. (1985), *Handbook of Optical Constants of Solids*, Academic Press.

Palik, E. D. (1991), *Handbook of Optical Constants of Solids II*, Academic Press.

Paolini, F. (1967), Charged Particle Transmission Through Spherical Plate Electrostatic Analyzers, *Rev. Sci. Inst.*, *38*(5), 579.

Parker, E. N. (1958), Dynamics of the Interplanetary Gas and Magnetic Fields, *Astrophys. J*, pp. 664–676.

Parker, E. N. (1960), The Hydrodynamic Treatment of the Expanding Solar Corona., *Astrophys. J.*, *132*(3), 821–866.

Pelletier, J., and A. Anders (2005), Plasma-based ion implantation and deposition: A review of physics, technology, and applications, *IEEE Trans. Plasma Sci.*, *33*(6), 1944–1959.

Petersen, K. E. (1982), Silicon as a mechanical material, *Proc. IEEE*, *70*(5), 420–457.

Phipps, C. (2003), Laser applications overview: The state of the art and the future trend in the United States, *Riken Rev.*, *50*, 11–19.

Pollock, C. J., et al. (2000), Medium energy neutral atom (MENA) imager for the IMAGE mission, *Space Sci. Rev.*, *91*, 113–154.

Powell, K. G., P. L. Roe, T. J. Linde, T. I. Gombosi, and D. De Zeeuw (1999), A solution-adaptive upwind scheme for ideal magnetohydrodynamics, *J. Comp. Phys.*, *154*(2), 284–309.

Priest, E. R., C. R. Foley, J. Heyvaerts, T. D. Arber, D. Mackay, J. L. Culhane, and L. W. Acton (2000), A Method to Determine the Heating Mechanisms of the Solar Corona, *Astrophys. J.*, *539*(2), 1002–1022.

Quémerais, E., R. Lallement, D. Koutroumpa, and P. Lamy (2007), Velocity Profiles in the Solar Corona from Multi-Instrument Observations, *Astrophys. J.*, *667*, 1229–1234.

Radelaar, S. (1993), Technology and fabrication of quantum devices: Submicron lithography and etching techniques, in *Physics and Technology of Semiconductor Quantum Devices*, *Lecture Notes in Physics, Berlin Springer Verlag*, vol. 419, edited by K. H. Ploog and L. Tapfer, pp. 27–51.

Raether, H. (1988), *Surface plasmons on smooth and rough surfaces and on gratings*, Springer-Verlag New York.

Rajurkar, K. P., G. Levy, A. Malshe, M. M. Sundaram, J. McGeough, X. Hu, R. Resnick, and A. DeSilva (2006), Micro and Nano Machining by Electro-Physical and Chemical Processes, *CIRP Ann.*, *55*(2), 643–666.

Randhawa, H. (1991), Review of plasma-assisted deposition processes, *Thin Solid Films*, *196*, 329–349.

Reisenfeld, D. B., et al. (2007), Elemental Abundances of the Bulk Solar Wind: Analyses from Genesis and ACE, *Space Sci. Rev.*, *130*, 79–86.

Reiter, D. (2008), The Monte Carlo Method, an Introduction, *Lecture Notes in Physics*, *739*, 63.

Resnick, D. J., S. V. Sreenivasan, and C. G. Willson (2005), Step & flash imprint lithography, *Materials Today*, *8*(2), 34–42.

Rizvi, N. H. (2003), Femtosecond laser micromachining: Current status and applications., *Riken Rev.*, *50*, 107–112.

Robbins, H., and B. Schwartz (1959), Chemical Etching of Silicon I: The System HF, HNO_3, and H_2O, *J. Electrochem. Soc.*, *106*(7), 505–508.

Robbins, H., and B. Schwartz (1960), Chemical Etching of Silicon II: The System HF, HNO_3, H_2O, and $HC_2C_3O_2$, *J. Electrochem. Soc.*, *107*(2), 108–111.

Rogers, J. A., and R. G. Nuzzo (2005), Recent progress in soft lithography, *Materials Today*, *8*(2), 50–56.

Romoli, M., C. Benna, S. Fineschi, L. D. Gardner, J. L. Kohl, and G. Noci (1998), The white light polarimeter of SOHO/UVCS, *Memorie della Societa Astronomica Italiana*, *69*, 703–+.

Romoli, M., et al. (2003), The Ultraviolet and Visible-light Coronagraph of the HERSCHEL experiment, in *Solar Wind Ten*, *American Institute of Physics Conference Series*, vol. 679, edited by M. Velli, R. Bruno, F. Malara, and B. Bucci, pp. 846–849.

Rossnagel, S. M. (1999), Sputter deposition for semiconductor manufacturing, *IBM J. Res. Develop.*, *43*(1), 163.

Rossnagel, S. M. (2003), Thin film deposition with physical vapor deposition and related technologies, *J. Vac. Sci. Technol. A*, *21*(5), S74–S97.

Roy, S. (2007), Fabrication of micro-and nano-structured materials using mask-less processes, *J. Phys. D: Appl. Phys.*, *40*(22), R413–R426.

Rucinski, D., and M. Bzowski (1995), Modulation of interplanetary hydrogen density distribution during the solar cycle., *Astron. Astrophys.*, *296*, 248–+.

Ruciński, D., and M. Bzowski (1996), Modelling of the Interstellar Hydrogen Distribution in the Heliosphere, *Space Sci. Rev.*, *78*, 265–276.

Ruciński, D., A. C. Cummings, G. Gloeckler, A. J. Lazarus, E. Möbius, and M. Witte (1996), Ionization processes in the heliosphere —Rates and methods of their determination, *Space Sci. Rev.*, *78*, 73–84.

Ruciński, D., M. Bzowski, and H. J. Fahr (2003), Imprints from the solar cycle on the helium atom and helium pickup ion distributions, *Annales geophysicae*, *21*(6), 1315–1330.

Rueger, N. R., J. J. Beulens, M. Schaepkens, M. F. Doemling, J. M. Mirza, T. Standaert, and G. S. Oehrlein (1997), Role of Steady State Fluorocarbon Films in the Etching of Silicon Dioxide using CHF3 in an Inductively Coupled Plasma Reactor, *J. Vac. Sci. Technol. A*, *15*(4), 1881–1889.

Sablik, M. J., D. Golimowski, J. R. Sharber, and J. D. Winningham (1988), Computer simulation of a 360 field-of-view top-hatelectrostatic analyzer, *Rev. Sci. Inst.*, *59*, 146.

Schaepkens, M., R. C. M. Bosch, T. Standaert, G. S. Oehrlein, and J. M. Cook (1998), Influence of reactor wall conditions on etch processes in inductively coupled fluorocarbon plasmas, *J. Vac. Sci. Technol. A*, *16*, 2099.

Schaffer, C. B., A. Brodeur, and E. Mazur (2001), Laser-induced breakdown and damage in bulk transparent materials induced by tightly focused femtosecond laser pulses, *Meas. Sci. Technol.*, *12*(11), 1784–1794.

Scheer, J. A., M. Wieser, P. Wurz, P. Bochsler, E. Hertzberg, S. A. Fuselier, F. A. Koeck, R. J. Nemanich, and M. Schleberger (2006), Conversion surfaces for neutral particle imaging detectors, *Adv. Space Res.*, *38*, 664–671.

Scheer, J. A., P. Wahlström, and P. Wurz (2007), Scattering of light molecules from Al_2O_3 surfaces, *Nucl. Inst. Meth. Phys. Res., B*, *256*(1), 76–80.

Schift, H. (2008), Nanoimprint lithography: An old story in modern times?, *J. Vac. Sci. Technol. B*, *26*, 458–480.

Schwadron, N. A. (1998), A model for pickup ion transport in the heliosphere in the limit of uniform hemispheric distributions, *J. Geophys. Res.*, *103*, 20,643–20,650.

Schwadron, N. A., and J. Geiss (2000), On the processing and transport of inner source hydrogen, *J. Geophys. Res.*, *105*, 7473–7482.

Schwadron, N. A., J. Geiss, L. A. Fisk, G. Gloeckler, T. H. Zurbuchen, and R. von Steiger (2000), Inner source distributions: Theoretical interpretation, implications, and evidence for inner source protons, *J. Geophys. Res.*, *105*, 7465–7472.

Schwartz, B., and H. Robbins (1961), Chemical Etching of Silicon III: A Temperature Study in the Acid System, *J. Electrochem. Soc.*, *108*(4), 365–372.

Schwartz, B., and H. Robbins (1976), Chemical Etching of Silicon IV: Etching Technology, *J. Electrochem. Soc.*, *123*(12), 1903–1909.

Scime, E. E., E. H. Anderson, D. J. McComas, and M. L. Schattenburg (1995), Extreme-ultraviolet polarization and filtering with gold transmission gratings, *Appl. Opt.*, *34*(4), 648–654.

Seidel, H., L. Csepregi, A. Heuberger, and H. Baumgärtel (1990a), Anisotropic Etching of Crystalline Silicon in Alkaline Solutions I: Orientation Dependence and Behavior of Passivation Layers, *J. Electrochem. Soc.*, *137*(11), 3612–3626.

Seidel, H., L. Csepregi, A. Heuberger, and H. Baumgärtel (1990b), Anisotropic Etching of Crystalline Silicon in Alkaline Solutions II: Influence of Dopants, *J. Electrochem. Soc.*, *137*(11), 3626–3632.

Senturia, S. D. (2001), *Microsystem Design*, Kluwer Academic Publishers.

Senturia, S. D., D. R. Day, M. A. Butler, and M. C. Smith (2005), Programmable diffraction gratings and their uses in displays, spectroscopy, and communications, *J. Microlith. Microfab. Microsys.*, *4*, 041,401.

Shah, L., A. Arai, S. Eaton, and P. Herman (2005), Waveguide writing in fused silica with a femtosecond fiber laser at 522 nm and 1 MHz repetition rate, *Opt. Exp.*, *13*(6), 1999–2006.

Shao, L., J. Liu, Q. Y. Chen, and W. K. Chu (2003), Boron diffusion in silicon: the anomalies and control by point defect engineering, *Mat. Sci. Eng. R*, *42*(3-4), 65–114.

Shukla, P. (2001), A survey of dusty plasma physics, *Physics of Plasmas*, *8*, 1791.

Silvestri, H. H. (2004), Diffusion in Silicon Isotope Heterostructures, Ph.D. thesis, University of California, Berkeley, Berkeley, CA.

Singh, P. K., and D. K. Das (1999), Modeling of diffusion and oxidation in two dimensions during silicon device processing, *Bull. Mater. Sci.*, *22*(3), 353–362.

Sittler, E. C., Jr., and M. Guhathakurta (1999), Semiempirical Two-dimensional MagnetoHydrodynamic Model of the Solar Corona and Interplanetary Medium, *Astrophys. J.*, *523*, 812–826.

Smith, D. L. (1995), *Thin-film Deposition: Principles and Practice*, McGraw-Hill Professional.

Solak, H. H. (2006), Nanolithography with coherent extreme ultraviolet light, *J. Phys. D: Appl. Phys*, *39*, R171–R188.

Solar Probe, S. (2008), Report of the Science and Technology Definition Team.

Solomon, S. C., R. L. McNutt, R. E. Gold, and D. L. Domingue (2007), MESSENGER Mission Overview, *Space Sci. Rev.*, *131*, 3–39.

Spierings, G. A. C. M. (1993), Wet chemical etching of silicate glasses in hydrofluoric acid based solutions, *J. Mater. Sci.*, *28*(23), 6261–6273.

Standaert, T., M. Schaepkens, N. R. Rueger, P. G. M. Sebel, G. S. Oehrlein, and J. M. Cook (1998), High density fluorocarbon etching of silicon in an inductively coupled plasma: Mechanism of etching through a thick steady state fluorocarbon layer, *J. Vac. Sci. Technol. A*, *16*, 239.

Standaert, T., C. Hedlund, E. A. Joseph, G. S. Oehrlein, and T. J. Dalton (2003), Role of fluorocarbon film formation in the etching of silicon, silicon dioxide, silicon nitride, and amorphous hydrogenated silicon carbide, *J. Vac. Sci. Technol. A*, *22*, 53.

Stark, B. (Ed.) (1999), *MEMS Reliability Assurance Guidelines for Space Applications*, Pasadena, CA, JPL Publication 99-1.

Steinsland, E., M. Nese, A. Hanneborg, R. W. Bernstein, H. Sandmo, and G. Kittilsland (1996), Boron etch-stop in TMAH solutions, *Sens. Actuators A*, *54*, 728–732.

Stoffel, A., A. Kovács, W. Kronast, and B. Müller (1996), LPCVD against PECVD for micromechanical applications, *J. Micromech. Microeng.*, *6*(1), 1–13.

Stolk, P. A., et al. (1997), Physical mechanisms of transient enhanced dopant diffusion in ion-implanted silicon, *J. Appl. Phys.*, *81*(9), 6031–6050.

Stone, E. C., A. M. Frandsen, R. A. Mewaldt, E. R. Christian, D. Margolies, J. F. Ormes, and F. Snow (1998), The Advanced Composition Explorer, *Space Sci. Rev.*, *86*, 1–22.

Strachan, L., R. Suleiman, A. V. Panasyuk, D. A. Biesecker, and J. L. Kohl (2002), Empirical Densities, Kinetic Temperatures, and Outflow Velocities in the Equatorial Streamer Belt at Solar Minimum, *Astrophys. J.*, *571*(2), 1008–1014.

Straub, H. C., M. A. Mangan, B. G. Lindsay, K. A. Smith, and R. F. Stebbings (1999), Absolute detection efficiency of a microchannel plate detector for kilo-electron volt energy ions, *Rev. Sci. Inst.*, *70*, 4238.

Su, S. Z., A. Rodríguez, S. M. Olaizola, C. S. Peng, Y. K. Verevkin, T. Berthoud, and S. Tisserand (2007), Current developments and applications using multi-beam laser interference lithography for nanoscale structuring of materials, *Proc. SPIE*, *6593*, 65,930G.

Sun, X., L. Zhuang, W. Zhang, and S. Y. Chou (1998), Multilayer resist methods for nanoimprint lithography on nonflat surfaces, *J. Vac. Sci. Technol. B*, *16*, 3922.

Sun, X. Q., T. Masuzawa, and M. Fujino (1996), Micro ultrasonic machining and its applications in MEMS, *Sens. Actuators A.*, *57*(2), 159–164.

Szegö, K., et al. (2000), Physics of Mass Loaded Plasmas, *Space Sci. Rev.*, *94*, 429–671.

Tan, H., A. Gilbertson, and S. Y. Chou (1998), Roller nanoimprint lithography, *J. Vac. Sci. Technol. B*, *16*, 3926.

Taniguchi, N. (1983), Current Status in, and Future Trends of, Ultraprecision Machining and Ultrafine Materials Processing, *CIRP Ann.*, *32*(2), 573–582.

Tas, N., T. Sonnenberg, H. Jansen, R. Legtenberg, and M. Elwenspoek (1996), Stiction in surface micromachining, *J. Micromech. Microeng*, *6*(4), 385–397.

Theiss, S. K., M. J. Caturla, M. D. Johnson, J. Zhu, T. Lenosky, B. Sadigh, and T. Diaz de la Rubia (2000), Atomic scale models of ion implantation and dopant diffusion in silicon, *Thin Solid Films*, *365*, 219–230.

Theodoridis, G., and F. Paolini (1969), The Angular Response of Spherical Plate Electrostatic Analyzers, *Rev. Sci. Inst.*, *40*, 621.

Thoe, T. B., D. K. Aspinwall, and M. L. H. Wise (1998), Review on ultrasonic machining, *Int. J. Mach. Tools Manuf.*, *38*(4), 239–255.

Tian, W. C., J. W. Weigold, and S. W. Pang (2000), Comparison of Cl_2 and F-based dry etching for high aspect ratio Si microstructures etched with an inductively coupled plasma source, *J. Vac. Sci. Technol. B*, *18*(4), 1890–1896.

Tiaw, K. S., M. H. Hong, and S. H. Teoh (2008), Precision laser micro-processing of polymers, *J. Alloys and Compounds*, *449*(1-2), 228–231.

Tobiska, W. K., W. R. Pryor, and J. M. Ajello (1997), Solar hydrogen Lyman-alpha variation during solar cycles 21 and 22, *Geophys. Res. Lett.*, *24*(9), 1123.

Tran, D. V., Y. C. Lam, H. Y. Zheng, B. S. Wong, and D. E. Hardt (2007), Direct observation of the temperature field during ablation of materials by multiple femtosecond laser pulses, *Appl. Surf. Sci.*, *253*(17), 7290–7294.

Tseng, A. A. (2004), Recent developments in micromilling using focused ion beam technology, *J. Micromech. Microeng*, *14*, R15–R34.

Turck-Chièze, S., and I. Lopes (1993), Toward a unified classical model of the Sun: on the sensitivity of neutrinos and helioseismology to the microscopic physics, *Astrophys. J.*, *408*(1), 347–367.

Turck-Chièze, S., S. Couvidat, L. Piau, J. Ferguson, P. Lambert, J. Ballot, R. A. García, and P. Nghiem (2004), Surprising Sun: A New Step Towards a Complete Picture?, *Phys. Rev. Lett.*, *93*(21), 211,102.

Turck-Chièze, S., et al. (2004), Looking for Gravity-Mode Multiplets with the GOLF Experiment aboard SOHO, *Astrophys. J.*, *604*, 455–468.

Uchida, T., and S. Hamaguchi (2008), Magnetic neutral loop discharge (NLD) plasmas for surface processing, *J. Phys. D: Appl. Phys*, *41*(083001), 083,001.

van Beek, J. T. M., R. C. Fleming, P. S. Hindle, J. D. Prentiss, M. L. Schattenburg, and S. Ritzau (1998), Nanoscale freestanding gratings for ultraviolet blocking filters, *J. Vac. Sci. Technol. B*, *16*(6), 3911–3916.

van Rijn, C. J. M. (2006), Laser interference as a lithographic nanopatterning tool, *J. Microlith. Microfab. Microsys.*, *5*(1), 011,012.

Vasile, M. J., C. Biddick, and S. A. Schwalm (1994), Microfabrication by ion milling: The lathe technique, *J. Vac. Sci. Technol. B*, *12*, 2388–2393.

Venables, J. A., G. D. T. Spiller, and M. Hanbücken (1984), Nucleation and growth of thin films, *Rep. Prog. Phys.*, *47*, 399–459.

Volland, B., F. Shi, P. Hudek, H. Heerlein, and I. W. Rangelow (1999), Dry etching with gas chopping without rippled sidewalls, *J. Vac. Sci. Technol. B*, *17*, 2768–2771.

Wang, Y., N. Dai, Y. Li, X. Wang, and P. Lu (2007), Ablation and cutting of silicon wafer and micro-mold fabrication using femtosecond laser pulses, *J. Las. Appl.*, *19*, 240–244.

Watanabe, T., K. Tatsumura, and I. Ohdomari (2006), New Linear-Parabolic Rate Equation for Thermal Oxidation of Silicon, *Phys. Rev. Lett.*, *96*(19), 196,102.

Webb, A., M. Osborne, G. Foster-Turner, and D. W. Dinkel (2008), Precision laser processing for micro electronics and fiber optic manufacturing, *Proc. SPIE*, *6880*, 688,003.

Weidenschilling, S. J., and A. A. Jackson (1993), Orbital Resonances and Poynting-Robertson Drag, *Icarus*, *104*(2), 244–254.

Weisskopf, M. C. (2003), The Chandra X-Ray Observatory: An overview, *Adv. Space Res.*, *32*(10), 2005–2011.

Wenzel, K.-P., R. G. Marsden, D. E. Page, and E. J. Smith (1989), Ulysses: The first high-latitude heliospheric mission, *Adv. Space Res.*, *9*, 25–29.

Wenzel, K.-P., R. G. Marsden, D. E. Page, and E. J. Smith (1992), The ULYSSES Mission, *Astron. Astrophys. Supl.*, *92*, 207–+.

Wesolek, D. M., F. A. Hererro, R. Osiander, and M. A. G. Darrin (2005), Design, fabrication, and performance of a micromachined plasma spectrometer, *J. Microlith. Microfab. Microsys.*, *4*, 041,403.

Wesolek, D. M., M. Darrin, and R. Osiander (2008), Wafer Scale Integration Enabling Space Science, *2008 IEEE Aerospace Conf.*, pp. 1–7.

Wilck, M., and I. Mann (1996), Radiation pressure forces on typical interplanetary dust grains, *Planetary and Space Science*, *44*(5), 493–499.

Wilhelm, K. (2006), Solar VUV measurements obtained by SOHO instruments and their radiometric calibration, *Adv. Space Res.*, *37*(2), 225–233.

Williams, K. R., and R. S. Muller (1996), Etch rates for micromachining processing, *J. Microelectromech. Syst.*, *5*(4), 256–269.

Williams, K. R., K. Gupta, and M. Wasilik (2003), Etch rates for micromachining processing II, *J. Microelectromech. Syst.*, *12*(6), 761–778.

Willoughby, A. F. W. (1978), Atomic diffusion in semiconductors, *Rep. Prog. Phys.*, *41*(10), 1665–1705.

Wimmer-Schweingruber, R. F., and P. Bochsler (2003), On the origin of inner-source pickup ions, *Geophys. Res. Lett.*, *30*(2), 020,000–1.

Winterhalter, D., E. J. Smith, M. E. Burton, N. Murphy, and D. J. McComas (1994), The heliospheric plasma sheet, *J. Geophys. Res*, *99*(A4), 6667–6680.

Winters, H. F., and J. W. Coburn (1992), Surface science aspects of etching reactions, *Surf. Sci. Rep.*, *14*(4-6), 162–269.

Wiza, J. L. (1979), Microchannel plate detectors, *Nucl. Instrum. Methods*, *162*, 587–601.

Woldering, L. A., R. W. Tjerkstra, H. V. Jansen, I. D. Setija, and W. L. Vos (2008), Periodic arrays of deep nanopores made in silicon with reactive ion etching and deep UV lithography, *Nanotechnology*, *19*(145304), 145,304.

Woo, R., and S. R. Habbal (2005), Origin and acceleration of the slow solar wind, *Astrophys. J. Lett.*, *629*(2), 129–132.

Wood, R. W. (1902), On a remarkable case of uneven distribution of light in a diffraction grating spectrum, *Proc. Phys. Soc. London*, *18*, 269–275.

Wood, R. W. (1935), Anomalous Diffraction Gratings, *Phys. Rev.*, *48*(12), 928–936.

Wu, B., and A. Kumar (2007), Extreme ultraviolet lithography: A review, *J. Vac. Sci. Technol. B*, *25*(6), 1743–2664.

Wurz, P., L. Saul, J. A. Scheer, E. Möbius, H. Kucharek, and S. A. Fuselier (2008), Negative helium generation upon surface scattering: Application in space science, *J. Appl. Phys.*, *103*, 054,904.

Wyatt, S. P., and F. L. Whipple (1950), The Poynting-Robertson effect on meteor orbits, *Astrophy. J.*, *111*, 134.

Xie, Q., M. H. Hong, H. L. Tan, G. X. Chen, L. P. Shi, and T. C. Chong (2008), Fabrication of nanostructures with laser interference lithography, *J. Alloys Compd.*, *449*(1-2), 261–264.

Xie, Y., A. R. Zakharian, J. V. Moloney, and M. Mansuripur (2006a), Transmission of light through periodic arrays of sub-wavelength slits in metallic hosts, *Opt. Exp.*, *14*(14), 6400–6413.

Xie, Y., A. R. Zakharian, J. V. Moloney, and M. Mansuripur (2006b), Optical transmission at oblique incidence through a periodic array of sub-wavelength slits in a metallic host, *Opt. Exp.*, *14*(22), 10,220–10,227.

Young, D. T. (1998), Space plasma particle instrumentation and the new paradigm: Faster, cheaper, better, *Geophysical monograph*, *102*, 1–16.

Young, D. T., S. J. Bame, M. F. Thomsen, R. H. Martin, J. L. Burch, J. A. Marshall, and B. Reinhard (1988), 2π-radian field-of-view toroidal electrostatic analyzer, *Rev. Sci. Inst.*, *59*, 743.

Young, D. T., et al. (2004), Cassini Plasma Spectrometer Investigation, *Space Sci. Rev.*, *114*, 1–112.

Yu, Z., W. Wu, L. Chen, and S. Y. Chou (2001), Fabrication of large area 100 nm pitch grating by spatial frequency doubling and nanoimprint lithography for subwavelength optical applications, *J. Vac. Sci. Technol. B*, *19*, 2816.

Zhou, R., H. Zhang, Y. Hao, and Y. Wang (2004), Simulation of the Bosch process with a string-cell hybrid method, *J. Micromech. Microeng.*, *14*(7), 851–858.

Ziegler, J. F. (2004), SRIM-2003, *Nucl. Instrum. Methods Phys. Res. B*, *219*, 1027–1036.

Zurbuchen, T., P. A. Bochsler, and F. Scholze (1995), Reflection of ultraviolet light at 121.6 nm from rough surfaces, *Opt. Eng.*, *34*, 1303–1315.

Zurbuchen, T. H., G. Gloeckler, J. C. Cain, S. E. Lasley, and W. Shanks (1998), A low-weight Plasma Instrument to be used in the Inner Heliosphere, *Proc. SPIE*, *3442*, 217–224.